



Michigan Technological University  
*Create the Future* Digital Commons @ Michigan Tech

---

Dissertations, Master's Theses and Master's  
Reports - Open

Dissertations, Master's Theses and Master's  
Reports

---

2013

## Development and characterization of fluorescent pH sensors based on porous silica and hydrogel support matrices

Qili Hu

*Michigan Technological University*

Follow this and additional works at: <https://digitalcommons.mtu.edu/etds>

 Part of the [Chemistry Commons](#)


Copyright 2013 Qili Hu

---

### Recommended Citation

Hu, Qili, "Development and characterization of fluorescent pH sensors based on porous silica and hydrogel support matrices", Dissertation, Michigan Technological University, 2013.  
<https://doi.org/10.37099/mtu.dc.etds/757>

Follow this and additional works at: <https://digitalcommons.mtu.edu/etds>

 Part of the [Chemistry Commons](#)

THE DEVELOPMENT AND CHARACTERIZATION OF FLUORESCENT pH  
SENSORS BASED ON SILICA AND HYDROGEL SUPPORT MATRICES

By

Qili Hu

A DISSERTATION

Submitted in partial fulfillment of the requirements for the degree of

DOCTOR OF PHILOSOPHY

In Chemistry

MICHIGAN TECHNOLOGICAL UNIVERSITY

2013

© 2013 Qili Hu





This dissertation, “The development and characterization of fluorescent pH sensors based on silica and hydrogel support matrices,” is hereby approved in partial fulfillment for the requirements for the Degree of DOCTOR OF PHILOSOPHY in IN CHEMISTRY.

Chemistry

Dissertation Advisor: Dr. Sarah A. Green

Committee Member: Dr. Rudy Luck

Committee Member: Dr. Lynn R. Mazzoleni

Committee Member: Dr. Paul L. Bergstrom

Department Chair: Dr. Sarah A. Green



To my parents & my brother.



# CONTENTS

<b>List of Figures</b>	xvi
<b>List of Tables</b>	xxiv
<b>Acknowledgments</b>	xxv
<b>Lists of abbreviations</b>	xxvii
<b>Abstract</b>	xxix
<b>1 Introduction</b>	1
1.1 Dissertation overview	1
1.1.1 Dissertation goal	1
1.1.2 Dissertation outline	2
1.2 pH definition and measurement	3

1.2.1	pH definition . . . . .	3
1.2.2	Traditional pH measurements . . . . .	5
1.2.2.1	Potentiometric methods . . . . .	5
1.2.2.2	Spectrophotometric methods . . . . .	7
1.3	Fluorescence . . . . .	11
1.3.1	Physical principles . . . . .	11
1.3.2	Fluorescence sensing . . . . .	16
1.4	Literature review of optical pH sensors . . . . .	18
1.4.1	Indicator immobilization methods . . . . .	19
1.4.1.1	Adsorption . . . . .	19
1.4.1.2	Entrapment . . . . .	20
1.4.1.3	Covalent binding . . . . .	22
1.4.2	Detection methods . . . . .	23
1.4.2.1	Absorption . . . . .	23
1.4.2.2	Fluorescence . . . . .	24
1.4.2.3	Fluorescence lifetime . . . . .	25
1.4.3	Other kinds of pH sensors . . . . .	26

1.4.4	Applications . . . . .	28
<b>2</b>	<b>Covalent binding of fluorescein to porous silica for optical pH sensing . . . .</b>	<b>30</b>
2.1	Introduction . . . . .	30
2.1.1	Mesoporous silica . . . . .	30
2.1.2	Fluorescein . . . . .	34
2.1.3	Specific aims of this study . . . . .	35
2.2	Experimental . . . . .	36
2.2.1	Reagents and materials . . . . .	36
2.2.2	Monolayer preparation . . . . .	37
2.2.3	Instrumentation . . . . .	39
2.3	Results and Discussion . . . . .	40
2.3.1	Confirmation of covalent binding of FITC on substrates surface . .	40
2.3.1.1	Substrate color change . . . . .	40
2.3.1.2	Monolayer quantification . . . . .	41
2.3.1.3	FTIR spectrum of porous silica . . . . .	41
2.3.2	Fluorescence measurements . . . . .	42
2.3.2.1	Fluorescein in buffer solution . . . . .	42



2.3.2.2	FITC bound on quartz slides . . . . .	47
2.3.2.3	FITC bound on glass beads . . . . .	49
2.3.2.4	FITC bound in porous silica . . . . .	52
2.3.3	Effects of porous silica on FITC fluorescence . . . . .	54
2.3.3.1	$pK_a^*$ shift . . . . .	54
2.3.3.2	Ionic strength effects . . . . .	56
2.3.3.3	Fluorescence lifetimes . . . . .	60
2.3.4	Sensor performance . . . . .	62
2.4	Conclusion . . . . .	64
2.5	Future work . . . . .	64
<b>3</b>	<b>Physical entrapment of indicators in porous silica through sol-gel process for</b>	
	<b>pH sensing . . . . .</b>	<b>65</b>
3.1	Introduction . . . . .	65
3.1.1	the Sol-Gel process . . . . .	65
3.1.2	pH-sensitive indicators information . . . . .	70
3.1.3	Specific aims of this study . . . . .	72
3.2	Experimental . . . . .	74

3.2.1	Reagents and materials . . . . .	74
3.2.2	Synthesis of ion-pairs . . . . .	75
3.2.3	Synthesis of sol-gel films . . . . .	76
3.2.4	Instrumentation . . . . .	77
3.3	Results and discussion . . . . .	78
3.3.1	Sol-gel film characterization . . . . .	78
3.3.1.1	Catalyst effects . . . . .	78
3.3.1.2	Morphology . . . . .	78
3.3.1.3	Film thickness . . . . .	79
3.3.1.4	FTIR spectra . . . . .	80
3.3.2	Fluorescent spectral behavior of indicator ion-pairs in sol-gel films .	80
3.3.2.1	FS-CTAB in sol-gel films . . . . .	82
3.3.2.2	HPTS-CTAB in sol-gel films . . . . .	83
3.3.3	pK <sub>a</sub> shift . . . . .	87
3.3.3.1	Sol-gel matrix effect . . . . .	87
3.3.3.2	Ionic strength effect . . . . .	88
3.3.3.3	Film thickness effect . . . . .	89

3.3.3.4	GPTMS-ETEOS ratio effect . . . . .	90
3.3.4	Fluorescence lifetime data . . . . .	90
3.3.5	Sensor performance . . . . .	91
3.4	Conclusion . . . . .	99
3.5	Future work . . . . .	100
<b>4</b>	<b>Spectral behaviors and pH sensitivity of indicators immobilized in hydrogel .</b>	<b>101</b>
4.1	Introduction . . . . .	101
4.1.1	Hydrogel . . . . .	101
4.1.2	pH sensitive indicators . . . . .	107
4.1.2.1	DHPDS . . . . .	108
4.1.2.2	DHNDs . . . . .	110
4.1.2.3	CR . . . . .	112
4.1.3	Specific aims of this study . . . . .	112
4.2	Experimental . . . . .	122
4.2.1	Reagents and materials . . . . .	122
4.2.2	Synthesis of hydrogels . . . . .	123
4.2.2.1	Synthesis of methacryloyl-analogs . . . . .	123

4.2.2.2	Synthesis of PEG hydrogels . . . . .	123
4.2.2.3	Physical entrapment of indicator ion-pairs in hydrogel . .	127
4.2.2.4	Covalent bound of indicator in hydrogel . . . . .	128
4.2.3	Characterization and Instrumentation . . . . .	129
4.3	Results and Discussion . . . . .	130
4.3.1	Properties of PEG hydrogels . . . . .	130
4.3.1.1	Swelling ratio . . . . .	131
4.3.1.2	Structural properties . . . . .	134
4.3.2	Synthesis of methacryloyl-analogs and hydrogels . . . . .	134
4.3.2.1	FTIR conformation of methacryloyl-analogs . . . . .	135
4.3.2.2	NMR spectra conformation of methacryloyl-analogs . . .	137
4.3.2.3	FTIR spectra of PEG and CR-PEG hydrogels . . . . .	138
4.3.3	Spectral behaviors of immobilized indicators in hydrogels . . . . .	143
4.3.3.1	FS-CTAB in hydrogel . . . . .	143
4.3.3.2	HPTS-CTAB in hydrogel . . . . .	146
4.3.3.3	HPDS-PEG hydrogel . . . . .	148
4.3.3.4	HNDS-PEG hydrogel . . . . .	152

4.3.3.5	CR-PEG hydrogel . . . . .	155
4.3.4	pK <sub>a</sub> shift of immobilized indicators in hydrogel . . . . .	158
4.3.5	Fluorescence lifetime measurements . . . . .	160
4.3.6	Sensor performance . . . . .	162
4.3.6.1	Potential use of CR-PEG hydrogel as reusable "pH paper" . . . . .	162
4.3.6.2	Equilibrium time . . . . .	162
4.3.6.3	Long term stability . . . . .	165
4.4	Conclusion . . . . .	165
4.5	Future work . . . . .	166
<b>5</b>	<b>Conclusions . . . . .</b>	<b>168</b>
	<b>References . . . . .</b>	<b>173</b>
	<b>Appendices . . . . .</b>	<b>192</b>
<b>A</b>	<b>Supplement information . . . . .</b>	<b>193</b>
A.1	List of indicators . . . . .	193
A.1.1	Indicator structures . . . . .	193
A.1.2	Indicators pK <sub>a</sub> values in solution and different matrix . . . . .	193

A.2	Supplement information for Chapter 2 . . . . .	196
A.2.1	Extinction coefficients and quantum yield of fluorescein in buffer .	196
A.2.2	Fluorescence spectra of FITC on quartz slide . . . . .	198
A.2.3	$pK_a^*$ of FITC on glass beads . . . . .	198
A.3	Supplement information for Chapter 3 . . . . .	200
A.3.1	FTIR spectra of indicator ion-pairs and sol-gel films . . . . .	200
A.3.2	Thin film thickness of sol-gel films . . . . .	201
A.4	Supplement information for Chapter 4 . . . . .	202
A.4.1	Absorption and fluorescence excitation spectra of DHPDS in buffer	202
A.4.2	Normalized absorption and fluorescence excitation spectra of DHNDs in buffer . . . . .	202
A.4.3	Calculated swelling ratio against ionic strength of solution . . . . .	203
A.4.4	Equilibrium time of HPDS-PEG hydrogel upon pH change . . . . .	203
<b>B</b>	<b>Copyright agreements . . . . .</b>	<b>207</b>

# LIST OF FIGURES

1.1	Representative absorbance spectra of protonated and deprotonated spectra of cresol red in buffer solution . . . . .	9
1.2	One Jabłoński diagram of absorbance, fluorescence and phosphorescence .	12
1.3	Fluorescence excitation and emission spectra of HPTS in solution . . . . .	15
1.4	Phase transition behavior of polyelectrolyte hydrogels . . . . .	26
2.1	The schematic illustration of the synthesis of mesoporous silica . . . . .	30
2.2	Optical photographs of mesoporous silicon and mesoporous silica . . . . .	31
2.3	SEM images of porous silicon and porous silica samples . . . . .	32
2.4	The measured refractive index and extinction coefficient of mesoporous silica	33
2.5	UV-Vis absorption spectra of fluorescein in solution . . . . .	35
2.6	Schematic representation of FITC covalently bound to silica surface . . . .	38
2.7	Top view of the fluorescence spectra measurement setup . . . . .	40

2.8	Images of glass beads and porous silica substrates before and after reaction	41
2.9	Monolayer thickness fitting by ellipsometry for FITC bound to silicon wafer surface . . . . .	41
2.10	FTIR spectrum of porous silica substrate . . . . .	42
2.11	Normalized UV-Vis absorption spectra of fluorescein in solution . . . . .	44
2.12	Ground state $pK_a$ of dissolved fluorescein in solution . . . . .	44
2.13	The protolytic equilibrium of ground and excited state fluorescein . . . . .	45
2.14	Fluorescence excitation and emission spectra of fluorescein in solution . . .	46
2.15	Normalized fluorescence excitation spectra of fluorescein in solution . . . .	48
2.16	Excited state $pK_a^*$ of dissolved fluorescein in solution . . . . .	48
2.17	Fluorescence excitation and emission spectra of FITC on quartz slide . . . .	49
2.18	Fluorescence excitation spectra of FITC in different matrices . . . . .	50
2.19	Normalized fluorescence excitation spectra of FITC on glass beads . . . . .	51
2.20	Normalized fluorescence excitation spectra of FITC in porous silica . . . .	52
2.21	pH sensitive range and $pK_a^*$ value of FITC in porous silica in solution . . .	53
2.22	Schematic representation of silanol groups at the silica surface . . . . .	55
2.23	Experimental and ideal behavior of FITC dissociation in porous silica . . .	55



2.24	Comparison of pH measurement from optical sensor and pH from electrode	57
2.25	$pK_a$ and $pK_a^*$ of fluorescein in buffer with different ionic strength . . . . .	58
2.26	$pK_a^*$ of fluorescein in silica in solution with different ionic strength . . . . .	59
2.27	Fluorescence decay curves for fluorescein in buffer and FITC in porous silica	61
2.28	Repeatability of the excitation ratio of FITC in porous silica at different pH	63
3.1	Schematic picture of the sol-gel transition . . . . .	68
3.2	Structure of GPTMS-derived network after epoxy ring opening . . . . .	70
3.3	UV-Vis absorption spectra of HPTS in solution . . . . .	71
3.4	Fluorescence spectra of HPTS in ethanol and solution . . . . .	73
3.5	Fluorescence excitation spectra of HPTS in solution with different pH . . .	74
3.6	Chemical structure of ion-pairs . . . . .	75
3.7	The top view of fluorescence spectra measurement set-up . . . . .	77
3.8	SEM image of sol-gel thin film . . . . .	79
3.9	FTIR spectra of mesoporous silica and sol-gel films . . . . .	81
3.10	Fluorescence excitation and emission spectra of FS-CTAB in sol-gel film .	83
3.11	Normalized fluorescence excitation spectra and $pK_a^*$ of FS in sol-gel film . .	84
3.12	pH sensitive ranges of FS and HPTS in sol-gel film . . . . .	85

3.13	The protolytic equilibrium of ground and excited state HPTS . . . . .	85
3.14	$pK_a$ of HPTS in solution . . . . .	86
3.15	Fluorescence spectra of HPTS in ethanol, sol-gel films and solution . . . .	93
3.16	Normalized fluorescence excitation spectra and $pK_a$ of HPTS-CTAB in sol-gel film . . . . .	94
3.17	$pK_a^*$ of FS and $pK_a$ of HPTS in solution and sol-gel films with different ionic strengths . . . . .	95
3.18	$pK_a^*$ of FS-CTAB in sol-gel films with different thickness in solution . . . .	95
3.19	$pK_a$ of HPTS-CTAB in sol-gel films with different thickness in buffer solution	96
3.20	$pK_a$ of HPTS in sol-gel films with different GPTMS-ETEOS ratios . . . . .	96
3.21	Fluorescence decay curves for FS and HPTS in buffer and sol-gel films . .	97
3.22	Equilibrium time of HPTS immobilized sol-gel films in solution . . . . .	98
4.1	Illustration of crosslinked hydrogel structure . . . . .	102
4.2	Illustration of chain entanglements and network defects that can form during crosslinking . . . . .	103
4.3	UV-Vis absorption spectra of DHPDS in ethanol and different pH solution .	109
4.4	Protonic equilibrium of DHPDS in buffer . . . . .	109

4.5	Fluorescence excitation and emission spectra of DHPDS in ethanol and different pH solution . . . . .	114
4.6	$pK_a$ values of DHPDS in solution from absorption and fluorescence excitation spectra . . . . .	115
4.7	UV-Vis absorption spectra of DHNDS in both solution and ethanol . . . .	116
4.8	Fluorescence spectra of DHNDS in both ethanol and solution . . . . .	117
4.9	$pK_a$ values of DHNDS in solution . . . . .	118
4.10	Fluorescence intensity change of DHNDS in different solutions in 1 day . .	118
4.11	UV-Vis absorption spectra of DHNDS in different solution after 1 day . . .	119
4.12	Fluorescence spectra of HNDS in buffer solution . . . . .	120
4.13	UV-Vis absorption spectra of cresol red in solution . . . . .	121
4.14	$pK_a$ of cresol red in solution . . . . .	121
4.15	Reaction scheme of preparation of MA-CR, MA-HPDS and MA-HNDS . .	124
4.16	Reaction setup for hydrogel synthesis with free radical initiator . . . . .	125
4.17	Teflon mold and cover for hydrogel synthesis with redox initiation system .	127
4.18	UV-Vis Absorption and fluorescence measurement set-up . . . . .	130
4.19	Swelling ratio of PEG hydrogels of different precursor percentages in DI water . . . . .	131

4.20	SEM images of freeze dried PEG hydrogels . . . . .	133
4.21	FTIR spectra of cresol red sodium salt and MA-CR . . . . .	136
4.22	FTIR spectra of DHNDS and MA-HNDS . . . . .	136
4.23	FTIR spectra of DHNDS and MA-HNDS . . . . .	137
4.24	$^1\text{H}$ -NMR spectra of CR in $\text{D}_2\text{O}$ . . . . .	139
4.25	$^1\text{H}$ -NMR spectra of MA-CR in $\text{D}_2\text{O}$ . . . . .	140
4.26	$^1\text{H}$ -NMR spectra of DHPDS in $\text{D}_2\text{O}$ . . . . .	141
4.27	$^1\text{H}$ -NMR spectra of MA-HPDS in $\text{D}_2\text{O}$ . . . . .	142
4.28	FTIR spectra of dried PEG and CR-PEG hydrogels . . . . .	143
4.29	The fluorescence spectra of FS-CTAB in hydrogel in solution . . . . .	144
4.30	Normalized fluorescence excitation spectra and $\text{pK}_a^*$ of FS-CTAB in hydrogel	145
4.31	Fluorescence excitation and emission spectra of HPTS-CTAB in hydrogel	147
4.32	Fluorescence emission spectra of precursor solution of HPTS-CTAB with or without free radical initiator, AIBN . . . . .	149
4.33	Normalized fluorescence excitation spectra and $\text{pK}_a$ of HPTS-CTAB in hy- drogel . . . . .	150
4.34	pH sensitive range of FS-CTAB and HPTS-CTAB in hydrogel . . . . .	151
4.35	Fluorescence spectra of HPDS-PEG hydrogel in hydrogel . . . . .	152

4.36	Normalized fluorescence excitation spectra and $pK_a$ of HPDS-PEG hydrogel in solution . . . . .	153
4.37	pH sensitive range of HPDS-PEG, HNDS-PEG and CR-PEG hydrogels . .	154
4.38	Fluorescence spectra of HNDS-PEG hydrogel in solution . . . . .	155
4.39	Normalized fluorescence excitation spectra and $pK_a$ of HNDS-PEG hydrogel in solution . . . . .	156
4.40	UV-Vis absorption spectra and $pK_a$ of CR-PEG hydrogel in solution . . . .	157
4.41	Fluorescence decay curves for indicators physically entrapped in hydrogel .	161
4.42	Fluorescence decay curves for fluorescent indicators bound in hydrogel . .	163
4.43	The Color change of CR-PEG in different pH buffer solution . . . . .	164
4.44	The equilibrium time of CR-PEG upon media pH change . . . . .	164
A.1	Extinction coefficients of monoanion and dianion fluorescein in various wavelength . . . . .	197
A.2	Quantum yield of monoanion and dianion fluorescein . . . . .	198
A.3	Normalized fluorescence excitation spectra of FITC on quartz slide in solution	199
A.4	$pK_a^*$ of FITC on glass beads in solution . . . . .	199
A.5	FTIR spectra of HPTS, CTAB and indicator ion-pair HPTS-CTAB . . . . .	200
A.6	FTIR spectra of sol-gel precursors ETEOS and GPTMS and sol-gel film . .	201

A.7	Ellipsometry data and fitting of sol-gel thin films . . . . .	202
A.8	Absorption and fluorescence excitation spectra of DHPDS in solution . . .	203
A.9	Normalized UV-Vis absorption and fluorescence excitation spectra of DHNDS in solution . . . . .	204
A.10	Swelling ratio of 7.5% PEG hydrogels in KCl solution with different con- centration . . . . .	205
A.11	Equilibrium time of HPDS-PEG upon pH change of solution . . . . .	205

## LIST OF TABLES

2.1	The acid dissociation constants of fluorescein and FITC in porous silica . .	59
2.2	Fluorescence lifetime of fluorescein in buffer and FITC in porous silica . .	60
3.1	Film thickness of different sol-gel thin films . . . . .	80
3.2	Fluorescence lifetimes of fluorescent dyes in solution and sol-gel thin films	92
4.1	Swelling ratios of PEG hydrogels in different pH media . . . . .	132
4.2	Properties of PEG hydrogels with different precursor percentage . . . . .	135
4.3	A list of $pK_a$ values of indicators in solution and hydrogels. . . . .	158
4.4	Fluorescence lifetimes of fluorescent dyes in solution and PEG hydrogels .	160
5.1	Comparison of properties of mesoporous silica, sol-gel films and hydrogels	171
A.1	A list of indicators used in this dissertation . . . . .	194
A.2	A list of indicators $pK_a$ values in solution and different matrix . . . . .	195

## ACKNOWLEDGMENTS

An important stage in my life comes to an end, and I would not be able to complete my Ph.D without the guidance and the help of the ones who in one way or another contributed and extended their valuable assistance.

First and foremost, I want to thank my advisor, Dr. Sarah Green, for welcoming me into her group, for believing in me and for her guidance and support through all these years.

I owe great thanks to my committee members: Dr. Rudy Luck, Dr. Lynn Mazzoleni and Dr. Paul Bergstrom, for their valuable advice for my original research proposal and my dissertation.

I would like to thank Dr. Paul Bergstrom and Dr. Kumar Vanga for all the support for the mesoporous silica project. I also want to thank Dr. Patrica Heiden and Xiaochu Ding for their valuable suggestions and help for hydrogel synthesis.

I want to thank Bill Knudsen, Owen P Mills, Thomas Daunais, and Felicia Nip for helping me use the spinner, the elliposometer and taking SEM images for me.

I am grateful to Chemistry Department for the financial support. I appreciate the support from my TA supervisor, Lorri Reilly, and Aparna Pandey. They made everything so easy,



clear and efficient, and I really enjoyed working with them. Many Thanks go to Jerry Lutz, Jerry Norkol, and Dean Seppala for all the technique support during these years.

During my time at MTU I am so happy that I have met so many great friends, with them I shared unforgettable times through these years. Thanks for everything, Ding Chu, Liu Chen, Yunzhu Zhao, Kenny Ng, Martha Barajas, Xi Lin, Na Hu and Libin Jia.

Last but not least, I want to say special thanks to my family, my father, Jianming Hu, my mother, Guiling Fan, my brother, Qilong Hu and my boyfriend, Jindong Zhang. Thanks for believing in me and for making me feel all your love and support from such a long distance.

## LISTS OF ABBREVIATIONS

ABIN	azobisisobutyronitrile
APTES	3-aminopropyltriethoxysilane
CR	cresol red
CTAB	hexadecyltrimethylammonium bromide
DHPDS	6,8-dihydroxypyrene-1,3-disulfonic acid, disodium salt
DHNS	2,7-dihydroxynaphthalene-3,6-disulfonic acid, disodium salt
ETEOS	ethyltriethoxysilane
FITC	fluorescein-5-isothiocyanate
FS	fluorescein-5-(and-6)-sulfonic acid, trisodium salt
IS	ionic strength
GPTMS	3-glycidoxypentyltrimethoxysilane
HNDS	2-hydroxynaphthalene-3,6-disulfonic acid, disodium salt
HPTS	8-hydroxypyrene-1,3,6-trisulfonic acid, trisodium salt
KPS	potassium persulfate
MA	methacrylic anhydride
MI	1-methylimidazole
PEG	poly(ethylene glycol)
PEGDA	poly(ethylene glycol) diacrylate
$pK_a$	ground state acid dissociation constant
$pK_a^*$	excited state acid dissociation constant



# **The development and characterization of fluorescent pH sensors based on silica and hydrogel support matrices**

Qili Hu

Michigan Technological University, 2013

Advisor: Dr. Sarah A. Green

## **Abstract**

The hydrogen ion activity (pH) is a very important parameter in environment monitoring, biomedical research and other applications. Optical pH sensors have several advantages over traditional potentiometric pH measurement, such as high sensitivity, no need of constant calibration, easy for miniaturization and possibility for remote sensing. Several pH indicators has been successfully immobilized in three different solid porous materials to use as pH sensing probes.

The fluorescent pH indicator fluorescein-5-isothiocyanate (FITC) was covalently bound onto the internal surface of porous silica (pore size  $\sim 10$  nm) and retained its pH sensitivity. The excited state  $pK_a^*$  of FITC in porous silica (5.58) was slightly smaller than in solution (5.68) due to the free silanol groups (Si-OH) on the silica surface. The pH sensitive range for this probe is pH 4.5 - 7.0 with an error less than 0.1 pH units. The probe response was reproducible and stable for at least four month, stored in DI water, but exhibit a long equilibrium of up to 100 minutes.

Sol-gel based pH sensors were developed with immobilization of two fluorescent pH indicators fluorescein-5-(and-6)-sulfonic acid, trisodium salt (FS) and 8-hydroxypyrene-1,3,6-trisulfonic acid (HPTS) through physical entrapment. Prior to immobilization,

the indicators were ion-paired with a common surfactant hexadecyltrimethylammonium bromide (CTAB) in order to prevent leaching. The sol-gel films were synthesized through the hydrolysis of two different precursors, ethyltriethoxysilane (ETEOS) and 3-glycidoxypopyltrimethoxysilane (GPTMS) and deposited on a quartz slide through spin coating. The  $pK_a$  of the indicators immobilized in sol-gel films was much smaller than in solutions due to silanol groups on the inner surface of the sol-gel films and ammonium groups from the surrounding surfactants. Unlike in solution, the apparent  $pK_a$  of the indicators in sol-gel films increased with increasing ionic strength. The equilibrium time for these sensors was within 5 minutes (with film thickness of  $\sim 470$  nm).

Polyethylene glycol (PEG) hydrogel was of interest for optical pH sensor development because it is highly proton permeable, transparent and easy to synthesize. pH indicators can be immobilized in hydrogel through physical entrapment and copolymerization. FS and HPTS ion-pairs were physically entrapped in hydrogel matrix synthesized via free radical initiation. For covalent immobilization, three indicators, 6,8-dihydroxypyrene-1,3-disulfonic acid (DHPDS), 2,7-dihydroxynaphthalene-3,6-disulfonic acid (DHNS) and cresol red were first reacted with methacrylic anhydride (MA) to form methacryloyl-analogs for copolymerization. These hydrogels were synthesized in aqueous solution with a redox initiation system. The thickness of the hydrogel film is controlled as  $\sim 0.5$  cm and the porosity can be adjusted with the percentage of polyethylene glycol in the precursor solutions. The  $pK_a$  of the indicators immobilized in the hydrogel both physically and covalently were higher than in solution due to the medium effect. The sensors are stable and reproducible with a short equilibrium time (less than 4 minutes). In addition, the color change of cresol red immobilized hydrogel is vivid from yellow (acidic condition) to purple (basic condition). Due to covalently binding, cresol red was not leaching out from the hydrogel, making it a good candidate of reusable "pH paper".

# **1. INTRODUCTION**

## **1.1 Dissertation overview**

### **1.1.1 Dissertation goal**

My dissertation project focuses on optical pH sensor development and characterization. pH is a commonly measured parameter in many applications such as environment monitoring, bioprocessing and biomedical diagnosis. The traditional pH electrodes behave unpredictable in low ionic strength solution and need to be calibrated frequently. Optical pH sensing has many advantages over electrochemical technique including high sensitivity, no need for a reference signal, immunity to electrical interference, and possibility of remote sensing. Optical pH sensors are obtained by covalently binding or physically entrapment of various pH indicators into three different matrices: mesoporous silica, sol-gel films and hydrogel films. The properties of these matrices such as network structure were characterized. The spectra behavior of indicators in different matrices as well as in buffer solution was studied. The potential of these dyes immobilized matrices as optical pH sensors was also evaluated.

The purpose of this dissertation work is two-fold:

- First, to synthesize three different matrices: mesoporous silica, sol-gel films and hydrogels and to covalently bind or physically entrap various pH indicators in to these matrices.
- Second, to study the performance of these pH sensors including the properties of the matrices and the behaviors of dyes in matrices such as spectral shifts,  $pK_a$  shifts, fluorescence lifetimes, leaching, reproducibility and stability to evaluate their potential for pH sensing.

### 1.1.2 Dissertation outline

This chapter first introduces pH and the present methods for pH measurement, and then introduces fluorescence spectroscopy as fluorescent ratiometric method was the detection method for pH measurements in this study. Lastly, this chapter reviews the present works of optical pH sensor development.

Chapter 2 presents the optical sensor development based on covalently binding a fluorescent pH indicator, fluorescein, on the internal surface of mesoporous silica. The morphology of the mesoporous silica and the fluorescence behavior of fluorescein in porous silica were studied.

In chapter 3 we present sol-gel based pH sensors. The sol-gel thin films were synthesized based on the catalyzed hydrolysis of ORganically MOdified SILicates (ORMOSILs). Fluorescent pH indicators were first ion-paired with a common surfactant and then physically doped in the thin films during the sol-gel process. The spectra behavior of these two indicators in sol-gel thin films was studied and compared with solution phase.

Chapter 4 presents hydrogel based pH sensors. The polyethylene glycol hydrogel was synthesized by polymerization of polyethylene glycol diacrylate (PEGDA) using both free radical initiator and redox initiation system. Network properties such as morphology and swelling properties of the hydrogel were studied. Various fluorescent indicators were immobilized in the hydrogel by both physical entrapment and covalent binding. The spectral behavior of immobilized indicators in hydrogel was obtained. Sensor performances such as equilibrium time, leaching, stability were studied.

Finally, chapter 5 presents the conclusion for this dissertation work as well as the outlook for further work based on the analysis of the material presented in the previous chapters.

## **1.2 pH definition and measurement**

### **1.2.1 pH definition**

The concept of pH was first introduced by Danish chemist Søren Peder Lauritz Sørensen in 1909 and revised to the modern pH in 1924 because of its definition and measurements in terms of electrochemical cells. In chemistry, pH is a measure of the activity of the hydrogen ion,  $H^+$ . pH is defined as the negative logarithm of the hydrogen ion activity,  $a_{H^+}$  in a solution.

$$pH = -\log_{10}(a_{H^+}) \quad (1.1)$$



This definition was adopted because ion-selective electrodes are used to measure pH, and the pH glass electrode is sensitive to hydrogen ion activity  $a_{H^+}$ . The activity of the hydrogen ion can be defined by its relation to concentration ( $[H^+]$ , M) and the activity coefficient,  $\gamma_{H^+}$ , according to Debye-Hückel theory:

$$a_{H^+} = \gamma_{H^+} [H^+] \quad (1.2)$$

If the activity coefficient is unity, then activity is equal to concentration. This assumption is true only in diluted solutions, where ionic strength is low. It is important to know what factors influence the activity coefficient in order to know how they influence the pH measurement.

The factors that affect the activity coefficient are temperature ( $T$ ), the ionic strength ( $I$ ), the dielectric constant ( $\varepsilon$ ), the ion charge ( $z_i$ ), the size of the ion ( $\text{\AA}$ ) and density of the solvent ( $d$ ) [1]. All of these factors are characteristics of the solution and can influence the activity through two main effects. The first one is the salt effect designated as  $\gamma_{H^+}^x$ . It can be approximated for hydrogen ions by the following expression:

$$\log \gamma_{H^+}^x = \frac{-0.5I^{1/2}}{1 + 3I^{1/2}} \quad (1.3)$$

where  $I$  is the ionic strength, which is defined as one half the sum of molarity times the square of the charge of the ionic species:

$$I = \frac{1}{2} \sum [i] z_i^2 \quad (1.4)$$

The second effect is the medium effect, which is designated as  $\gamma_{H^+}^m$ . This effect relates the influence of the solvent on the hydrogen ion activity. It reflects the electrostatic and chemical interactions between the ion and the solvent, of which the primary interaction is solvation. This brings up the question of pH measurements in nonaqueous solvent or mixed solvents. Most often an aqueous pH buffer solution is used to standardize the pH measuring system.

Thus, the activity is related to concentration through both salt effect and medium effect.

$$a_{H^+} = \gamma_{H^+}^x \gamma_{H^+}^m [H^+] \quad (1.5)$$

The pH scale was established to provide a convenient and effective means of communication with regard to the relative acidity of a particular solution. Its range is based on the dissociation constant for water,  $K_w$  ( $K_w = a_{H^+} \cdot a_{OH^-}$ ). In pure water, hydrogen ion and hydroxyl ion concentrations are equal at  $10^{-7}$  M, which is a neutral solution with pH = 7. Since most samples have less than 1 M  $H^+$  or  $OH^-$ , the extremes of pH 0 and pH 14 are established. For concentrated strong acid or base, their pH may be below 0 or above 14, but they are not frequently measured.

## 1.2.2 Traditional pH measurements

### 1.2.2.1 Potentiometric methods

The most common systems for pH sensing are based upon potentiometric devices. The most popular potentiometric approach utilizes a glass electrode because of its high selec-

tivity for hydrogen ions in a solution. pH measurement based on potentiometric method are highly reliable fairly straightforward to operate [2].

The electrode potential ( $E$ ) in a solution follows the Nernst equation:

$$E = E^0 + \frac{RT}{F} \ln(a_{H^+}) = E^0 - \frac{2.303RT}{F} pH \quad (1.6)$$

where  $E$  is a measured potential,  $E^0$  is the standard electrode potential,  $R$  is the gas constant,  $T$  is the temperature in Kelvin,  $F$  is the Faraday constant. For each  $H^+$ , number of electrons transferred is 1. As shown in the equation, Electrode potential,  $E$ , is proportional to pH. The reference electrode may be a silver chloride or a calomel electrode. An in-built reference electrode is usually included in a combined glass electrode.

Reference electrode | concentrated solution of KCl || test solution |  $H_2$  | Pt

For measurement of pH of a certain solution, the electrode has to be calibrated against buffer solutions of known hydrogen ion activity, i.e. pH. Both electrode potential of standard buffer solution and unknown solution are measured, and the pH of unknown solution can be calculated with the Nernst equation, eq 1.6.

The problem for potentiometric measurement of pH is that they are done in cells with liquid junction, which separates the inner reference electrode compartment from the measured solution and contributes liquid junction potential,  $E_j$ , to the cell voltage [3]. The variation of liquid-junction potential with ionic strength for many types of commercial reference electrode causes 0.1 up to 1 pH unit error when measuring pH in solutions of low ionic strength (conductivity  $< 150 \mu S cm^{-1}$ ) such as in fresh water [4,5].

Although these systems are popular because of their simplicity and low cost, glass pH electrodes have several shortcomings for autonomous sensing in natural waters. The main problems result from irreproducible junction potentials as discussed in the above paragraph. And the glass electrodes need to be calibrated frequently which is not convenient for remote sensing and field studies. Even when the electrodes are frequently calibrated, large systematic errors can arise from differences between standard and sample junction potentials [6–8].

#### 1.2.2.2 *Spectrophotometric methods*

The earliest method of pH measurement was by chemical indicators, e.g. litmus paper and pH paper, which change color based on the pH of a solution [2]. When a basic solution is added to the litmus paper, it turns to blue; while an acidic solution is added to the litmus paper, it turns pink. Commercially available universal pH paper is made from absorbent paper, in which several indicators (e.g. phenolphthalein, methyl red, bromothymol blue and thymol blue) are impregnated. pH is measured with visual comparison of the color of a test solution with a standard color chart, with sensitivity,  $\pm 1$  pH unit. pH can be more precisely determined through absorbance measurement with a spectrophotometer.

The spectrophotometric method for pH measurement is based on the equilibrium dissociation of a weak acid indicator [7]:



where  $HL^-$  is the protonated form and  $L^{2-}$  is the deprotonated form. The sulfoneph-

thalein type indicators ( $H_2L$ ) are most commonly used pH indicators. The diprotonated form is not present at typical freshwater pH ( $pK_a$  is  $\sim 2$ ). The equilibrium expression for the second dissociation is:

$$K_a = \frac{a_{H^+}a_{L^{2-}}}{a_{HL^-}} = \left( \frac{[H^+][L^{2-}]}{[HL^-]} \right) \left( \frac{\gamma_{H^+}\gamma_{L^{2-}}}{\gamma_{HL^-}} \right) \quad (1.8)$$

where  $K_a$  is the indicator equilibrium constant (acid dissociation constant) and the  $\gamma$  is the individual ion activity coefficient. The logarithm form of eq 1.8 can be used to determine the pH:

$$pH = pK_a + \log\left(\frac{R - e_1}{e_2 - Re_3}\right) + \log\left(\frac{\gamma_{L^{2-}}}{\gamma_{HL^-}}\right) \quad (1.9)$$

$$R = \frac{A_2}{A_1} \quad (1.10)$$

$$e_1 = \frac{\epsilon_{HL_2}}{\epsilon_{HL_1}}, e_2 = \frac{\epsilon_{L_2}}{\epsilon_{HL_1}}, e_3 = \frac{\epsilon_{L_1}}{\epsilon_{HL_1}} \quad (1.11)$$

where  $pK_a$  is  $-\log K_a$ ,  $R$  is the absorbance ratio (eq 1.10), with  $A_2$  and  $A_1$  as the absorbance for the base and acid form of the indicator at their absorbance maximum wavelength 2 and 1, respectively.  $e_i$  are the molar absorptivity ratios as shown in eq 1.11, where  $\epsilon$  is the molar absorptivity of either the acid or base form of the indicator at either wavelength 1 or 2 (the ion charges are omitted for clarity). The absorbance spectra of both protonated and deprotonated forms of a typical indicator are shown in Figure 1.1.

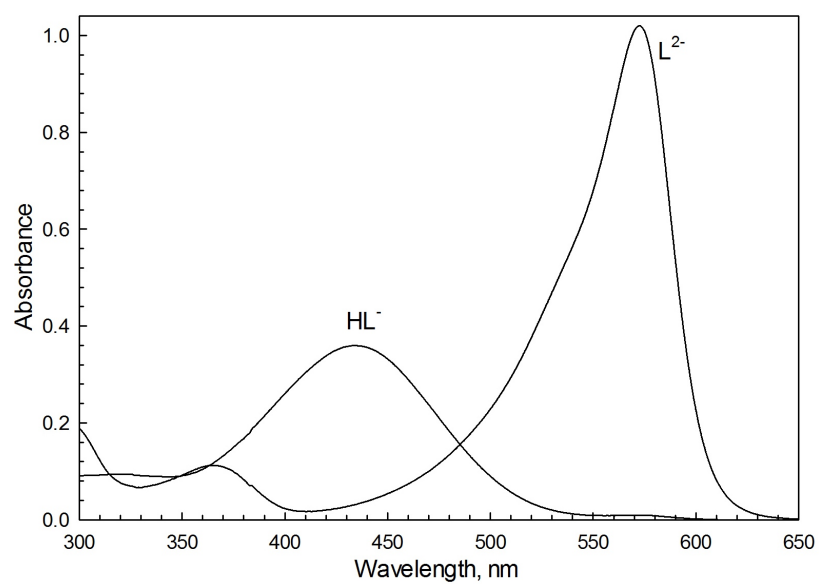


**Figure 1.1.** Representative absorbance spectra of protonated and deprotonated spectra of cresol red (14.9  $\mu\text{M}$ ) in buffer solution (IS = 0.100 M).

Spectrophotometric techniques using pH indicators offer an alternative to potentiometric pH measurements. Indicators have the advantages of very rapid equilibrium and obviate most of the problems associated with potentiometric measurements. Over the past few decades, spectrophotometric procedures developed for measurement of fresh water and seawater pH have improved the precision by more than one order of magnitude [7,9]. Indicator-based *in situ* pH measurements for fresh water and sea water were developed [5,6,8,10]. Martz et al. developed a flow-through instrument for pH measurement, which is simply based on spectrophotometric absorbance measurements of a mixture of water sample and indicator stock solution pumped into the cuvette [8].

One concern regarding indicator-based pH measurements is that the addition of a weak acid indicator can change the pH of weakly buffered water samples. The path length of the cuvette is increased to 10 cm to minimize the amount of indicator added [5]. However, for some application, a 10 cm path length may be impractical.

In the past few decades, various pH sensitive indicators (lots of them are fluorescent indicators) have been immobilized in different kinds of solid matrix to used as optical sensors for pH measurements. Optical pH sensors are more advanced than spectrophotometric methods because they does not need an indicator reservoir. Instead, indicators are immobilized into a solid matrix without leaching, and no moving parts are required to pumping indicator and samples, thus the cost is reduced. Compared to potentiometric pH methods, they offer more advantages such as high sensitivity, no need for a reference signal, immunity to electrical interference, easy miniaturization and possibility of remote sensing. The recently developed optical pH sensors are reviewed in section 1.4.

## 1.3 Fluorescence

### 1.3.1 Physical principles

Luminescence is the emission of light from the electronically state of some substances. Luminescence is divided into fluorescence and phosphorescence, based on the nature of the excited states. Fluorescence is emission of light from singlet excited states and phosphorescence is the emission from triplet excited states. For fluorescence, the electron in excited-state orbital is paired to the electron in the ground-state orbital. Thus electron returning from excited state to the ground state is spin-allowed and occurs rapidly by emission a photon (typically  $10^8 \text{ s}^{-1}$ ), therefore a typical fluorescence lifetime is near 10 ns ( $10 \times 10^{-9} \text{ s}$ ). For phosphorescence, the transitions from the triplet excited states to the ground states are usually forbidden because the electrons in the triplet excited state and singlet ground state have the same spin orientation. Thus the phosphorescence has a slow emission rate, about  $10^3$ - $10^0 \text{ s}^{-1}$ , resulting long lifetimes (up to milliseconds, even seconds) [11].

The processes which occur between the absorption and emission of light are usually illustrated by a Jabłoński diagram (Figure 1.2). These diagrams are named after Professor Alexander Jabłoński, who is now well known as the father of fluorescence spectroscopy. The energy state,  $S_0$ ,  $S_1$ ,  $S_2$  are the singlet ground state, first singlet excited state and second singlet excited state, respectively. At each of these electronic energy levels the fluorophores can exists in a number of vibrational levels. Light absorption between the ground state and excited state is an instantaneous process (typically  $10^{-15} \text{ s}$ ). Following light absorption, several processes usually occur. A fluorophore is usually excited to some



higher vibrational level of the excited states, and then rapidly relax to the lowest vibrational level. This process is called internal conversion and generally occurs in  $10^{-12}$  s or less. Hence, fluorescence emission generally results from the lowest-energy vibrational state of  $S_1$ . Return to the ground state typically occurs to higher excited vibrational ground-state level, which then quickly reaches the lowest vibrational states through internal conversion as well.

Molecules in the singlet excited state,  $S_1$ , can also undergo a spin conversion (intersystem crossing) to the first triplet state,  $T_1$ . Emission from triplet excited state is called phosphorescence and is generally shifted to longer wavelengths (lower energy) compared to the fluorescence. The heavy atoms such as bromide and iodine facilitate intersystem crossing and enhance phosphorescence quantum yields and that is why those molecules containing heavy atoms are often phosphorescent.

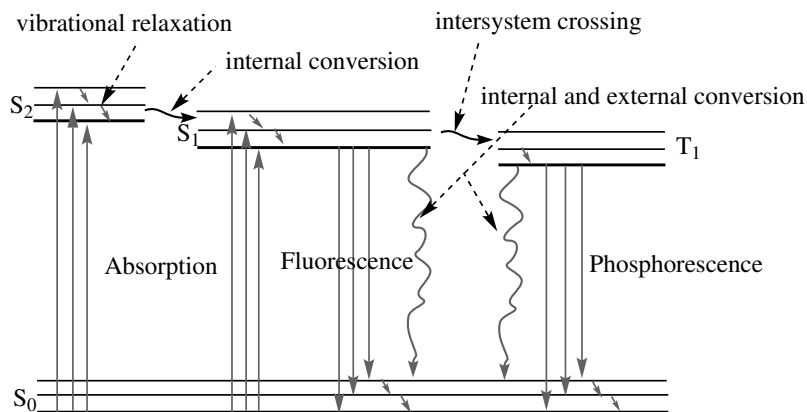


**Figure 1.2.** One Jabłński diagram of absorbance, fluorescence and phosphorescence.

The energy of fluorescence is usually less than that of absorption, i.e. fluorescence occurs at longer wavelengths than absorption. Energy losses between excitation and emission called the Stokes' Shift are often observed for fluorescent molecules in solution. One common cause of the Stokes' shift is the internal conversion from higher vibrational level

to the lowest vibrational level in both the excited state and ground state. In addition to the internal conversion effect, solvent effects, excited-state reactions, complex formation, and/or energy transfer can result in further Stokes' shift [11].

The fluorescence lifetime and quantum yield are important characteristics of a fluorophore. The quantum yield is the number of emitted photons relative to the number of absorbed photons. The lifetime determines the time available for the fluorophore stays in the excited states in its environment.

The quantum yield is determined by the relative rate constants for the processes that depopulate the lowest excited state. Following the light absorption, there are several process responsible for return to the ground state. These process are categorized into two groups, fluorescence ( $k_f$ ), and all the possible nonradiative decay ( $k_{nr}$ ), which are intersystem crossing and phosphorescence, internal and external conversion, predissociation and dissociation. The Quantum yield,  $\phi$ , which is the fraction of fluorophores which decay through emission, is given by:

$$\phi = \frac{k_f}{k_f + k_{nr}} \quad (1.12)$$

The quantum yield can be close to unity if the radiationless decay rate is much smaller than the rate of fluorescence decay, that is,  $k_{nr} \ll k_f$ . Substances with the largest quantum yields, such as rhodamines, display the brightest emissions.

The lifetime ( $\tau$ ) is defined by the average time a fluorophore spends in the excited state before returns to its ground state:

$$\tau = \frac{1}{k_f + k_{nr}} \quad (1.13)$$

Fluorescence emission is a random process, and not all the molecules emit their protons at  $t = \tau$ . It is average of time that all the molecules spends in their excited states. For a single exponential decay, 63% of the molecules have decayed prior to  $t = \tau$  and 37% decay at  $t > \tau$  [11].

A decrease in fluorescence intensity is called quenching, and it can happen through various processes and by different mechanisms. When the excited state fluorophore contacts with some other molecule (quencher) in condensed phase, it will be deactivated. Such a process is called collisional quenching. In this case, the excited-state fluorophore returned to its ground state during a collision with the quencher without emitting lights. Molecules such as oxygen, halogens, amines and acrylamide (electron-deficient molecules) can act as collisional quenchers. For different fluorophore-quencher pairs, the quenching mechanism are quite different. For instance, Quenching by halogens and heavy atoms occurs due to spin-orbit coupling and intersystem crossing to the triplet state [11].

Besides collisional quenching, fluorescence quenching can occur by other processes. Static quenching or contact quenching refers to a process that fluorophores can form non-fluorescent complexes with quenchers in the ground state. Another type of quenching mechanism is based on the energy transfer between two molecules, which is commonly known as resonance energy transfer (RET). For example, quenching of indole by acrylamide is probably due to electron transfer from indole to acrylamide, which does not occur in the ground state [11]. Fluorescence sensing based on RET is of great interest in the nowadays. Quenching can also occurs by nonmolecular mechanisms, for example, the

incident light can be attenuated by the fluorophore itself or other absorbing species.

Fluorescence typically occurs from fused aromatic molecules with low energy  $\pi \rightarrow \pi^*$  transition. In contrast, atoms are generally nonfluorescent in condensed phases. One exception is the lanthanides elements, such as cerium. The fluorescence of these atoms results from electronic transitions between  $f$  orbitals.

Fluorescence spectral data are generally presented as emission and excitation data. A fluorescence excitation or emission spectrum is a plot of fluorescence intensity versus wavelength (nanometers, nm). Figure 1.3 shows the fluorescence excitation and emission spectra of a common fluorophore, 8-hydroxypyrene-1,3,6-trisulfonic acid (HPTS) in solution.

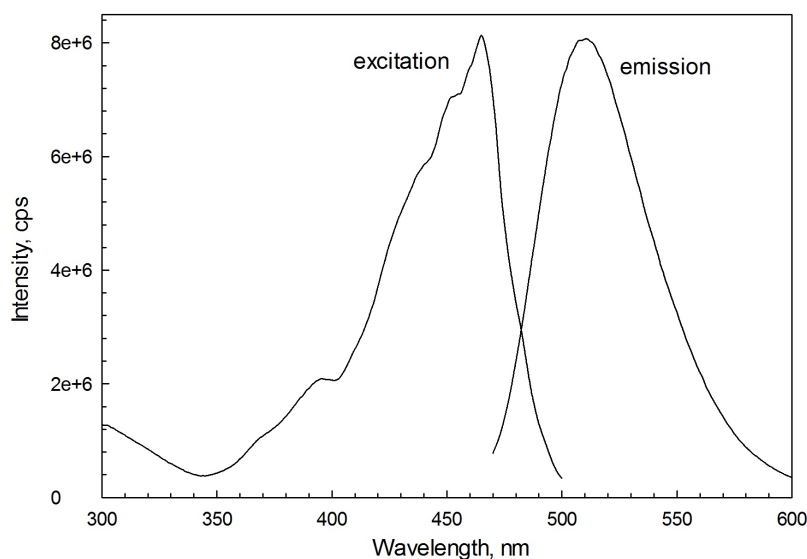


**Figure 1.3.** Fluorescence excitation and emission spectra of HPTS (0.99  $\mu\text{M}$ ) in solution, the emission wavelength for the excitation spectra is 510 nm and the excitation wavelength for the emission spectra is 467 nm.

Fluorescence measurements can be broadly classified into two types, steady-state measurement and time-resolved measurement. Steady-state measurements are most common

fluorescence measurement, which are performed with constant illumination and observation. The sample is illuminated with a continuous beam of light, and the excitation or emission spectrum is recorded. When the sample is first exposed to light, steady state is reached almost immediately, because the lifetime of fluorescence is in the range of nanosecond. The second type of measurements, time-resolved measurements, is used for measuring intensity decays. To perform these measurements, the sample is exposed to a pulse of light, where the pulse width is shorter than the decay time of the sample. This intensity decay is then recorded with a high-speed detection system which can measure the intensity on the nanosecond timescale.

Steady-state fluorescence measurement are simple and most commonly used. Nanosecond time-resolved measurement require complex and expensive instrumentation, however, it can resolve much more information which are lost during the time-averaging process in steady-state measurement.

### **1.3.2 Fluorescence sensing**

Fluorescence sensing of chemical and biochemical analytes is an active area of research because of its high sensitivity. Fluorescent molecule concentration as low as 1 part per trillion (1ppb) can be measured [12].

Fluorescence method instead of absorption method is often used for high-sensitivity detection. The reason for this lies in the different ways of measurements for absorbance and fluorescence. Absorption measurement is based on the difference in the intensity between light passing through the reference and the sample. In fluorescence method, the intensity of the emitting light is recorded directly without comparing with a reference light. In

other words, the advantage of fluorescence measurement is due to the measurement of lights relative to a dark background not a reference beam, which is required for absorption measurements.

The most direct fluorescence sensing method is based on decrease or increase on fluorescence intensity of a fluorophore in response to the concentration of some specific analyte. This type of measurement is based on collisional quenching, in which the fluorescence of a fluorophore is decreased by a relevant species. These measurements are only useful with a few clinic related analytes such as  $O_2$  [11]. The fluorescence sensing based on intensity is less reliable because fluorescence intensity is affected by the variation of fluorophore concentration and the fluctuation of the excitation light sources. For this reason, it is important to use measurements that are independent of the concentration of the fluorescence compound. This has been accomplished using ratiometric probes, which display shifts in their absorption or emission spectra upon contact of the concerned analyte. The concentration of the analyte can then be determined from the ratio of fluorescence intensities measured at two excitation or two emission wavelengths. Because these ratios are independent of the fluorophore concentration or fluctuation of excitation lights, sensing based on ratiometric methods are desirable. For example, Wencel et al has developed an optical pH sensor based on the ratiometric method of a dual excitation fluorescent indicator, HPTS [13].

Fluorescence lifetime can be used for sensing, because fluorescence decay is not affected by the concentration of fluorophores or the fluorescence intensity. A fluorescence lifetime pH sensitive probe was developed by Berezin et al. [14].

Resonance energy transfer (RET) is a valuable phenomenon for fluorescence sensing. In resonance energy transfer, a photon from the excited fluorophore (donor) raises the en-

ergy state of an electron in another molecule (acceptor), and results in a decreases in donor intensity and/or decay time. The donor and acceptor have to be close enough for RET to happen, typically macromolecular distance (1 - 10 nm) and the emission spectrum of the donor molecule must overlap with the absorption spectrum of the acceptor molecule. RET is commonly used to detect association of proteins as occurs in immunoassays [11]. Sensors has also been developed which cation acceptors whose absorption spectra are dependent on pH. A change in pH results in a change in absorption spectrum of the acceptor, which in turn increase or decrease the fluorescence intensity of the donor. One of the earliest reported RET pH sensor used eosin as the donor and phenol red as the acceptor [15]. The basic form of phenol red absorbs at 546 nm, where eosin emits. Thus, the emission intensity of eosin decreased as the pH increased.

Fluorescence sensing is considered as one of the rapid and low-cost testing methods for various application in clinical, bioprocess, and environmental area. Fluorescence is widely used in life science because most cellular components are nonfluorescent and thus less interference and it is a non-destructive measurement of biological molecules. In this case, a protein or other component is often labeled with an fluorophore. For instance, Yapici, et al. have synthesized new rhodamine nitroxide based fluorophores to detect hydrogel radicals in the living cells [16].

## **1.4 Literature review of optical pH sensors**

Optical pH sensor is the sensing of pH based on pH-sensitive indicators which are immobilized in some kind of supporting material such as cellulose, sol-gel films and hydrogel films. The first optical pH sensor (optode) was developed by Peterson et al. in 1980, by

utilizing absorbance of the indicator, phenol red [17]. In 1982, the first fluorescence-based pH-optode was described by Seitz and coworkers by covalently immobilization of fluoresceinamine in controlled porosity glass [18]. Over the past few decades, the development of pH sensors has grown rapidly, because of the need of pH measurement in various scientific research and practical applications. Optical and fiber-optic pH sensors offer numerous advantages over traditional potentiometric method such as no effect from electrical interference, easy miniaturization, and possibility of remote sensing and *in vivo* measurement [19].

#### **1.4.1 Indicator immobilization methods**

The immobilization of pH indicators is a key step in the development of optical pH sensors. There are three widely used methods for immobilization of pH indicator on/in a solid substrate : adsorption, entrapment and covalent binding.

##### *1.4.1.1 Adsorption*

In the adsorption method, a pH indicator is adsorbed physically or chemically on a solid porous substrate. This method is relatively simple but not very reliable since the adsorbed indicator may leach out [19]. In 1986, Moreno et al. described a pH sensitive optical fiber sensor based on electrostatic immobilization of cresol red on the anionic Dowex resin and applied it to the determination of pH in pasteurized dairy milk [20]. The commercially available ion exchange polymer matrix, Nafion film, was used for electrostatic immobilization of a dye pair acriflavine and rhodamine 6G [21]. This optical pH



optode is based on the pH dependent energy transfer from acriflavine to rhodamine 6G. An electrostatic layer-by-layer technique has been used to immobilize pH indicator to charged polyelectrolyte such as polycation, poly(allylamine hydrochloride) (PAH) and polyanion, poly(acrylic acid) (PAA) to use as pH sensors [22,23]. However these sensitive coatings show short lifetimes due to their high rate of photobleaching; some post-treatments like thermal curing showed improved performance [24,25]. Shi et al. developed an optical pH sensor based on the electrostatic immobilization of 8-hydroxy-1,3,6-pyrenetrisulfonic acid (HPTS) on a polyelectrolyte-containing silica, which can be used in solution with low ionic strength but leaching of HPTS became a problem at high concentration of electrolytes [26]. Hulth et al. used a transparent film consisting of a thick polyester foil with cellulose acetate coating for adsorbing pH indicators to work as pH sensors [27,28]. The adsorption was accomplished through immersing the sensing foil in a high ionic strength solution of pH indicator solution. The immobilization was based on the fluorophore-foil interactions, and according to their result, the immobilization was irreversible. Nivens et al. successfully developed a pH sensor based on the electrostatic attachment of HPTS in sol-gel film coated fiber by soaking the coated fiber in the HPTS solution; the sensor needed to be stored under dry condition to prevent leaching [29].

#### *1.4.1.2 Entrapment*

In the entrapment method, a pH indicator is physically entrapped within a porous polymeric substrate. This method is quite easy and reliable but indicator may slowly leach out. Cellulose is widely used in the development of pH sensors because it is permeable for both water molecules and ions, and it is inert in both acidic and basic solutions. Choi and Hakonen et al. have developed pH sensors based on the physical entrapment of HPTS and flu-

orescein in ethyl cellulose; an ion-pair reagent tetraoctylammonium ions ( $\text{TOA}^+$ ) was used to form ion-pairs with pH indicators before immobilization to prevent leaching [30–32]. Sol-gels have also been widely used as supporting matrices for pH indicator immobilization because of they are highly porous thin films that are optical transparent and provide a stable and inert environment for dye immobilization, and they are really easy to attach to glass or silica [33–36]. Normally, pH indicators were first paired with ion-pair reagent before entrapment in sol-gel films to prevent leaching [13,37,38]. Another key advantage of sol-gel derived matrix is the ability to entrap multiple species within a confined space. Gulceci et al. have developed a biosensing using a fluorescently-labelled dextran co-entrapped with a hydrolytic enzyme in sol-gel films to sense the acidic or basic products generated by the enzymes through the changes in emission of the pH sensitive dye [39]. Kasik et al. increased the sensitivity of the pH sensor by co-entrapped HPTS with dichlorotris-(1,10-phenanthroline)ruthenium(II) hydrate (Ru-phen dichloride) to work as an internal reference [40]. A commercially available sol-gel material, Liquicoat was also used for entrapment of pH indicators [41]. Hydrogel materials have also been used in pH indicator entrapment for pH sensor development mainly because of their high proton-permeability. Kermis et al. developed a pH sensor by first immobilizing HPTS onto Dowex resin and then entrapping into a hydrogel layer [42]. Modified pH indicators with long chains were physically embedded in an uncharged hydrogel matrix for use in a marine system by Schroder et al. [43]. Besides cellulose, sol-gel and hydrogel films, silica nanoparticles have been used for pH indicator entrapment [44].

#### *1.4.1.3 Covalent binding*

In the covalent binding method, a pH indicator is bound onto a solid substrate or in a porous polymeric substrate through chemical bond. This method is usually time-consuming and much complicated compared to physical entrapment method. The advantage of this method is that immobilized indicators are not likely to leach out. The same support material discussed in entrapment method such as cellulose, sol-gel and hydrogel films are also widely used for covalent binding of pH indicators for pH sensing. Kostov et al. [45] and Ensafi et al. [46] have successfully bound several indicators to acetylcellulose film by previous hydrolysis of the cellulose films. The commonly used pH indicator HPTS was covalently bound to cellulose acetate material through a sulfonamide linkage [47,48]. Covalent binding can also be accomplished through previously modification of pH indicator, as Liu et al., first reacted phenolphthalein with formaldehyde to produce a series of prepolymers with hydroxymethyl groups which can be covalently bound to diacetylcellulose membrane [49]. Covalent binding of pH indicators to sol-gel films or glass surface normally through reacting the indicators with a silane reagent with amino groups before or after silane hydrolysis [50–52]. Recently several researchers have worked on copolymerization of pH indicators in hydrogel films as pH sensor [53–57]. In this approach, the pH sensitive dye was first modified with attachment of alkenyl groups which can be linked with hydrogel monomers during the polymerization reaction. In addition to the frequently used materials, carbon nanotubes were also fabricated for covalent immobilization of HPTS to produce a pH sensor [58].

### 1.4.2 Detection methods

Most optical pH sensors are based on absorption and fluorescence detection methods. Absorption measurements are not very sensitive and required the use of high concentration of pH indicator or a thick sensing layer. In contrast, fluorescence methods are more sensitive because of the dark background and no need of a reference beam. Measurements of absorption and fluorescence intensity often suffer from instabilities resulting from the decrease in the concentration of pH indicators due to leaching and photobleaching, and fluctuations in the intensity of light source as well. Ratiometric methods have been used to overcome these problems. Lifetime based measurements can also overcome these problem because the fluorescence decay time of a dye usually does not depend on its concentration.

#### 1.4.2.1 Absorption

Absorption detection is widely used in the development of optical pH sensors. In the pH range of interest, a pH sensitive dye behaves as a weak acid and exists in protonated or deprotonated forms, each having a different absorption spectrum. As the pH of the solution varies, the relative concentration of protonated or deprotonated forms varies. Fiber optic pH sensor based on absorption of phenol red was first developed by Peterson et al. [17]. Other pH sensitive indicators such as Neutral Red [45],  $\alpha$ -Naphthyl Red [46] Alizarin red [35] and phenolphthalein [49] have been immobilized in solid support as pH sensors based on absorption. Absorption detection is simple but not very sensitive, and also suffers from leaching or photobleaching of pH indicator in solid support and the variations in the light sources. Such instabilities can be resolved by measuring absorbance at multiple wavelengths, such as at peak absorption (to respond to pH), at isobestic point(to account

for indicator concentration) and at zero absorption (as the baseline to account for light intensity) [59]. A broad range fiber-optic pH sensor based on absorption was presented by Dong et al. [60]. The sensor was prepared by immobilizing a mixture of three different pH sensitive indicators: cresol red, bromophenol blue and chlorophenol red into sol-gel materials. Another broad range optical pH sensor based on absorption was presented by Arregui et al. by immobilizing several universal indicators to a commercially available sol-gel material, Liquicoat [41].

#### *1.4.2.2 Fluorescence*

Fluorescence detection is much more sensitive compared to absorption because it does not require a reference beam, thus it works at very low concentration of indicators. Over the past few decades, many optical pH sensors based on the fluorescence method have been developed [24,26,29,36,44,50,51,54,57,61]. The effect of leaching or photobleaching of indicators from the solid support and fluctuations in the intensity of the light source can be overcome by the ratiometric method (the use of the ratio of intensities at two excitation or emission wavelength). An Optical pH sensor based on a fluorescence ratiometric method is widely developed [34,39,43,52,53,56,62]. Among the pH indicators, HPTS is one of the commonly used ones for pH sensing, because of its large Stokes' shift, high stability and high quantum yield. In addition, its dual excitation can be used for fluorescence ratiometric method of pH measurement [13,22,24,32,40,42,48,55,58,63]. The encapsulation of HPTS in a suitable nanoparticles for application as pH and ammonia sensor was developed by Amali et al. based on fluorescent ratiometric method [64,65]. Another widely used fluorescent indicator for pH measurement is fluorescein because of its high molar absorptivity, large fluorescence quantum yield and high photostability [66]. Fluorescein and its derivatives

based optical pH sensors are mostly studied in biological research [67–71].

#### *1.4.2.3 Fluorescence lifetime*

Fluorescence lifetime is an intrinsic parameter that is independent to both the concentration of indicator and the intensity of the excitation light, so lifetime-based sensing of pH can prevent signal fluctuations due to instrumental effects and varying sample background. However, many luminescent pH indicators have lifetimes of  $< 10$  ns, which causes a substantial instrumental effort, in terms of precise determination. In addition, the luminescence background cannot be eliminated by time gating [72]. pH probes with long fluorescence lifetime are not very common [73]. Berezin et al. synthesized near-infrared pH-sensitive dyes that can be used for biological applications in physiological range, but they have not so far been immobilized in a solid support for use as a pH sensor [14]. Goncalves et al. synthesized long-lifetime ruthenium complexes that are visible indicators for fiber-optic lifetime sensing of pH [74]. Their excited-state lifetimes show a typical sigmoidal variation with pH in the pH range of 3 - 9 and with a long lifetime in the microseconds range. Dual-lifetime referencing (DLR) method was applied to lifetime-based pH sensing, because it enables the pH to be determined by measuring the phase shift or the overall apparent lifetime (in units of  $\mu s$ ) as a function of pH. Bare et al, presented a multicomponent lifetime-based pH sensor that used dyes with constant lifetimes to generate an pH dependent change in the apparent sensor lifetime [73]. A red light-excitable dual lifetime referenced optical pH sensor was developed by Borisov et al. [75]. A fluorescent seminaphthorhodafluor indicator and the reference, a luminescent inorganic phosphor were both immobilized in hydrogel to use the DLR method for pH sensing. Wang et al. presented a pH sensor nanoparticles with both pH indicator dye and a long-lived reference luminophore immobilized [71].

### 1.4.3 Other kinds of pH sensors

Recently, stimuli-responsive hydrogels based pH sensors have been widely studied. With a small alternation of certain environmental parameters, Stimuli-responsive hydrogels can change their volume significantly. Sensing pH by making use of hydrogel that swell as a function of pH has attracted substantial interest, because such materials are potentially quite stable over time and no indicators are needed therefore problems such as leaching or photobleaching of indicators from the matrix do not exist [72]. The state of art in this field has been presented by Richter et al. [76]. Figure 1.4 shows how hydrogel polymers can swell, then undergo phase transitions, as a function of pH.

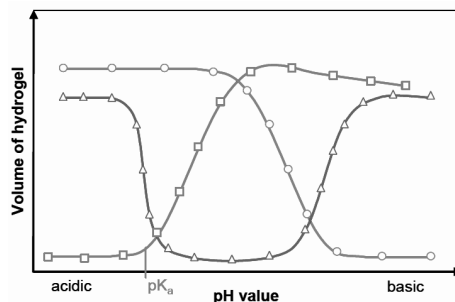


**Figure 1.4.** Phase transition behavior of polyelectrolyte hydrogels. Acidic hydrogels (squares) are ionized by deprotonation in basic solutions, which have an excess of hydroxyl groups. Basic hydrogels (circles) swell in acidic solutions due to the ionization of their basic groups by protonation. Amphiphilic hydrogels (triangles) contain both acidic and basic groups. Therefore they show two phase transitions.

Polyelectrolyte hydrogels contains weak acidic or basic groups in their structure, which can be ionized. For example, gels containing acidic groups are deprotonated under basic condition. The density of negatively charged groups within the network increase, and generate an adequate amount of counterions inside the gel, there a gel volume increase is induced due to electrostatic repulsion. In an acidic condition, the acidic groups in the gels are protonated resulting in a decrease of both the charge density and the amount of

counterions, thus lead to gel shrinking. Because this is also dependent on the acid-base equilibrium of a weak acid group in the structure, the phase transition of the gels occurs in a small range close to the apparent acid dissociation constant,  $pK_a$ . Richter et al. have developed a polyelectrolytic hydrogel based pH sensor using the quartz crystal microbalance technique [77]. Several groups have developed hydrogel-based pH sensors using bending plate transducers [78,79]. Principally, the pH sensitive hydrogel is placed in a fixed volume between a rigid grate, which is permeable for protons, and a bending plate. If the hydrogel swells the plate deflects resulting in a change of the resistance of the piezo-resistive bridge. Zhao et al. synthesized a biodegradable pH-responsive hydrogels for controlled drug release by copolymerization of pH-sensitive poly(*L*-glutamic acid)(PGA) into the hydrogel matrix [80].

Resonance energy transfer has also been applied in optical pH sensor development. Photon upconverting luminescent lanthanide nanorods were used by Sun et al. [81]. The nanorods upon illumination display visible luminescence. They were immobilized along with the pH sensitive indicator bromothymol blue (BTB) in a hydrogel matrix. The red luminescence of the nanorods is reabsorbed by BTB at alkaline conditions where BTB is blue. However, at acidic conditions, BTB does not cause a strong inner filter effect. Its long-wave excitation and emission are said to make the sensor well-suited for sensing pH.

Two-dimensional pH imaging is needed for application such as bioturbated sediments and monitoring complex disease process such as wound healing and tumor metabolism. These optical pH sensor are still based on fluorescence emission of pH indicators change upon on pH changes, however the images are readily obtained with light-emitting diode (LED) or a CCD camera. A few planar optical pH sensor has been developed by immobilization of the most common fluorescent pH sensitive indicator, HPTS, into different thin



films for diagenetic studies of sediments [27,62,82]. Schreml et al. studied 2D luminescence imaging pH *in vivo* by time-domain luminescence imaging of pH sensitive indicator FITC and a reference ruthenium (II) complex. To create a biocompatible 2D sensor, these dyes were bound in polyurethane hydrogel [69]. Meier et al. have developed a simultaneous photographing sensor for oxygen and pH sensing *in vivo* [83].

#### 1.4.4 Applications

The pH sensors are widely used in chemical and biological applications such as environmental monitoring, biomedical research, medical application such as blood pH measurement and laboratory pH measurements.

Because optical pH sensors can be easily fabricated for *in situ*, remote and underground sensing, they are very useful for environmental monitoring. Jorge et al. developed a luminescence-based optical fiber chemical sensors for remote monitoring of oxygen, pH and temperature [84]. Wolfbeis et al. have developed a fiber-optic sensors for monitoring dissolved carbon dioxide in water sample in 0 - 900 ppm concentration range based on immobilization of a pH sensitive dye in cellulose films [85]. A gas phase carbon dioxide sensor was developed by Chu et al. by entrapment of HPTS in sol-gel films [37,86]. Motellier et al. developed a fiber-optical pH sensor and used it for routine *in situ* measurements in an underground laboratory devoted to studies in connections with nuclear waste repositories [59]. Two-dimensional pH imaging was used to measure the pH in sediments [27,62, 82].

Optical sensors have been used for measurement of intracellular pH inside individual biological cells [87,88]. Fluorescent indicators for intracellular pH sensing is reviewed

by Han et al. [89]. Non-invasive, simultaneous optical monitoring of oxygen and pH during bacterial cultivation is presented using an integrated dual sensor [90]. Arain et al. developed integrated fluorescence-based optical sensors for oxygen and pH and their applications to enzyme screening and monitoring of bacterial respiratory activity [91].

Optical pH sensors have been developed for continuous monitoring of blood pH and gases ( $\text{CO}_2$  and  $\text{O}_2$ ), which are important parameters in the operation room and intensive care unit. Since fiber-optic sensor can be easily miniaturized, they can potentially be used for *in vivo* measurement of pH,  $\text{pCO}_2$  and  $\text{pO}_2$ . Many optical sensors for blood pH and gas measurement have been developed [92–95]. pH sensor based on 2D luminescence imaging pH *in vivo* has also been developed [69,83,96,97].

In general, all optical pH sensors, as well as  $\text{CO}_2$  and  $\text{NH}_3$  sensors, can be used in monitoring and control of industrial processes. Optical pH sensors for monitoring pH in bioreactor were described [98,99]. Bultzingslowen et al. developed a carbon dioxide sensor by immobilization of HPTS in sol-gel films for modified atmosphere packaging applications [100].

## 2. COVALENT BINDING OF FLUORESCCEIN TO POROUS SILICA FOR OPTICAL pH SENSING

### 2.1 Introduction

#### 2.1.1 Mesoporous silica

A great deal of intensive research has been conducted to obtain high-quality transparent porous silica thin film for microoptics and microelectronics applications [101]. Mesoporous silica membranes with high surface area represent a potential material for optical dye immobilization [102]. In this project, the mesoporous silica used as the material for immobilization of pH sensitive indicator was provided by Dr. Pual L. Bergstrom and Dr. Kumar L. Vanga. Here, the synthesis and properties of mesoporous silica is briefly introduced as illustrated in Figure 2.1

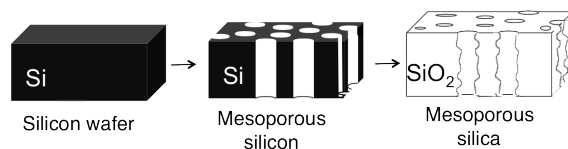


**Figure 2.1.** The schematic illustration of the synthesis of mesoporous silica.

Mesoporous silicon was first fabricated from a silicon wafer. The fabrication of mesoporous silicon utilized unmasked boron doped p-type (100) silicon substrate with resistivity of  $0.001 - 0.002 \Omega \cdot \text{cm}$  and a thickness of  $525 \pm 25 \mu\text{m}$ . The mesoporous silicon membrane was produced by electrochemical anodization of the silicon substrate in ethanoic-hydrofluoric acid solution with a pore size of about 20 nm diameter. Mesoporous silicon samples were then thermally oxidized at  $950^\circ\text{C}$  to grow a 10 - 15 nm oxide layer on the sidewalls. As the sidewalls of the pores are in the range of 5 - 10 nm, complete oxidation of the membrane occurs as silicon is fully consumed produced a full wafer thickness porous silica membrane that is optically transparent over a wide range of wavelengths (from UV to near IR) [102]. The mesoporous silicon and mesoporous silica membranes are shown in Figure 2.2. As shown in the figure, the mesoporous silica is translucent to human eyes. The top-view and cross-section scanning electron microscopy (SEM) images of mesoporous silicon and mesoporous silica are shown in Figure 2.3.

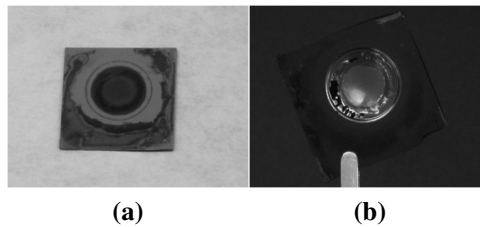


**Figure 2.2.** Optical photographs of mesoporous silicon (a) and mesoporous silica (b). (Reprinted with permission from ref [102])

Mesoporous silica membranes are very brittle because of high compressive stress and the thickness of the mesoporous silica is less than  $500 \mu\text{m}$ . For mesoporous silica membranes, at such small dimensions, the side walls of the pore cannot be considered to be smooth as shown in Figure 2.3, bottom.

It is important to understand the optical properties of the mesoporous silica. The refractive index can be measured and is related to porosity. The porosity of the films was

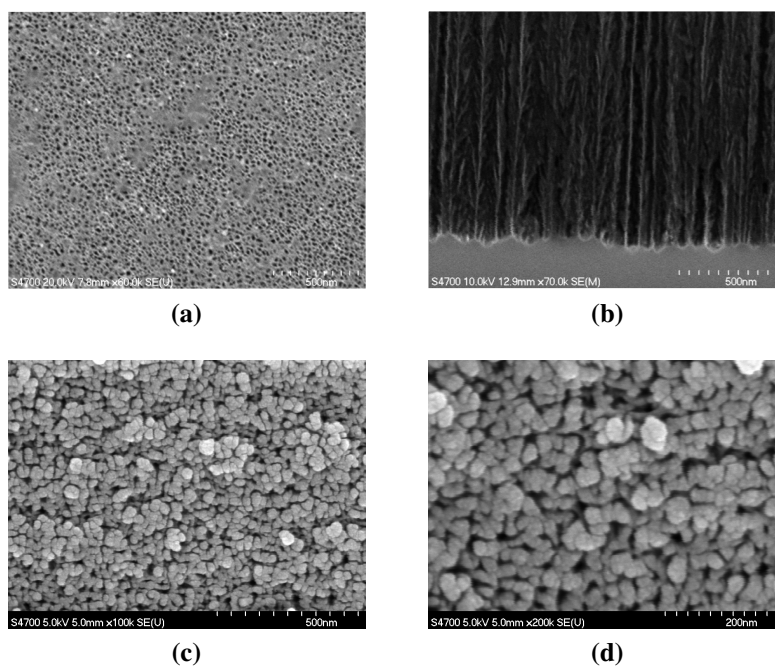


**Figure 2.3.** SEM images of porous silicon and porous silica samples. (a and b): top-view and cross-section SEM images of porous silicon, respectively. (Reprinted with permission from [102]); (c and d): top-view SEM images of porous silica with scale of 500 nm and 200 nm.

calculated according to the Lorentz-Lorenz equation [101]:

$$porosity = 1 - \frac{n^2 - 1}{n_d^2 - 1} \quad (2.1)$$

where  $n$  is the refractive index of the film, and  $n_d = 1.46$  is the refractive index of bulk  $\text{SiO}_2$ . The refractive indices of the films were measured using an ellipsometer at 800 nm wavelength and  $70^\circ$  incidence, for which the measurement error was as small as 2% [101]. The measured refractive index ( $n$ ) for porous silica are shown in Figure 2.4. The porosity of mesoporous silica was calculated using the refractive index of mesoporous silica, 1.36 at 800 nm. The porosity of mesoporous silica was 24.9% which corresponds to Dr. Kumar L. Vanga's result 24% (using Bruggeman Equation) and 27% (obtained from the SEM image and Image J analysis) [102]. The porosity of mesoporous silicon was between 57.6% and 67% [102]. Compared to mesoporous silicon, the porosity of mesoporous silica was reduced due to oxidation, which brings two oxygen per silicon atom.

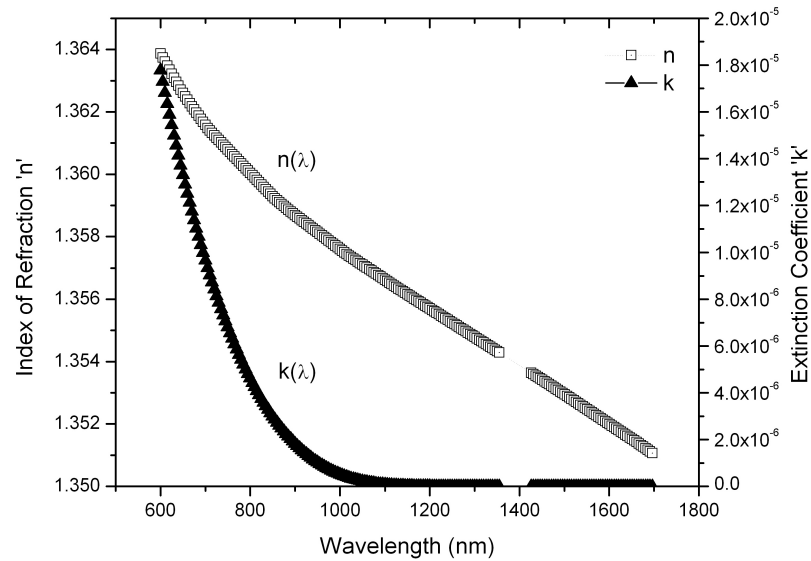


**Figure 2.4.** The measured refractive index ( $n$ ) and extinction coefficient ( $k$ ) of mesoporous silica.

In this study, a mesoporous silica membrane was used as the solid matrix for pH indicator immobilization because it is relatively transparent and the intensity could be greatly enhanced because of the large surface area.

### 2.1.2 Fluorescein

Fluorescein (structure is shown in Table A.1 in the Appendices) was selected as the pH indicator because of its high fluorescence quantum yield, and excellent photostability [66]. Fluorescein has four different forms in aqueous solution: cation (acid dissociation constant,  $pK_a$ , 2.2), neutral species ( $pK_a$ , 4.4), monoanion ( $pK_a$ , 6.7), and dianion, each with different optical properties [66,103].

The absorption spectra of neutral, monoanionic and dianionic fluorescein in buffer solution are shown in Figure 2.5. The cation has maximum absorption at 437 nm with extinction coefficient ( $\epsilon$ ),  $53,000 \text{ M}^{-1} \text{ cm}^{-1}$  [66]. The neutral species has the weakest absorption in the visible region, with a maximum peak at 437 nm ( $\epsilon$ ,  $11,000 \text{ M}^{-1} \text{ cm}^{-1}$ ) and a side maximum at 475 nm ( $\epsilon$ ,  $3,600 \text{ M}^{-1} \text{ cm}^{-1}$ ) [66]. When  $\text{pH} > 4.4$ , the carboxylic group gets deprotonated, and fluorescein becomes a monoanion. The monoanion has weak absorption in the visible region with peaks at 450 nm and 476 nm ( $\epsilon$ ,  $19,000 \text{ M}^{-1} \text{ cm}^{-1}$  and  $16,000 \text{ M}^{-1} \text{ cm}^{-1}$  respectively). When  $\text{pH} > 6.7$ , both the carboxylic group and the phenol group get deprotonated, and fluorescein is a dianion. The dianion has the highest and most red-shifted absorption peak at 495 nm ( $\epsilon$ ,  $72,000 \text{ M}^{-1} \text{ cm}^{-1}$ ), with a shoulder around 471 nm ( $\epsilon$ ,  $31,000 \text{ M}^{-1} \text{ cm}^{-1}$ ). (Detailed information is shown in the Appendices A.1.1)

The fluorescence quantum yields of fluorescein in different pH solution were measured using quinine sulfonate as the standard. The fluorescence quantum yields of fluorescein

in pH 4.25 under 450 nm and 467 nm excitation is 0.17 and 0.26, respectively; and the fluorescence quantum yield of fluorescein in pH 8.03 under 495 nm excitation is 0.82. (data are shown in Appendices A.1.1)

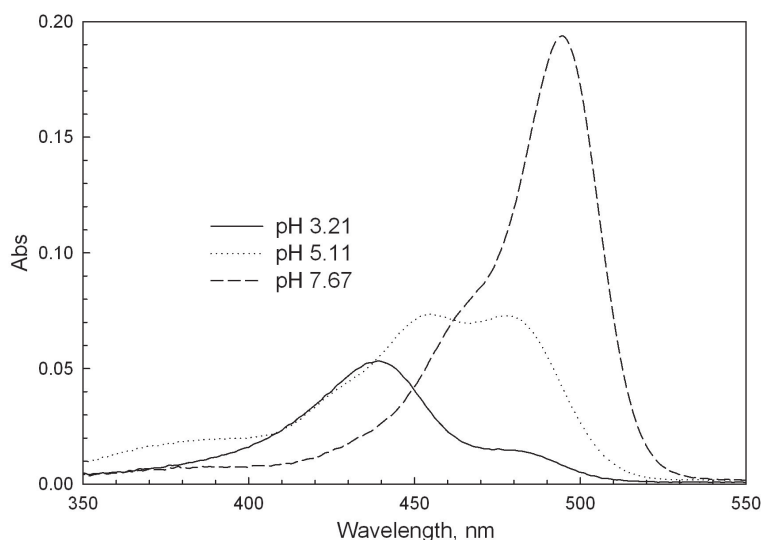


**Figure 2.5.** UV-Vis absorption spectra of three dominate species of fluorescein ( $2.5 \mu\text{M}$ ) in solution ( $\text{IS} = 0.120 \text{ M}$ ). pH 3.21 - neutral species; pH 5.11 - monoanion; pH 7.67 - dianion.

Fluorescein-5-isothiocyanate (FITC) is one of many commercially available fluorescein derivatives. The structure of FITC is shown in Table A.1. It has the same UV-Vis absorption and fluorescence properties as fluorescein. The isothiocyanate reactive group of fluorescein can be used to covalently bind the dye to nucleophiles such as amine groups.

### 2.1.3 Specific aims of this study

- Covalently bind FITC on the surface of mesoporous silica through surface reaction with self-assembled monolayer of trichlorosilanes.
- Study the spectral properties and pH sensitivity of FITC in porous silica.



- Evaluate the potential of FITC bound porous silica as optical pH sensor

## 2.2 Experimental

### 2.2.1 Reagents and materials

#### Reagents:

Toluene, dichloromethane, and 30% hydrogen peroxide ( $\text{H}_2\text{O}_2$ ) were purchased from Mallinckrode Inc.. 3-aminopropyltriethoxysilane (APTES), triethylamine, and concentrated sulfuric acid ( $\text{H}_2\text{SO}_4$ ) were purchased from Sigma-Aldrich. Acetonitrile was purchased from Tedia. Ethanol (200 proof) was purchased from Pharmco-Aaper. The pH dependent fluorescent dye fluorescein-5-isothiocyanate was purchased from Thermo Scientific. All the chemicals were used as received without additional purification.

#### Materials:

Quartz slides, glass beads, silicon wafers and porous silica were used as substrates for dye immobilization. Both quartz slides ( $1\text{ cm} \times 1\text{ cm} \times 0.5\text{mm}$ ) and p-type silicon wafers,  $525 \pm 25\text{ }\mu\text{m}$  thickness with a resistivity of  $0.001\text{-}0.002\text{ }\Omega \cdot \text{cm}$ , were purchased from University Wafer. The glass beads (3 mm and 2 mm diameter) were purchased from Fisher Scientific. The transparent porous silica substrate (0.2 mm thickness,  $\sim 10\text{ nm}$  diameter pore size) was achieved by complete oxidization of mesoporous silicon membrane produced by electrochemical anodization of single crystal silicon in ethanoic-hydrofluoric acid solutions.

**Test solution:**

Acetate buffers (pH 3.5 - 5.5) were prepared from acetic acid and sodium acetate solutions. Phosphate buffers (pH 6.0 - 8.0) were prepared from monobasic potassium phosphate and potassium hydrogen phosphate solutions. The concentration of the buffers were 0.010 M. Potassium chloride was used as an additional electrolyte to adjust ionic strength.

**2.2.2 Monolayer preparation**

The covalent immobilization of FITC on silica surface was accomplished using a previously published procedure [104] with modification for this study. Briefly, the substrates (except porous silica) were cleaned in boiling piranha (solution of 1:4 30%  $\text{H}_2\text{O}_2$  and concentrated  $\text{H}_2\text{SO}_4$ ), rinsed several times with deionized (DI) water and dried in a stream of nitrogen. Porous silica samples were used as obtained. The covalent binding of FITC on the surface of quartz slides, glass beads or inner surface of porous silica was achieved under a dry nitrogen atmosphere. The freshly cleaned substrates were immersed in APTES solution (10 mM in dry toluene) for 4 hours. Then, the substrates were removed from the solution, and rinsed with toluene, dichloromethane, and ethanol several times to remove any physically absorbed material. Subsequently, the substrates were placed in a solution of triethylamine (36 mM) and FITC (1.2 mM) in dry acetonitrile for 16 hours. After the substrates were removed from solution, they were rinsed with acetonitrile, ethanol, dichloromethane and deionized water to remove any physically absorbed material. The schematic synthesis is shown in Figure 2.6. A control porous silica sample was prepared by the same procedure, but without APTES, to quantify the degree of physisorption of FITC. All prepared substrates were stored in deionized water before and after testing.

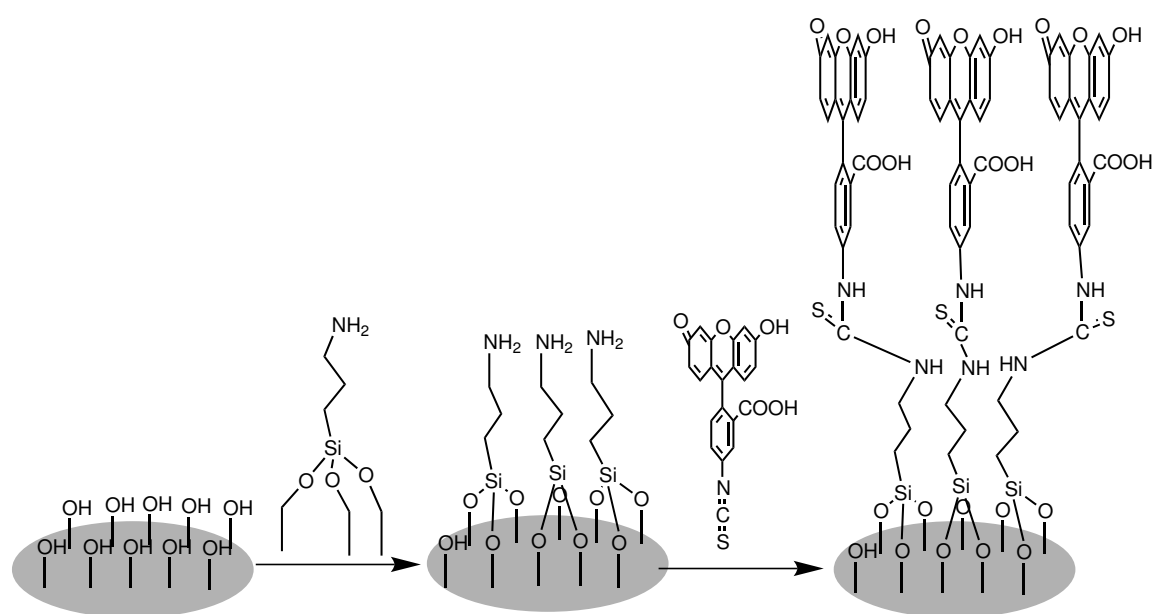


**Figure 2.6.** Schematic representation of FITC covalently bound to silica surface.

### 2.2.3 Instrumentation

**SEM:** The SEM images of the mesoporous silica were taken with a field-emission scanning electron microscope (Hitachi S-4700) after coating 5 nm platinum on sample surface.

**Ellipsometry:** Film thickness of FITC coated silicon wafer substrate was measured by a Variable Angle Spectroscopic Ellipsometer (VASE 32 from J.A. Woollam Co.). The model fit was performed taking account of 0.5 mm silicon layer and 2 nm of native oxide present on the silicon wafer.

**FTIR:** The FTIR spectra of porous silica and FTIC bound porous silica were taken with a Fourier transform infrared spectrometer (Spectrum one, Perkin Elmer). The substrates were ground to powder before recording the spectra.

**UV-Vis absorption and fluorescence spectra:** UV-Vis absorption spectra were taken with a Lambda 35 UV/Vis Spectrometer (Perkin Elmer) using quartz cuvettes. Fluorescence spectra were measured with a SPEX FLUOROLOG 1681 spectrofluorometer. The porous silica sample was placed in acrylic plastic cuvette filled with buffer solution for the fluorescence spectra measurements (Figure 2.7). Multiple measurements were recorded at different parts of the sample in order to report the uniformity of sample. Error estimates are the standard deviations of these multiple measurements. Fluorescence lifetimes were acquired with TM-200 LED Strobe Lifetime Spectrofluorometer (PTI). Single exponential decays were used to fit the fluorescence lifetimes.

The pH meter (Orion 2 star pH benchtop, Thermo Scientific) was calibrated in NIST (National Institute of Standards and Technology) standard buffers by a three-point calibra-

tion procedure (pH 4.00, 7.00 and  $10.00 \pm 0.02$ ). FITC bound substrates were immersed in buffer solutions for all optical measurements. All experiments were conducted at room temperature.

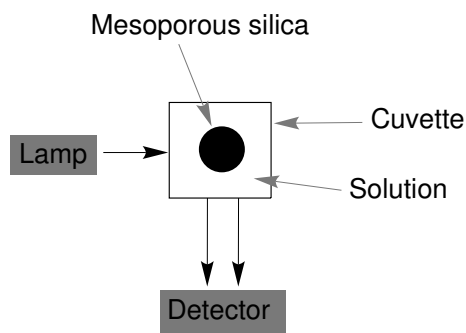


**Figure 2.7.** Top view of the fluorescence spectra measurement setup.

## 2.3 Results and Discussion

### 2.3.1 Confirmation of covalent binding of FITC on substrates surface

#### 2.3.1.1 Substrate color change

The covalent binding of FITC on glass beads and the internal surface of porous silica were easily confirmed by the change in color. After immobilization of FITC on the surface, the glass beads turned light yellow-green, which is the color of FITC (Figure 2.8, a). Porous silica was colorless before immobilization (Figure 2.8, b). With FITC chemically bound on the internal surface, the porous silica sample turned yellow (Figure 2.8, d). The control sample, which had only physisorbed FITC solution, turned light yellow color in the solution, but the color was quickly removed by rinsing (Figure 2.8, c).

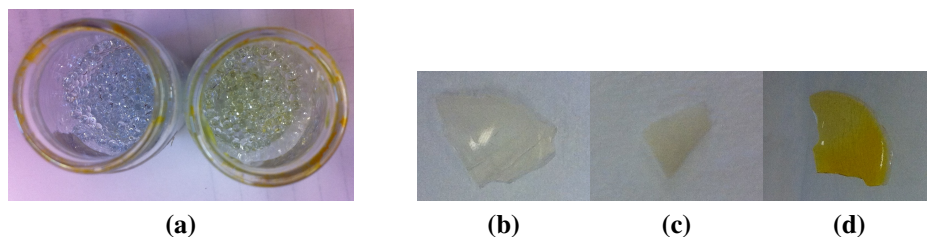


**Figure 2.8.** Images of substrates before and after reaction. a: images of glass beads untreated (left) and with FITC covalently bound (right); b: Images of porous silica untreated (left), controlled physisorbed (middle) and with FITC covalently bound (right) on a white surface.

### 2.3.1.2 Monolayer quantification

The measured thickness of the monolayer film on a silicon wafer was  $3.01 \pm 0.09$  nm with a mean square error (MSE) of 1.775 (Figure 2.9), close to expected range for a monolayer of FITC and APTES (1.9 - 2.2 nm, through simple estimations of bond distances).

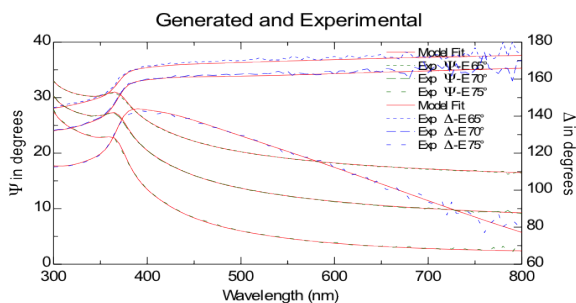


**Figure 2.9.** Monolayer thickness fitting by ellipsometry for FITC bound to silicon wafer surface.

### 2.3.1.3 FTIR spectrum of porous silica

The FTIR spectrum of porous silica was recorded and is shown in Figure 2.10. The two characteristic absorption peaks of Si-O-Si at around  $1080 \text{ cm}^{-1}$  and  $800 \text{ cm}^{-1}$  are the only two peaks shown in the spectrum, indicating the complete oxidation of porous silicon. The FTIR spectrum of FITC covalently bound to porous silica (data not shown) matches

exactly the spectrum of porous silica itself due to the huge excess of SiO<sub>2</sub> compared to only a monolayer of FITC.

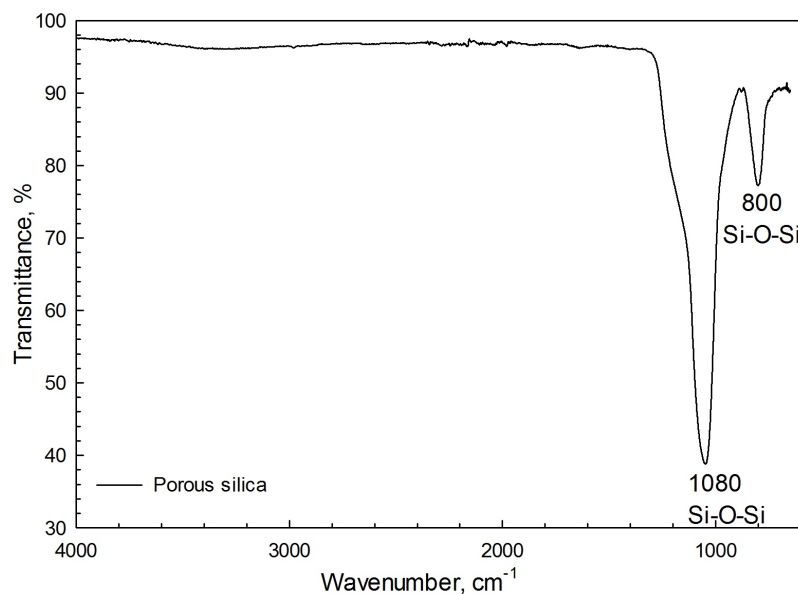


**Figure 2.10.** FTIR spectrum of porous silica substrate.

## 2.3.2 Fluorescence measurements

### 2.3.2.1 *Fluorescein in buffer solution*

In order to interpret the behavior of surface-bound fluorescein, its solution properties have to be understood. The protolytic equilibrium of the acidic and basic forms of the phenol groups on fluorescein in buffer solution is :



where  $FOH^-$  is fluorescein monoanion, and  $FO^{2-}$  is fluorescein dianion. The acid dissociation constant,  $pK_a$ , can be calculated using the normalized absorption spectra [30] as shown in Figure 2.11, Assuming the absorbance of the monoanion and dianion forms of fluorescein in aqueous phase follow Beer-Lambert's law:

$$\alpha_{FOH^-} = \frac{A^{450} - A_{FO^{2-}}^{450}}{A_{FOH^-}^{450} - A_{FO^{2-}}^{450}} \quad (2.3)$$

$$\alpha_{FO^{2-}} = \frac{A^{491} - A_{FOH^-}^{491}}{A_{FO^{2-}}^{491} - A_{FOH^-}^{491}} \quad (2.4)$$

where  $A^{450}$  and  $A^{491}$  are the measured absorbance values at 450 nm and 491 nm;  $A_{FOH^-}$  and  $A_{FO^{2-}}$  are the limiting absorbance values for the monoanion and dianion forms of fluorescein, respectively.  $\alpha_{FOH^-}$  and  $\alpha_{FO^{2-}}$  are the fraction of fluorescein presents as monoanion and dianion, respectively. Applying eq 2.3 and eq 2.4,  $\alpha_{FOH^-}$  and  $\alpha_{FO^{2-}}$  can be plotted as a function of pH (Figure 2.12). At low pH values,  $\alpha_{FOH^-}$  is equal to 1 and  $\alpha_{FO^{2-}}$  is equal to 0 when all fluorescein is present in monoanion form. Likewise at high pH values,  $\alpha_{FOH^-}$  is equal to 0 and  $\alpha_{FO^{2-}}$  is equal to 1 when all fluorescein exists in dianion form. The acid dissociation constant,  $pK_a$ , of fluorescein can be easily obtained from the pH value at which  $\alpha_{FOH^-}$  and  $\alpha_{FO^{2-}}$  are equal to 0.50. The  $pK_a$  of fluorescein in buffer was found to be 6.52 (IS = 0.030 M), which corresponds to the literature value 6.41 (buffer 0.050 M) [66], 6.36 (IS = 0.1 M) [104]. The slight different in these values is due to the ionic strength effect.

The fluorescence excitation and emission spectra of fluorescein in buffer solution were also studied. The protolytic equilibrium of ground and excited states fluorescein is shown



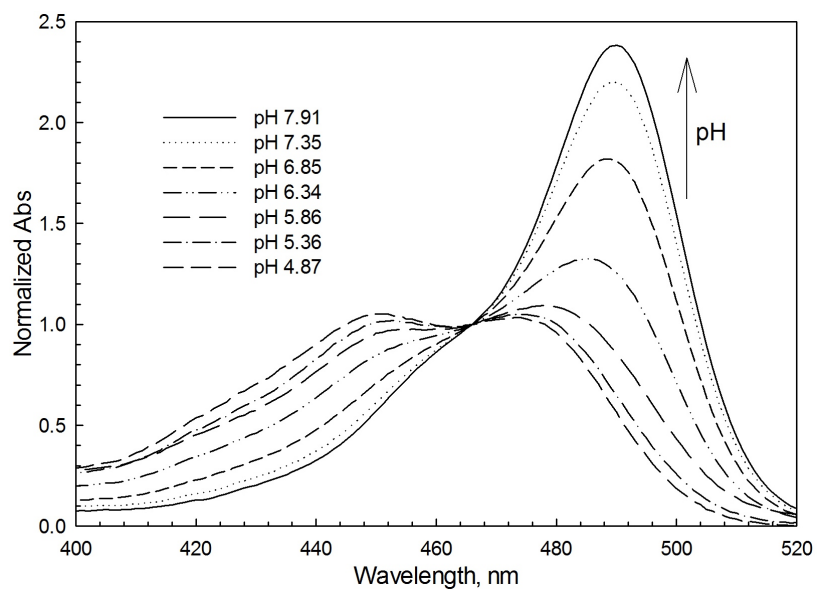


**Figure 2.11.** Normalized UV-Vis absorption spectra of fluorescein ( $2.0 \mu\text{M}$ ) in solution ( $\text{IS} = 0.030 \text{ M}$ ).

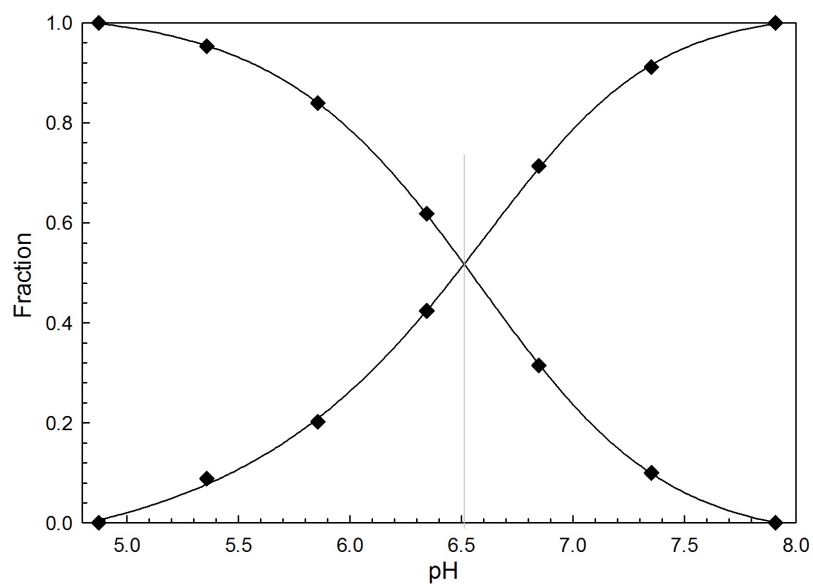


**Figure 2.12.** Ground state  $\text{pK}_a$  of dissolved fluorescein ( $2.0 \mu\text{M}$ ) in solution ( $\text{IS} = 0.030 \text{ M}$ ).

in Figure 2.13. The  $pK_a$  of fluorescein shifts in its excited state, so absorption by the monoanion can result in emission from the dianion excited states. As shown in Figure 2.14, fluorescein emits at around 515 nm independent of buffer pH. However, in pH 3.21 and pH 4.42 buffer solutions, the emission shows an additional shoulder peak at 550 nm. At high pH (>7), there is only one emission peak at 515 nm. This indicates that there are different emitting species in each solution, reflecting the change in  $pK_a$  of the excited state relative to ground state fluorescein. At high pH, only the fluorescein dianion exists in both ground and excited states; so the single emission peak at 515 nm corresponds to the emission of the dianion excited states. Hence, the emission of monoanion fluorescein excited states is the other one. At pH 3.21, only neutral species of fluorescein exists, if excited at 437 nm (the absorption peak of neutral species), the neutral excited state deprotonates rapidly and forms the monoanion excited state, which emits at 515 nm with a broad shoulder peak at 550 nm.

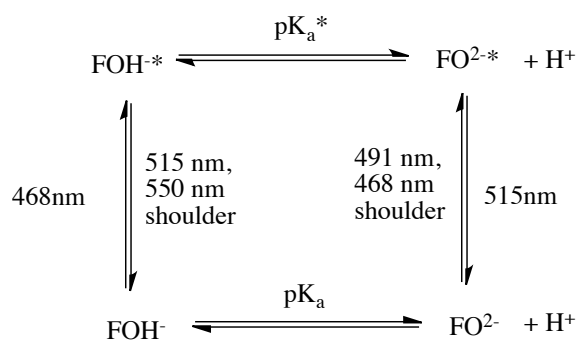


**Figure 2.13.** The protolytic equilibrium of ground and excited state fluorescein.

The normalized fluorescence excitation spectra of fluorescein in buffer are shown in Figure 2.15. The excited state  $pK_a^*$  can be calculated from the fluorescence excitation spectra as shown in Figure 2.16 using the same method as for the ground state  $pK_a$ .

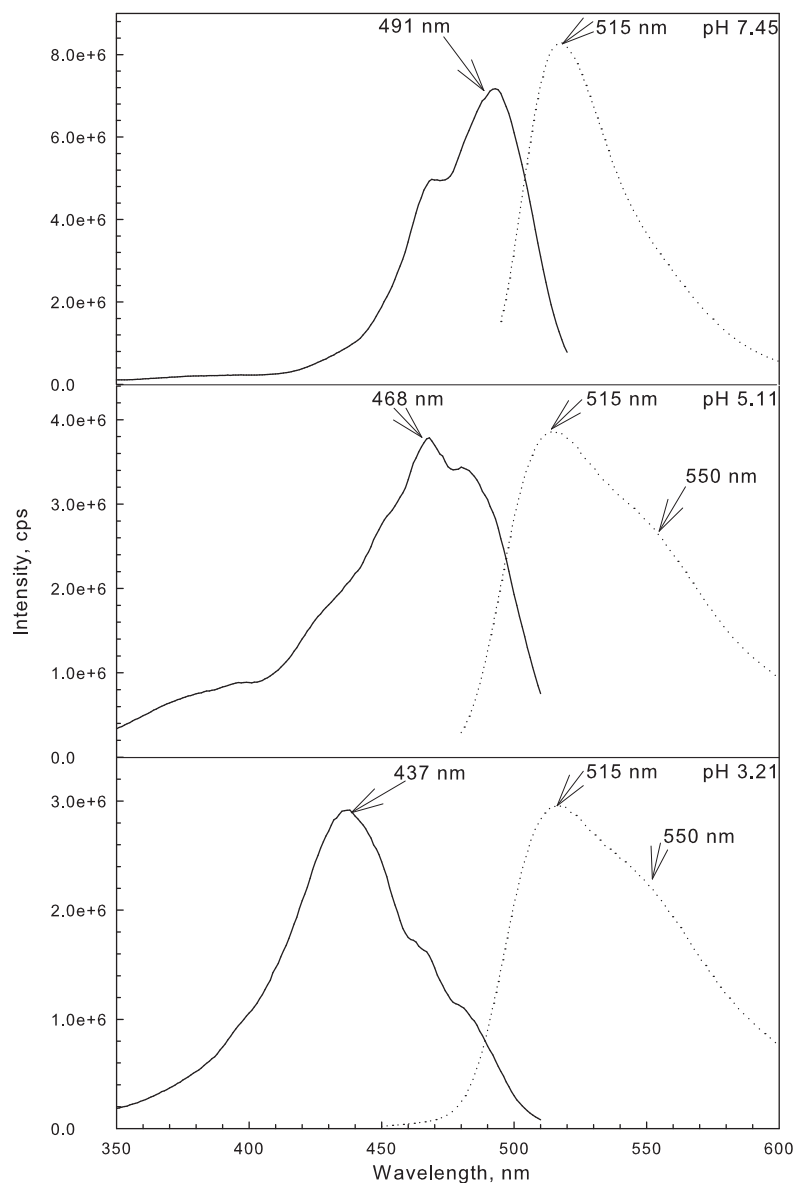


**Figure 2.14.** Fluorescence excitation (solid line) and emission (dotted line) spectra of fluorescein ( $2.5 \mu\text{M}$ ) in solution ( $\text{IS} = 0.120 \text{ M}$ ). Fixed emission wavelength for excitation spectra were 530 nm (pH 7.45) and 520 nm (pH 5.11 and pH 3.21); Fixed excitation wavelength for emission spectra were 491 nm (pH 7.45), 468 nm (pH 5.11) and 437 nm (pH 3.21).

$$\alpha_{FOH^{-*}} = \frac{I^{468} - I_{FO^{2-*}}^{468}}{I_{FOH^{-*}}^{468} - I_{FOH^{2-*}}^{468}} \quad (2.5)$$

$$\alpha_{FO^{2-*}} = \frac{I^{491} - I_{FOH^{-*}}^{491}}{I_{FO^{2-*}}^{491} - I_{FOH^{-*}}^{491}} \quad (2.6)$$

where  $I^{468}$  and  $I^{491}$  are the measured fluorescence intensity values at 468 nm and 491 nm in the excitation spectra;  $I_{FOH^{-*}}$  and  $I_{FO^{2-*}}$  are the limiting intensity values for the monoanion and dianion forms of fluorescein, respectively.  $\alpha_{FOH^{-*}}$  and  $\alpha_{FO^{2-*}}$  are the fraction of the excited states fluorescein presents as monoanion and dianion, respectively. Applying eq 2.5 and eq 2.6,  $\alpha_{FOH^{-*}}$  and  $\alpha_{FO^{2-*}}$  can be plotted as a function of pH (Figure 2.16). The excited state  $pK_a^*$  of fluorescein can be easily obtained from the pH value at which  $\alpha_{FOH^{-*}}$  and  $\alpha_{FO^{2-*}}$  are equal to 0.50. The  $pK_a^*$  of fluorescein in buffer was found to be 5.68 (IS = 0.030 M), much smaller than the ground state  $pK_a$ , 6.52, at the same ionic strength.

#### 2.3.2.2 FITC bound on quartz slides

Fluorescence spectra of FITC covalently bound to a quartz slide (as shown in Figure 2.17) are similar to fluorescence spectra of free fluorescein in buffer solution. At pH 7.2, the most dominant species is the dianion. It emits at 515 nm with excitation peak at 491 nm (shoulder peak at 468 nm). At pH 4.4, the most dominant species is the monoanion, which emits at 515 nm with a shoulder peak at 550 nm. The excitation peak for the monoanion is at 468 nm. As shown in the figure, the fluorescence spectra of immobilized FITC on quartz slide maintained sensitivity to pH. However, the fluorescence intensity was quite low due

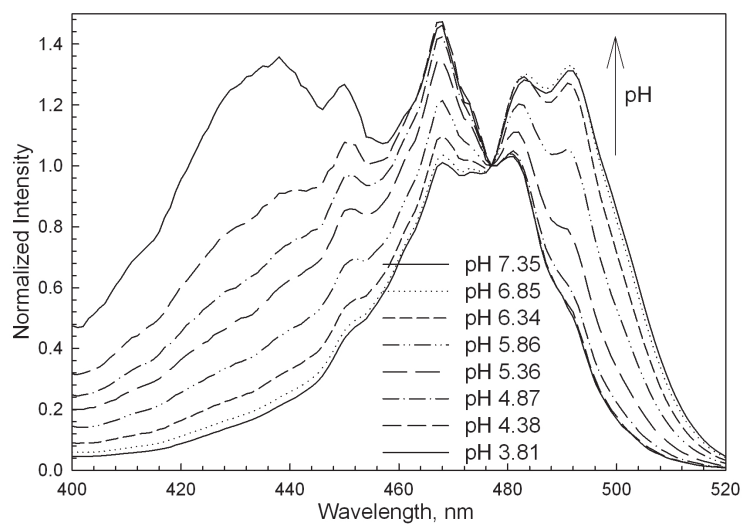


**Figure 2.15.** The normalized fluorescence excitation spectra of fluorescein (2.0  $\mu\text{M}$ ) in solution (IS = 0.030 M) with different pH.

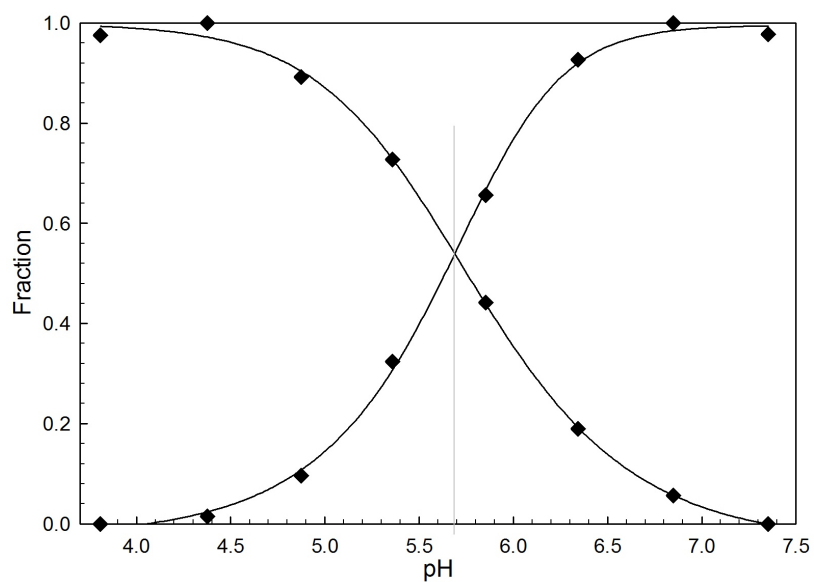


**Figure 2.16.** Excited state  $\text{pK}_a^*$  of dissolved fluorescein (2.0  $\mu\text{M}$ ) in solution (IS = 0.030 M).

to small amount of FITC exposed to the light and noise level was relatively high (as shown in Appendices, Figure A.3).

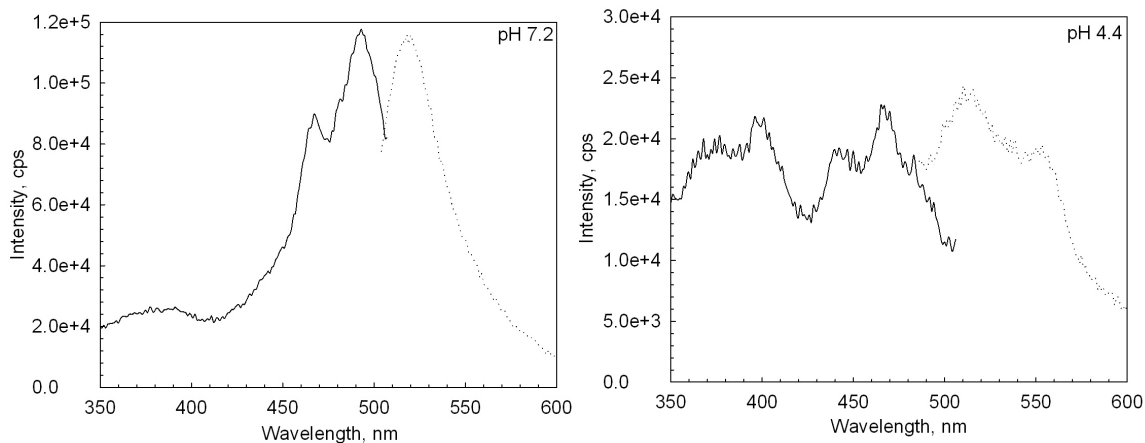


**Figure 2.17.** Fluorescence excitation (solid lines) and emission (dotted lines) spectra of FITC on quartz slide in solution (IS = 0.030 M). Fixed emission wavelength for excitation spectra were 520 nm (pH 7.2 and pH 4.4); Fixed excitation wavelength for emission spectra were 491 nm (pH 7.2) and 468 nm (pH 4.4).

### 2.3.2.3 FITC bound on glass beads

In order to increase the active surface area of SiO<sub>2</sub> relative to the quartz slides, glass beads with diameter as 2 - 3 mm were used as a substrate for FITC immobilization. The fluorescence intensity was increased about 22 times compare to FITC on quartz slide (from  $8.0 \times 10^3$  cps to  $1.8 \times 10^5$  cps) as shown in Figure 2.18. The fluorescence excitation spectra of FITC on glass beads surface in different buffer solution was recorded as shown in Figure 2.19. The excited states  $pK_a^*$  value is around pH 5.52 (as shown in Figure A.4 in Appendices), which is close to excited state  $pK_a^*$  in buffer solution, 5.68.

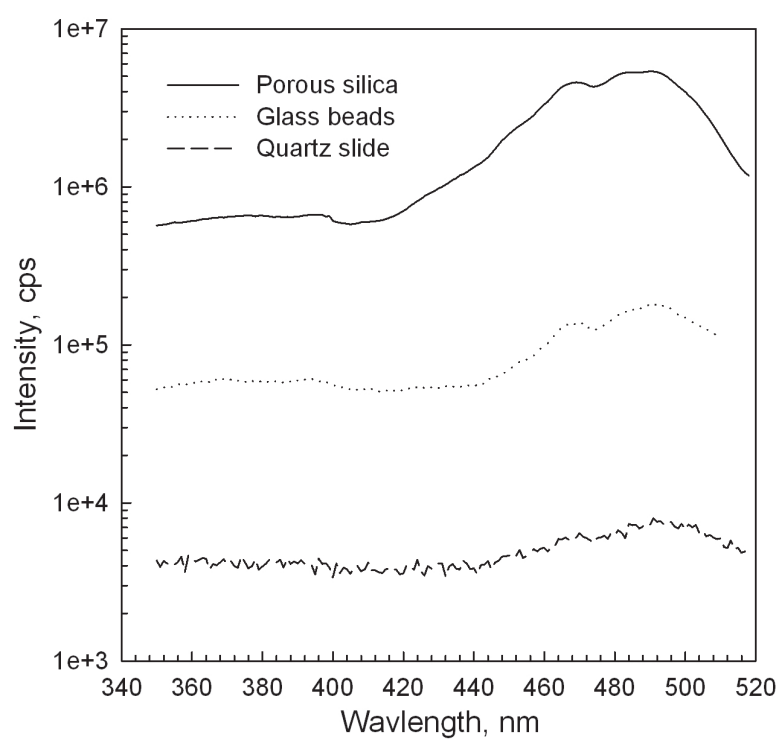


**Figure 2.18.** Fluorescence excitation spectra of FITC in different matrices in pH 7.0 solution with emission wavelength at 530 nm.

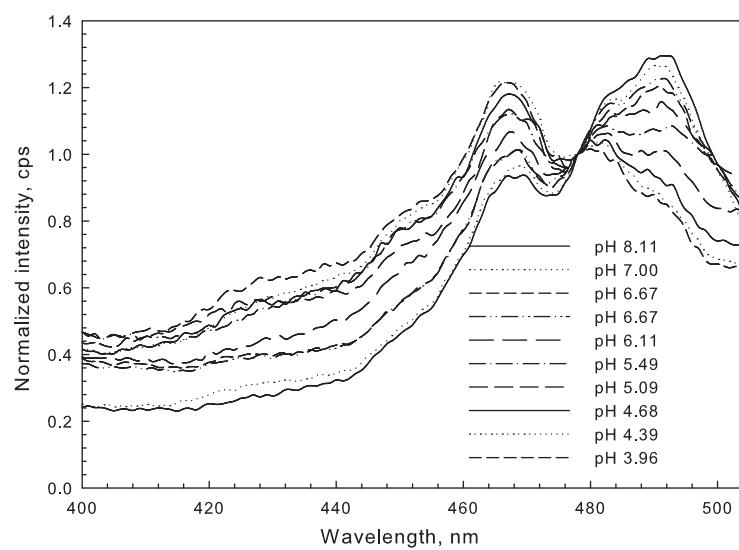


**Figure 2.19.** Normalized fluorescence excitation spectra of FITC on glass beads in solution (IS = 0.120 M) with emission wavelength at 530 nm.



#### 2.3.2.4 FITC bound in porous silica

With FITC immobilized on the internal surface of porous silica, the fluorescence intensity was increased 600 times compare to FITC bound on a quartz slide (from  $8.0 \times 10^3$  cps to  $5.4 \times 10^6$  cps, as shown in Figure 2.18). The normalized fluorescence excitation spectra of FITC in porous silica in different buffer are shown in Figure 2.20. FITC was still sensitive to the pH of the buffer solution as it was in buffer solution. The pH sensitive range for FITC in porous silica in buffer solution (IS = 0.030 M) is pH 4.5 - 7.0 (Figure 2.21, top). The excited states  $pK_a^*$  value is around pH 5.58 (as shown in Figure 2.21, bottom).

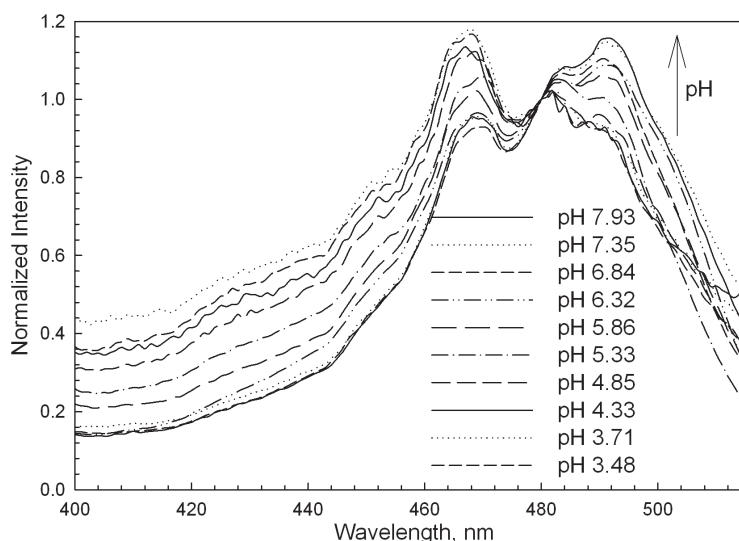


**Figure 2.20.** Normalized fluorescence excitation spectra of FITC in porous silica in solution (IS = 0.030 M) with emission wavelength at 540 nm.

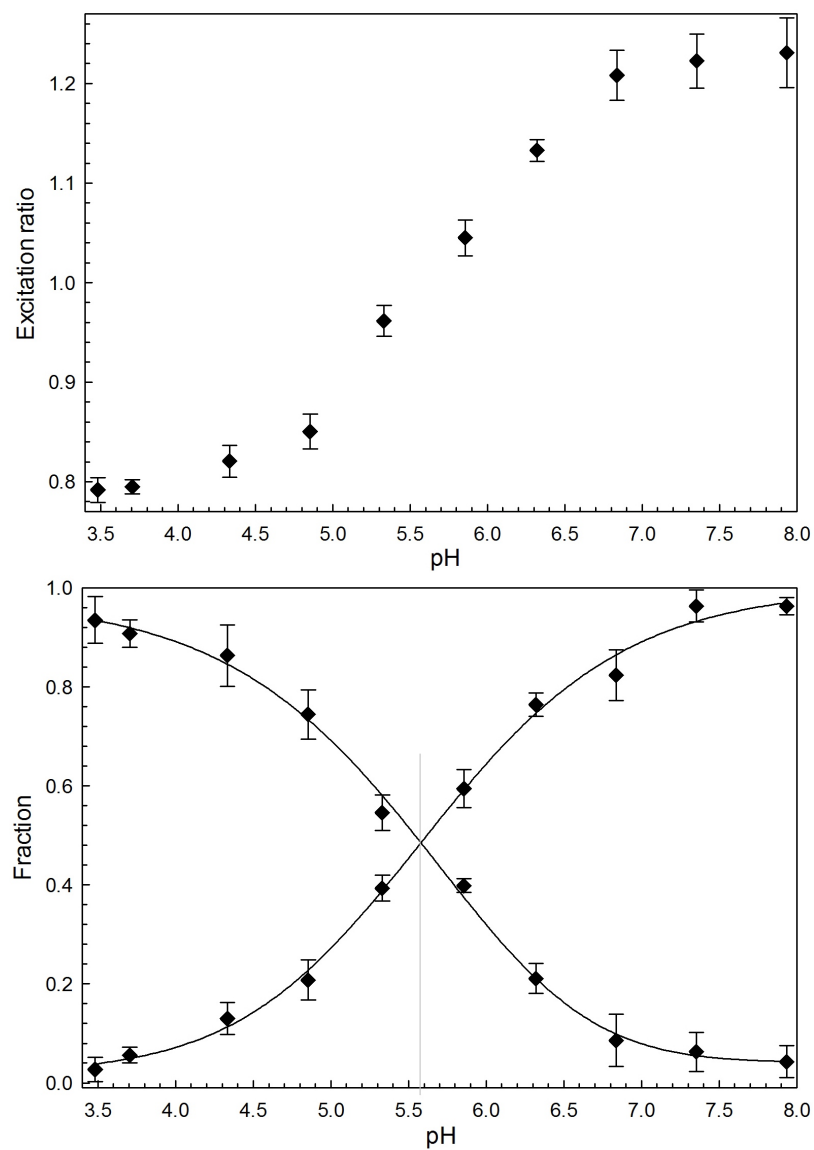


**Figure 2.21.** pH sensitive range (top) and  $pK_a^*$  (bottom) of FITC in porous silica in solution (IS = 0.030 M). The standard deviation was between 0.014 - 0.062 (n =4).

### 2.3.3 Effects of porous silica on FITC fluorescence

#### 2.3.3.1 $pK_a^*$ shift

The apparent  $pK_a^*$  of FITC in porous silica (5.58) was smaller (0.1 pH unit) than in buffer solution (5.68) (Figure 2.16 and 2.21). The apparent  $pK_a^*$  shift could indicate either (i) a change in the acidity of the dye, or (ii) a different  $H^+$  activity inside the porous silica relative to the bulk solution. A change in dye structure is unlikely because fluorescence excitation and emission spectra of the surface bound dye were identical to the spectra in bulk solution. A change in  $H^+$  activity inside the pores is plausible because of the free silanol (Si-OH) group on the internal surface of porous silica. Different types of silanol groups are present on the silica surface. They can form hydrogen bonds with their neighbors either directly or via water molecules (Figure 2.22) [105,106]. These silanol groups are able to accept and donate protons and form a highly active surface. The surface acidity of the silanol groups has been studied but is not well defined. A range of  $pK_a$  values has been reported for surface silanol groups. Usually two values are found, one in the range of 3.8 - 5.94 and a second in the range of 8.0 - 11.24 [105,107–109]. In our system, unreacted free amine groups from APTES further complicated buffering by the surface silanols.

The free silanol groups affect dye behavior in the pores of the porous silica by donating or accepting the protons, effectively acting as an additional buffer. As shown in Figure 2.23, fluorescein on the silica surface does not match ideal acid-base behavior as calculated using the Henderson-Hasselbalch equation:

$$pH = pK_a^* + \lg \frac{[FO^{2-}]}{[FOH^-]} \quad (2.7)$$

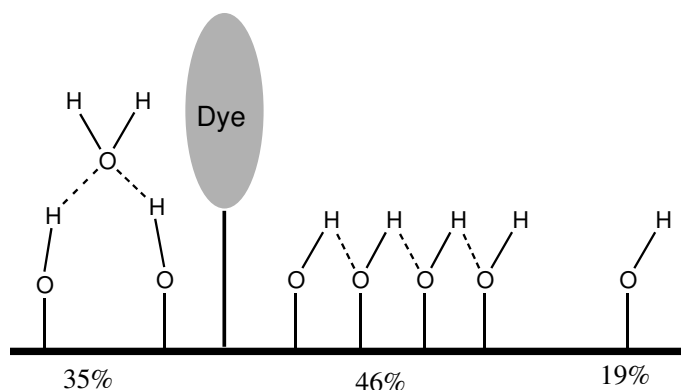


**Figure 2.22.** Schematic representation of silanol groups at the silica surface.

where the value of  $pK_a^*$  is 5.58 (the apparent  $pK_a^*$  value for FITC in porous silica, ionic strength of 0.030 M). Additional buffering inside the pores slightly flattens the titration curves relative to the ideal titration curves.

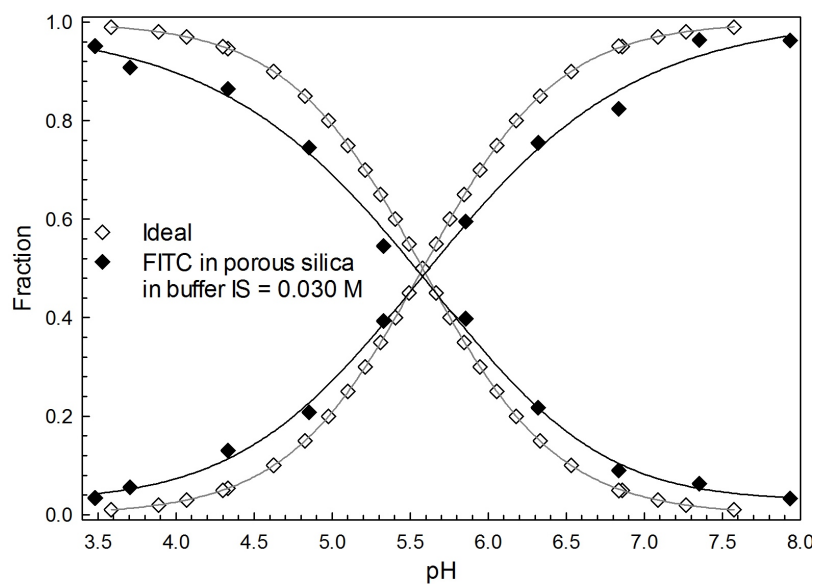


**Figure 2.23.** Experimental and ideal behavior of FITC dissociation in porous silica.

In other words, the pH in the pores is different from the pH of the bulk solution. The dye reports the actual pH inside the pores. Assuming no true shift in the dye  $pK_a^*$ , the pH

inside the pores can be calculated using the following equation [110]:

$$pH = pK_a^* + \lg \frac{R_{min} - R}{R - R_{max}} \quad (2.8)$$

where, the value of  $pK_a^*$  is 5.68 (the apparent  $pK_a^*$  value for fluorescein in buffer, ionic strength of 0.030 M).  $R$  is the excitation ratio,  $I_{491}/I_{468}$ . The pH calculated by this equation using excitation ratio is plotted against the bulk solution pH (pH reading from electrode) in Figure 2.24, a. At pH lower than  $pK_a^*$ , pH inside the pores is higher than bulk solution. At pH higher than  $pK_a^*$ , pH inside the pores is lower than bulk solution. This shift reflects the buffering effect of the free surface silanol groups. To calculate the bulk solution pH, eq 2.8 can be adjusted by adding an empirical parameter,  $\alpha$ , for considering the buffering effect from the silanol groups. From our data, for solution with ionic strength 0.030 M, the value for  $\alpha$  is 1.17, as shown in eq 2.9. The bulk pH from optical sensor using eq 2.9 is plotted against bulk pH from electrode in Figure 2.24, b.

$$pH = pK_a^* + \alpha \cdot \lg \frac{R_{min} - R}{R - R_{max}} \quad (2.9)$$

### 2.3.3.2 Ionic strength effects

As a weak acid, the acid dissociation constant of fluorescein is affected by ionic strength as approximated by the following equation [111]:

$$\Delta pK_a = pK_a^{th} - pK_a^I = 0.512(z_{FO^{2-}}^2 - z_{FOH^-}^2) \frac{I^{0.5}}{1 + 1.6I^{0.5}} \quad (2.10)$$

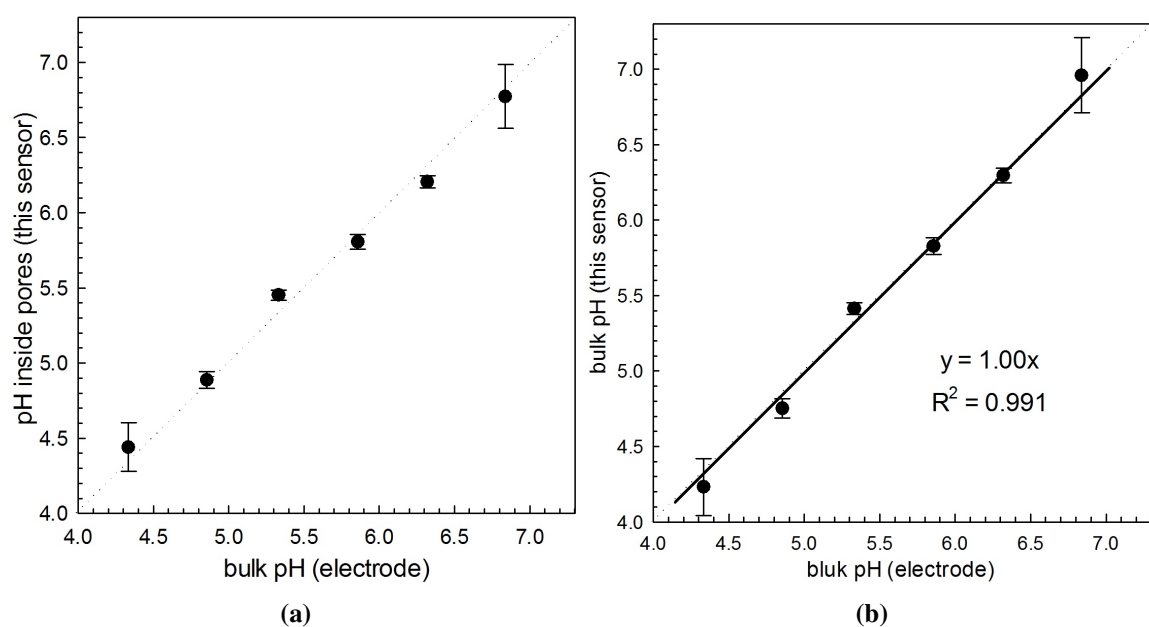


**Figure 2.24.** Comparison of pH measurement from optical sensor and pH from electrode. (a): pH inside pores (from this optical sensor, eq 2.8) vs. bulk pH (from electrode); (b): bulk pH (from this optical sensor, eq 2.9) and bulk pH (from electrode). The standard deviation was between 0.043 - 0.114 ( $n = 4$ ).

where  $pK_a^{th}$  is the true thermodynamic  $pK_a$  of the dye,  $z_{FO^{2-}}$  and  $z_{FOH^-}$  are the charges on the dianion and the monoanion form of fluorescein, respectively;  $I$  is the ionic strength of the solution. This relationship arises due to changes in the activity of the ionic species. The ionic strength dependence of the dye over the observed range (0.030 - 0.120 M) was studied and the shift of  $pK_a$  and  $pK_a^*$  was shown in Figure 2.25. As ionic strength increases, the acid dissociation constants of ground state and excited state fluorescein,  $pK_a$  and  $pK_a^*$ , respectively, decrease. The effect is most pronounced at low ionic strength. For fluorescein, the shifts are not large; increasing ionic strength from 0.030 M to 0.120 M results in a  $pK_a$  shift of 0.13. The thermodynamic ground state  $pK_a$  and excited state  $pK_a^*$  can be calculated from eq 2.10. Using  $\Delta pK_a$  of 0.21 at  $IS = 0.030$  M, the thermodynamic  $pK_a$  and  $pK_a^*$  were calculated to be 6.73 and 5.89, which match the calculated literature values, 6.7 [112] and 5.97 [66], respectively (Table 2.1).

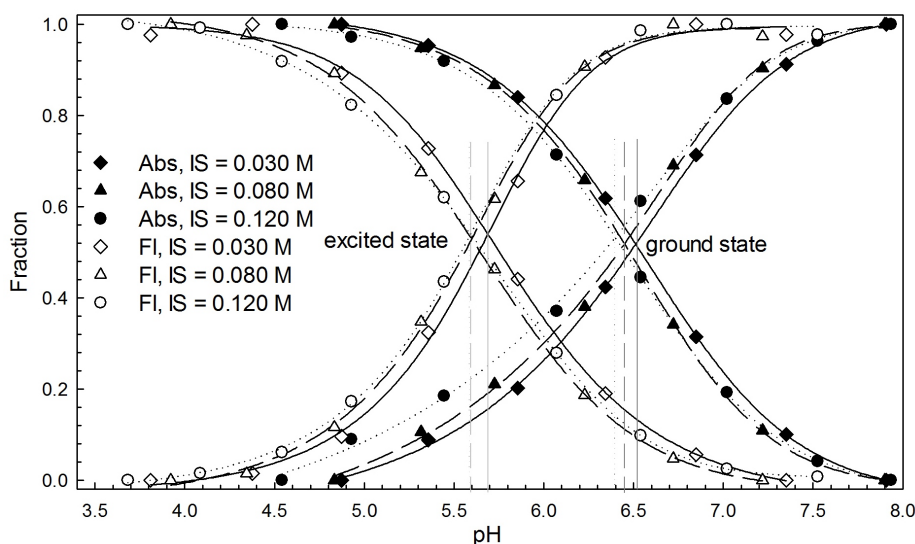


**Figure 2.25.**  $pK_a$  and  $pK_a^*$  of fluorescein in buffer with different ionic strength, calculated from absorption and fluorescence spectra, respectively.

The ionic strength effect on  $pK_a^*$  of FITC in porous silica was also studied. As shown in Figure 2.26, at low ionic strength, as 0.030 M, the  $pK_a^*$  of FITC in porous silica was 5.58.

At high ionic strength, as 0.080 M and 0.120 M, the  $pK_a^*$  of FITC in porous silica were 5.42 and 5.41, respectively. The  $pK_a^*$  shift of FITC on porous silica is a little larger than fluorescein in buffer, suggesting that the surface charges on the internal surface of porous silica may also influence local ionic strength.

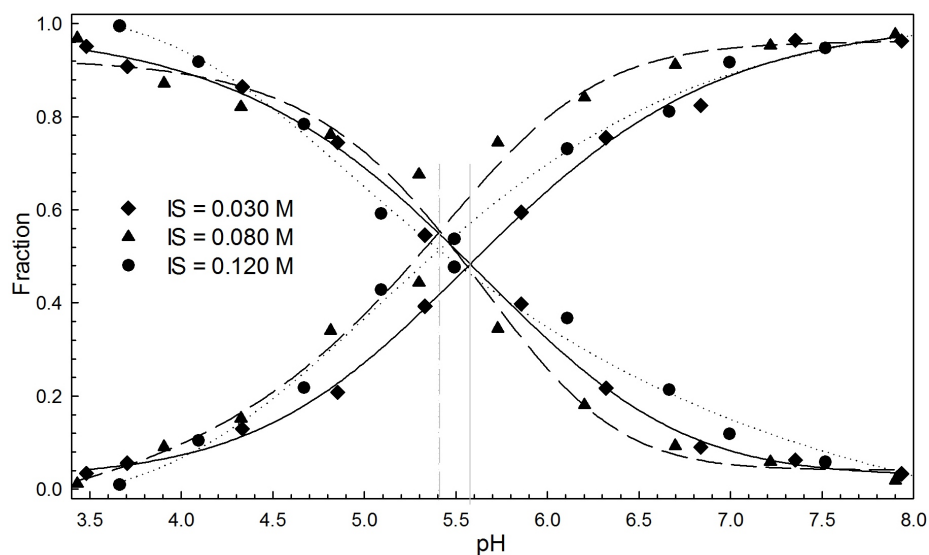


**Figure 2.26.**  $pK_a^*$  of fluorescein in silica in solution with different ionic strength, calculated from fluorescence spectra.

**Table 2.1**

The acid dissociation constants of fluorescein and FITC in porous silica.

	Thermodynamic values		Ionic strength		
	literature	this study	0.030 M	0.080 M	0.120 M
Fluorescein, $pK_a$	6.7 <sup>1</sup>	6.73	6.52	6.46	6.40
Fluorescein, $pK_a^*$	5.97 <sup>2</sup>	5.89	5.68	5.58	5.58
FITC in porous silica, $pK_a^*$		5.79	5.58	5.42	5.41

1.R. Markuszewski, et al., Abstracts of the American Chemical Society 180 (1980) 179-ANYL.

2.R. Sjoback, et al., Spectrochimica Acta Part a-Molecular and Biomolecular Spectroscopy 51(1995) L7-L21.



### 2.3.3.3 Fluorescence lifetimes

The fluorescence lifetimes of fluorescein in buffer solution and in porous silica were measured. The fluorescence decay was well described in a single exponential component (Figure 2.27). The fluorescence lifetimes of fluorescein in buffer solution and in porous silica are listed in Table 2.2.

The lifetime of fluorescein increases with increasing pH in solution. At high pH, 7.93, the main species in buffer solution was the dianion, and the lifetime of excited dianion fluorescein was 3.9 ns. At low pH, 4.36, the main species in buffer was the monoanion, and the lifetime of excited monoanion fluorescein was 3.0 ns; both agree with literature values [113–115]. The lifetime of the excited state of dianion FITC in porous silica was slightly shorter compared to free fluorescein in buffer, which were 3.5 ns and 3.9 ns, respectively. At low pH, the fluorescein lifetime of the excited state monoanion FITC in both mesoporous silica and in solution was almost the same,  $2.9 \pm 0.1$  ns and  $3.0 \pm 0.1$  ns, respectively.

**Table 2.2**

Fluorescence lifetime of fluorescein in buffer and FITC in porous silica (IS = 0.030 M).

Sample	Excitation, nm	Emission, nm	Lifetime, ns	$\chi^2$	pH
Fluorescein	468	515	$3.0 \pm 0.1$	1.057	4.36
Fluorescein	490	515	$3.9 \pm 0.1$	1.054	7.93
FITC in porous silica	468	515	$2.9 \pm 0.1$	1.023	3.48
FITC in porous silica	490	515	$3.5 \pm 0.1$	1.022	7.93

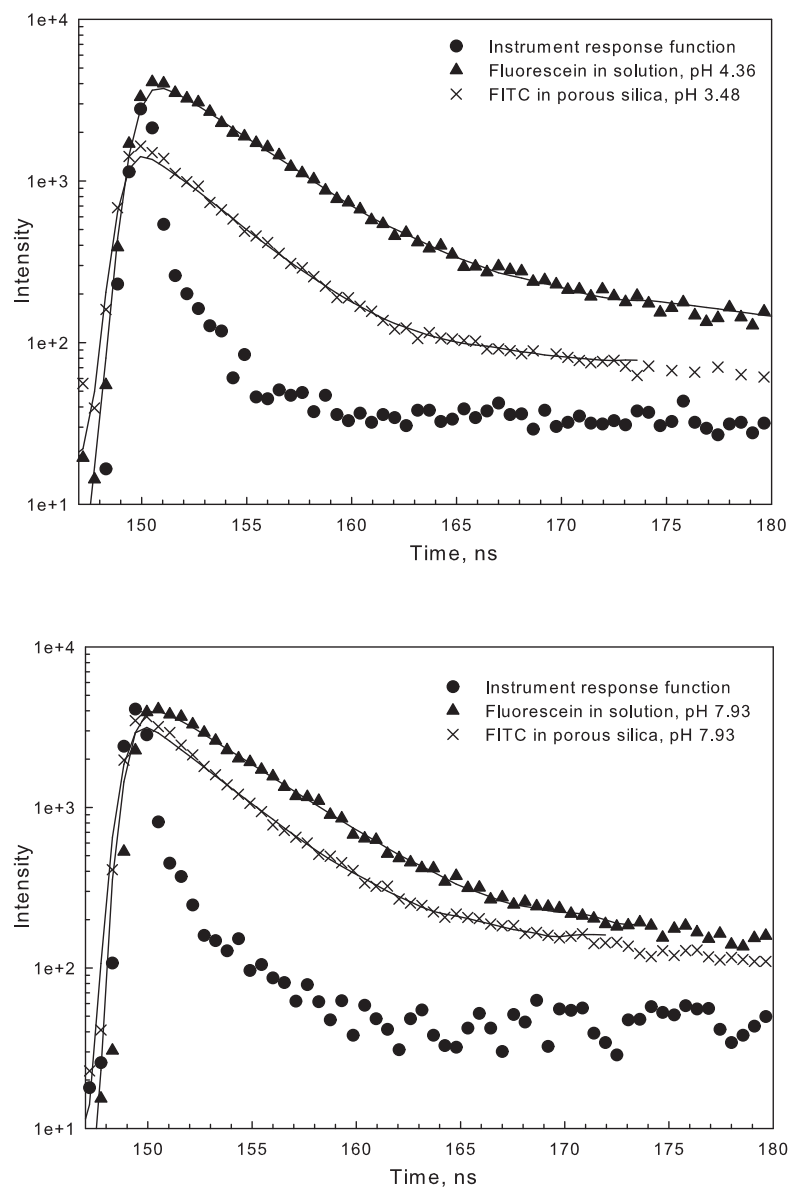


**Figure 2.27.** Fluorescence decay curves for fluorescein in buffer and FITC in porous silica. The solid lines represent the best fits to the data.  $\lambda_{ex} = 468$  nm (top);  $\lambda_{ex} = 490$  nm (bottom);  $\lambda_{em} = 515$  nm (top and bottom)

### 2.3.4 Sensor performance

The excitation ratio of FITC in porous silica in buffer solution is reproducible with reported pH changes from 3.5 to 7.4 as shown in Figure 2.28. In the pH sensitive range 4.5 - 7.0, the error was small,  $\pm 0.1$  pH unit. The greatest source of error appears to be related to the slow equilibrium time (up to 100 minutes); slow diffusion into small and possibly non-uniform pores can expose each dye molecule to slightly different pH environment. In addition, the pore size of the sample might be reduced by the attachment of the fluorescein single layer (3.01 nm) on the surface, which could cause a stronger diffusion resistance. Porous silica with larger pore size would enhance the response time and the accuracy of the sensor. Although larger pores would reduce surface area and thus fluorescence intensity, intensity is not a limiting factor.

No leaching was found for FITC in porous silica sample after thoroughly washed with deionized water. The sensor was stable for over 4 months.

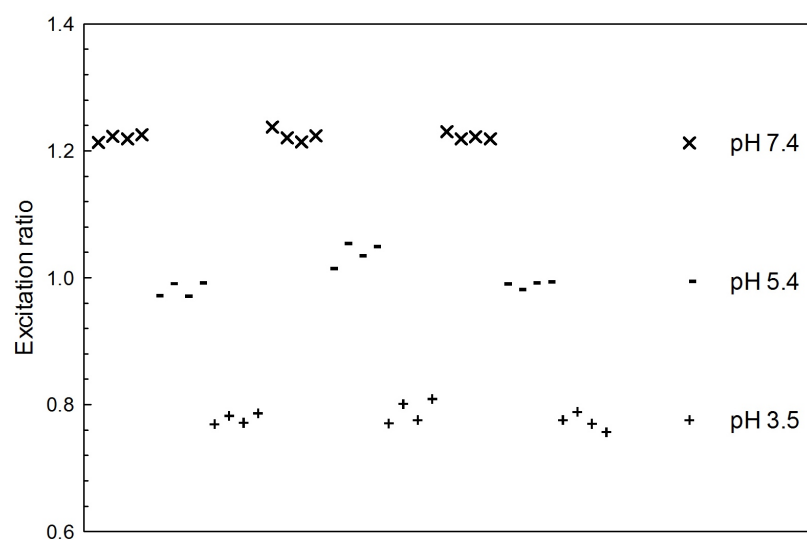


**Figure 2.28.** Repeatability of the excitation ratio of FITC in porous silica at pH 7.4, 5.4 and 3.5. The standard deviation was between 0.005 - 0.019 (n=4). Time between each data point at the same pH was 2 minutes. Time between each buffer solution was 100 minutes.

## 2.4 Conclusion

The study shows that fluorescein covalently bound to a silica surface retains pH sensitivity. Mesoporous silica was proved to be a viable matrix for fluorescein immobilization. Fluorescence excitation spectra were recorded, and the excitation ratio  $I_{491}/I_{648}$  was used to calculate the pH. The excitation state  $\text{pK}_a^*$  of fluorescein in porous silica was obtained through fluorescence excitation spectra as 5.58 (ionic strength at 0.030 M). The excited state  $\text{pK}_a^*$  in porous silica shifts down by about 0.1 pH units compared to fluorescein in buffer solution due to the free silanol groups on silica surface. The ionic strength effect of the buffer was studied, with increasing ionic strength, the excited state  $\text{pK}_a^*$  of fluorescein in both buffer and porous silica decreased. As the ionic strength changes from 0.030 M to 0.0120 M, the  $\text{pK}_a^*$  value in porous silica changes from 5.58 to 5.41, about 0.17 pH units. The sensor was most sensitive at pH 4.5 to 7.0, with error less than 0.1 pH unit. After washing thoroughly, no leaching was detected and the sensor was reproducible and stable for over 4 month stored in DI water.

## 2.5 Future work

Mesoporous silica with more uniform and larger pores would be needed for future study and testing. Equilibrium time would be expected to decrease if pores size of porous silica is larger. Neutralization of the untreated silanol groups on the silica surface might increase the sensor sensitivity.

### **3. PHYSICAL ENTRAPMENT OF INDICATORS IN POROUS SILICA THROUGH SOL-GEL PROCESS FOR PH SENSING**

#### **3.1 Introduction**

As chemically sensitive optical materials, sol-gel materials have gained great interest because they are optically transparent, mechanically stable, chemically inert and flexible for sensor configurations [100]. In addition, the sol-gel process only requires relatively simple chemistry at low hydrolysis temperature [29]. Hence, sol-gels have been extensively studied with respect to their applications to chemical sensing of analytes such as  $H^+$  [13, 34,35,38,39,51,116], carbon dioxide [37,86,100] and ammonia [29].

##### **3.1.1 the Sol-Gel process**

In the sol-gel process, a silica gel is made by hydrolysis of an alkoxide precursor followed by condensation of silanol. The sol-gel aged solution can be cast to form thin films.

The solvent is then evaporated to form a highly porous and three-dimensional network. Sol-gel films are usually transparent and stable, which provide an inert matrix for immobilization of optical probe molecules [29].

The principle of the sol-gel process is rather simple: a network of an oxide is progressively built through inorganic polymerization reactions at room or elevated temperature [117]. Crystalline (e.g., quartz) or amorphous (e.g., glass) materials may be prepared based on the regularity of the macromolecular structure. The usual molecular precursors are metallo-organic compound such as alkoxides  $M(OR)_n$  where M is a metal or a metalloid and R is an alkyl group. For example, tetraethylorthosilicate (TEOS),  $Si(OC_2H_5)_4$ , is commonly used in the sol-gel synthesis of silica and glasses. Such chemicals are dispersed in a solvent (usually organic, e.g., ethyl alcohol) and react according to the well-known steps in polymer chemistry:

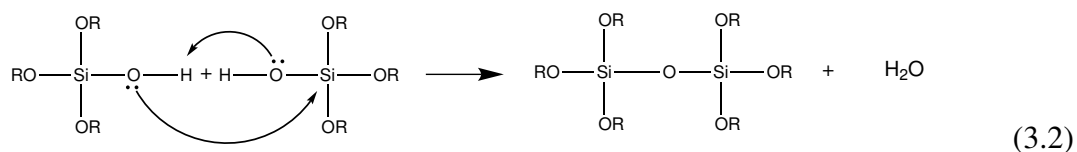
*Initiation:* the hydrolysis of the alkoxide:



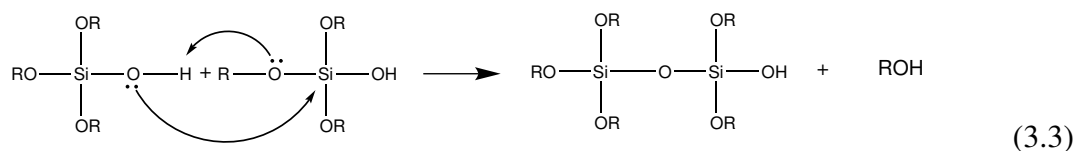
The reactive bond Si-OH, which is necessary for the continuation of the reaction, is formed during this step.

*Propagation:* the condensation of the hydrolyzed species, with formation of bridging oxygens, occurs according to two possible mechanisms:

*oxolation:* a dehydration (i.e., the leaving group is  $H_2O$ )-



or *alcoxolation*: a dealcoholation (i.e., the leaving group is ROH)-



At the end, every oxygen is bridging and hence a pure and highly homogeneous oxide network is obtained.

Silicon alkoxides generally react slowly with water, but the reaction process, hydrolysis and condensation, can be sped up by acid or base catalysts. The gelation of the precursor sols can be shortened from 1000 hours to 92 hours by addition of 0.05 M HCl [118]. The rate and extent of the hydrolysis reaction is most influenced by the strength and the concentration of the catalysts. Different catalysts result in gels with different properties and microstructures, which can be related to the differences in the catalytic mechanism. With acidic catalyst, hydrolysis is faster compared to condensation and more open, three-dimensional structures are formed. In contrast, with base catalyst, condensation is much faster than hydrolysis, leaving hydrolysis as the rate limiting step. And a much denser and more colloidal sol-gel is formed [33].



Between the starting solution and the final solid, several intermediate steps occurs during which sols or gels are formed. First, a sol is obtained. As the polymerization reactions are going on, the particles grow and coalesce to form clusters continuously increasing in size. After a time, a giant cluster appears, a macromolecule as large as the vessel in which it was formed. This is a gel, which is a semisolid system comprising two phases, solid and fluid, embedded in each other and the pores of the solid are of colloidal dimensions [117]. This process is shown in Figure 3.1.

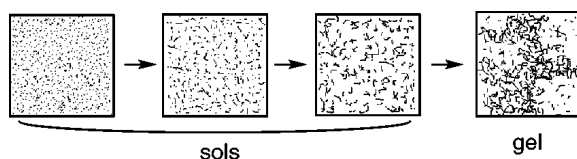


**Figure 3.1.** Schematic picture of the sol-gel transition. Molecular species grow by polycondensation (sol) until a giant cluster is formed (gel). Reprinted with permission from ref [117].

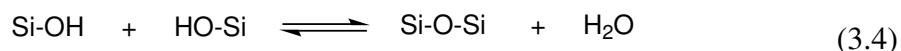
The gel strengthens improved as the residual isolated clusters form bonds with the developing network, which is called aging. The growing number of bonds and the occurrence of dissolving-precipitation reactions make the elastic modulus increase with time. The gel then reaches the favorable conditions for which it becomes possible to dry it with the lowest number of cracks.

Sol-gel thin film can be obtained by spin-coating or dip-coating of the aged sols. The thickness of the thin film can be controlled by the solution viscosity and the spin- or dip-coating speed [116].

Drying is another essential process that can control the density and porosity of the sol-gel film, which can be achieved either under normal pressure (microporous xerogrels) or supercritical conditions (mesoporous aerogels). Drying under normal pressure causes capillary pressure between the gas and liquid phases on the pore surface. These capillary

pressure can combine with shrinking force and leads to collapse of the pores in the network, resulting in low porosity and low surface area. Mesoporous areogels with high porosity, high surface area and low density can be achieved by supercritical drying (CO<sub>2</sub>) [119].

Pure silica (when using tetraethoxysilane) contain a large amount of of unreacted surface silanol groups (Si-OH) on the internal surface, which can still go through water condensation reaction after the gel is dry, resulting in shrinking and cracking of the films and limiting their long term stability [120].



Several methods have been used to prevent shrinking and the collapse of the pores. Thermal treatment (500 °C - 800 °C) of silica sol-gels has been used to minimize the amount of the unreacted surface silanol groups, but the porosity of the sol-gel film was greatly decreased by the high temperature thermal treatment [120]. The most used approach to improve the stability of the sol-gel films for chemical sensor membranes is physical entrapment of organic polymers into sol-gel pores and addition of organic functional groups through organo-silane coupling precursors (such as 3-glycidoxypropyltrimethoxysilane, GPTMS). Adding organo-silane coupling precursors increases flexibility and decreases the amount of reactive silanol groups on the gel surface, thus directly reduces gel shrinkage [33].

In this study, the microstructure of the film is a composite of two precursors, ethyltriethoxysilane (ETEOS) and 3-glycidoxypropyltrimethoxysilane (GPTMS). ETEOS is an organically modified alkoxysilane with a -C<sub>2</sub>H<sub>5</sub> functional group. During the hydrolysis of the ethoxy groups with HCl as the catalyst, silanol groups were formed and then condensed

to form a silicate network. GPTMS is another organically modified alkoxide with an epoxy ring which can be opened and crosslinked to form a poly(ethylene oxide) chain in certain condition [38]. The structure of the poly(ethylene oxide) chain is shown in Figure 3.2. The base catalyst for the hydrolysis of GPTMS, 1-methylimidazole (MI) is also an initiator for the epoxy ring opening.

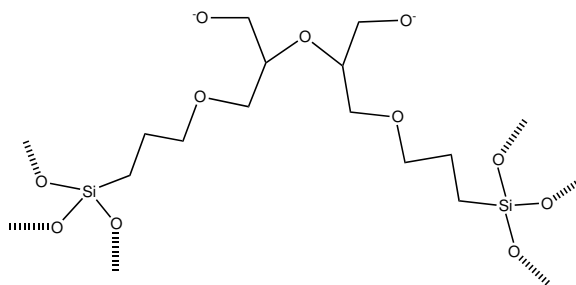


**Figure 3.2.** Structure of GPTMS-derived network after epoxy ring opening.

The thin film was deposited by spin coating, and the thickness of the film was controlled by the viscosity of the sols, which was controlled by the molar ratio of the precursors and the solvent, ethanol. The film was cured at various temperature, and pH sensitivity of the dyes in the sol-gel films were studied.

### 3.1.2 pH-sensitive indicators information

Two pH-sensitive fluorescent indicators were used in this study, fluorescein-5-(and-6)-sulfonic acid trisodium salt (FS) and 8-hydroxypyrene-1,3,6-trisulfonic acid trisodium salt (HPTS). Their structures are shown in Table A.1. FS is one of the fluorescein derivatives, with the same absorption and fluorescence properties and pH sensitivity as fluorescein (see Chapter 2). The sulfonate groups were used for ion-pair with ion-pair agents.

HPTS is a fluorescent pH indicator with large fluorescence quantum yield, high photo-

stability, in addition, its  $pK_a$  value at 7.3 [13,32] makes it quite suitable for pH measurement in biological research and environment monitoring. HPTS is composed of four fused aromatic rings, three sulfonate groups and a hydroxyl group. The sulfonate groups provide water solubility and the hydroxy group provides pH sensitivity. HPTS is highly photo-acidic, which means it is more acidic in its electronically excited state. The  $pK_a^*$  of excited photo-acidic compounds is usually 6-7 pH unit lower than  $pK_a$  in the ground state [121]. As for HPTS,  $pK_a^*$  in solution is  $\sim 1.0$  [28].

The absorption spectra of HPTS in solution vary with pH of the solution. In acidic condition, where HPTS is protonated, the absorption maximum is near 400 nm. As the pH of the solution becomes more basic and HPTS is deprotonated, a peak at 450 nm grows in. The UV-Vis absorption spectra of HPTS in solution is shown in Figure 3.3. The molar extinction coefficients were calculated based on experimental data:  $\epsilon_{HPTS}^{400} = 24,000 \text{ cm}^{-1} \text{ M}^{-1}$ ;  $\epsilon_{HPTS}^{450} = 2,330 \text{ cm}^{-1} \text{ M}^{-1}$ ;  $\epsilon_{PTS^-}^{400} = 6,340 \text{ cm}^{-1} \text{ M}^{-1}$ ;  $\epsilon_{PTS^-}^{450} = 23,800 \text{ cm}^{-1} \text{ M}^{-1}$ .

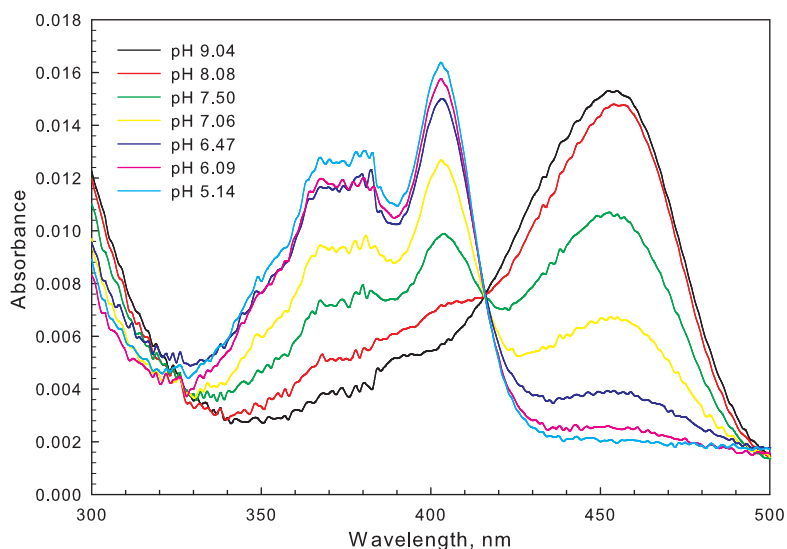


**Figure 3.3.** UV-Vis absorption spectra of HPTS ( $0.99 \mu\text{M}$ ) in solution ( $\text{IS} = 0.030 \text{ M}$ ).

Regardless of solution pH, HPTS emits near 510 nm and this emission is from the excited deprotonated form. Due to its low  $pK_a^*$ , HPTS is deprotonated upon excitation and emission before protonation of the excited state may occur. In ethanol solution, the deprotonation of the excited state HPTS is forbidden because there are no water molecules for hydrogen bonding with the protons. Thus the emission of the excited state protonated HPTS can be observed at  $\sim 425$  nm. The fluorescence excitation and emission spectra of HPTS in both ethanol and aqueous solution with different pH are shown in Figure 3.4.

The excitation wavelength of the protonated and deprotonated forms of HPTS are different, and therefore the excitation spectra of HPTS is still dependent upon solution pH as shown in Figure 3.5. The peak maximum of the deprotonated form from the excitation spectra is red shifted to 467 nm compared to 450 nm in absorption spectra. This shift probably is due to the electronic vibration in the excited state.

These dual excitation spectra of both FS and HPTS allow the ratiometric method of pH determination to overcome the possible leaching problem in sol-gel films. Both indicators were physically entrapped in sol-gel films. To eliminate the leaching from the film, both indicators were ion-paired with a common cationic surfactant cetyltrimethylammonium bromide (CTAB) before entrapment.

### 3.1.3 Specific aims of this study

- Synthesize sol-gel thin films with two precursors ETEOS and GPTMS and study the morphology of the thin films.
- Physically entrap both pH indicators FS and HPTS in sol-gel films and eliminate the leaching problem.

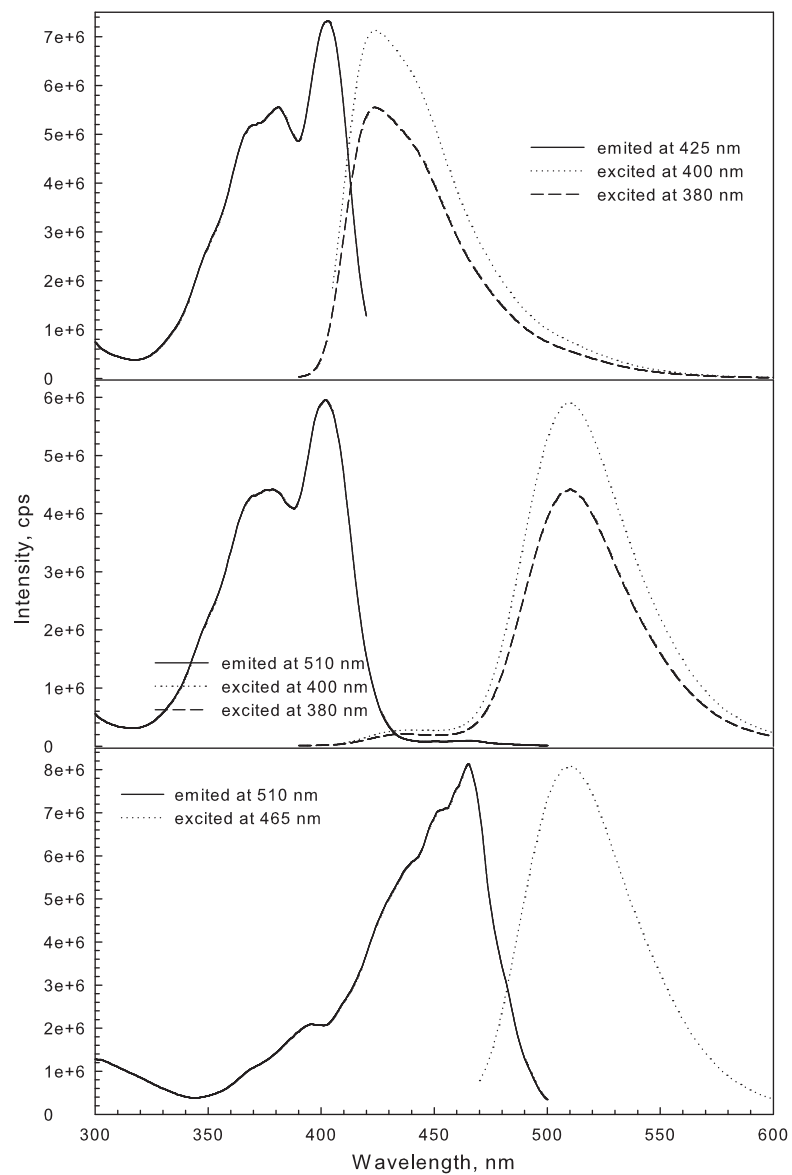


**Figure 3.4.** Fluorescence spectra of HPTS (0.99  $\mu\text{M}$ ) in ethanol (top) and solution pH 5.32 (middle) and pH 9.97 (bottom).

- Study the spectra behavior of FS and HPTS in sol-gel films and compare with that in buffer solution.
- Evaluate the potential of both FS and HPTS in sol-gel films as pH sensors

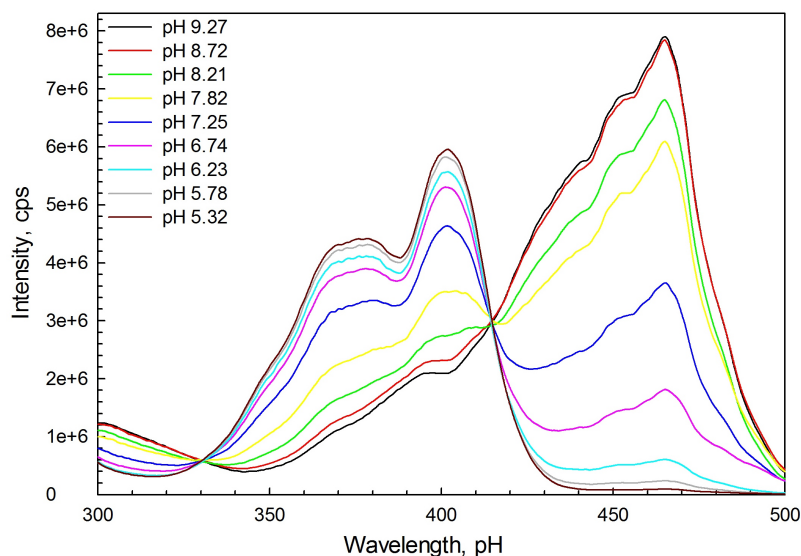


**Figure 3.5.** Fluorescence excitation spectra of HPTS ( $0.99 \mu\text{M}$ ) in solution ( $\text{IS} = 0.030 \text{ M}$ ) with different pH with emission wavelength at 510 nm.

## 3.2 Experimental

### 3.2.1 Reagents and materials

Ethyltriethoxysilane (ETEOS), (3-glycidoxypopyl)trimethoxysilane (GPTMS), 1-methylimidazole (MI),  $\text{NH}_3$  and 8-hydroxypyrene-1,3,6-trisulfonic acid, trisodium salt (HPTS) were purchased from Aldrich. Fluorescein-5-(and-6)-sulfonic acid, trisodium salt (FS) was purchased from Invitrogen (Life Technologies Corporation). The ion-pair agent hexadecyltrimethylammonium bromide (CTAB) was purchased from Acros Organics. All chemicals were used as received without further purification.

Silicon wafers and Quartz wafers were purchased from University wafers (South Boston, MA). Quartz wafers were cut to  $1 \text{ cm} \times 1 \text{ cm}$  pieces before film deposition.

Phosphate buffer and acetate buffer solutions of desired pH and ionic strength were prepared from  $\text{NaH}_2\text{PO}_4$ ,  $\text{Na}_2\text{HPO}_4$  and  $\text{CH}_3\text{COONa}$ ,  $\text{CH}_3\text{COOH}$ , respectively, with sodium chloride as the background electrolyte. The pH of phosphate buffer solution was measured using an Accumet model 15 pH meter (Fisher Scientific).

### 3.2.2 Synthesis of ion-pairs

The indicator ion-pairs were fabricated using a previous published procedure [13] with modification for this study. Briefly, the ion pair was synthesized by dissolving 0.76 mmol of CTAB in 25 mL of DI water at around 50 °C. Subsequently, 0.25 mmol of indicator HPTS (or 0.76 mmol FS) that was previously dissolved in 25 mL of DI water was added to the CTAB solution. The precipitate of ion pairs (HPTS-CTAB, or FS-CTAB) was filtered and dried in the oven at 70 °C for 12 hours before use. The chemical structures of HPTS-CTAB and FS-CTAB are shown in Figure 3.6.

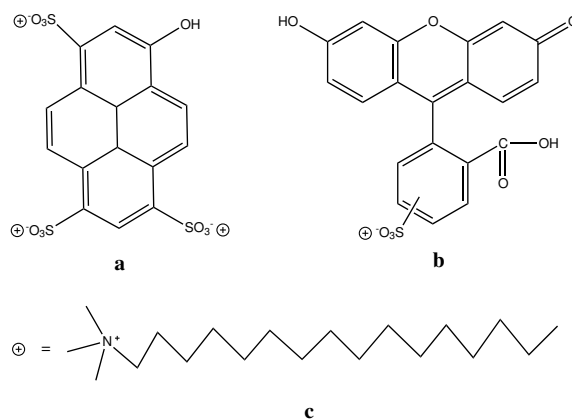


**Figure 3.6.** Chemical structure of ion-pairs. a: HPTS-CTAB; b: FS-CTAB; c: CTAB cation.



### 3.2.3 Synthesis of sol-gel films

The sol-gel films synthesis employed a previous published procedure [13]. The sensor films were prepared from a mixture of ETEOS- and GPTMS-derived sols. The ETEOS-based sol were prepared by mixing ETEOS, 0.1 M HCl and ethanol in a 1:0.007:6.25 molar ratio. The GPTMS-based sol was prepared by mixing GPTMS, MI (or  $\text{NH}_3$ ), dionized water and ethanol in 1:0.69:4:6.25 molar ratio. The GPTMS-ETEOS hydrid sol was prepared by mixing the two separate sols at 1:1 molar ratio. FS-CTAB (or HPTS-CTAB) was dissolved in ethanol (2.5 mM) before making the sols. The final silane/dye ratio was 1000. The final mixture was aged for at least 3 days under ambient conditions.

The effect of different precursors was studied by changing the ratio of GPTMS- and ETEOS-derived sols. Sol-gel solutions were made of the following GPTMS-ETEOS ratios: 1-0, 2-1, 1-1, 1-2 and 0-1. The effect of GPTMS:ETEOS ratio was studied only with HPTS immobilized in these sol-gel films.

Sensor film was fabricated by spin-coating onto silicon wafers and quartz slides using a spinner; the spin speed was 4000 rpm (rounds per minute) and the spin time was 1 minute. To produce films with different thickness, the sol-gel solution was diluted 2-fold, 5-fold and 10-fold before spin-coating.

After deposition, the films were cured at 140 °C, 200 °C, 250 °C, 300 °C and 400 °C for 4 hours, 4 hours, 4 hours, 3 hours and 3 hours, respectively. All sensor films were uniform and crack-free. They were soaked in phosphate buffer (pH 6.8) over night before testing. All experiments were performed at room temperature.

### 3.2.4 Instrumentation

**UV-Vis absorption and fluorescence spectra:** Sol-gel films were immersed in buffer solutions for all optical measurements. UV-Vis absorption spectra were recorded with a Lambda 35 UV/Vis spectrometer (PerkinElmer Inc). Fluorescence spectra were measured with a SPEX FLUOROLOG 1681 Spectrometer. The top view of fluorescence measurement set-up is shown in Figure 3.7. Fluorescence lifetimes were acquired with TM-200 LED strobe Lifetime Spectrofluorometer (PTI). A single exponential decay was used to fit the fluorescence lifetime.

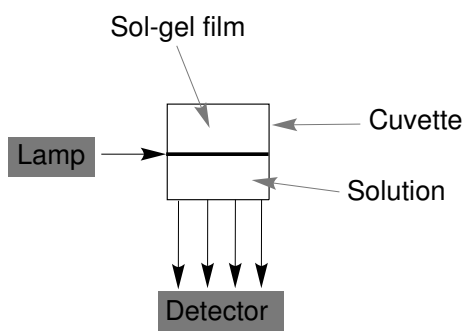


**Figure 3.7.** The top view of fluorescence spectra measurement set-up.

**FTIR:** The FTIR spectra of ion pairs and sol-gel films were taken with a Fourier transform infrared spectrometer (Spectrum one, Perkin Elmer). The substrates were ground to powder before recording the spectra.

**Ellipsoemetry:** Silicon wafers were used as the substrates for sol-gel film deposition for film thickness measurements. Film thickness of sol-gel films were measured by a Variable Angle Spectroscopic Ellipsometer (VASE 32 from J.A. Woollam Co.). The model fit was performed with taking account of 0.5 mm silicon layer and 2 nm of native oxide present on the silicon wafer.

**SEM:** The SEM image of the sol-gel films on silicon wafers were taken with a field-emission scanning electron microscope (Hitachi S-4700) after coating 5 nm platinum on sample surface.

### **3.3 Results and discussion**

#### **3.3.1 Sol-gel film characterization**

##### *3.3.1.1 Catalyst effects*

With  $\text{NH}_3$  as the catalyst for GPTMS-derived sols, the reaction rate increased a lot compared to MI. Within 3 days, all sol-gel precursor solutions became a solid. So, the sol-gel precursor solution was aged for 2 days before spin-coating. However, these thin films with dyes immobilized did not respond to pH, with only protonated excitation peak at 400 nm showed even in basic solution (pH 11.00).

##### *3.3.1.2 Morphology*

It is important that the thin film are uniform as heterogeneity has an impact on a number of factors, such as the optical transparency and mechanical properties of the materials. It is also important in mass production of these materials as reproducibility is a critical factor in sensor material development. The sol-gel thin films were optically transparent as judged by the eye, which indicates there was no phase separation. SEM was performed to evaluate alternations in morphology of the films as a result of phase separation (Figure

3.8). The films did not show any features when imaged with SEM, which demonstrates a homogenous material at the micrometer scale. However, from previously published research, heterogeneity in sol-gels can occur at a very fine level examined by Atomic force microscopy and nanofeatures were observed at lower Z-range (0 - 10 nm for height) [38].

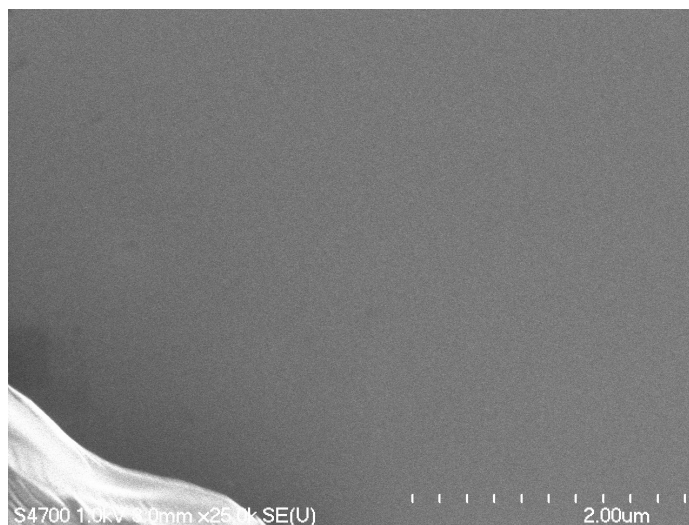


**Figure 3.8.** SEM image of sol-gel thin film.

#### *3.3.1.3 Film thickness*

There were 4 different sol-gel thin films developed, S1, S2, S5 and S10. S1 was made by the original sol-gel solution. S2, S5, and S10 were made by the sol-gel solution 2, 5, 10 times diluted from the original solution. The thickness of S1, S2, S5, and S10 were 1294 nm, 472 nm, 145 nm and 54 nm, respectively, as listed in Table 3.1. The generated and Experimental data of thin film optical constants for thickness fitting of S1, S2, S5, S10 are shown in Figure A.7.

**Table 3.1**  
Film thickness of different sol-gel thin films.

Film	S1	S2	S5	S10
Thickness, nm	$1294 \pm 12.1$	$471.9 \pm 1.3$	$162.5 \pm 0.8$	$64.3 \pm 1.6$
MSE (should <10)	46.13	5.773	8.218	2.984

#### 3.3.1.4 FTIR spectra

The FTIR spectrum of the synthesized sol-gel film is shown in and compared with the FTIR spectrum of the mesoporous silica substrate in Figure 3.9. The Mesoporous silica was made from the full oxidation of porous silicon, thus it is pure SiO<sub>2</sub> and had a much simple FTIR spectra with the only two characteristic peaks of the Si-O-Si bonds, centered at around 800 cm<sup>-1</sup> and 1080 cm<sup>-1</sup>. The FTIR spectra of sol-gel film is much more complicated because it contains organic functional groups. The absorption peak around 2900 cm<sup>-1</sup> is due to the aliphatic groups in the precursor GPTMS. The absorption peak for C-O stretching at 1100 cm<sup>-1</sup> is not clearly evident because it overlaps with Si-O-Si stretch peak. The small peak at 950 cm<sup>-1</sup> is due to the free silanol group Si-OH on the surface of silica network.

#### 3.3.2 Fluorescent spectral behavior of indicator ion-pairs in sol-gel films

Different cure temperatures were applied to the dye immobilized sol-gel films. For sol-gel films cured at higher temperature than 140 °C, the indicators in sol-gel films lost its sensitivity to pH probably due to the collapse of the pores. For the one cured at 140 °C for 4 hours, the dyes in the sol-gel film were still sensitive to pH.

UV-Vis absorption and fluorescence spectra of dyes in sol-gel films were recorded. UV-

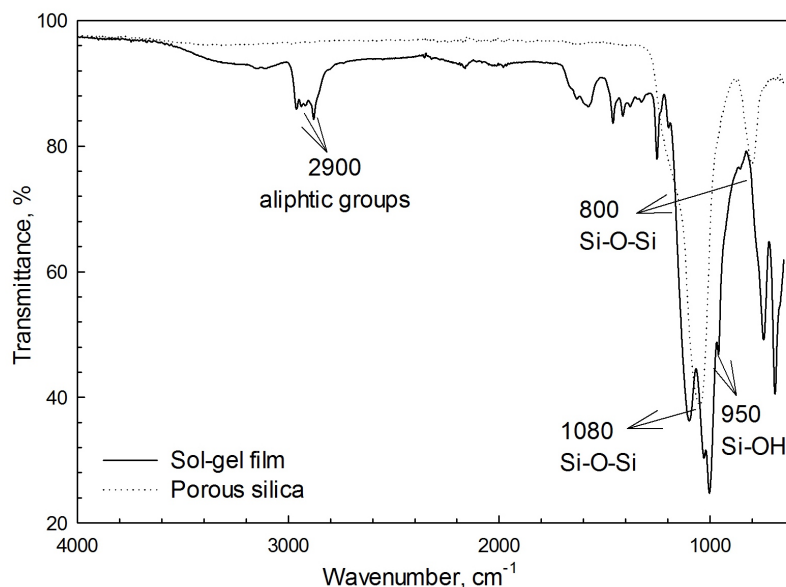


**Figure 3.9.** FTIR spectra of mesoporous silica and sol-gel films.

Vis absorption spectra are not shown and discussed here because the absorption spectra have low intensity. Due to the thickness of the films are in the range of 60 nm to 1400 nm, only a small amount of dyes are immobilized in the thin films, resulting in the low intensity of the absorption spectra. In addition, the background absorbance from the blank sol-gel films made the signal to noise level even lower and the dyes in sol-gel films not suitable for absorbance measurements. In contrast, fluorescence spectra with high sensitivity are not affected by the small amount of indicators in sol-gel films. In addition, the blank sol-gel films are not fluorescent. Thus the fluorescence spectra behavior of dyes in sol-gel films were studied and compared with their spectra in solution.

### 3.3.2.1 FS-CTAB in sol-gel films

The fluorescence spectral behavior of fluorescein in buffer was discussed in Chapter 2. To summarize here, FS has the same behavior as fluorescein. The excitation peaks for monoanion and dianion forms of FS are at 467 nm and 490 nm, respectively. Both monoanion and dianion forms of FS have single emission peak at 515 nm corresponding to the excited state dianion form. The  $pK_a$  values of ground state and excited state fluorescein in buffer (IS = 0.030 M) are 6.52 (Figure 2.12) and 5.68 (Figure 2.16), respectively.

Fluorescence spectra of FS in sol-gel film in buffer solution were recorded and shown in Figure 3.10. A red shift of both the emission and the dianion excitation peaks in sol-gel film compared to in buffer solution (Figure 2.14) were observed. The fluorescence emission peak of FS in sol-gel film was at 528 nm, a shift of 13 nm to the longer wavelength. The maximum dianion excitation peak was at 510 nm, a shift of 20 nm to the longer wavelength. As with fluorescein in buffer solution, two emission peaks for excited state monoanionic and dianionic FS were observed, 520 nm with 550 nm shoulder peak and 528 nm, respectively.

The normalized fluorescence excitation spectra of fluorescein in sol-gel films are shown in Figure 3.11, top. The acid dissociation constant of excited state,  $pK_a^*$ , was measured for FS thin film using the fluorescence excitation spectra with the same method used in Chapter 2. Fractions of both monoanion and dianion FS in sol-gel films were plotted against the solution pH. The  $pK_a^*$  was defined when the fractions of monoanion and dianion are both equal to 0.50 as shown in Figure 3.11, bottom. The  $pK_a^*$  of fluorescein immobilized sol-gel (thickness, 162 nm) in buffer solution with ionic strength at 0.050 M is 4.22. Compared to solution phase  $pK_a^*$  (5.68), it is smaller by about 1.5 pH units. The pH sensitive range for

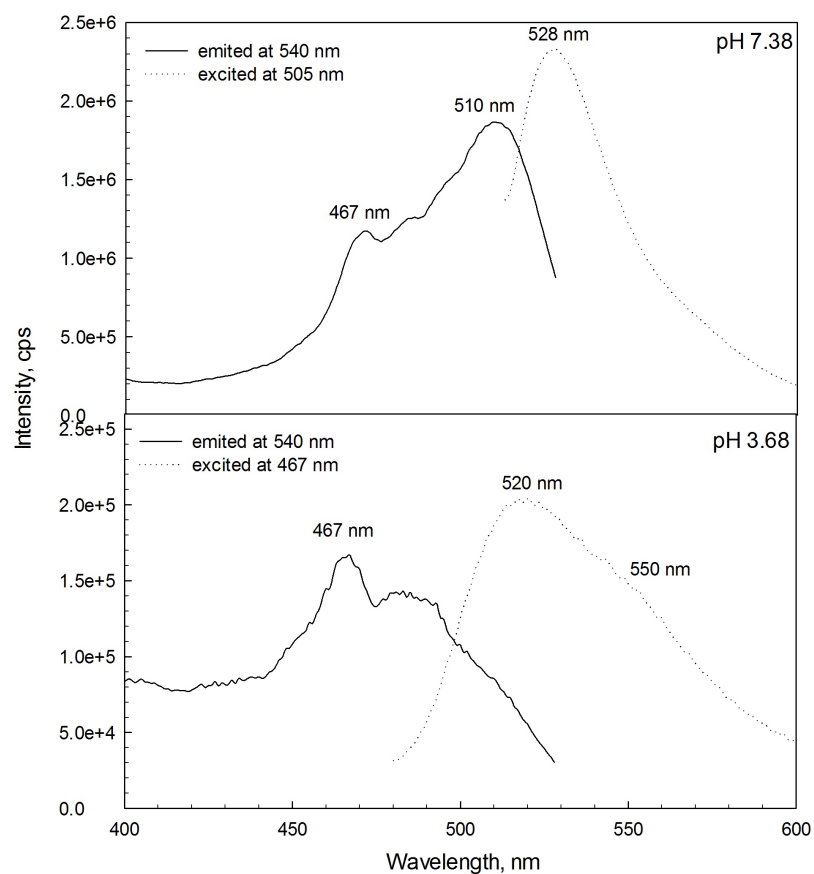


**Figure 3.10.** Fluorescence excitation and emission spectra of FS-CTAB in sol-gel film at different pH (IS = 0.030 M).

this one is pH 3.5 - 5.5 as shown in Figure 3.12.

### 3.3.2.2 HPTS-CTAB in sol-gel films

The fluorescence spectra of HPTS in buffer solution was discussed in the introduction part of this chapter. Fluorescence excitation spectra of HPTS in buffer are sensitive to pH of the solution as shown in Figure 3.5. Because of its photoacidity, HPTS has only one emission peak in aqueous solution with different pH. The protolytic equilibrium of ground



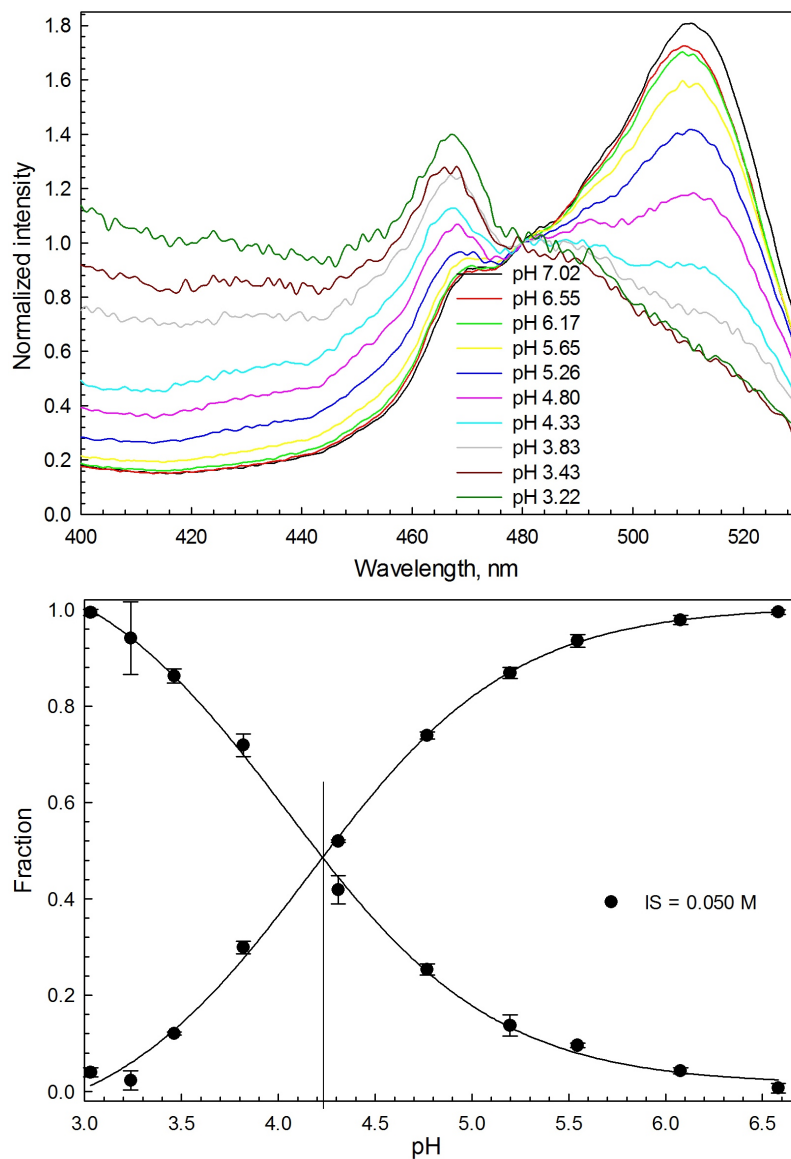


**Figure 3.11.** Normalized fluorescence excitation spectra of FS-CTAB in sol-gel film (top) and  $pK_a^*$  of FS-CTAB in sol-gel film (IS = 0.050 M) (bottom). The emission wavelength was 540 nm.

and excited state HPTS is shown in Figure 3.13.

The ground state  $pK_a$  of HPTS in buffer was also calculated as 7.30 from absorption spectra and 7.35 from fluorescence spectra as shown in Figure 3.14.

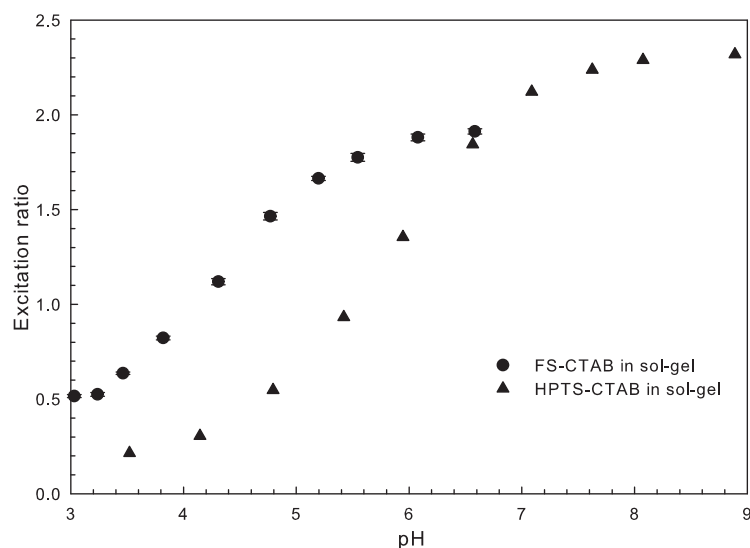


**Figure 3.12.** pH sensitive ranges of FS and HPTS in sol-gel film. (GPTMS-EGEOS 1-1, film thickness 1300 nm, and IS = 0.050 M)

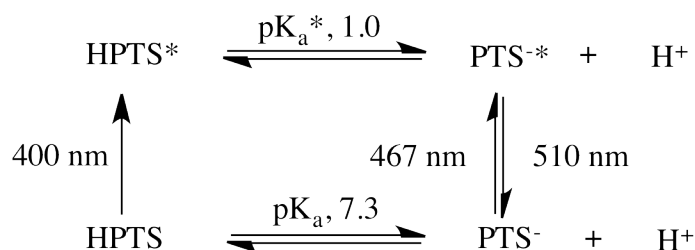


**Figure 3.13.** The protolytic equilibrium of ground and excited state HPTS.

Fluorescence spectra of HPTS immobilized in sol-gel films in buffer solution were recorded and are shown in Figure 3.15, and compared with fluorescence spectra of HPTS in buffer solution and ethanol. In pH 7.50 buffer, when excited at 400 nm, dissolved HPTS has only one emission peak at 510 nm, while immobilized HPTS has two emission peaks, 420 nm (with 435 nm shoulder peak) and 510 nm. This peak at 420 nm corresponds to the emission peak of HPTS in ethanol. This indicates a decrease in acidity of immobilized HPTS in the excited states. This effect has also been observed by other researchers in their

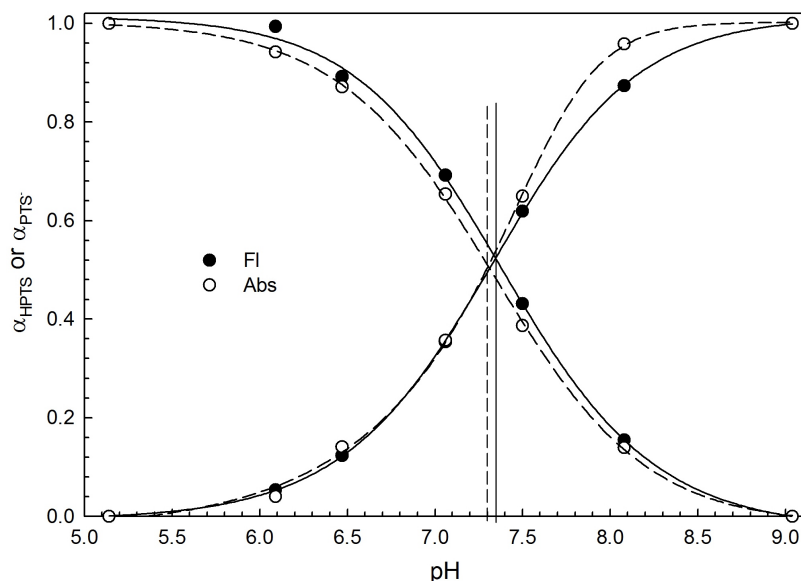


**Figure 3.14.**  $pK_a$  of HPTS ( $0.628 \mu\text{M}$ ) in buffer ( $\text{IS} = 0.030 \text{ M}$ ) from both fluorescence and absorption spectra.

studies [30,47,48,122].

One of the possible explanations of this phenomenon is the hydrogen bonding effect. Because of enhanced hydrogen bonding would stabilize the excited state of the deprotonated form with respect to the protonated form and make prototropic dissociation easier. However, in the sol-gel films, the hydrophobic environment makes insufficient water molecules available to hydrate and stabilize the dissociated protons from the excited acidic HPTS leading to the strong recombination of the  $\text{H}^+$  and the excited state  $\text{PTS}^-$  [30]. This decrease in photoacidity of HPTS in sol-gel films may also be a result of the ionic interaction between HPTS and the surfactant, CTAB, which reduces the electron donating properties of the triply sulfonate pyrene ring to the hydroxy group, hence stabilizing the acid form of HPTS and reducing its photoacidity [48]. It is also possible that the hydrogel groups on the pyrene condensed with the silanol groups during the sol-gel process and its acidic site was blocked, and showed the emission of the excited state  $\text{HPTS}^*$  upon excitation.

The normalized fluorescence excitation spectra of HPTS immobilized sol-gel film in buffer solution are shown in Figure 3.16,top. There are two excitation peaks of HPTS immobilized sol-gel thin films, same with HPTS in solution. The excitation spectral behavior of HPTS after immobilized in sol-gel film is sensitive to pH. The  $pK_a$  value of HPTS immobilized sol-gel film is calculated as 5.78 (IS = 0.030 M, as shown in Figure 3.16, bottom, which is much smaller than the  $pK_a$  value of HPTS in solution (7.35). The pH sensitive range of HPTS in sol-gel film is around pH 4.5 - 7.0 as shown in Figure 3.12.

### 3.3.3 $pK_a$ shift

#### 3.3.3.1 *Sol-gel matrix effect*

For both FS and HPTS, a shift of  $pK_a^*$  and  $pK_a$  to the lower pH value was observed when they were immobilized in sol-gel films. To summarize, the  $pK_a^*$  and  $pK_a$  values in buffer and sol-gel film (IS = 0.030 M, except for FS in sol-gel film, IS = 0.050 M) for FS and HPTS are 5.68 and 4.22, and 7.35 and 5.78, respectively.

The shift of  $pK_a$  values of indicators immobilized in solid matrix was also observed in other studies [13,30,47]. The increase in acidity of the immobilized dyes in sol-gel films can be explained largely by the sol-gel environment.

The microstructure of the sol-gel films are porous silica. There are free silanol (Si-OH) group on the internal surface of the silica network, which can accept and donate protons and act as a substantial buffer as discussed in Chapter 2. Different types of silanol groups are present on the silica surface as shown in Figure 2.22. A range of  $pK_a$  values has been reported for surface silanol groups. Usually two values are found, one in the range of 3.8 -

5.94 and a second of 8.0 - 11.24 [105,107–109]. In porous silica project, some amount of the internal surface of porous silica was reacted and covalently bound to FITC. So fewer free silanol groups are available for accepting or donating protons, which confirms that there is only a small decrease in  $pK_a$  value when FITC was covalently bound in porous silica compared to in buffer solution, 5.58 and 5.68, respectively. However, in sol-gel films, the internal surface of the sol-gel network was not modified, all the free silanol groups were able to accept and donate protons when placed in buffer solution. Thus it is not surprising that a larger  $pK_a$  shift was observed when FS was physically entrapped in sol-gel films. It is also possible as the micellar interface is densely charged with the positive ammonium ions, a higher concentration of protons is required to reach a  $pK_a$  situation. Thus the apparent  $pK_a$  become even smaller [123].

#### 3.3.3.2 *Ionic strength effect*

The  $pK_a$  value of the indicator in solution is affected by the ionic strength as discussed in Chapter 2. As the ionic strength of the solution increased, a decrease in  $pK_a$  value is expected (eq 2.10). The ionic strength effect on the  $pK_a$  values of FS and HPTS in both solution and sol-gel films are plotted in Figure 3.17. As shown in the figure, the  $pK_a$  of indicators in solution decrease with increasing ionic strength. In contrast to the shift of indicators in solution, an opposite behavior in  $pK_a$  shift of both indicators in sol-gel films was observed. As the solution ionic strength increases, the apparent  $pK_a$  values of FS and HPTS in sol-gel films also increase. For FS in sol-gel films (film thickness, 1300 nm), in solution with ionic strength at 0.050 M, 0.100 M and 0.200 M, the  $pK_a^*$  values were 4.22, 4.53 and 4.58, respectively. For HPTS in sol-gel films, in solution with ionic strength at 0.003 M, 0.030 M and 0.300 M, the  $pK_a$  values were 4.84, 5.40 and 6.43, respectively.

A possible explanation to this opposite  $pK_a$  shift of indicators in sol-gel films is the swelling effect. Although swelling is impossible for some oxide gels such as  $SiO_2$  [124, 125], the poly(ethylene oxide) groups from the GPTMS precursor stayed in the sol-gel film, and they can swell in solution. The sol-gel films swell more in high ionic strength solution than in low ionic strength solutions. When the sol-gel films swell, the pores size increased. More aqueous solution gets into the pores, the indicators immobilized will experiences a less hydrophobic environments and they can be less affected by the free silanol groups on the surface.

#### 3.3.3.3 *Film thickness effect*

In addition to the  $pK_a$  shift caused by the matrix and ionic strength effects, a  $pK_a$  shift related to the film thickness was observed. The  $pK_a^*$  of FS in sol-gel films decreases with decreasing the film thickness as shown in Figure 3.18. The thickness of these four sol-gel films, S1, S2, S5 and S10 were 1294 nm, 472 nm, 145 nm and 54 nm, and the  $pK_a^*$  values for four sol-gel films in buffer solution with ionic strength as 0.100 M were 4.76, 4.52, 4.22, and 4.14, respectively.

The reason for this  $pK_a$  shift related to the film thickness is unclear. One possibility is that the pore size of the network might be different with different thickness. Pores with different sizes may have different accessibility for aqueous solutions. However, the sizes of the pores were not evident in the SEM images we obtained.

The opposite effect of film thickness was observed for HPTS in sol-gel films as shown in Figure 3.19. The reason for this is unclear.

#### 3.3.3.4 GPTMS-ETEOS ratio effect

The effect of two precursor GPTMS-ETEOS ratio on  $pK_a^*$  of HPTS in these sol-gel films was studied. As shown in Figure 3.20, the  $pK_a^*$  of immobilized HPTS increased with increased of precursor GPTMS. As for the sol-gel films prepared by only ETEOS, no pH sensitivity of immobilized HPTS was observed (data not shown). The precursor GPTMS is a polar precursor; it provides a hydrophilic matrix, which promotes proton permeability. With increase of proton permeability, the sol-gel matrix prepared with more GPTMS are less hydrophobic, and more like an aqueous environment. Thus the  $pK_a$  of immobilized HPTS was more similar to its  $pK_a$  values in solution.

#### 3.3.4 Fluorescence lifetime data

The fluorescence lifetimes of FS and HPTS in both solution and sol-gel films were measured. The fluorescence decay was well described by a single exponential component. Fluorescence decay of FS and HPTS in solution and sol-gel film with pH 6.7 and 7.01, respectively, are shown in Figure 3.21. Fluorescence lifetimes of dissolved dyes and immobilized dyes in buffer solution and ethanol are listed in Table 3.2. The excited state lifetime of both protonated and deprotonated species decreased in thin films compared to bulk solution.

For FS in solution, the fluorescence lifetime decreased from 4.2 ns to 2.8 ns as solution pH decrease from 6.65 to 4.41. Ryder et al reported the fluorescence lifetime of fluorescein in pH 7.8 buffer solution was 4.1 ns [113], which matches with our data. As the pH of solution decrease from 6.7 to 3.2, the dominant species in solution changes from dianion

to monoanion. As the quantum yield of the excited state monoanion is much smaller than the excited state dianion (0.26 and 0.82, respectively), which means there are more radiationless pathways for the relaxation of excited state monoanion. From eq 1.12 and eq 1.13, adding radiationless pathways, increases  $k_n r$ , thus decreases quantum yield and lifetime.

The fluorescence lifetime of FS in sol-gel films was shorter than in buffer solution as in more basic solution, 3.3 ns as compared to 4.2 ns. However, the fluorescence lifetime of FS in sol-gel film is independent of solution pH, with an average of 3.3 ns. This unchange lifetime upon changing of solution pH is due to the  $pK_a$  shift of FS in sol-gel films. As the  $pK_a$  of FS in sol-gel films is about 4.22 (IS = 0.050 M), in the pH range of 4.41 - 6.65, the dominant species in solution is still dianion, thus it is not surprising that there was no change in its lifetime.

The excited state lifetime of protonated HPTS, decreased to 1.9 ns compared to HPTS\* in ethanol, which was 4.0 ns. The excited state lifetime of deprotonated HPTS, PTS<sup>-\*</sup>, decreased to 4.1 ns, compared to PTS<sup>-\*</sup> in buffer solution, which was 5.5 ns [126,127].

The decrease of fluorescent lifetimes reflects the restricted mobility of indicators inside sol-gel pores.

### 3.3.5 Sensor performance

The equilibrium time of the sensor has been examined using  $t_{90}$  (as time to 90% of total response). A rapid response of fluorescence excitation spectra occurred for dyes in sol-gel films when changed buffer solutions. Taking HPTS immobilized sol-gel films as an example: for thin films formed with the original precursor solutions with (thickness = 1300



**Table 3.2**

Fluorescence lifetimes of fluorescent dyes in solution and sol-gel thin films.

Name	Excitation, nm	Emission, nm	Lifetime, ns	$\chi^2$	pH
FS in solution	468	515	$2.8 \pm 0.1$	1.063	4.41
FS in solution	490	515	$3.9 \pm 0.1$	1.049	5.57
FS in solution	490	515	$4.2 \pm 0.1$	1.054	6.65
FS in sol-gel	468	530	$3.2 \pm 0.1$	1.000	4.41
FS in sol-gel	505	530	$3.4 \pm 0.0$	0.9543	5.57
FS in sol-gel	505	530	$3.3 \pm 0.0$	0.9679	6.65
HPTS in ethanol	400	435	$4.0 \pm 0.0$	1.079	\
HPTS in solution	415	510	$5.4 \pm 0.1$	1.026	4.13
HPTS in solution	470	510	$5.5 \pm 0.1$	0.9928	7.01
HPTS in sol-gel	400	440	$1.9 \pm 0.1$	0.9417	3.30
HPTS in sol-gel	400	510	$4.1 \pm 0.1$	0.8539	3.30
HPTS in sol-gel	470	510	$4.0 \pm 0.1$	0.9336	7.01

nm, it took about 8 minutes to reach equilibrium, as for the thin films formed with 2 times diluted precursor solutions (thickness = 470 nm), the equilibrium time was shortened to 5 minutes. The result is shown in Figure 3.22.

Both FS and HPTS immobilized sol-gel films were studied to investigate the extent of leaching of indicators from the pores. The thin films were placed in a cuvette filled with buffer solution (pH = 6.8, IS = 0.100 M) for a few hours up to a week. Then the thin films was removed and the fluorescence spectra of the leftover buffer solution was recorded. No fluorescence was observed indicating that no indicators were leached out. (data not shown).

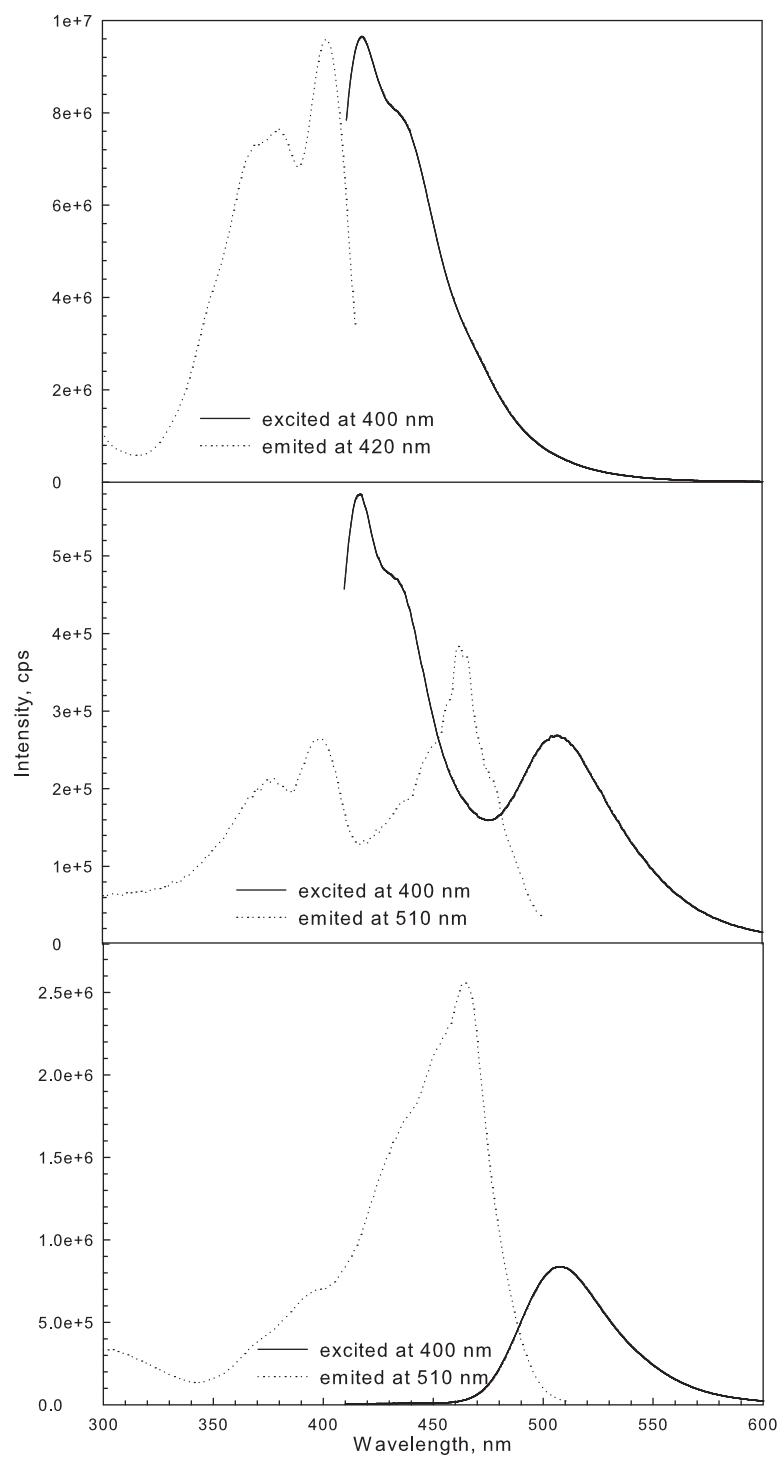


**Figure 3.15.** Fluorescence spectra of HPTS ( $0.99 \mu\text{M}$ ) in ethanol (top), sol-gel film at, pH 7.91 (middle) and solution, pH 8.53 (bottom).

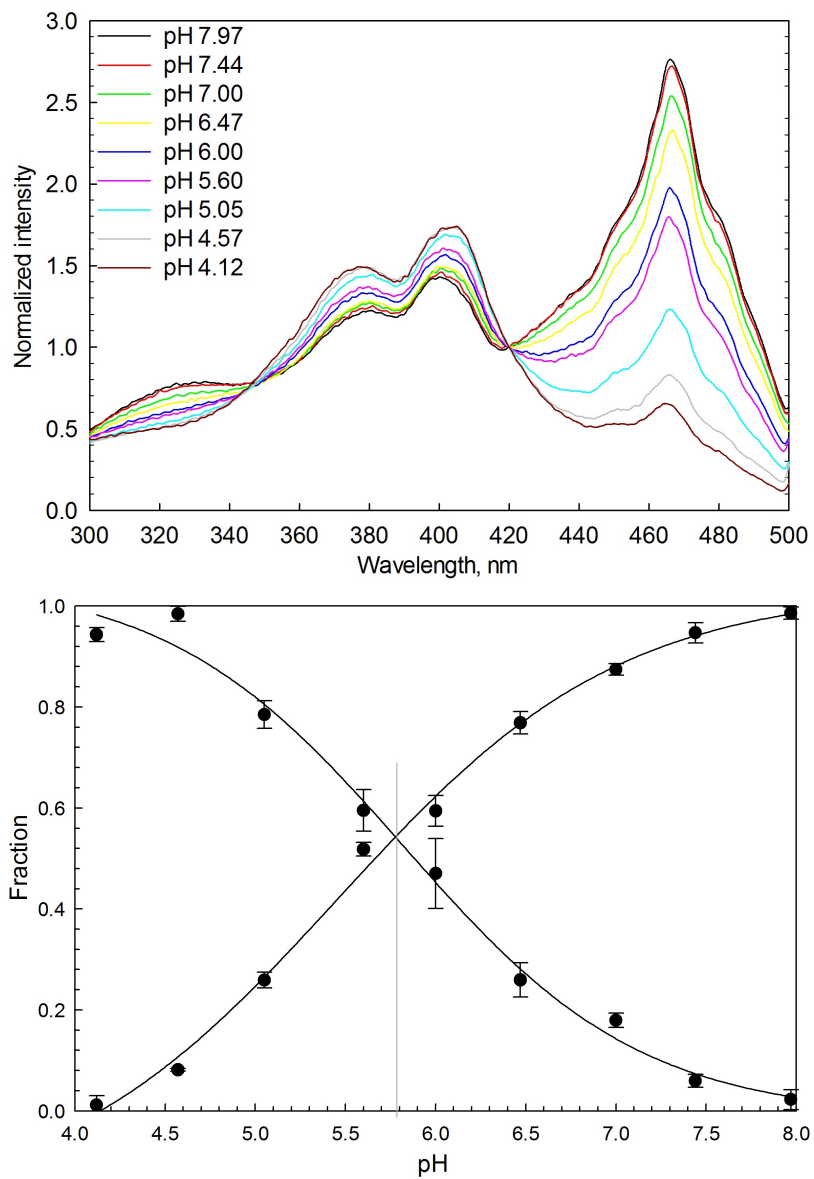


**Figure 3.16.** Normalized fluorescence excitation spectra of HPTS-CTAB in sol-gel films (top) and  $pK_a$  of HPTS-CTAB in sol-gel film (bottom) (IS = 0.030 M). The emission wavelength was 520 nm.

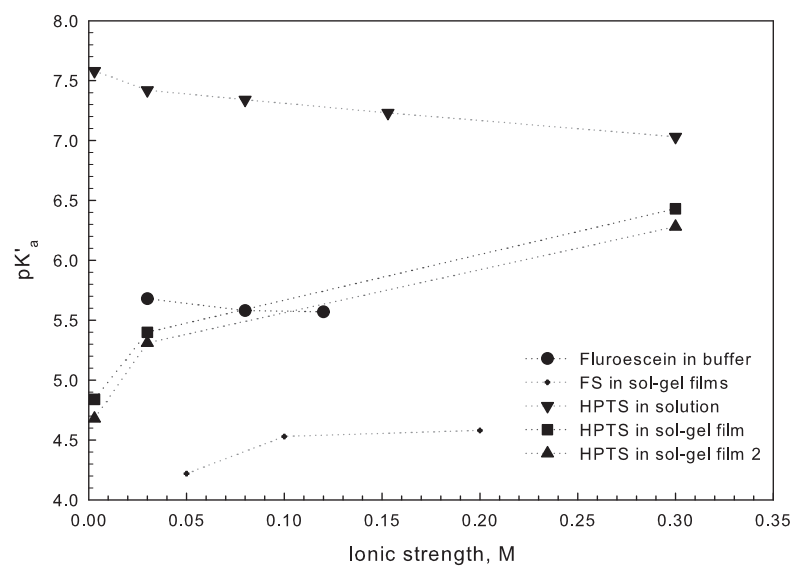


**Figure 3.17.**  $pK_a^*$  of FS and  $pK_a$  of HPTS in solution and sol-gel films with different ionic strengths.

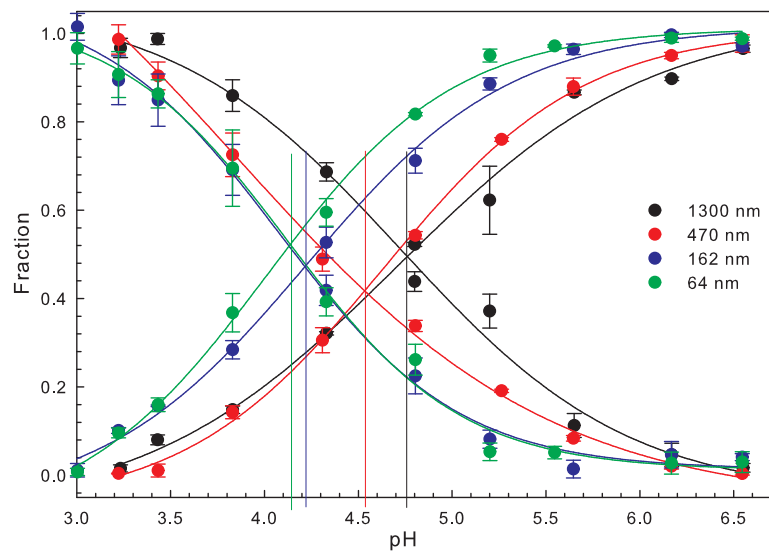


**Figure 3.18.**  $pK_a^*$  of FS-CTAB in sol-gel films with different thickness in buffer solution (IS = 0.100 M).

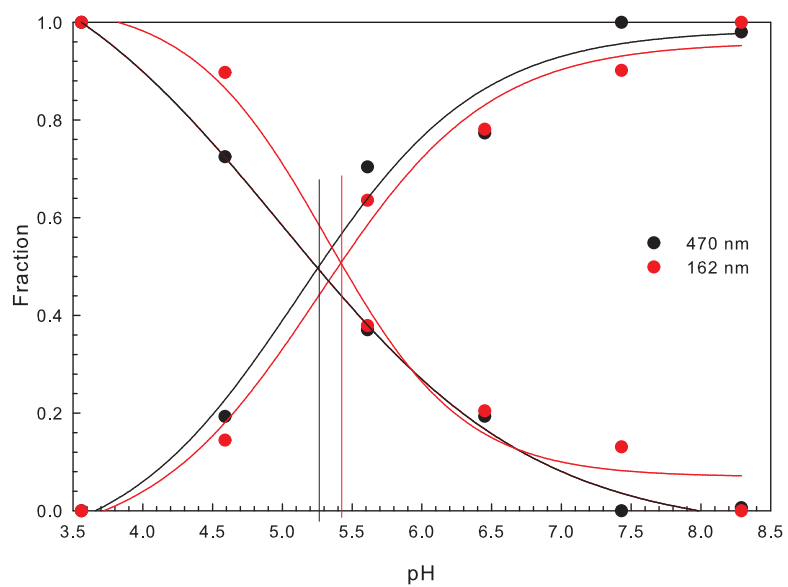


**Figure 3.19.**  $pK_a$  of HPTS-CTAB in sol-gel films with different thickness in buffer solution (IS = 0.100 M).

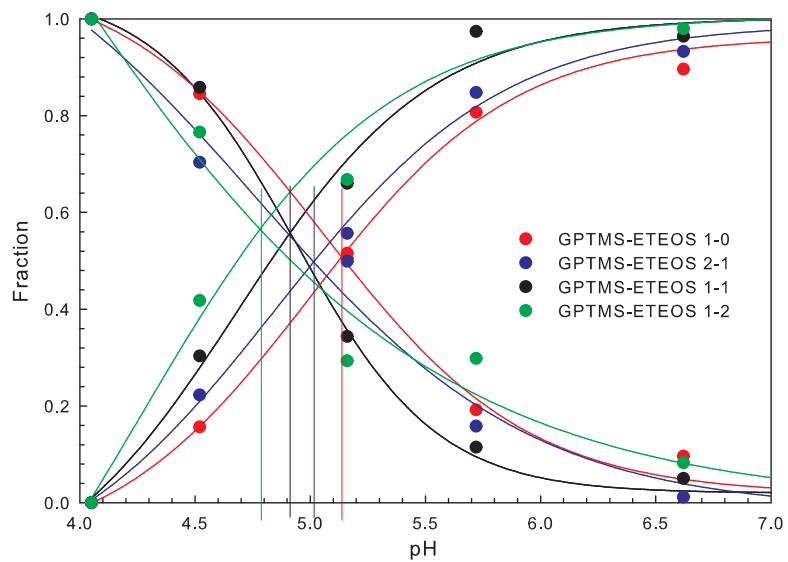


**Figure 3.20.**  $pK_a$  of HPTS in sol-gel films with different GPTMS-ETEOS ratios.

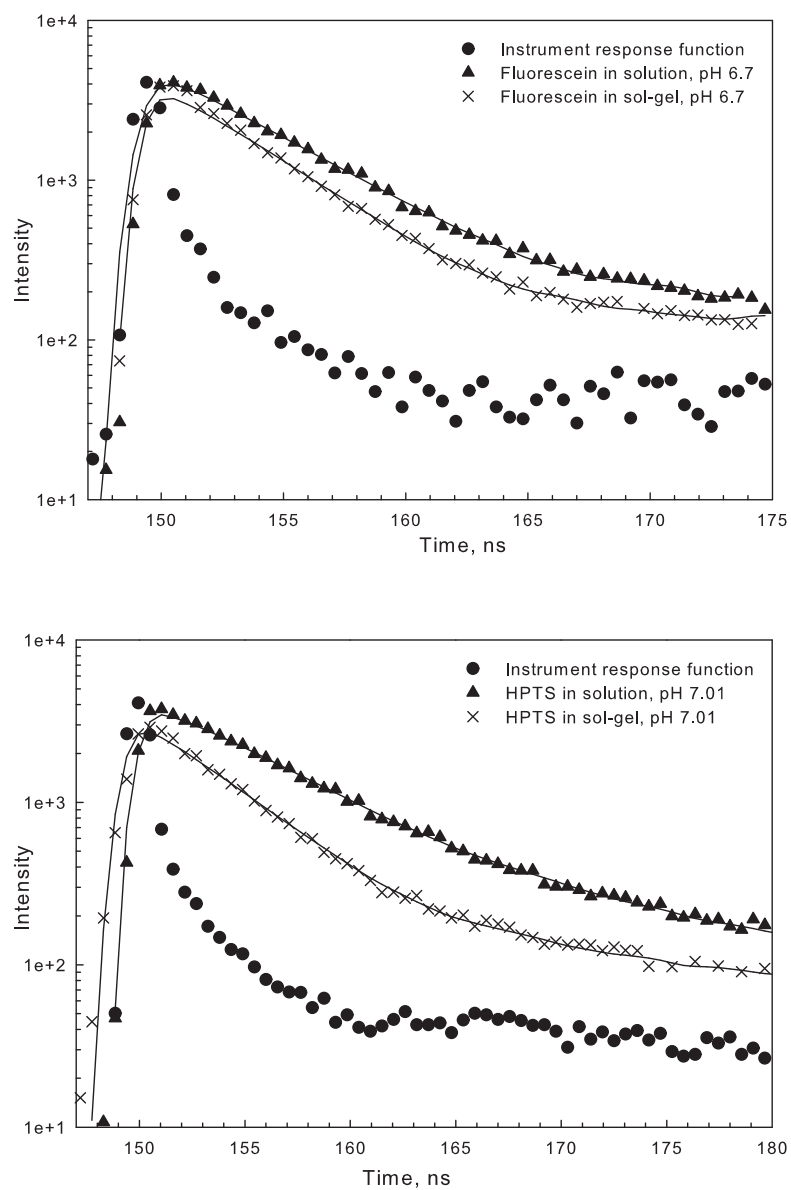


**Figure 3.21.** Fluorescence decay curves for FS and HPTS in buffer and sol-gel films. The solid lines represent the best fits to the data. (top): FS in buffer and sol-gel films, with  $\lambda_{ex} = 467$  nm and  $\lambda_{em} = 530$  nm; (bottom): HPTS in buffer and sol-gel films, with  $\lambda_{ex} = 470$  nm and  $\lambda_{em} = 510$  nm.

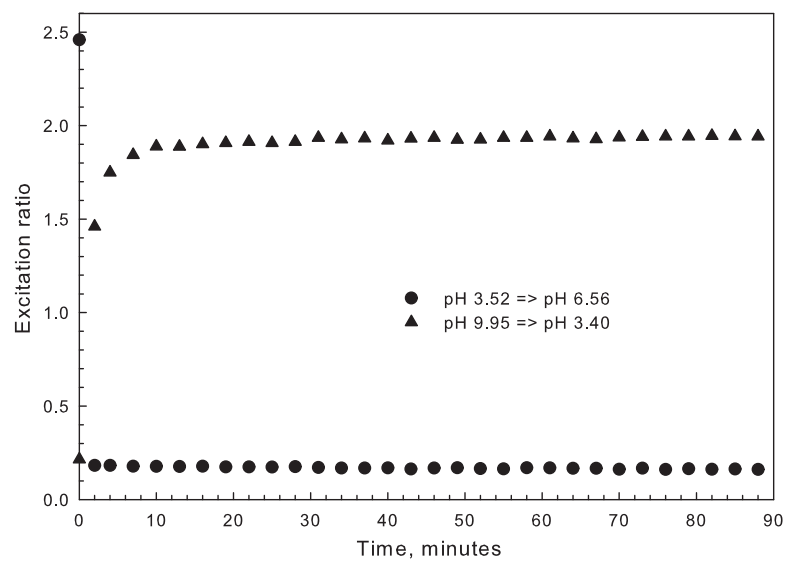


**Figure 3.22.** Equilibrium time of HPTS immobilized sol-gel films in solution (IS = 0.030 M).

### 3.4 Conclusion

Two pH dependent fluorescence dyes, FS and HPTS were immobilized in sol-gel thin film through physical entrapment for pH sensing. The sol-gel films were synthesized from the hydrolysis of two precursors, ETEOS and GPTMS with HCl and MI as the catalyst, respectively. The sol-gel solution was spin coated on the surface of a 1 cm  $\times$  1 cm quartz slide to form a thin layer with thickness in the range of 64 nm to 1300 nm, which can be controlled with the concentration of the precursors in the starting solution.

Fluorescence spectra of indicators in sol-gel film were recorded and compared with that in solution phase. For FS in sol-gel films, there is a red shift of the excitation and emission peak of dianion FS compared to FS in solution, 490 nm to 510 nm, respectively. For HPTS, the excitation spectra remained the same as in buffer solution. However, the appearance of fluorescence emission peak 425 nm, which is the emission of the excited state protonated HPTS at pH  $\gg$  pK<sub>a</sub> indicated a decrease of photoacidity of HPTS in sol-gel films, which might be the result of the relatively hydrophobic sol-gel environment or the permanent protonation of the hydroxy group during the sol-gel process. Nevertheless, the fluorescence excitation spectra of both indicators in sol-gel films retained pH sensitivity.

The pK<sub>a</sub> values of FS and HPTS in sol-gel films were both shifted to the lower pH region compared to those in solution, 4.22 (GPTMS-ETEOS 1-1, film thickness 1300 nm, and IS = 0.050 M) and 5.68 (IS = 0.030 M), and 4.78 (GPTMS-ETEOS 1-1, film thickness of 1300 nm, and IS = 0.050 M) and 7.35 (IS = 0.030 M), respectively. This shift is due to the sol-gel environment, as there are free silanol (Si-OH) groups on the internal surfaces of the silica network, which can act as an additional buffer. The positively charged ammonium group from the ion-pair reagent could further enhance this shift. The ionic strength effect



on  $pK_a$  values of indicators in sol-gel films was opposite to that of indicators in solution. With increasing ionic strength, the  $pK_a$  values of both FS and HPTS in sol-gel films both increased. Compared to the fluorescence lifetime in aqueous solution, the lifetime of both indicators in sol-gel thin film were shorter, indicating restricted mobility in side pores.

No leaching of indicators from the sol-gel film was observed. The short response time (less than 5 minute) and great reproducibility made it a good candidate for pH sensing.

### **3.5 Future work**

The morphology and network structure of the sol-gel film was not fully studied. In the future, transmission electron microscopy (TEM) could be used to study the pore size of the sol-gel films and gas absorption method could be used to study the inner surface area of the sol-gel films.

## **4. SPECTRAL BEHAVIORS AND pH SENSITIVITY OF INDICATORS IMMOBILIZED IN HYDROGEL**

### **4.1 Introduction**

#### **4.1.1 Hydrogel**

Hydrogels are distinct three-dimensional macromolecular cross-linked networks of hydrophilic homopolymer or copolymers with the capability of imbibing a significant amount of aqueous solvent or a physiological liquid [76,128,129]. When placed in aqueous solution, hydrogel matrices tend to absorb a large volume of water and swell. This swelling ability in aqueous medium makes hydrogel an ideal material in many applications in biological such as drug delivery, immobilization of proteins and peptides.

Hydrogels crosslinked together either physically (entanglement, crystallites) or chemically (tie-points, junctions) to keep the networks insoluble in water. For a chemically crosslinked hydrogel, all polymer chains are crosslinked to each other by covalent bonds,

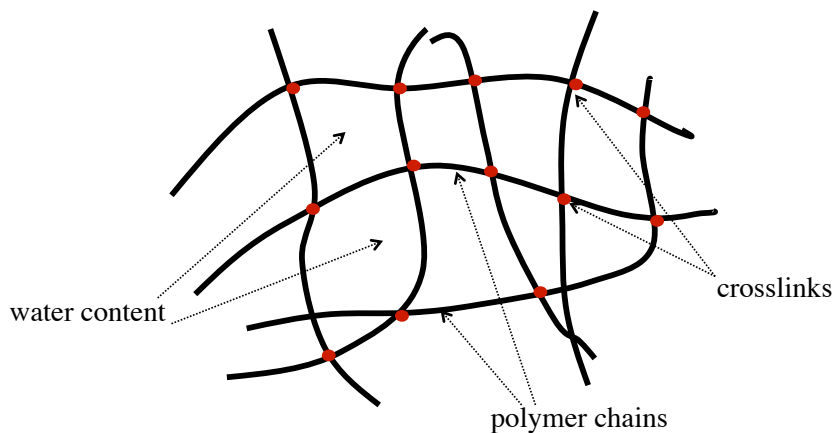


**Figure 4.1.** Illustration of crosslinked hydrogel structure.

which means that this type of hydrogel can be considered as one molecule independent on the size of the initial monomers. For this reason, hydrogels are often called infinite large molecules or supermacromolecules with no concept of molecular weight [130]. A schematic of the structure of a hydrogel crosslinked network is shown in Figure 4.1.

Hydrogels can be classified by their charge, preparation method or their network structure. Based on the nature of side groups, hydrogels can be either neutral or ionic. In neutral hydrogel, the driving force for swelling is attributed to the water-polymer contribution [131]. The interaction between the charged groups on the polymer and the free ions in the solution also affect the swelling behavior of the ionic hydrogels. Ionic hydrogels containing ionic groups, such as carboxylic acid groups, can absorb more water than neutral types because of their increased hydrophilicity and the repulsion between the deprotonated groups on the network structure.

Hydrogels can be classified as superporous, macroporous, microporous, or nonporous

based on their network structures[128]. Superporous hydrogels have high porosity with an interconnected open-cell structure, and most water molecules absorbed into superporous hydrogels are free. Macroporous hydrogels have varying porosity with closed-cell structures ( $0.1 - 1 \mu\text{m}$ ), and most absorbed water molecules are bound. Microporous hydrogels also have a range of porosities with smaller closed-cell structures ( $0.01 - 0.1 \mu\text{m}$ ). Non-porous hydrogels do not have a porous network.

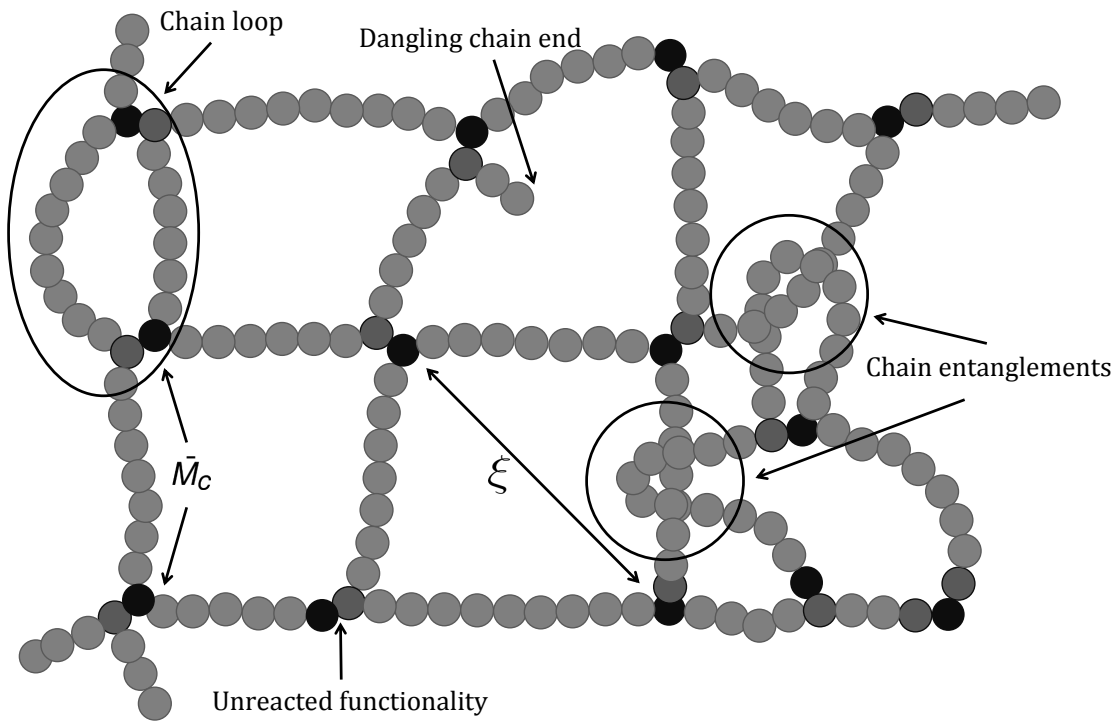


**Figure 4.2.** Illustration of chain entanglements and network defects that can form during crosslinking.  $\bar{M}_c$  is the average of molecular weight of the oligomers, and  $\xi$  is the mesh size of the hydrogel.

Hydrogel networks may include both permanent junctions and semipermanent junctions, such as chain entanglements as shown in Figure 4.2. When chains become entangled during the crosslinking process, effective crosslinks are formed in and around the perma-

nent junctions. These entanglements and other defects such as chain loops and dangling ends formed during the crosslinking process reduce the effective average molecular weight between crosslinks.

Polyethylene glycol (PEG) is one of the most extensively studied hydrogels because it presents outstanding properties, e.g. hydrophilicity, biocompatibility, nonbiodegradability [132]. For PEG hydrogels, the most common synthetic route is the free-radical crosslinking polymerization of functional PEG molecules, such as PEG diacrylate (PEGDA). The radicals may be generated from thermal energy, redox reactions or photo initiation. These free radicals propagate through unsaturated vinyl bonds on the PEG macromolecule monomer and chain polymerization occurs [133]. Properties of the PEG hydrogel such as swelling, elastic modulus and transport of solutes are highly affected by the pore size and crosslink density of the hydrogel, which are closely related to the conditions of hydrogel formation, such as polymerization methods, precursor percentages and monomer to free radical ratio.

Properties of PEG hydrogel, such as average molecular weight between two adjacent crosslinks, mesh size and swelling ratio are studied to better interpret the network structure.

The average molecular weight between two adjacent crosslinks ( $\bar{M}_c$ ) is determined using the Peppas-Merrill model, following the formula given below [134]:

$$\frac{1}{\bar{M}_c} = \frac{2}{\bar{M}_n} - \frac{(\frac{\bar{v}}{V_1})[\ln(1 - v_{2,s}) + v_{2,s} + \chi_1 v_{2,s}^2]}{v_{2,r}[(\frac{v_{2,s}}{v_{2,r}})^{\frac{1}{3}} - \frac{1}{2}(\frac{v_{2,s}}{v_{2,r}})]} \quad (4.1)$$

where  $\bar{M}_n$  is the average molecular weight of PEG oligomers,  $\bar{v}$  is the specific volume of PEGDA in its amorphous state (0.893 cm<sup>3</sup>/g),  $V_1$  is the molar volume of the solvent (18 cm<sup>3</sup>/mol for water),  $\chi_1$  is the Flory-Huggins' polymer-solvent interaction parameter (0.426

for PEG-water system),  $V_1$  is the molar volume of the solvent (18 cm<sup>3</sup>/mol for water),  $v_{2,s}$  is the polymer volume fraction in the swollen state, and  $v_{2,r}$  is the polymer fraction in the gel.

Mesh size  $\xi$  of the hydrogel is calculated by using the following formula [134]:

$$\xi = (\bar{r}_0^2)^{\frac{1}{2}} v_{2,s}^{-\frac{1}{3}} \quad (4.2)$$

$$(\bar{r}_0^2) = l^2 [2 \frac{\bar{M}_c}{M_r}] C_n \quad (4.3)$$

Where  $(\bar{r}_0^2)^{\frac{1}{2}}$  is the root mean square end to end distance of the polymer in its free state,  $l$  is the carbon-carbon bond length (0.154 nm),  $C_n$  is the rigidity factor of polymer (4 for PEG) and  $M_r$  is the molecular weight of repeating units (44 g/mol for PEG).

Swelling ratio,  $Q_m$ , is calculated by using the following formula:

$$Q_m = \frac{M_s}{M_0} \quad (4.4)$$

Where  $M_s$  and  $M_0$  are weight of hydrogel in its swollen and dry state, respectively.

Hydrogels can absorb a large amount of water, which is one of its most studied characteristics. The swelling of the hydrogel is controlled by both the osmotic pressure of water and the elastic nature of the hydrogel chains. When a hydrogel is immersed in an aqueous solution, the chains is forced apart by the osmotic pressure of water, and hydrogel is expanded in all directions equally. Along with the hydrogel chains is pushed apart by the

osmotic force, it is also restricted by the elastic nature of the crosslinks. The hydrogels reach to a state of equilibrium swelling when both forces driven by the osmotic pressure and the elastic nature of the crosslinks are equal [135].

$$\Delta F_{osmotic} = \Delta F_{elastic} \quad (4.5)$$

And the amount of water that hydrogel can absorbed during swelling process is proportional to pore size of the hydrogel. The pore size of the hydrogels can be altered by the ratio of the solvent (water) and precursor (monomer).

Hydrogel materials have many specific properties that make them attractive for a wide range of applications. Due to their high water content, stability in aqueous media, tunable chemical and physical network structure and biocompatibility, they have been widely used in biomedical applications, such as contact lenses [136], tissue engineering [134,137] and drug carriers [80,138–140]. Hydrogels may exhibit dramatic volume changes in response to specific small alteration of certain environmental parameters, such as temperature, pH [57,141–143], electric field or specific ions, which makes them useful as sensors of these variables.

Several types of hydrogel based pH sensors have been developed. Polyelectrolyte hydrogels comprise weak acidic or basic groups, which can be ionized. The protonation and deprotonation of these groups at different pH conditions can lead to a different volume of hydrogel. Richter, et al. [144] and Zhao et al. [80] have developed pH sensors based on this phase transition behavior of polyelectrolytic hydrogels. Lee, et al. [142] developed a hydrogel pH sensor based on the tunable optical response by measuring the diffraction wavelength shift of a hydrogel in different pH solutions. Fluorescent indicators have been

covalently bound to hydrogel matrix to measure the surrounding pH based on fluorescence intensity changes [57] or ratiometric methods [42,54,55,82,145].

#### **4.1.2 pH sensitive indicators**

Several pH indicators are used in this project to observe their spectral behavior and pH sensitivity after immobilized in hydrogel with covalent binding and physical entrapment.

FS is a fluorescein derivative, with the same absorption and fluorescence properties and pH sensitivity as fluorescein (see Chapter 2). HPTS is a commonly used pH indicator with a  $pK_a$  value at 7.35 ( $IS = 0.030\text{ M}$ ). The absorption and fluorescence spectra of HPTS in aqueous solution were discussed in Chapter 3. These two indicators was immobilized in a hydrogel matrix with physical entrapment. They were ion-paired with a commonly used surfactant CTAB to prevent leaching as discussed in Chapter 3.

Another derivative of pyrene, 6-8-dihydroxypyrene-1,3-disulfonic acid, disodium salt (DHPDS) was used. DHPDS have most of the advantageous properties of HPTS including excellent water solubility due to the sulfonate group, high quantum yield, lack of toxicity and one of the most important one ratiometric properties [28]. However, the stability of DHPDS is lower compared to HPTS. Because the structure of DHPDS includes two hydroxyl groups, it has two  $pK_a$  values (7.33 and 8.53 [146]) and ( $7.03 \pm 0.02$  and  $9.05 \pm 0.02$  [55]).

A naphthalene derivative, 2,7-dihydroxynaphthalene-3,6-disulfonic acid disodium salt (DHNDs) was selected because its pH sensitivity in the high pH range. To our knowledge, DHNDs has not been immobilized in any solid matrix to work as pH sensors.



Cresol red (CR) is commonly used pH indicator for spectrophotometric determination of fresh water pH with a  $pK_a$ , 8.2 [7] or 8.29 [8]. This indicator is not fluorescent, so the pH determination with cresol red is based on absorption. CR has not been immobilized in solid support as pH sensors.

These three indicators, DHPDS, DHNDS, and CR (see Table A.1 for structures) are selected as pH indicators for immobilization in hydrogel not only because they exhibit pH sensitivity but also all of them have two hydroxy groups. One hydroxy group can react with methacrylic anhydride (MA) to form a methacryloyl analog in order to covalently bind in the hydrogel matrix and meanwhile, the other hydroxy groups retain its pH sensitivity.

The absorption and fluorescence spectral behavior of these three indicators are presented below.

#### 4.1.2.1 DHPDS

The UV-Vis absorption spectra of the pyrene derivative, DHPDS, in ethanol and different pH buffer solutions are shown in Figure 4.3. In both ethanol and pH 2.50 solution, both hydroxyl groups on pyrene ring are protonated. The absorption peak is located at 400 nm. In really basic solution, pH 12.00, both hydroxyl groups are deprotonated, and an absorption peak occurs at 486 nm. At pH 7.98, most of the DHPDS exists as monoanion with only one hydroxyl group deprotonated, and the absorption peak falls in between, 460 nm with a shoulder peak at 410 nm.

A scheme of protolytic equilibrium of DHPDS in buffer solution is shown in Figure 4.4. DHPDS exists in three forms in buffer solution: neutral, monoanion and dianion. In

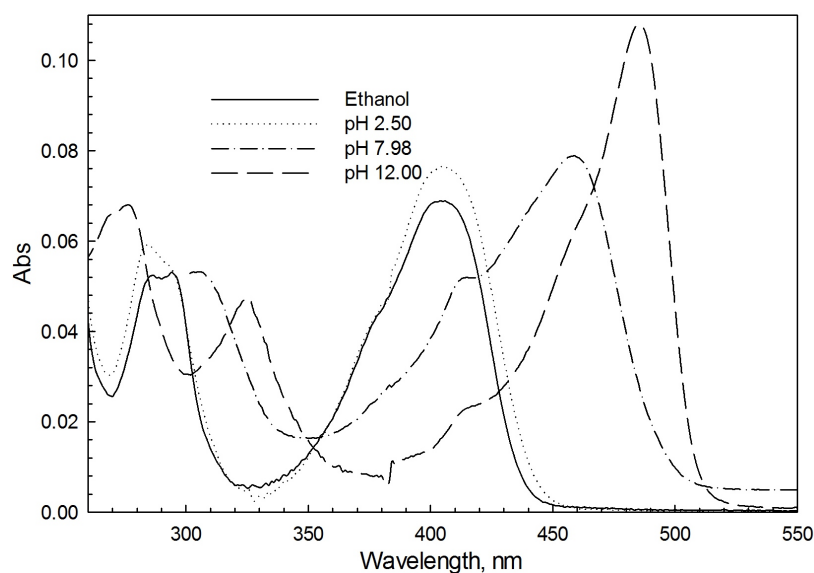


**Figure 4.3.** UV-Vis absorption spectra of DHPDS ( $4.43 \mu\text{M}$ ) in ethanol and different pH buffer solution.

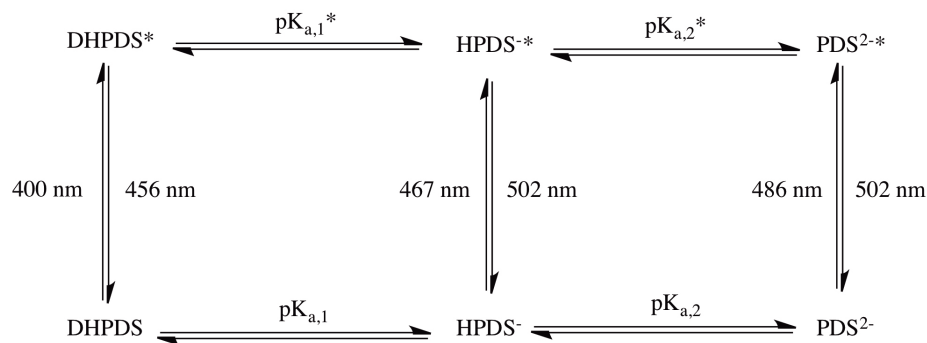


**Figure 4.4.** Protolytic equilibrium of DHPDS in buffer.

aqueous solution, the excitation and emission wavelengths for the neutral species of DHPDS are 400 nm and 454 nm, respectively. The emission wavelength in buffer is red shifted by 10 nm compared to in ethanol (444 nm). The excitation and emission wavelengths for the monoanion are 467 nm and 502 nm, respectively. As for the dianion, the excitation and emission wavelengths are 484 nm (with a shoulder peak at 467 nm) and 502 nm, respectively. The fluorescence excitation and emission spectra of DHPDS in both ethanol and

aqueous solution are shown in Figure 4.5.

The  $pK_a$  values of DHPDS in buffer were calculated using the same method as presented in Chapter 2 using both absorption and fluorescence excitation spectra of DHPDS in buffer (Figure A.8, top and bottom, respectively). DHPDS has two hydroxyl groups thus two  $pK_a$  values. As shown in Figure 4.6,  $pK_{a,1}$  and  $pK_{a,2}$  calculated from absorption spectra are 7.03 and 9.14 (IS = 0.030 M), respectively, which match the literature data,  $7.03 \pm 0.02$  and  $9.05 \pm 0.02$ , respectively [55].  $pK_{a,1}$  and  $pK_{a,2}$  calculated from fluorescence excitation spectra are 6.75 and 8.90 (IS = 0.030 M), respectively. The difference for  $pK_a$  values from absorption spectra and fluorescence spectra is due to the difference in quantum yields.

#### 4.1.2.2 DHNDS

The absorption spectra of the naphthalenene derivative, DHNDS, in both ethanol and aqueous solution are shown in Figure 4.7. In ethanol and slightly acidic solution, pH 6.78, DHNDS remains protonated and has a weak absorption at 340 nm and broad peak centered at 300 nm. In basic solution, pH 11.13, DHNDS is deprotonated and has two absorption peaks at 270 nm and 358 nm (relative low absorbance).

The fluorescence spectra of DHNDS in both ethanol and aqueous solution are shown in Figure 4.8. In ethanol, DHNDS has only one emission peak at 380 nm, which is the emission of excited state protonated form of DHNDS. In aqueous solution, DHNDS also only has one emission peak, but located at 465 nm, which is the emission of excited state deprotonated form of DHNDS. At pH 10.78, the excitation peak is at 365 nm, which should be the absorption peak of deprotonated form of DHNDS. At pH 3.76, the excitation peak

is at 336 nm, which should be the absorption peak of the protonated form of DHNDS.

Only one  $pK_a$  value of DHNDS was calculated based on the normalized absorption and fluorescence excitation spectra (as shown in Appendices, Figure A.9), despite that there are two hydroxy groups in its structure. It might be because after the first hydroxyl group is deprotonated, it is really hard to dissociate the second one, which make the second  $pK_a$  value really large number, out of this pH range. The calculated  $pK_a$  value for DHNDS in buffer solution is 8.85 and 8.70, from absorption spectra and fluorescence excitation spectra, respectively, as shown in Figure 4.9.

The  $pK_a$  value for DHNDS is not available in the literature. For similar compounds, the  $pK_a$  value of 2,7-dihydroxynaphthalene is listed as 9.14 [147] and 2-naphthol-6-sulfonate is listed as 9.16 [148]. And the excited state  $pK_a^*$  of 2-naphthol-6-sulfonate is listed as 1.7 [148].

DHNDS is not very stable in basic solution, it turns blue and loses a large amount of its fluorescence as shown in Figure 4.10. In 0.16 M NaOH solution, under continuing illumination, DHNDS lost its fluorescence completely within 4 hours. In pH 10.78 buffer solution, the fluorescence also decreases, but without illumination, the decrease rate is slower. In acidic condition (0.8 M acetic acid solution), the fluorescence of DHNDS is more stable, the fluorescence intensity stayed unchanged for a day, and the solution did not turn blue.

This change can also be confirmed from the absorption spectra (Figure 4.11). The absorbance peak at 358 nm in basic solution decreased and a new absorbance peak at 600 nm showed up, which conformed the color change of the solution.

2-hydroxynaphthalene-3,6-disulfonate (HNDS) is a similar compound as DHNDS with

only one hydroxy group. The absorption and fluorescence spectra of HNDS were studied and we expected the spectra behavior of DHNDS covalently bound in hydrogel to be similar to HNDS because both have only one hydroxy group. The fluorescence spectra of HNDS in buffer are shown in Figure 4.12. HNDS behaves similar with DHNDS, single emission peak at 460 nm. In pH 11.04 solution, it exists as monoanion, the excitation peaks are at 310 nm and 370 nm. In pH 7.28 solution, it exists as protonated neutral species, the excitation peaks are at 290 nm and 340 nm. The  $pK_a$  value of HNDS in buffer was calculated as 8.92 based on fluorescence excitation spectra.

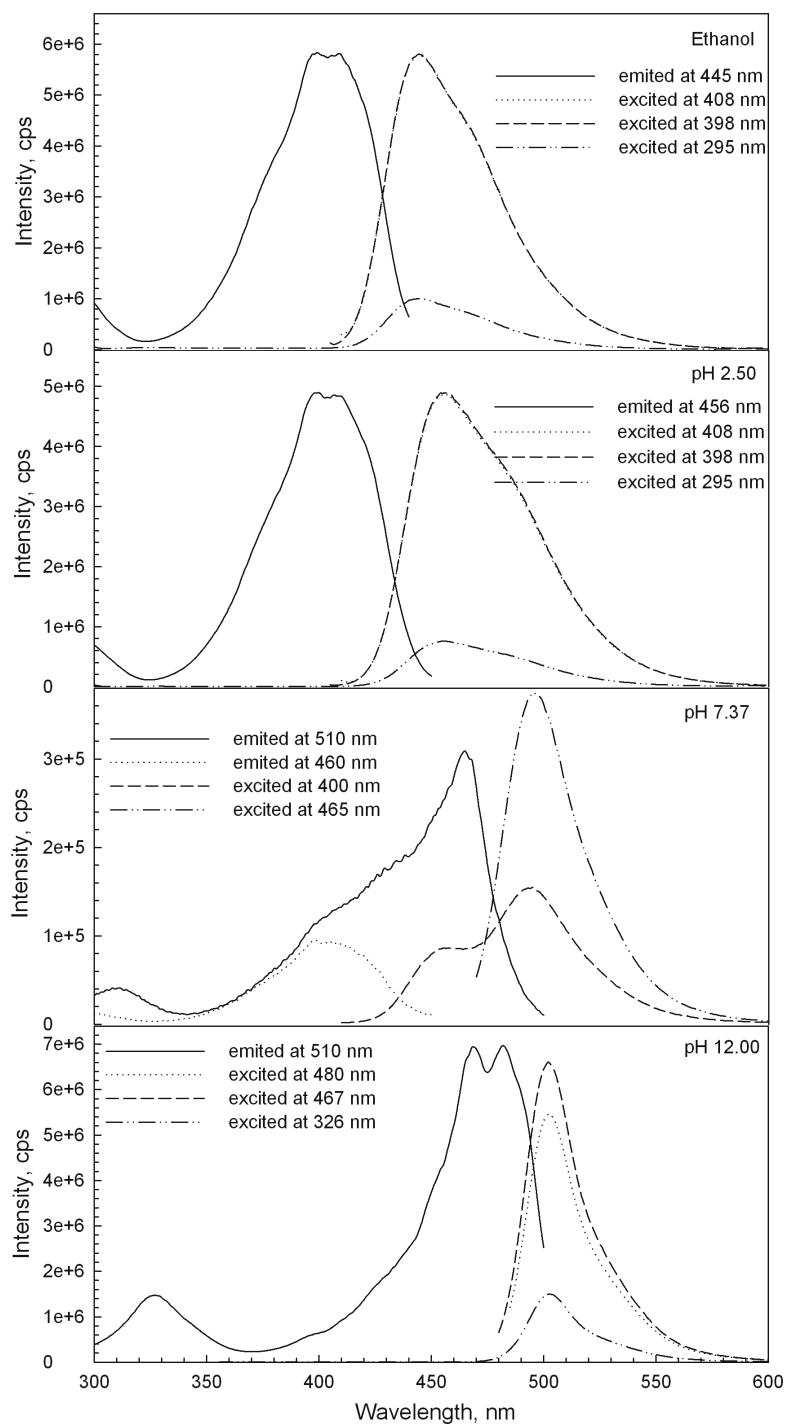
#### 4.1.2.3 CR

The UV-Vis absorption spectra of cresol red in buffer solution ( $IS = 0.100\text{ M}$ ) is shown in Figure 4.13. Cresol red has two absorption peaks at 434 nm and 575 nm for protonated and deprotonated forms, respectively. The absorbance values of these two peaks shifts according to pH. The  $pK_a$  value of cresol red in buffer ( $IS = 0.100\text{ M}$ ) is 8.23 as shown in Figure 4.14, which agrees with literature values, 8.2 [7] or 8.29 [8]. The small shift is due to the ionic strength effect.

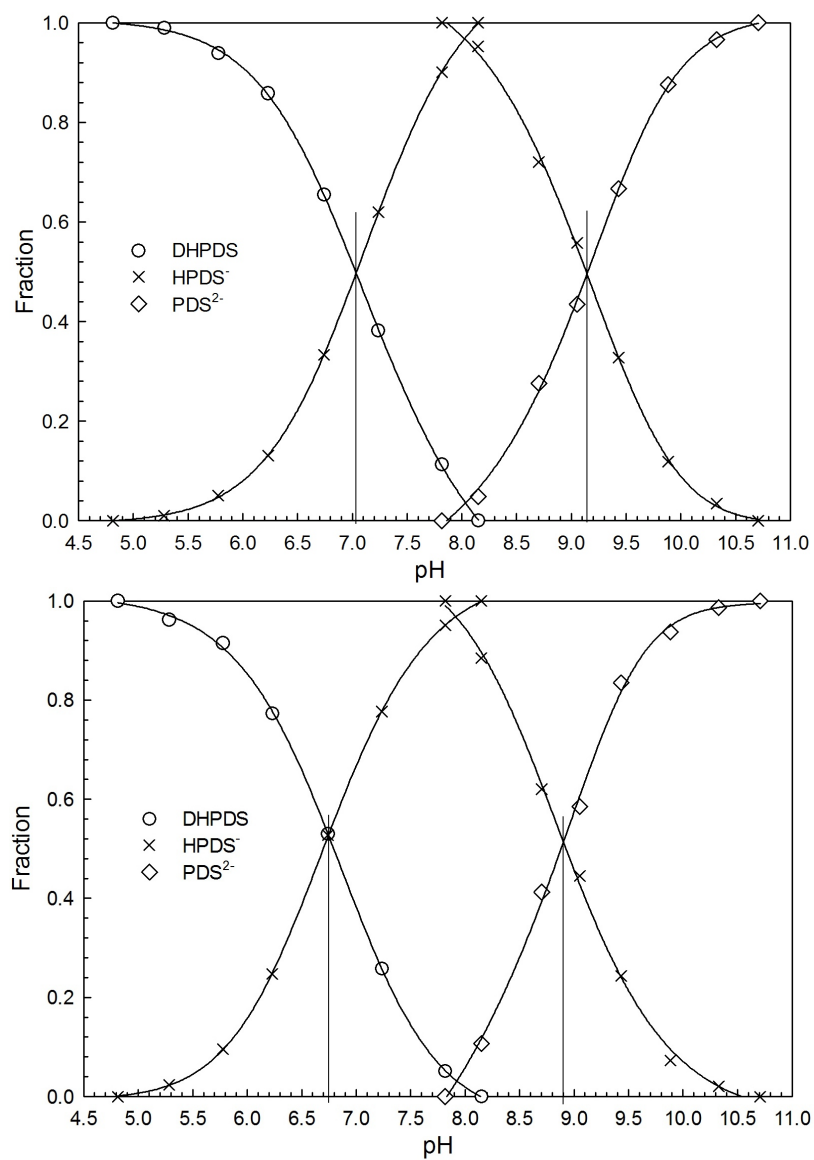
#### 4.1.3 Specific aims of this study

- Synthesize PEG hydrogels using both free radical initiator and redox initiation system.
- Characterize hydrogel properties, such as pores sizes and swelling ratio related to the percentage of precursors in the starting solution.

- Immobilize pH indicators in hydrogel through physical entrapment and covalent binding methods.
- Study and compare the spectral behavior of different indicators in both solution and hydrogel.
- Evaluate the potential of indicators immobilized in hydrogel as pH sensors.

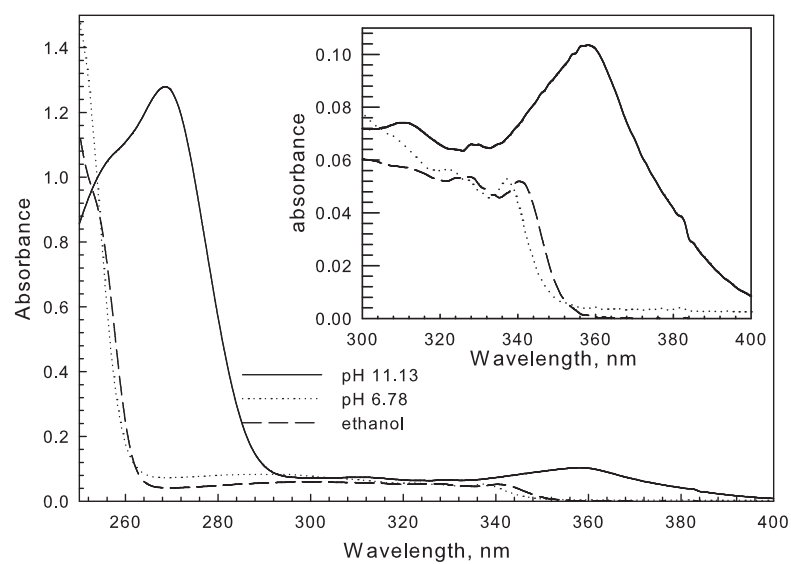


**Figure 4.5.** Fluorescence excitation and emission spectra of DHPDS (1.0  $\mu\text{M}$ ) in ethanol and different pH solution.

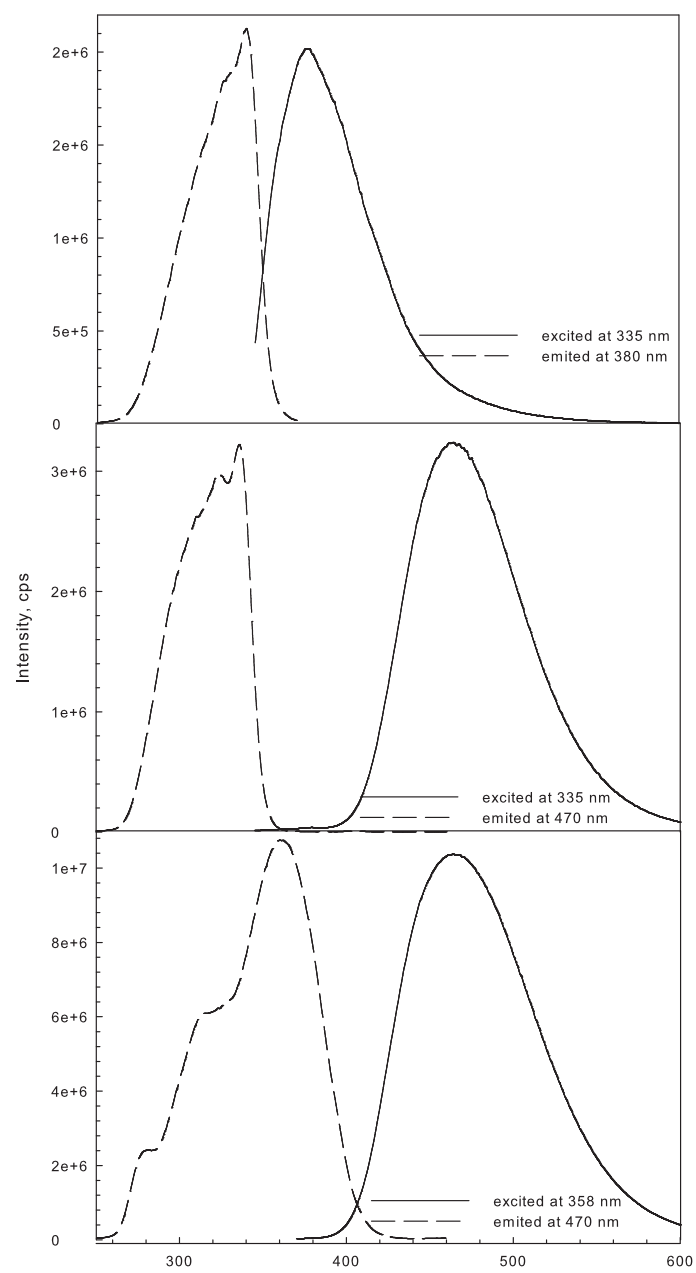


**Figure 4.6.**  $pK_a$  values of DHPDS in solution ( $IS = 0.030\text{ M}$ ) from absorption spectra (top) and fluorescence excitation spectra (bottom).





**Figure 4.7.** UV-Vis absorption spectra of DHNDS (20  $\mu$ M) in both solution and ethanol.



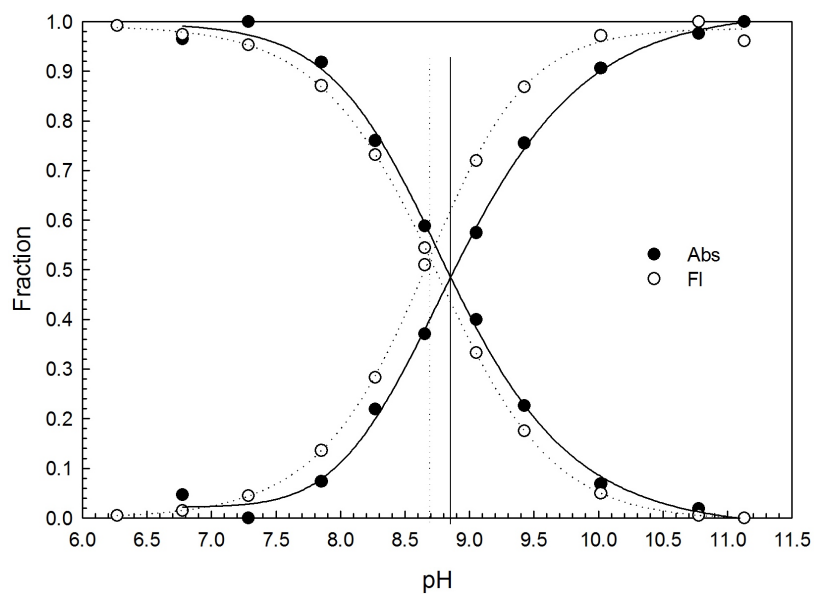


**Figure 4.9.**  $pK_a$  values of DHNDS in solution ( $IS = 0.030\text{ M}$ ) from both absorption and fluorescence excitation spectra.

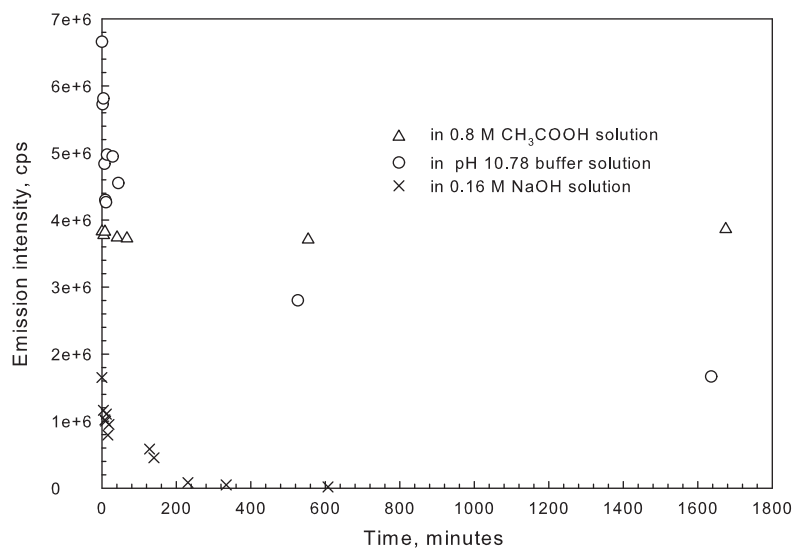


**Figure 4.10.** Fluorescence intensity change of DHNDS in different solutions in 1 day.

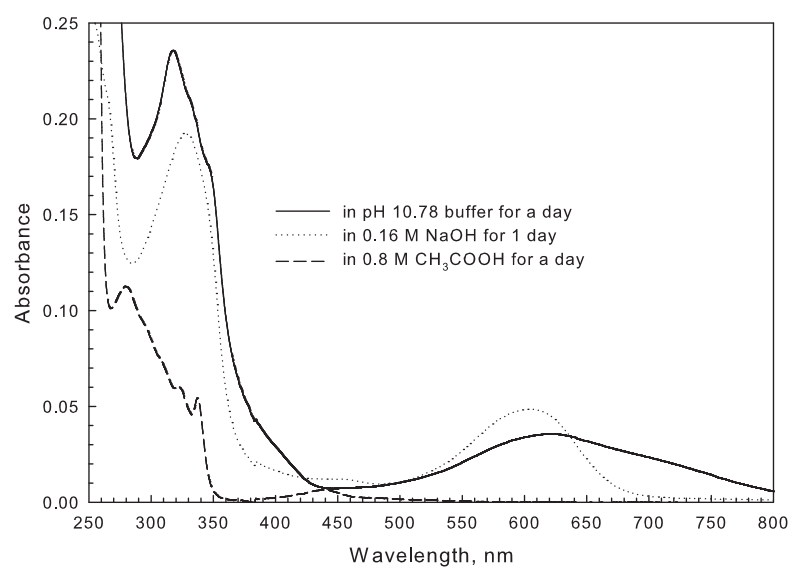


**Figure 4.11.** UV-Vis absorption spectra of DHNDS in different solutions after 1 day.

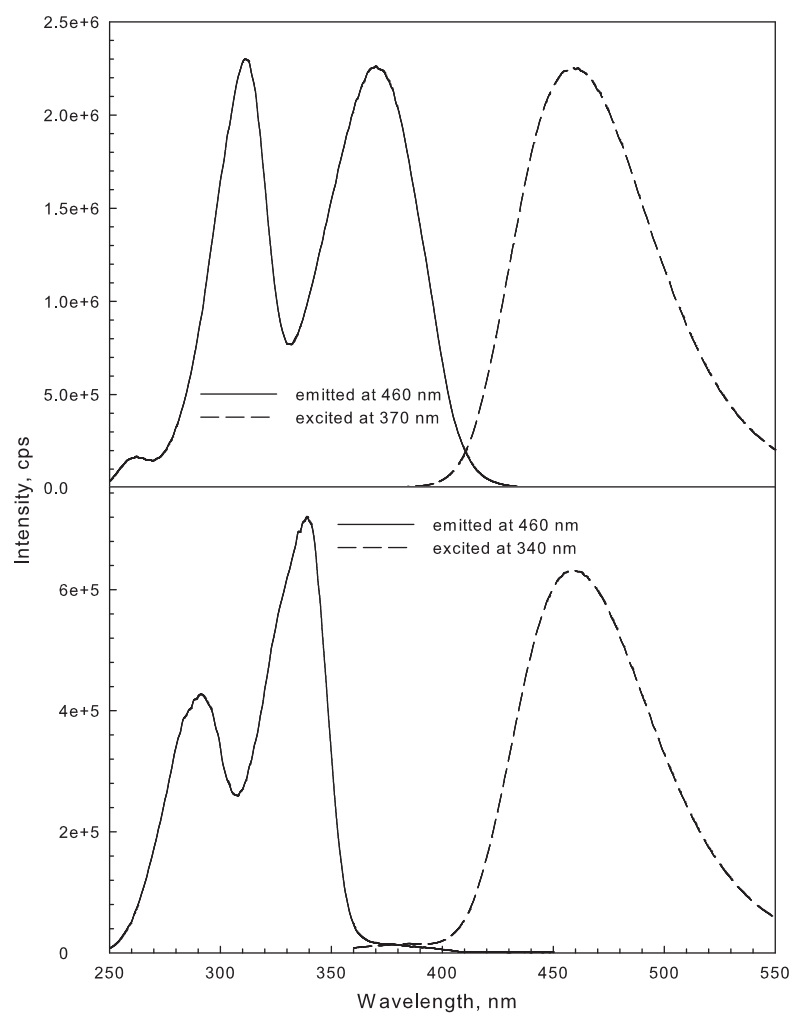


**Figure 4.12.** Fluorescence spectra of HNDS (10.5  $\mu$ M) in buffer solution. Top: pH 11.04; bottom: pH 7.28.

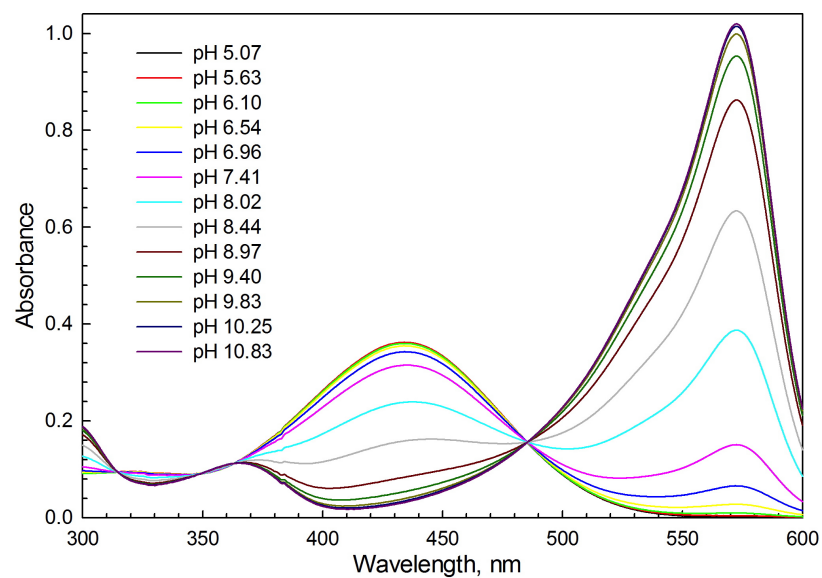


**Figure 4.13.** UV-Vis absorption spectra of cresol red (14.9  $\mu\text{M}$ ) in buffer (IS = 0.100 M).

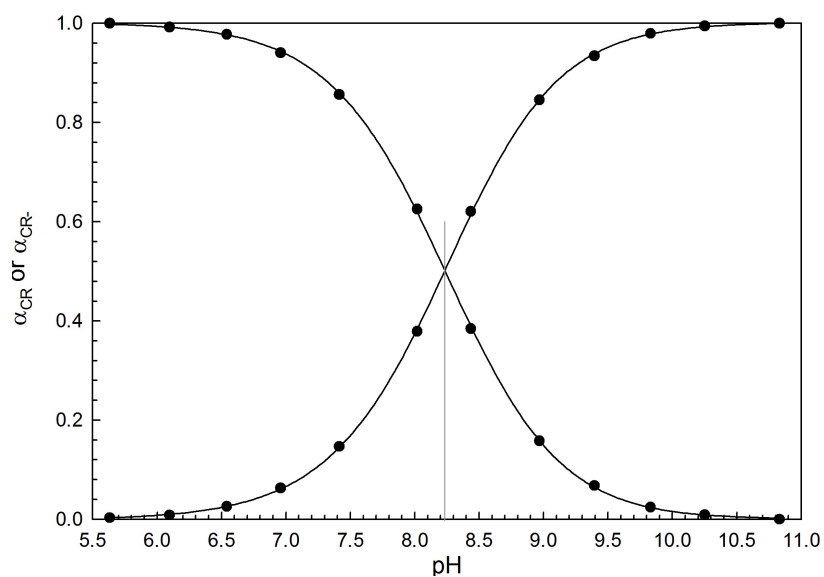


**Figure 4.14.**  $\text{pK}_a$  (bottom) of cresol red in solution (IS = 0.100 M).

## 4.2 Experimental

### 4.2.1 Reagents and materials

Cresol red (CR), sulfuric acid ( $\text{H}_2\text{SO}_4$ ), sodium metabisulfite ( $\text{Na}_2\text{S}_2\text{O}_5$ ), 2,7-dihydroxynaphthalene-3,6-disulfonic acid disodium salt (DHNDS), 8-hydroxypyrene-1,3,6-trisulfonic acid trisodium salt (HPTS), free radical initiator azobisisobutyronitrile (AIBN), dimethyl formamide (DMF), deuterium oxide ( $\text{D}_2\text{O}$ ) and poly(ethylene glycol) diacrylate (PEGDA) with an average molecular weight of 700 were purchased from Sigma-Aldrich. Potassium persulfate ( $\text{K}_2\text{S}_2\text{O}_8$ , KPS), ferrous sulfate ( $\text{FeSO}_4$ ), sodium hydrogen phosphate ( $\text{Na}_2\text{HPO}_4$ ), monobasic sodium phosphate ( $\text{NaH}_2\text{PO}_4$ ), sodium carbonate ( $\text{Na}_2\text{CO}_3$ ), sodium bicarbonate ( $\text{NaHCO}_3$ ), potassium carbonate ( $\text{K}_2\text{CO}_3$ ), sodium chloride ( $\text{NaCl}$ ) and dimethylformamide were purchased from Fisher. Methacrylic anhydride (MA) was purchased from Alfa Aesar. 6,8-dihydroxypyrene-1,3-disulfonic acid, disodium salt (DHPDS) was purchased from Molecule probes. The ion pair reagent hexadecyltrimethylammonium bromide (CTAB) was purchased from Acros Organics. All chemicals were used as received without further purification.

Phosphate buffer was prepared with monobasic sodium phosphate and sodium hydrogen phosphate solutions. Carbonate buffer was prepared with sodium carbonate and sodium bicarbonate solutions. The formal concentration of the buffer was 0.010 M and sodium chloride was used as the background electrolyte to adjust the ionic strength of the buffer solution to the desired strength, typically 0.100 M.

## 4.2.2 Synthesis of hydrogels

### 4.2.2.1 Synthesis of methacryloyl-analogs

In order to covalently bind dyes into hydrogel, methacryloyl-analogs were fabricated using a previous published procedure [42] with modifications for this study. Briefly, the indicator cresol red (92.3 mg) was dissolved in DMF (10 mL) in a 25 mL reaction vessel. Potassium carbonate (1 g) and methacrylic anhydride (1:1 eq., 36  $\mu$ L) were added. The vessel was stopped and placed in a 70 °C oil bath to react overnight with stirring. The cooled mixture was filtered. The solvent was removed from the filtrate in a rotary evaporator to yield the solid product methacryloyloxy-cresol red (MA-CR). 6-methacryloyloxy-8-hydroxypyrene-1,3-trisulfonate (MA-HPDS) or 2-methacryloyloxy-7-hydroxynaphthalene-3,6-disulfonate (MA-HNDS) were synthesized in an analogous manner, substituting DH-PDS or DHNDS for CR in the first step. The reactions are depicted in Figure 4.15.

### 4.2.2.2 Synthesis of PEG hydrogels

PEG hydrogels were synthesized with both free radical initiator and redox initiation system. Both polymerization reactions need to be conducted under oxygen free environment. For free radical initiators, the reaction needs to be conducted at elevated temperature and requires reaction time of several hours. On the other hand, polymerization by redox initiation system can be done at room temperature and the reaction is completed within 30 minutes. Details of these two polymerization reactions are described below. Polymerization with the redox initiation system was used as the main method for hydrogel synthesis with indicators because it can be conducted at room temperature and require less time



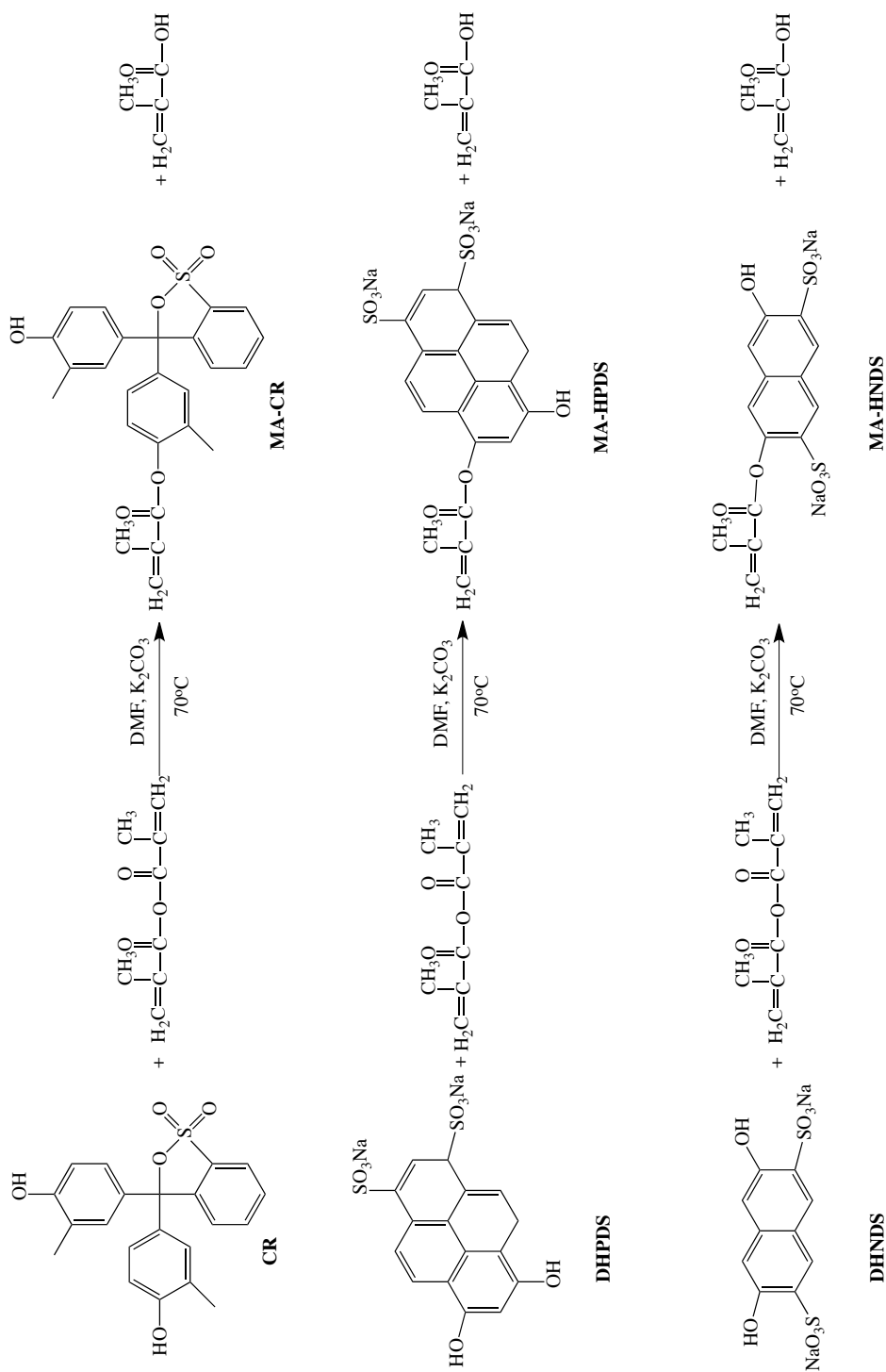


**Figure 4.15.** Reaction scheme of preparation of MA-HPDS (top), MA-HPDS (middle) and MA-HNDS (bottom).

compared to free radical initiator. Hydrogel synthesis with free radical initiator was only conducted for physically entrapment of indicator ion-pairs FS-CTAB and HPTS-CTAB, because these indicators ion-pairs are insoluble in water (which is solvent for synthesis with redox initiation system) but soluble in DMF, which was the solvent for free radical polymerization.

#### **Synthesis with free radical initiator:**

Polymer precursor solution was prepared by combining 400  $\mu\text{L}$  of PEGDA, 1000  $\mu\text{L}$  of DMF and 1.1 mg of AIBN. The precursor solution was bubbled with nitrogen for 1 hour to remove oxygen. In the meantime, an aluminum box (1 cm  $\times$  1 cm  $\times$  0.5 cm) covered with another piece of aluminum foil was placed in a small vial (as shown in Figure 4.16). The empty reaction vial was flushed with nitrogen for 1 hour to remove oxygen as well. The precursor solution was injected to the reaction vial using a syringe. The reaction vial was placed in an 70 °C oil bath and was bubbled nitrogen for 6 hours. After polymerization, the HPDS-PEG layer was peeled from the aluminum foil box and washed in deionized water for a few hours. This step served to both hydrate the matrix and remove any unbound dye.

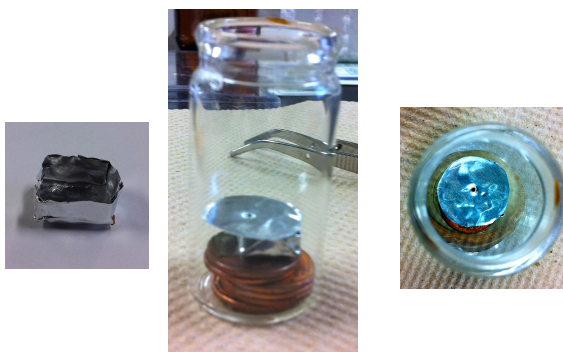
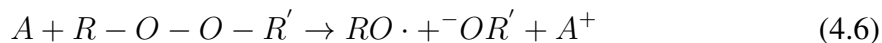


**Figure 4.16.** Reaction setup for hydrogel synthesis with free radical initiator.

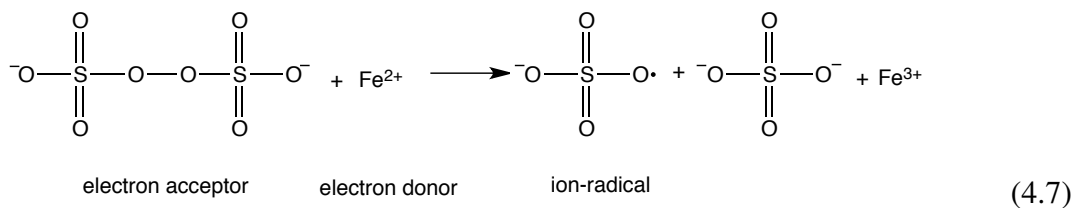
#### **Synthesis with redox initiation system:**

The redox initiation is based on bimolecular reactions involving electron transfer mechanisms such as decomposition of peroxides into initiating radicals. The reaction can be illustrated as follows:

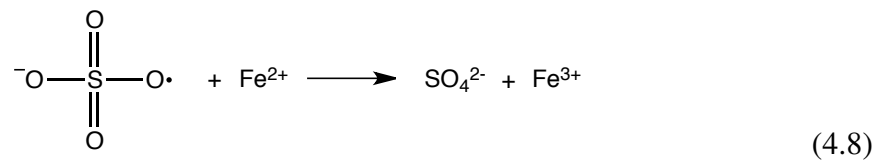


where  $A$  is the reducing agent (electron donor) and  $ROOR'$  is the peroxide (electron acceptor).

In this study, we used a decomposition of a persulfate (potassium persulfate) [149] by the ferrous ion:



Side reactions are possible in the presence of sufficient quantities of reducing ions:



The polymerization reaction of the PEG hydrogel was initiated by the previous published redox initiation system [54], which is a mixture of KPS,  $\text{Na}_2\text{S}_2\text{O}_5$  and  $\text{FeSO}_4$  solu-

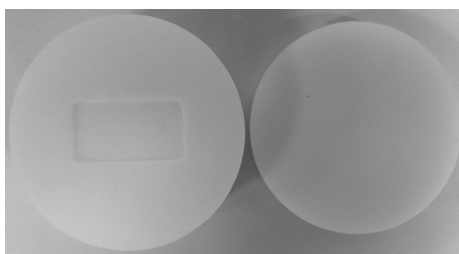


**Figure 4.17.** Teflon mold and cover for hydrogel synthesis with redox initiation system.

tions. A series of monomer solution with different percentage (4.9% - 15.5%, see Table 4.2) of PEGDA were used to form hydrogel with different properties. The monomer solution was bubbled with nitrogen for 15 minutes to remove oxygen and then immersed in an ice-water bath for 5 minutes. To the cooled monomer solution was added the redox initiation solution. The cold solution was then mixed by shaking in the ice-water bath for 30 seconds and immediately cast into a teflon mold ( $1.3\text{ cm} \times 2.5\text{ cm} \times 0.5\text{ mm}$ , as shown in Figure 4.17) and covered by another teflon piece in a sealed polyethylene bag (Ziploc, S. C. Johnson & Son, Racine, WI). Nitrogen gas was flowed into the bag for 1 hour and the bag remained sealed. The reaction was left on for 1 - 2 hours. The hydrogel film was washed off from the Teflon mold and immersed in DI water for several days in order to remove the unreacted salt from the redox initiation solution. The hydrogels were stored in DI water.

#### 4.2.2.3 *Physical entrapment of indicator ion-pairs in hydrogel*

Two indicators, FS and HPTS, were incorporated into ion-pairs in order to physically entrap them into hydrogels. The synthesis of indicator ion-pairs HPTS-CTAB and FS-CTAB was discussed in Chapter 3. The stock solution of HPTS-CTAB and FS-CTAB (1.0 mM) in DMF was prepared. The 9.8% polymer precursor solution was used to for

indicator ion-pair entrapment. 100  $\mu\text{L}$  of HPTS-CTAB or FS-CTAB stock solution was used to substitute DMF in the first step. The rest of the procedures were the same as the PEG hydrogel synthesis with the free radical initiator AIBN. After reaction, the indicator entrapped hydrogels were immersed in DI water for several days in order to let the non-trapped indicator leach out. The soaking solutions were intensely green indicating large leaching of non-trapped indicators. After several days, no dyes were leaching out, and the soaking solution was clear. The color change of dye immobilized hydrogels was not significant due to small amount of dyes entrapped into hydrogels.

#### *4.2.2.4 Covalent bound of indicator in hydrogel*

To covalently bind indicator in hydrogel matrix, the 9.8% of monomer solution was used by substituting 100  $\mu\text{L}$  of DI water with 100  $\mu\text{L}$  MA-CR, MA-HPDS or MA-HNDS (4.0 mM). The rest of the procedures were the same as PEG hydrogel synthesis with the redox initiation system. After reaction, the indicator covalently bound hydrogels (CR-PEG, HPDS-PEG, or HNDS-PEG) were immersed in DI water in order to let the unbound indicator and salt from the redox initiation system leach out. Compared to dye physically entrapped system, leaching even at the beginning is negligible. An intense yellow color for CR-PEG hydrogel was observed. HPDS-PEG and HNDS-PEG was transparent and colorless.

### 4.2.3 Characterization and Instrumentation

**FTIR:** The successful synthesis of methacryloyl-analogs (MA-CR, MA-HPDS and MA-HNDS), PEG hydrogel and CR-PEG hydrogel were confirmed by FTIR spectra. The PEG and CR-PEG hydrogel were dried and ground into powder and the FTIR spectra were then obtained with a fourier transform infrared spectrometer (Spectrum one, Perkin Elmer).

**NMR:**  $^1\text{H}$  proton NMR spectra of indicators and methacryloyl-analogs were taken with a NMR wide-bore spectrometer (Varian 400MHz), and  $\text{D}_2\text{O}$  was used as solvent.

**SEM:** The hydrogel samples were quickly frozen in liquid nitrogen and then freeze-dried in a Sharp Freeze-110 (aapptec) under vacuum at  $-108\text{ }^\circ\text{C}$  for 3 days until all water was sublimed. The dry hydrogel samples were coated with 5 nm Pt for interior morphology observation with a field-emission scanning electron microscopy (Hitachi S-4700). The experiments were performed at a low accelerating voltage (15kv), especially suitable for imaging the surface detail of low-density materials.

**UV-Vis:** UV-Vis absorption spectra were measured with a Lambda 35 UV/Vis Spectrometer (Perkin Elmer). The hydrogel films were placed in a Quartz cuvette filled with buffer solution for absorption spectra measurement as shown in Figure 4.18.

**Fluorescence:** Fluorescence spectra were measured with a SPEX FLUOROLOG 1681 Spectrometer with setup shown in Figure 4.18. Fluorescence lifetimes were acquired with TM-200 LED strobe Lifetime Spectrofluorometer (PTI). A single exponential decay was used to fit the fluorescence lifetime.

**Images:** Images of hydrogel in different buffer solution were taken using a Nikon COOLPIX S520c camera.

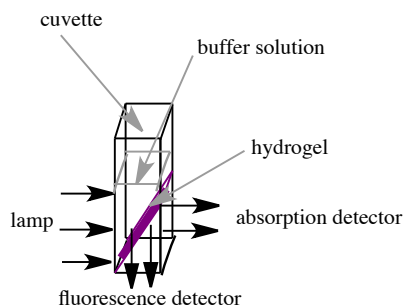


**Figure 4.18.** UV-Vis Absorption and fluorescence measurement set-up.

**Swelling:** After synthesis, the hydrogel was immersed in DI water for several days to remove unbound indicators and unreacted salt and to let the swelling of the hydrogel reach equilibrium. The mass of the swollen hydrogels was measured after removing the surface water using filter paper. The mass of freeze-dried hydrogels was measured. The swelling ratio was calculated as the ratio of the mass of hydrogel in the swollen and dry states.

The pH meter (Orion 2 star pH benchtop, Thermo Scientific) was calibrated in NIST (National Institute of Standards and Technology) standard buffer by a three-point calibration procedure (pH 4.00, 7.00 and  $10.00 \pm 0.02$ ). All the measurements were conducted at room temperature.

## 4.3 Results and Discussion

### 4.3.1 Properties of PEG hydrogels

PEG hydrogels properties such as swelling ratio ( $Q_m$ ), average molecular weight between the adjacent crosslinks ( $M_c$ ) and the network mesh size ( $\xi$ ) were studied.

#### 4.3.1.1 Swelling ratio

In this study, the structural properties of the PEG hydrogel were controlled by varying the precursor percentages (v/V, from 4.9% to 15.3%) during polymerization. The swelling ratios of PEG hydrogels with different precursor percentages were calculated using eq 4.4. Increasing the precursor percentage in the starting solution produced a decrease in the swelling ratio of the hydrogel. As shown in Figure 4.19, the precursor percentage increases from 4.9% to 15.3%, and the swelling ratio decreases from 50 to 7.1. The 4.9% and 7.5% PEG hydrogels with the highest swelling ratio, 50 and 31, respectively, were extremely pliable and showed poor mechanical integrity. The 9.8% PEG hydrogel with swelling ratio, 11.8, was robust, possessing an adequate balance between strength and flexibility. The 15.3% PEG hydrogel with swelling ratio, 7.1 was relatively hard and brittle. So 9.8% PEG hydrogel was chosen for indicator immobilization.

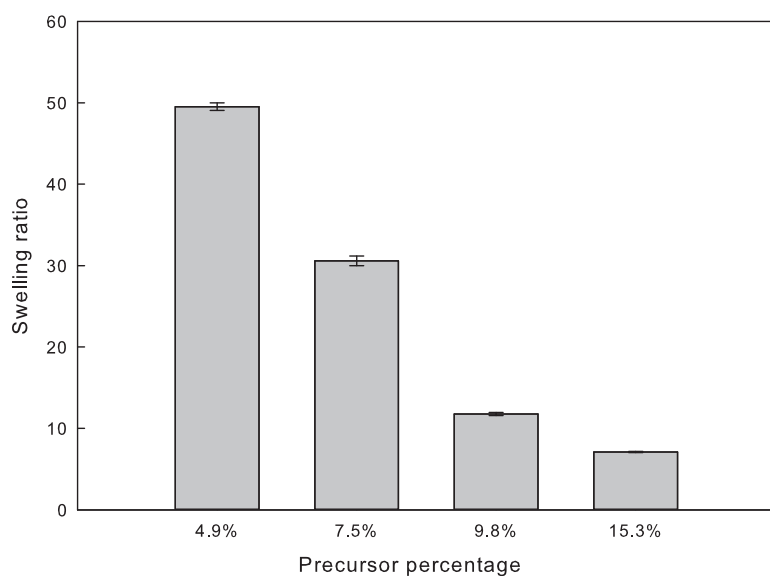


**Figure 4.19.** Swelling ratio of PEG hydrogels of different precursor percentages in DI water.



Figure 4.20 shows the SEM images of the corresponding freeze-dried PEG hydrogels. As anticipated, the pore size and density of hydrogels were highly correlated with the precursor percentages. Hydrogels with 4.9% of precursor exhibited a pore size of around 100  $\mu\text{m}$ , while those of 15.3% displayed a pore size of around 10  $\mu\text{m}$ .

The swelling ratio of PEG hydrogels mainly depends on the characteristics of their network structure. A compact network structure due to a high crosslinking density causes a reduction in water uptake capacity due to decreased pore volume.

The incorporation of charged groups to the network structure introduces a dominant driving force for swelling due to the inherent electrostatic repulsion between network charges. The media pH was not expected to affect the swelling behavior of the PEG hydrogels because PEG hydrogel do not contain charged groups. The swelling ratios of PEG hydrogels with different precursor percentages in different standard pH solutions (pHydrion Buffers) with approximate ionic strength of 0.55 M, are shown in Table 4.1. There was no change of swelling ratio upon changing the pH of solution.

**Table 4.1**  
Swelling ratios of PEG hydrogels in different pH solution (IS = 0.55 M).

pH	Precursor percentage		
	7.5%	9.8%	15.3%
4.00 $\pm$ 0.02	13.2 $\pm$ 0.4	9.4 $\pm$ 0.6	6.6 $\pm$ 0.2
7.00 $\pm$ 0.02	14.2 $\pm$ 0.3	9.2 $\pm$ 0.3	6.9 $\pm$ 0.1
10.00 $\pm$ 0.02	14.1 $\pm$ 0.9	9.8 $\pm$ 0.3	6.8 $\pm$ 0.9

A decreased swelling ratio in buffer solution compared to DI water was observed. However, it was not a real decrease of swelling ratio in buffer solution but was attributed to salts in the buffer. The ionic strength of standard buffer solutions were very high. When hydrogels were placed in buffer solution, the salt diffused into the network of the hydrogels. When the hydrogel was freeze dried, water was sublimed from the hydrogel, however, the

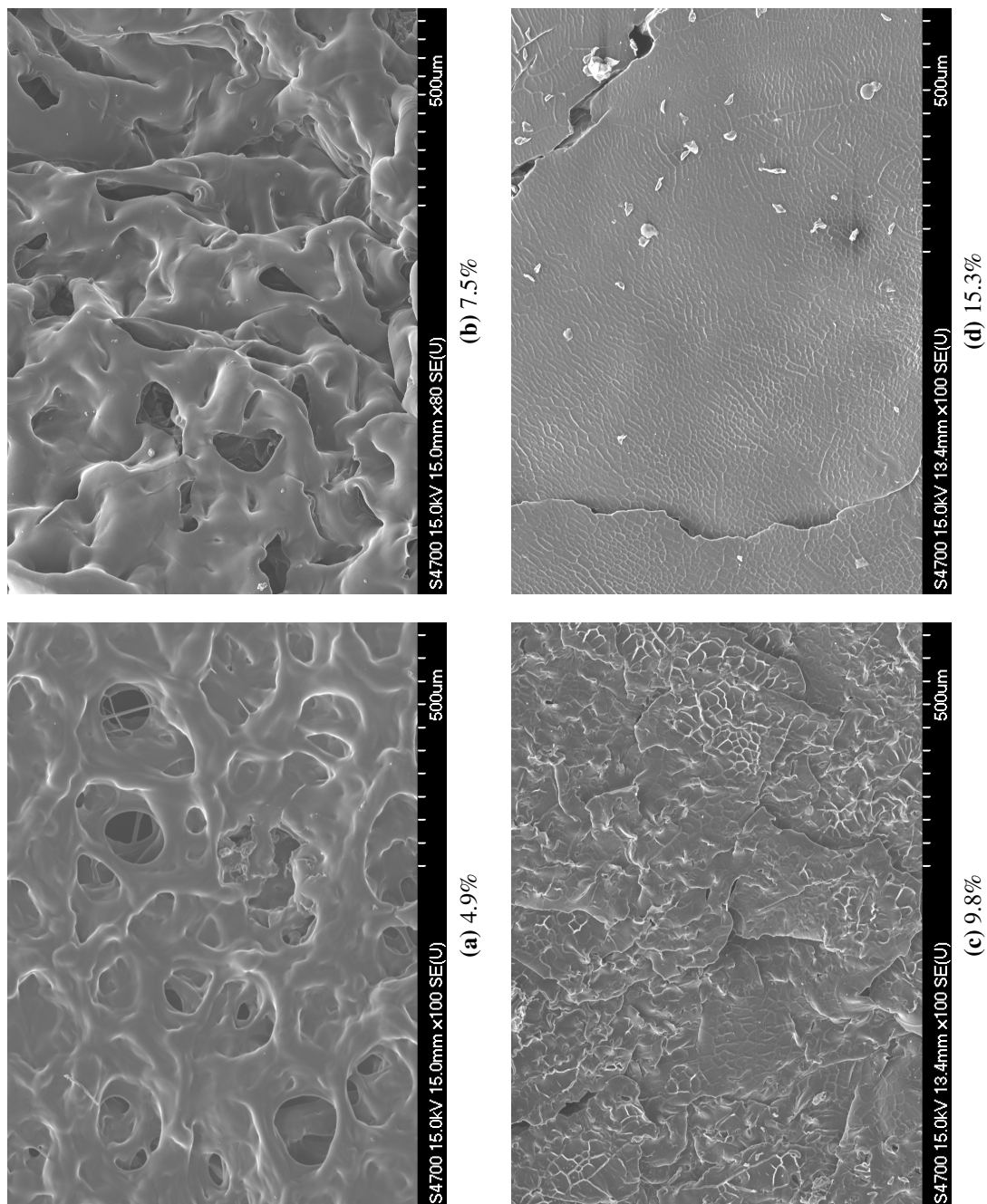


**Figure 4.20.** SEM images of freeze dried PEG hydrogels with different precursor percentages.

salt stayed. The swelling ratio was calculated using eq 4.4; the mass of dry hydrogel appeared to increase because of the salt left in it. So the calculated swelling ratio decreased. The calculated swelling ratio against the concentration of the soaking solution (KCl solution) was also studied. As expected, the calculated swelling ratio decreased when the concentration of the soaking solution increased as shown in Figure A.10.

#### 4.3.1.2 *Structural properties*

The average molecular weight between adjacent crosslinks ( $\bar{M}_c$ ) was calculated using eq 4.1, and  $v_{2,s}$  was estimated with the swelling ratio of the hydrogels and  $v_{2,r}$  was used with the percentage of the precursors in the gel. The network mesh size ( $\xi$ ) of these PEG hydrogels were calculated using eq 4.2. These values are given in Table 4.2. The average molecular weight between the adjacent crosslinks,  $\bar{M}_c$ , decreased from 334 g/mol to 245 g/mol with increasing precursor percentages from 4.9% to 15.3%. When chains become entangled during the crosslinking process, effective crosslinks are formed in and around the permanent junctions. These entanglements reduce the effective average molecular weight between crosslinks. Similarly, the mesh size  $\xi$  of the hydrogel decreased from 4.7 nm to 2.0 nm with the same increase of precursor percentages.

#### 4.3.2 **Synthesis of methacryloyl-analogs and hydrogels**

It is important to confirm the structure of hydrogel precursors to ensure covalent attachments. Characterization was accomplished by FTIR and NMR spectra.

**Table 4.2**  
Properties of PEG hydrogels with different precursor percentage.

Precursor percentage		4.9%	7.5%	9.8%	15.3%
precursor solution	PEGDA	115 $\mu\text{L}$	180 $\mu\text{L}$	240 $\mu\text{L}$	400 $\mu\text{L}$
	DI water	1400 $\mu\text{L}$	1400 $\mu\text{L}$	1400 $\mu\text{L}$	1400 $\mu\text{L}$
	H <sub>2</sub> SO <sub>4</sub> (0.0010 M)	100 $\mu\text{L}$	100 $\mu\text{L}$	100 $\mu\text{L}$	100 $\mu\text{L}$
Redox initiation system	KPS (0.00246 M)	120 $\mu\text{L}$	120 $\mu\text{L}$	120 $\mu\text{L}$	120 $\mu\text{L}$
	Na <sub>2</sub> S <sub>2</sub> O <sub>5</sub> (0.070 M)	300 $\mu\text{L}$	300 $\mu\text{L}$	300 $\mu\text{L}$	300 $\mu\text{L}$
	FeSO <sub>4</sub> (0.0010 M)	300 $\mu\text{L}$	300 $\mu\text{L}$	300 $\mu\text{L}$	300 $\mu\text{L}$
Structural properties	$M_c$ (g/mol)	344	339	293	245
	$\xi$ (nm)	4.7	3.9	2.6	2.0

#### 4.3.2.1 FTIR conformation of methacryloyl-analogs

The successful synthesis of MA-CR can be confirmed by FTIR spectra from the alkenyl C=C stretch peak at 1670  $\text{cm}^{-1}$  and the ester C=O stretch peak at 1730  $\text{cm}^{-1}$  as shown in Figure 4.21. A broad peak centered at 3400  $\text{cm}^{-1}$  is the typical absorption peak for O-H stretch. Absorption peaks at 2925  $\text{cm}^{-1}$  are C-H stretch from methylene groups, which also confirmed the successful attachment of methacryloyl group.

FTIR spectra of DHNDS and MA-HNDS are shown in Figure 4.22. The appearance of C=O and C=C stretch peaks confirms the successful synthesis.

FTIR spectra of DHPDS and MA-HPDS are shown in Figure 4.23. The appearance of C=O and C=C stretch peaks confirms the successful synthesis. The absorption peak at 1455  $\text{cm}^{-1}$  and 945  $\text{cm}^{-1}$  is from the methyl group in methacryloyl analog. The absorption peak at 1100  $\text{cm}^{-1}$  is for the C-O stretch.

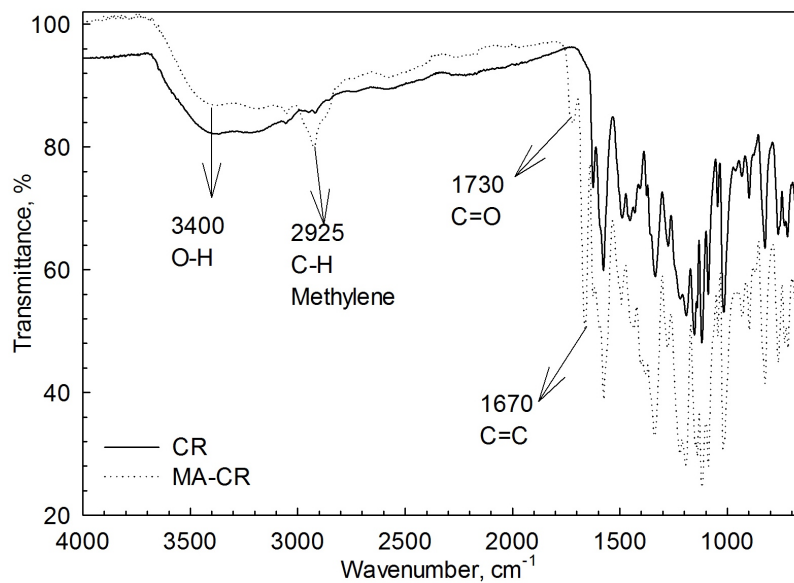


**Figure 4.21.** FTIR spectra of cresol red sodium salt and MA-CR.

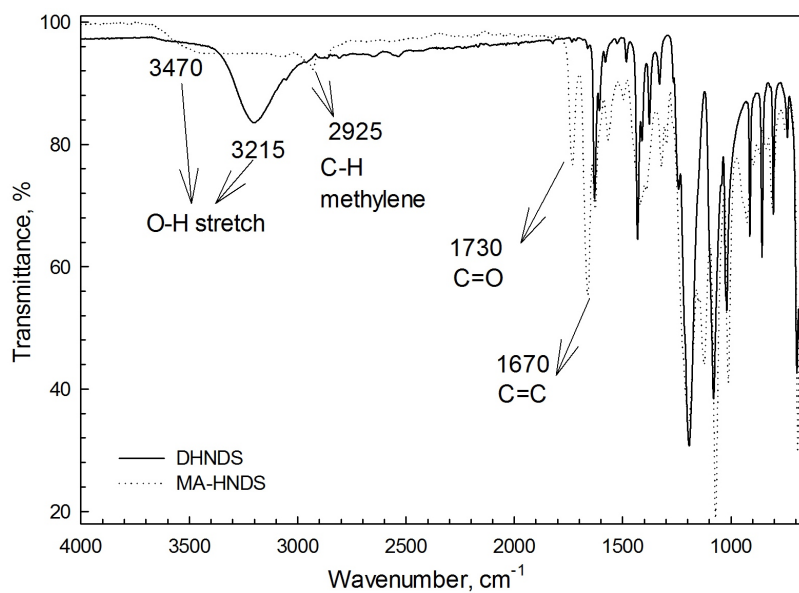


**Figure 4.22.** FTIR spectra of DHNDS and MA-HNDS.

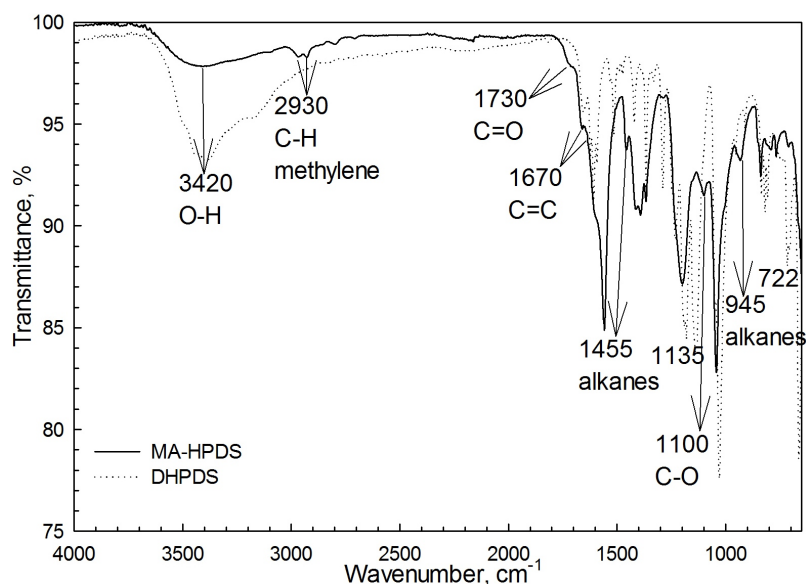


**Figure 4.23.** FTIR spectra of DHPDS and MA-HPDS.

#### 4.3.2.2 NMR spectra conformation of methacryloyl-analogs

The NMR spectra of indicator and methacryloyl indicators also confirmed the successful synthesis of methacryloyl analogs.

The  $^1\text{H}$ -NMR spectrum of cresol red in  $\text{D}_2\text{O}$  is shown in Figure 4.24. The  $^1\text{H}$ -NMR spectrum of CR is comprised of 2 singlets, 4 doublets and 3 triplets. The two singlets are due to the hydrogen atoms labeled h from the two identical methyl groups on the benzene ring and hydrogen atoms labeled e next to the methyl groups. The 4 doublets are due to the hydrogen atoms labeled a, d, g and f. The two triplets are due to the hydrogen atoms labeled b and c. Due to the electronegativity of sulfonate groups, the hydrogen atom labeled a are shifted downfield compared to d. Compared to CR, the  $^1\text{H}$ -NMR of MA-CR (Figure 4.25) is more complicated. Due to the methacryloyl group, the hydrogen atom labeled h and h' from the methyl group, g and g', e and e', f and f' are no longer identical. The peak at 1.85

due to the hydrogen atoms labeled j from the methyl group on methacryloyl group. The peaks at 5.20 and 5.48 are due the hydrogen atoms labeled i from the methylene group. The response at 4.63 is due to water in the sample solution.

The  $^1\text{H}$ -NMR spectra of DHPDS and MR-HPDS in  $\text{D}_2\text{O}$  are shown in Figure 4.26 and 4.27. The  $^1\text{H}$ -NMR spectrum of DHPDS is comprised of 2 singlets, 2 doublets. The two singlets are assigned to the hydrogen atoms labeled a and d. Due to the electronegativity of sulfonate groups, the hydrogen atom d on the DHPDS molecule near these groups are shifted downfield. The  $\text{H}_a$  atom is shifted furthest downfield to 8.88 ppm because of its proximity to two sulfonate groups. The two doublets are attributed to the hydrogen atoms labeled b and c. Compared to DHPDS, the  $^1\text{H}$ -NMR of MA-HPDS are much more complicated. Because of the low sample concentration, the peaks of hydrogen atoms from the pyrene are small. In addition, due to the methacryloyl group, hydrogen atoms labeled b and b', c and c' are no longer identical, resulting in a much more complicated spectrum. The peak at 1.71 is due to the hydrogen atoms labeled e from the methyl group on methacryloyl group. The peaks at 5.21 and 5.52 are attributed to the hydrogen atoms labeled f from the methylene group.

#### 4.3.2.3 FTIR spectra of PEG and CR-PEG hydrogels

FTIR spectra of dry PEG hydrogel and CR-PEG hydrogel are shown in Figure 4.28. The FTIR spectra of PEG and CR-PEG are almost identical because the CR:PEG ratio is really small in hydrogels (1:1300). However, the small absorption peaks of benzene and sulfonate groups from cresol red are visible at  $1582\text{ cm}^{-1}$  and  $1393\text{ cm}^{-1}$ , respectively.

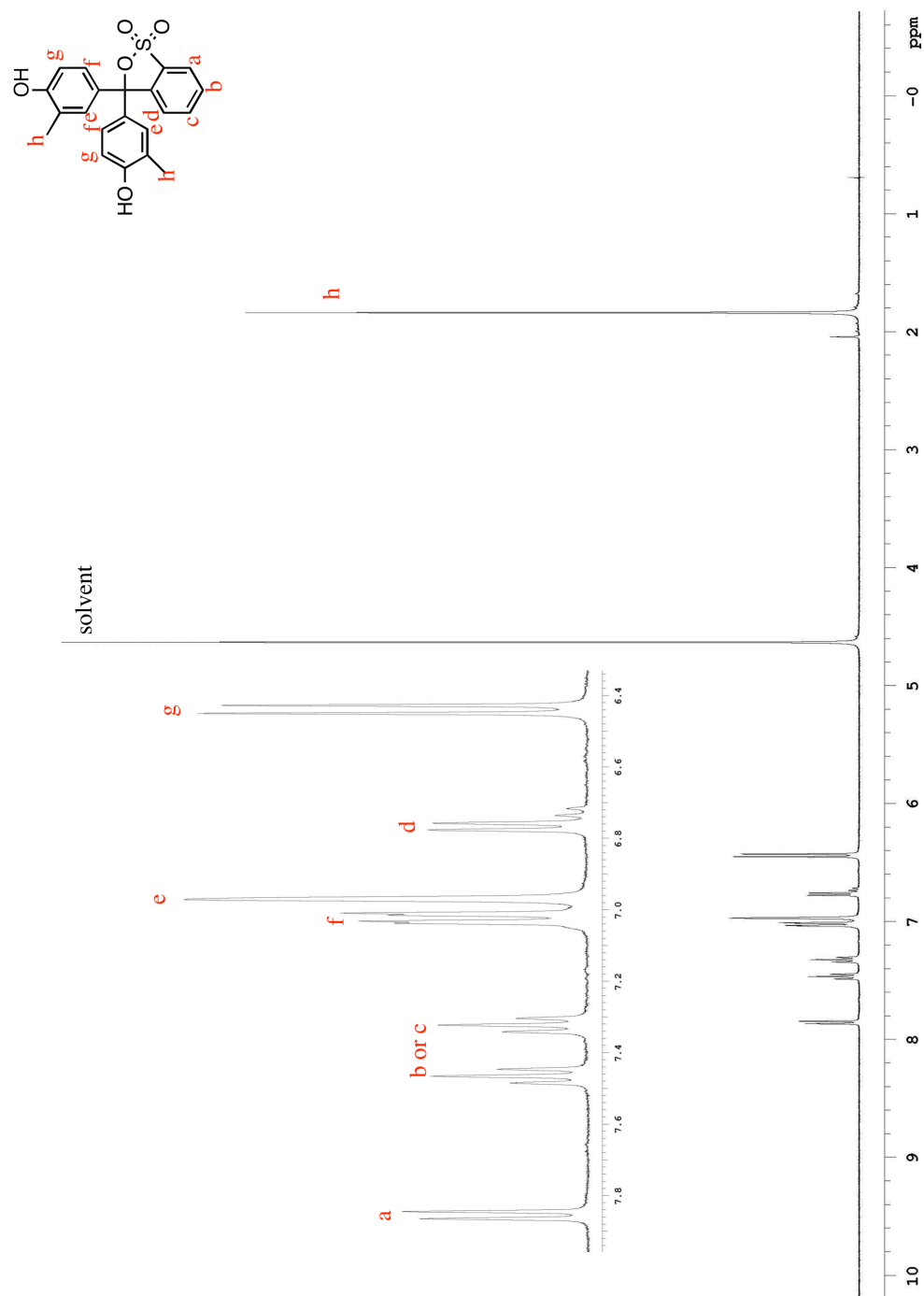


**Figure 4.24.**  $^1\text{H}$ -NMR spectra of CR in  $\text{D}_2\text{O}$ .



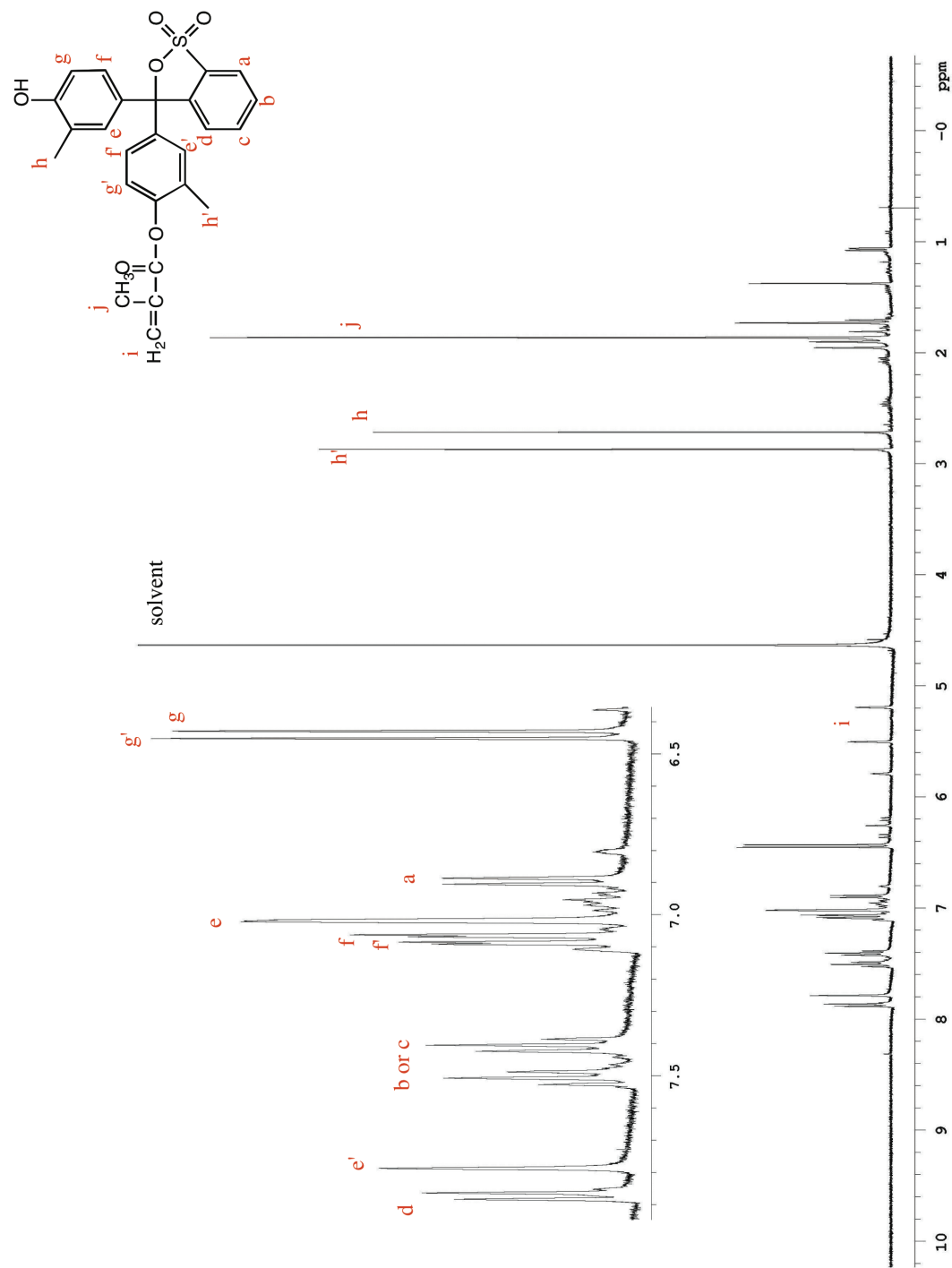


**Figure 4.25.** <sup>1</sup>H-NMR spectra of MA-CR in D<sub>2</sub>O.

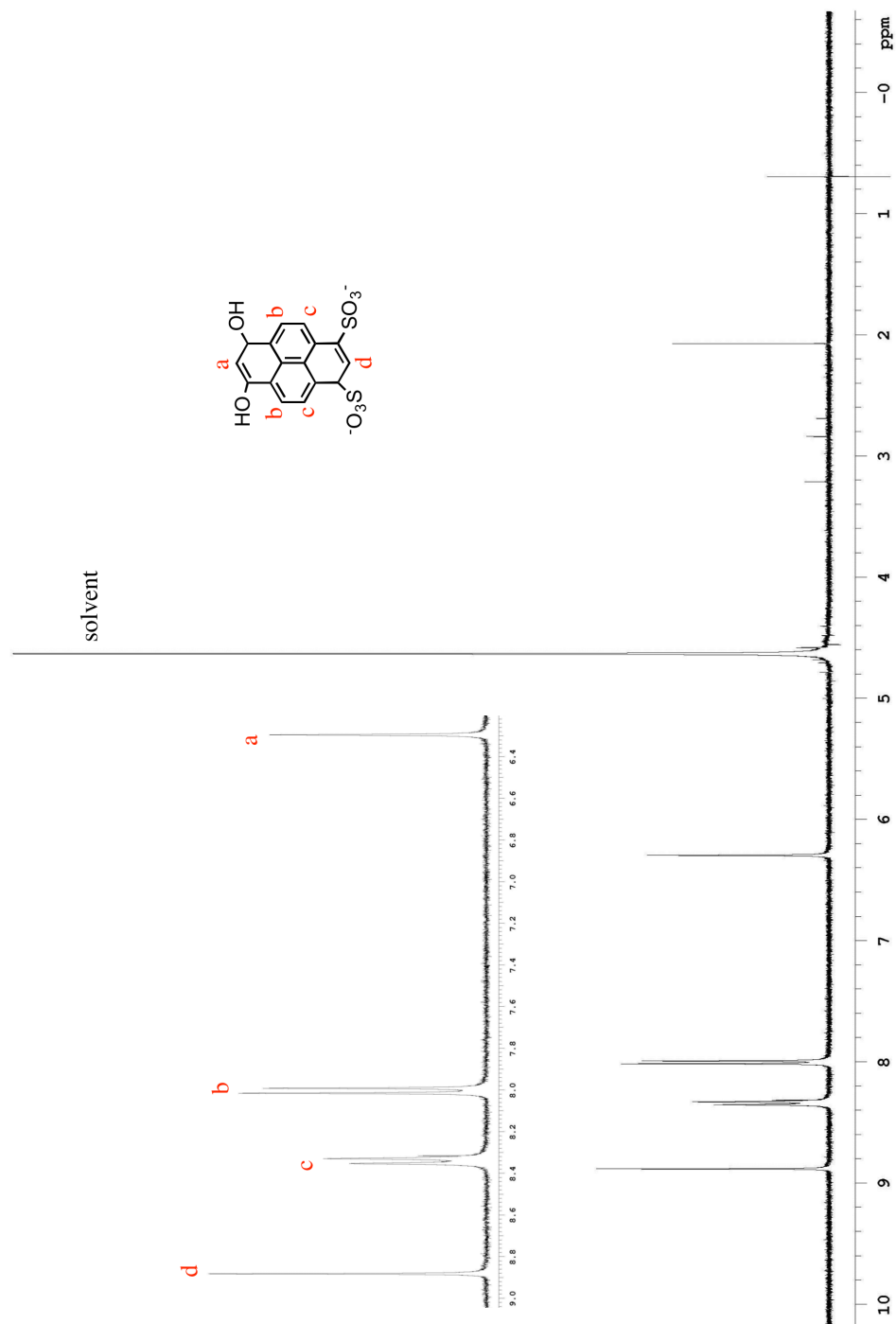
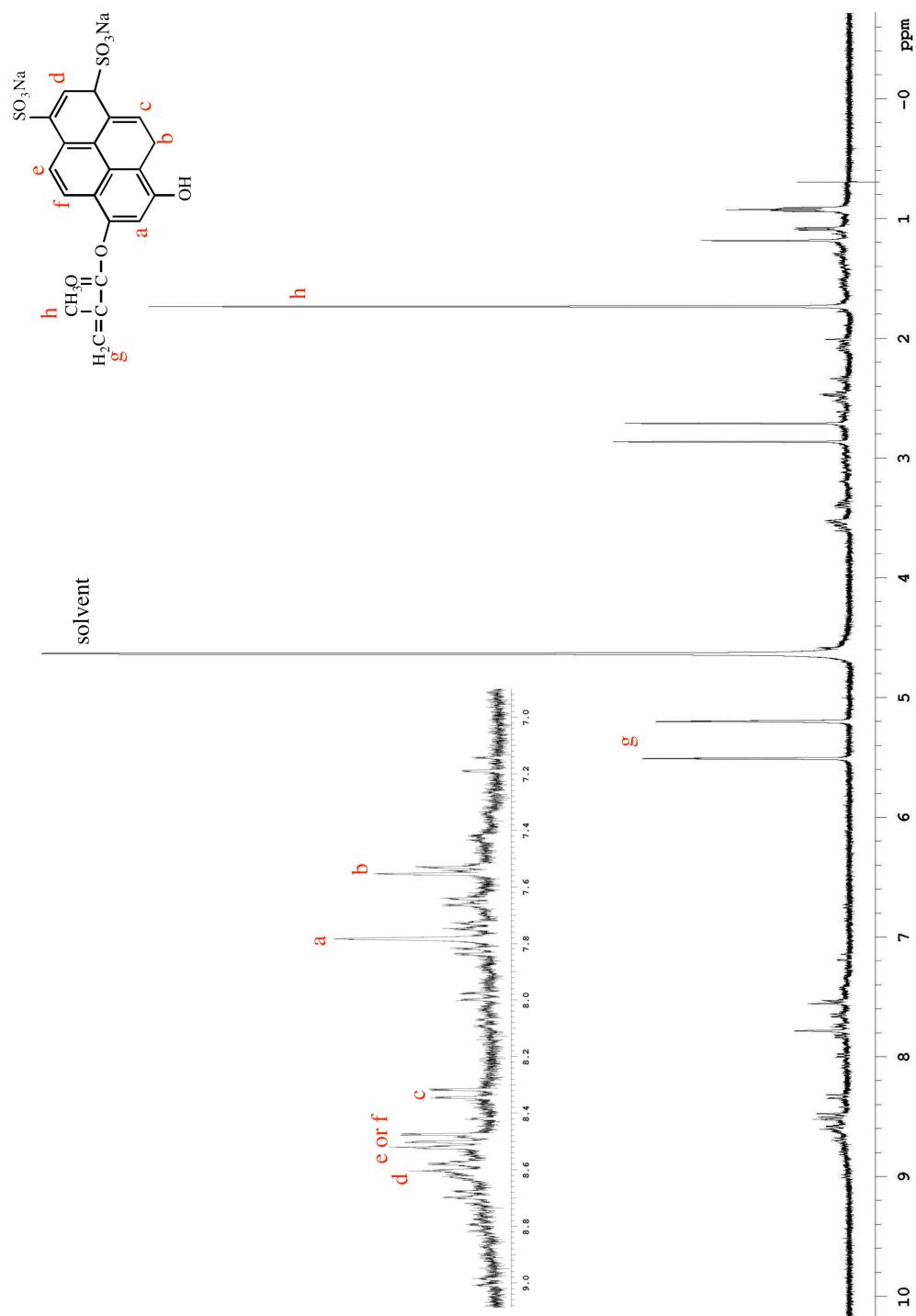
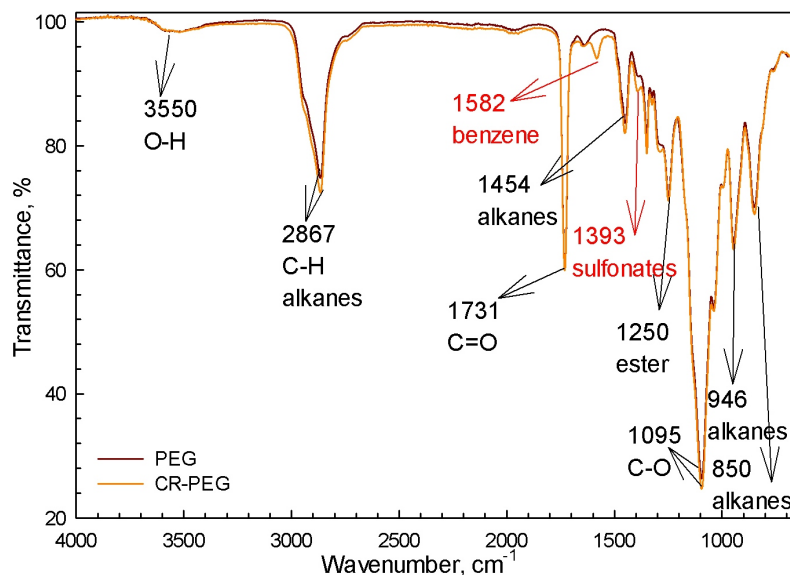


Figure 4.26.  $^1\text{H}$ -NMR spectra of DHPDS in  $\text{D}_2\text{O}$ .



**Figure 4.27.**  $^1\text{H}$ -NMR spectra of MA-HPDS in  $\text{D}_2\text{O}$ .



**Figure 4.28.** FTIR spectra of dried PEG and CR-PEG hydrogels.

### 4.3.3 Spectral behaviors of immobilized indicators in hydrogels

The spectral behavior of immobilized indicators in hydrogel is discussed in the following sections. Fluorescence spectra of all immobilized indicators except cresol red were recorded. For CR-PEG, which is non-fluorescent, the absorption spectra were recorded.

#### 4.3.3.1 FS-CTAB in hydrogel

The fluorescein-based indicator ion-pair FS-CTAB was immobilized in hydrogel through physical entrapment. After thorough washing until no further indicator leaching, the hydrogel with immobilized FS-CTAB is transparent and colorless, indicating that a very small amount of indicator was immobilized in the hydrogel. The fluorescence of FS-CTAB in hydrogel was easily detected and is shown in Figure 4.29. Compared to FS in solution

(Figure 2.14), the excitation peak for protonated FS is the same, at 467 nm. However, the excitation and emission peaks for deprotonated FS are each red shifted, from 490 nm to 510 nm and from 515 nm to 530 nm, respectively. This large red shift probably is because of the matrix effect, which was also observed in sol-gel films (Figure 3.10).

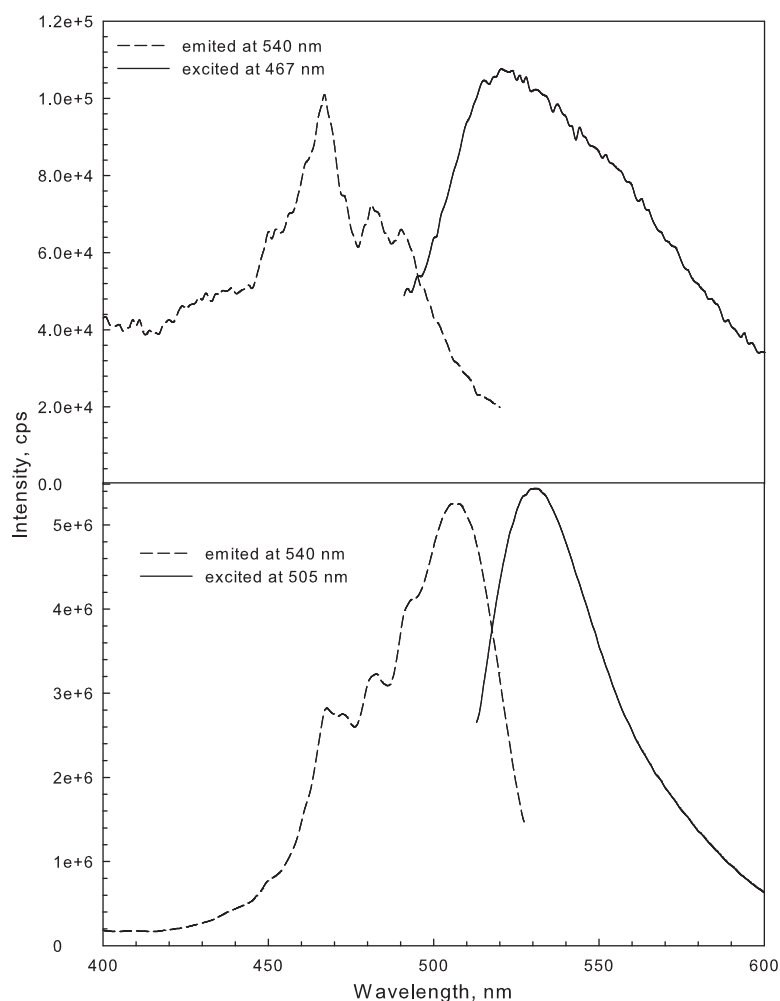


**Figure 4.29.** The fluorescence spectra of FS-CTAB in hydrogel in solution (IS = 0.100 M). Top: pH 4.36; Bottom: pH 9.03.

Immobilized FS in hydrogel retained its pH sensitivity. The normalized fluorescence excitation spectra of FS in hydrogel are shown in Figure 4.30, top. The  $pK_a^*$  value is 5.90,

slightly shifted to higher pH value compared to FS in solution ( $pK_a^*$ , 5.68) as shown in Figure 4.30, bottom. FS-CTAB in hydrogel has a pH sensitive range at pH 4.5-7.5 as shown in Figure 4.34.

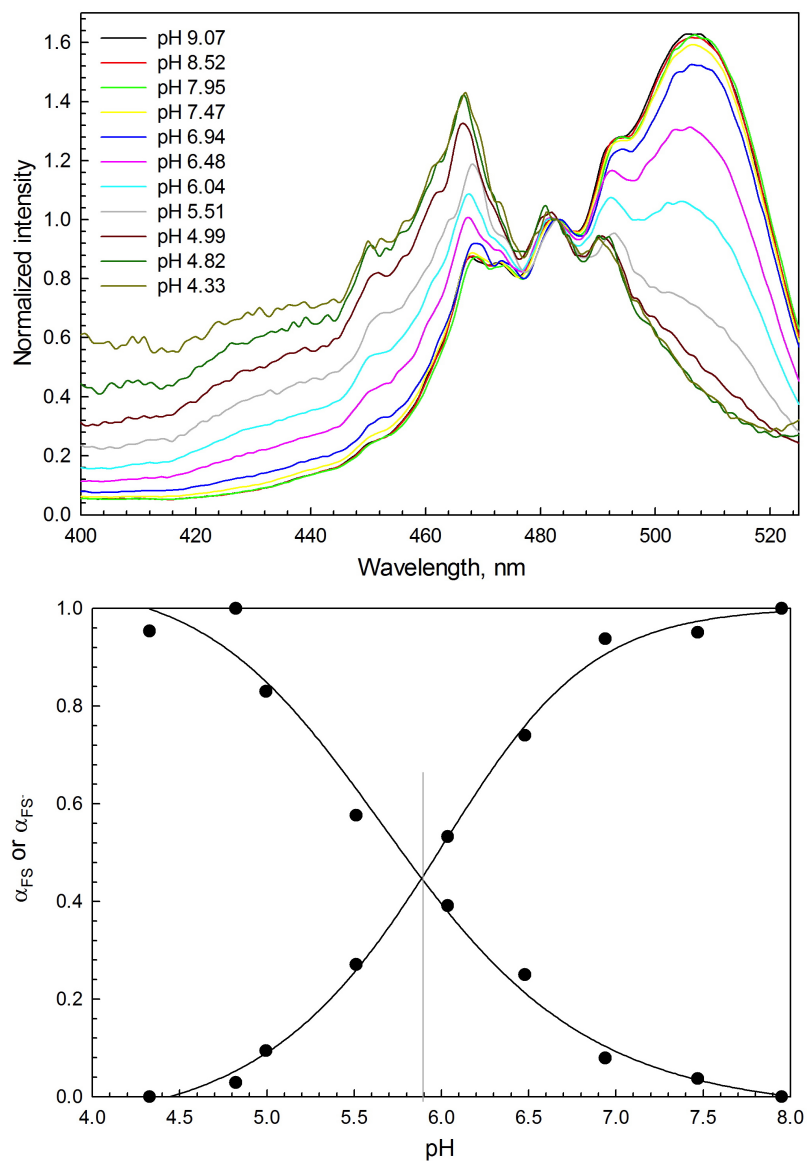


**Figure 4.30.** The normalized fluorescence excitation spectra of FS-CTAB in hydrogel with emission wavelength at 540 nm (top); and  $pK_a^*$  of FS-CTAB in hydrogel (bottom) (IS = 0.100 m).

#### 4.3.3.2 HPTS-CTAB in hydrogel

The ion-pair HPTS-CTAB was also physically trapped in PEG hydrogel matrix. Same as FS-CTAB immobilized in hydrogel, the HPTS-CTAB immobilized hydrogel was transparent and colorless as well because only small amount of indicator was immobilized.

The fluorescence excitation and emission spectra of HPTS-CTAB in hydrogel are shown in Figure 4.31. The excitation spectra of HPTS-CTAB in hydrogel are the same with HPTS in solution with excitation peaks at 402 nm and 467 nm, for protonated and deprotonated forms, respectively. However, the emission spectra is different from HPTS in buffer solution (Figure 3.4). HPTS in buffer solution only has one emission peak because the excited state  $pK_a^*$  is around 1.0, so the excited state HPTS\* disassociates to excited state  $PTS^{*-}$  rapidly and then emits light at 515 nm. In contrast, HPTS-CTAB in hydrogel, at pH 5.67, when excited at 400 nm, has two emission peaks, the emission peak from the excited state protonated form, HPTS\* and the excited deprotonated form,  $PTS^{*-}$ , at 425 nm and 510 nm, respectively. There could be several explanations for the unexpected appearance of the 425 nm peak.

The appearance of the emission from the excited state protonated form HPTS\* was also observed in HPTS-CTAB in sol-gel films, and explained as an effect of hydrogen bonding. That is because of the hydrophobicity of the sol-gel films, the fewer water molecules surround HPTS compared to in solution. The lack of hydrogen bonding makes the excited state of deprotonated  $PTS^{*-}$  less stable than in solution, which leads to the strong recombination of the hydrogen ions and  $PTS^{*-}$  (Chapter 3). This explanation is not valid in the hydrogel system, because hydrogel matrix is extremely hydrophilic. The 9.8% PEG hydrogel contains 92% of water in its swollen state (calculated from its swelling ratio).

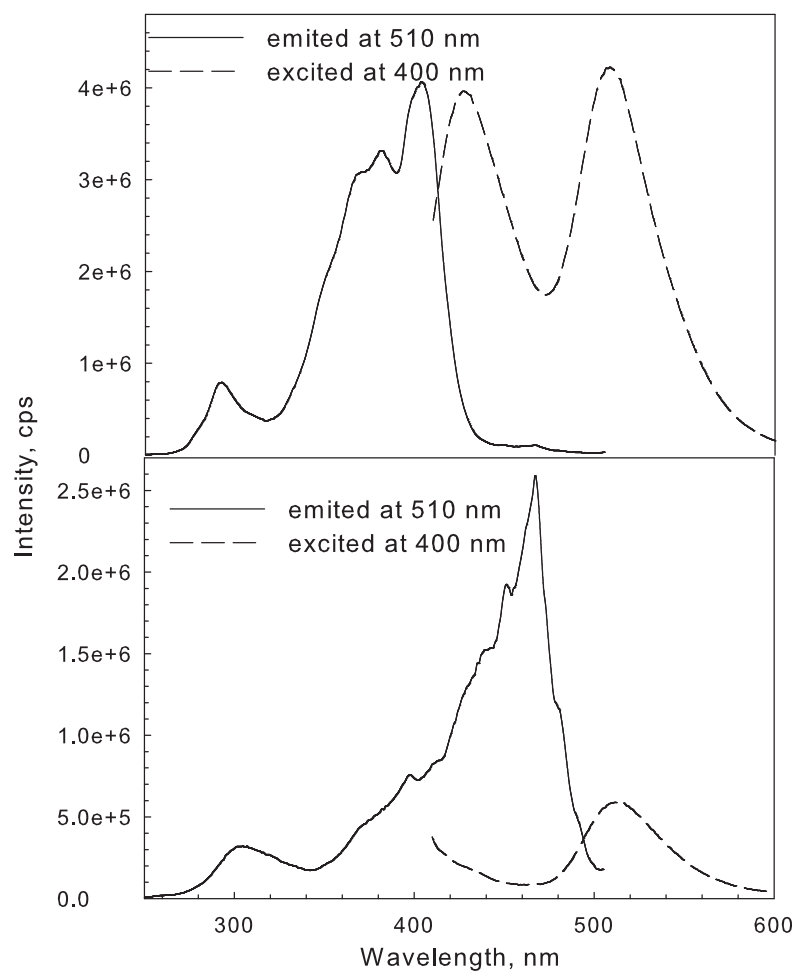


**Figure 4.31.** Fluorescence excitation and emission spectra of HPTS-CTAB in hydrogel in solution (IS = 0.100 M): pH 5.67 (top) and pH 9.82 (bottom).

One of the possibilities for the appearance of emission from the excited state of the protonated form HPTS is that during the polymerization reaction, the free radical might react with -OH group on the pyrene ring, converting it to an -OR group. The -OR species has no acidic group and would have the same fluorescence behavior as the protonated form of HPTS, as observed in ethanol.

To confirm this hypothesis of hydroxyl group reaction with the free radical initiators



during the polymerization, two solutions with and without free radical initiator AIBN were compared. Poly(methyl methacrylate)(PMMA) was used as the precursor instead of PEGDA, because after the polymerization reaction, PMMA can be separated with the solution from precipitation in a ice bath. The rest of the procedures were the same, both were degassed with nitrogen and both were reacted at 70 °C for 6 hours. As shown in Figure 4.32, the one without AIBN, at both acidic and basic solutions, only has one emission peak at 510 nm. On the other hand, the one with AIBN, at both acidic and basic conditions, has two emission peaks at 425 nm and 510 nm. This confirms that some amount of HPTS was permanently converted to a non-acidic, but still fluorescent form by the free radicals with some remaining acidic fraction still available to sense the media pH.

This unexpected emission peak did not interfere with the pH sensing, because instead of the emission spectra, the excitation spectra was used for pH sensing.

The normalized fluorescence excitation spectra of HPTS-CTAB in hydrogel were recorded in Figure 4.33, top; The  $pK_a$  of HPTS-CTAB in hydrogel was calculated, 8.06 as shown in Figure 4.33, bottom, which is larger than HPTS in solution, 7.35 (Figure 3.14). HPTS-CTAB in hydrogel has a pH sensitive range at pH 7.0 - 10.0 (Figure 4.34).

#### 4.3.3.3 HPDS-PEG hydrogel

After the reaction of DHPDS with methacrylic anhydride, one of the hydroxy groups on pyrene was substituted by a methacryloyl group and formed MA-HPDS. MA-HPDS only has one hydroxy group which can dissociate in aqueous solution. Therefore, the fluorescence spectra of MA-HPDS were expected to be similar with HPTS.

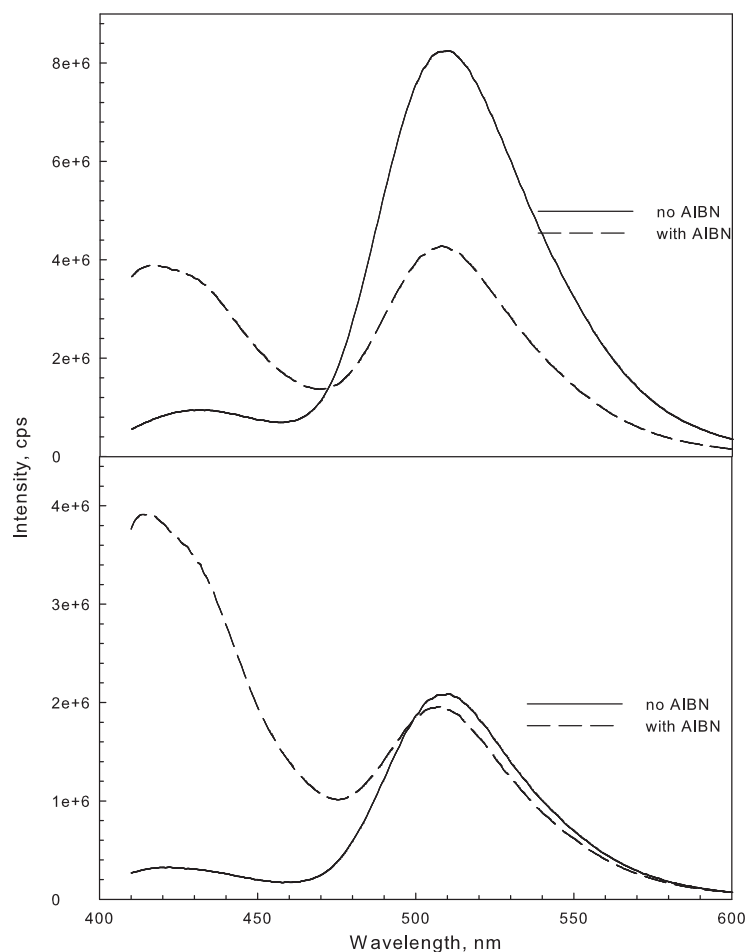


**Figure 4.32.** Fluorescence emission spectra of precursor solution of HPTS-CTAB with or without free radical initiator, AIBN. The excitation wavelength was 400 nm. Top: pH 3.5; Bottom: pH 9.5.

MA-HPDS was covalently bound in PEG hydrogel to form HPDS-PEG hydrogel, which is transparent and colorless. Unlike the physically entrapped FS-CTAB and HPTS-CTAB, little leaching of color into the solution was observed during the first rinse after reaction because of the covalent binding of the indicator into hydrogel matrix. The absorption spectra can not be measured due to the low concentration of the indicator. However, fluorescence spectra can be measured because of its high quantum yield (Figure 4.35).

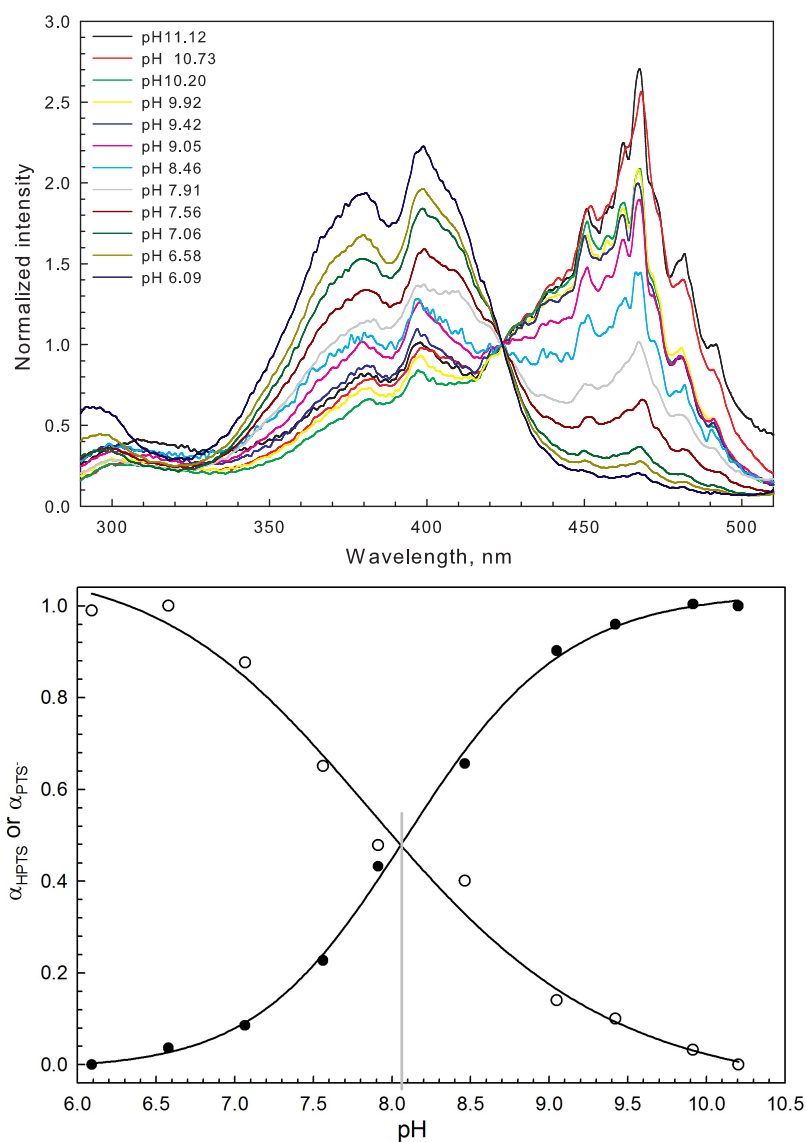


**Figure 4.33.** The normalized fluorescence excitation spectra of HPTS-CTAB in hydrogel with emission wavelength at 520 nm (top); and  $\text{pK}_a$  of HPTS-CTAB in hydrogel (bottom) ( $\text{IS} = 0.100 \text{ M}$ ).

The spectra of HPDS-PEG are similar to HPTS in solution (Figure 3.4) and do not resemble the precursor DHPDS (Figure 4.5). At low pH, 7.01, the main excitation peak is at 400 nm with a shoulder peak at 380 nm, which corresponds to the absorption peak

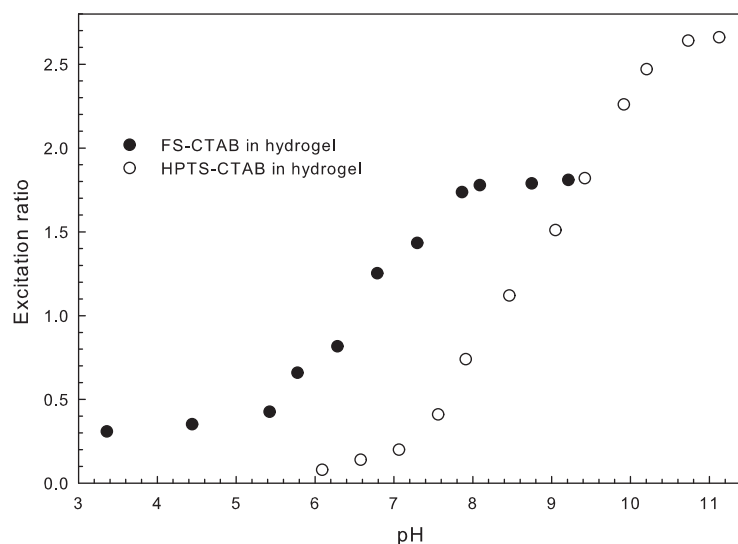


**Figure 4.34.** pH sensitive range of FS-CTAB and HPTS-CTAB in hydrogel (IS = 0.100 M).

of the protonated form. At high pH, 10.71, the main excitation peak is at 467 nm, which corresponds to the absorption peak of the deprotonated form. This confirmed that after the substitution reaction, the fluorophore only has one hydroxyl group remains, and it still responds to the pH change. Similar to HPTS in solution, the fluorescence excitation spectrum of HPTS-PEG hydrogel varies with pH and only one emission peak at 510 nm is observed.

The normalized fluorescence excitation spectra of HPDS-PEG hydrogel are shown in Figure 4.36, top. The  $pK_a$  of HPDS-PEG hydrogel is calculated to be 8.80, as shown in Figure 4.36, bottom. The pH sensitive range of HPDS-PEG hydrogel is pH 8.0 - 10.5 as shown in Figure 4.37.

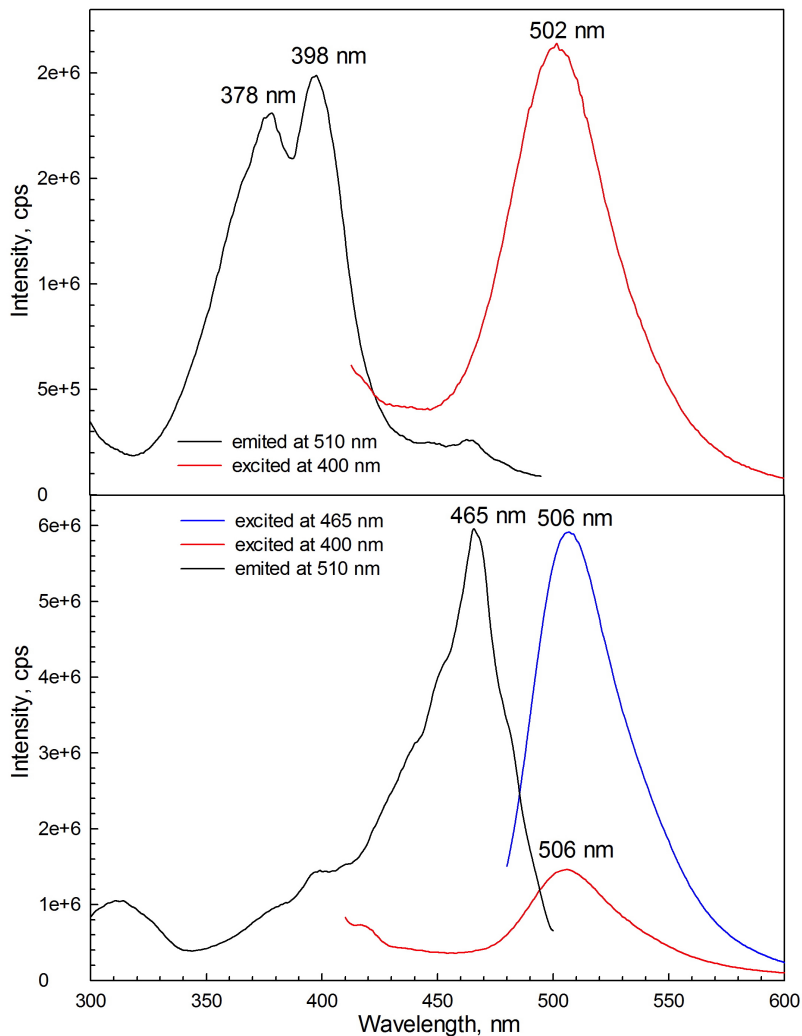


**Figure 4.35.** Fluorescence excitation and emission spectra of HPDS-PEG hydrogel in solution (IS = 0.100 M): pH 7.01 (top) and pH 10.71 (bottom).

#### 4.3.3.4 HNDS-PEG hydrogel

After the reaction of naphthalene derivative, DHNDS with methacrylic anhydride, one of the hydroxy group on the naphthalene was substituted by a methacryloyl group, by which the covalent binding of this indicator into the hydrogel was ensured. The HNDS-PEG hydrogel was transparent and colorless.

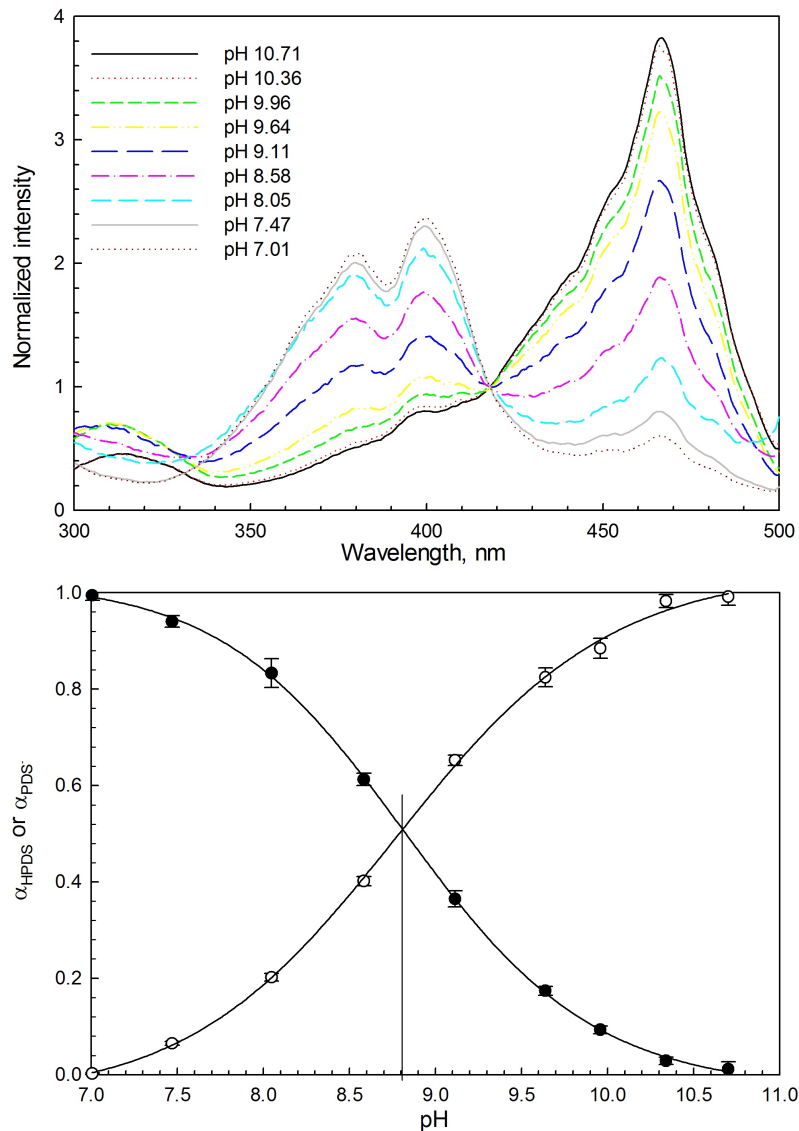


**Figure 4.36.** Normalized fluorescence excitation spectra of HPDS-PEG hydrogel (IS = 0.100 M) with emission wavelength at 520 nm (top) and  $pK_a$  value of HPDS-PEG hydrogel (bottom) (IS = 0.100 M).

The fluorescence spectra of HNDS-PEG hydrogel in buffer solution (0.100 M) were recorded and are shown in Figure 4.38. At pH 12.15, the emission peak of HNDS-PEG hydrogel is at 455 nm, the excitation peaks are at 314 nm and 370 nm. At pH 7.44, the emission peak of HNDS-PEG hydrogel is also at 455 nm and the excitation peaks at 290

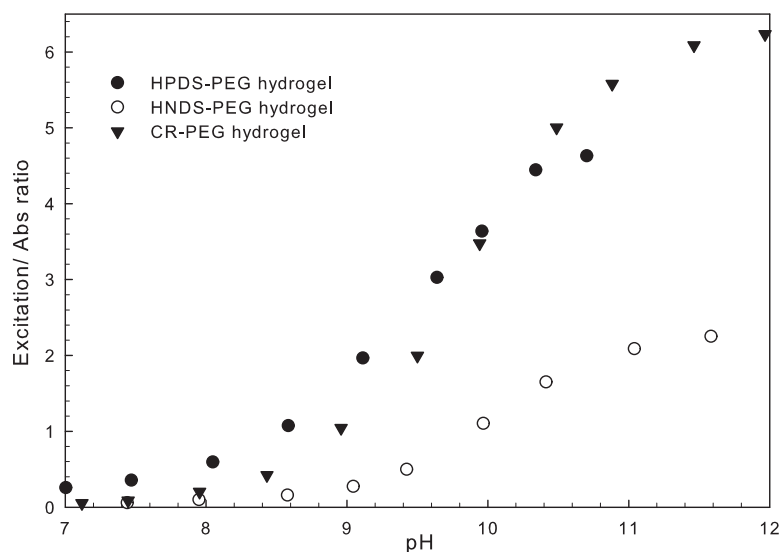


**Figure 4.37.** pH sensitive range of HPDS-PEG, HNDS-PEG and CR-PEG hydrogels (IS = 0.100 M).

nm and 340 nm, with much lower intensity. The excitation spectra of HNDS-PEG are more similar to HNDS in buffer solution than DHNDS, because after conversion, MA-HNDS contains only one hydroxyl group.

The normalized fluorescence excitation spectra of HNDS-PEG hydrogel in buffer are shown in Figure 4.39, top, very similar to HNDS in buffer solution (Figure 4.12). The  $pK_a$  value for HNDS-PEG hydrogel is 9.50 (Figure 4.39, bottom), shifted to higher pH value compared to HNDS in solution (8.92). The pH sensitive range of HNDS-PEG hydrogel is pH 8.5 - 11.5 as shown in Figure 4.37.

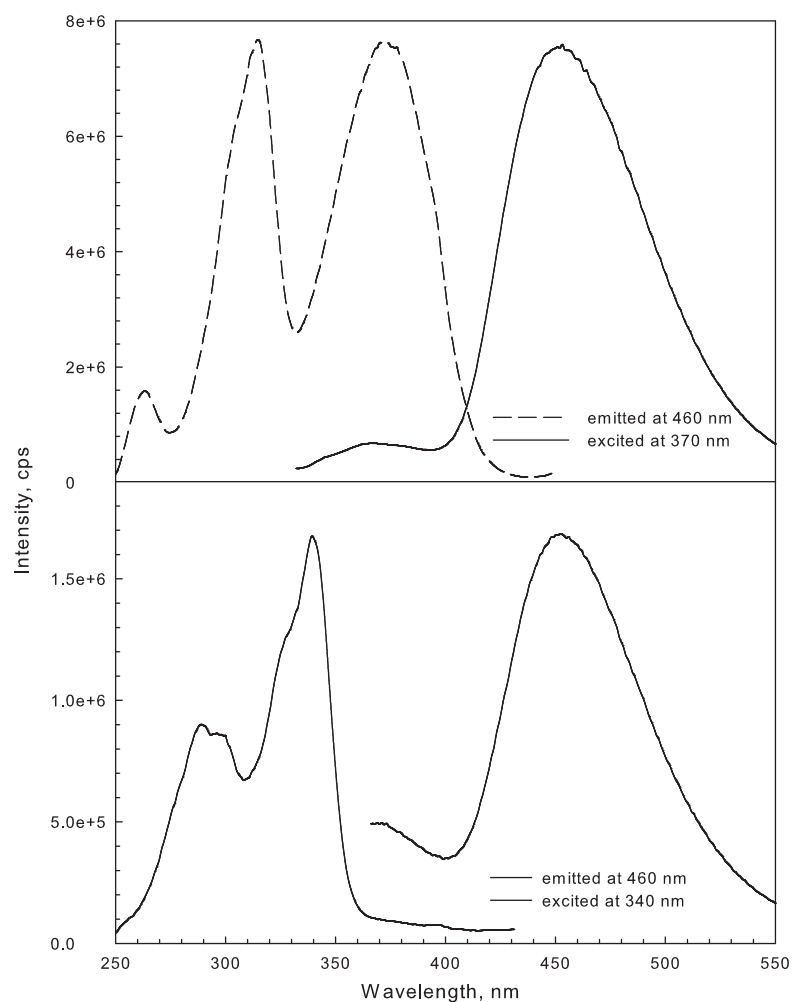


**Figure 4.38.** Fluorescence spectra of HNDS-PEG hydrogel in solution (IS = 0.100 M). Top: pH 12.15; Bottom: pH 7.44.

#### 4.3.3.5 CR-PEG hydrogel

The UV-Vis absorption spectra of CR-PEG hydrogel were recorded (UV-Vis absorption spectra of PEG hydrogel were subtracted) and are shown in Figure 4.40, top. In acidic and neutral media, the maximum absorption peak of protonated CR-PEG hydrogel is located at 420 nm, blue shifted by about 10 nm compared to CR in solution (430 nm). In more



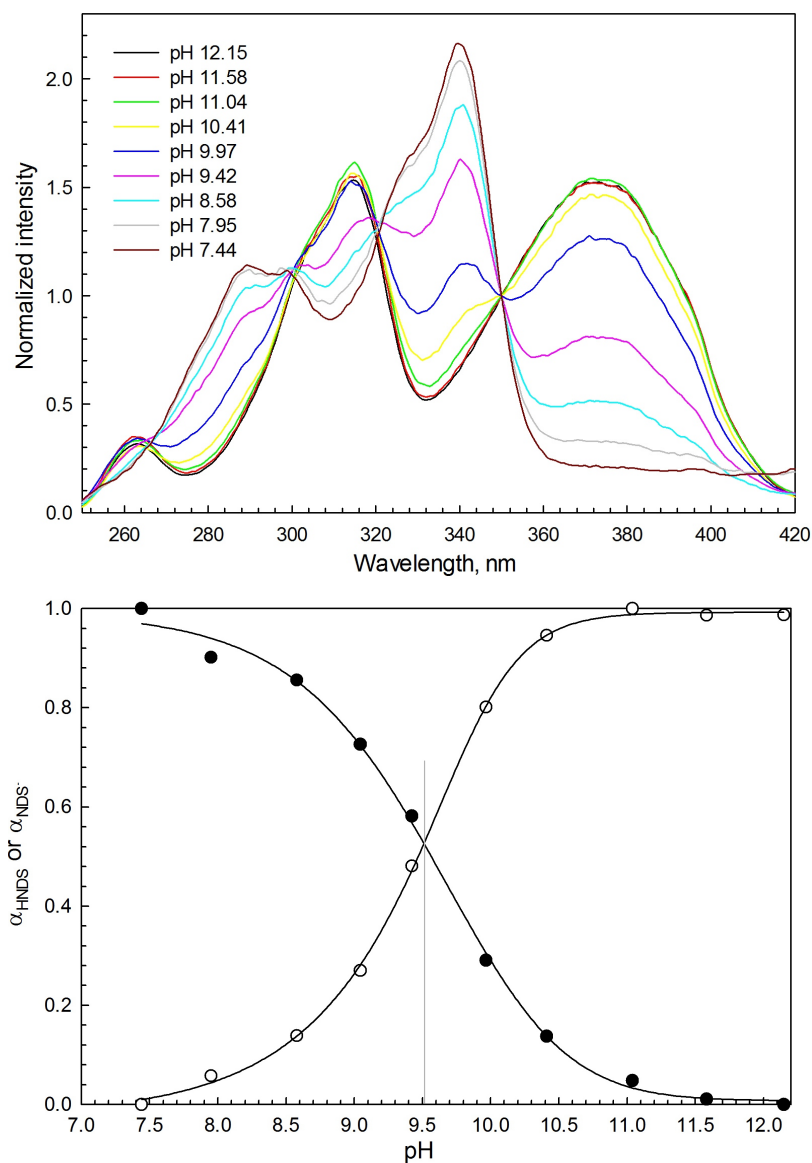


**Figure 4.39.** The normalized fluorescence excitation spectra of HNDS-PEG hydrogel (top) (IS = 0.100 M); and the  $pK_a$  values of HNDS-PEG hydrogel (bottom) (IS = 0.100 M).

basic media, cresol red in hydrogel matrix was deprotonated. The absorption peak for the deprotonated form occurs at 580 nm, red shifted by 5 nm comparing with cresol red in buffer solution (575 nm). The  $pK_a$  value of CR-PEG is calculated using the same method as for cresol red in buffer solution, giving 9.36, as shown in Figure 4.40, bottom. The  $pK_a$

value of CR in hydrogel is shifted to high pH range as compared in CR in solution (8.23).

The pH sensitive range for CR-PEG hydrogel is pH 8.0 -11.0 as shown in Figure 4.37.

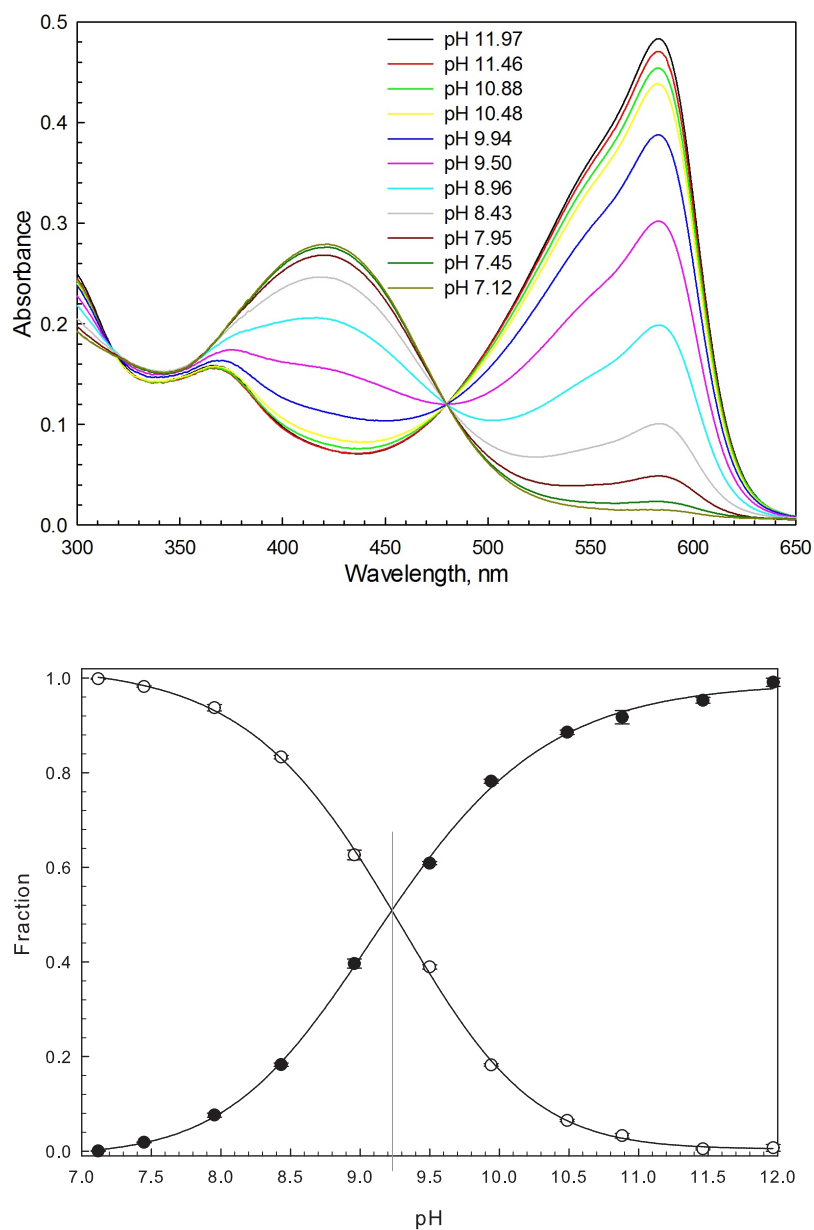


**Figure 4.40.** UV-Vis absorption spectra of CR-PEG in buffer (top) (IS = 0.100 M) and the  $pK_a$  value of CR-PEG hydrogel (bottom) (IS = 0.100 M).

#### 4.3.4 $pK_a$ shift of immobilized indicators in hydrogel

A  $pK_a$  shift to more basic values in hydrogel compared to in solution was observed. A summary of the  $pK_a$  values of indicators in both buffer solution and hydrogels is listed in Table 4.3.

**Table 4.3**  
A list of  $pK_a$  values of indicators in solution and hydrogels.

Indicators	solution (IS = 0.030 M)	hydrogels (IS = 0.100 M)	$\Delta pK_a$
FS	5.68	5.90	0.22
HPTS	7.35	8.06	0.71
DHPDS	7.03, 9.14	8.80	1.45*
DHNDS	8.70	9.50	0.58*
HNDS	8.92	\	\
CR	8.23	9.36	1.13

$\Delta$  values with \* are compared to HPTS and HNDS in solution for indicators DHPDS and DHNDS, respectively, because after copolymerization in hydrogel matrix, there are only one hydroxyl group available for dissociation.

As discussed in Chapter 2 and Chapter 3, the  $pK_a$  shift of indicators immobilized in porous silica matrix results from the free silanol groups (Si-OH) on the internal surface; Those silanol groups can be protonated and deprotonated in solution, acting as additional buffers. However, this explanation is not valid in hydrogel matrix, because the PEG hydrogels are uncharged hydrophilic polymers. This is confirmed from the structure of PEGDA and also the unchanged swelling ratio of hydrogel in different pH solutions. This  $pK_a$  shift to high values can be explained by the medium effect, as the activity of a species differs profoundly from the molarity when the composition of the solvent is altered by addition of an organic constituent to aqueous medium [150]. Adding nonelectrolytes such as alcohol to aqueous solution changes the dielectric constant of the solvent, which affects the dissociation constant of the weak acid in that solvent.

The simple Born treatment is often useful in predicting solvent effects on proton transfer reactions in a qualitative way. The general acidic dissociation reaction in the solvent  $S$  is formulated



The ratio of the values of  $K_{HA}$  in the two solvents can be expressed in the following equation [150]:

$$\Delta pK_a = {}_s pK_a - {}_w pK_a = 122 \left( \frac{1}{r_{SH^+}} + \frac{z_A^2}{r_A} - \frac{z_{HA}^2}{r_{HA}} \right) \left( \frac{1}{\epsilon_s} - \frac{1}{\epsilon_w} \right) \quad (4.10)$$

where  ${}_s pK_a$  and  ${}_w pK_a$  refers to the apparent  $pK_a$  values of a indicator in solvent  $S$  and water;  $r$  is the radii of the ions, and  $z$  is the charge on the ions.  $\epsilon_w$  is the dielectric constant of water, which is 81 [150];  $\epsilon_s$  is the dielectric constant of the solvent  $S$ . As in the swollen state of hydrogel, for 9.8% PEG hydrogel, it has up to 92% water content, and thus 8% of PEG. The dielectric constant of PEG-water mixture has been studied, and for a mixture with 90% of water and 10% of PEG (MW = 600), the dielectric constant is 74 [151]. Although our hydrogel matrix was not exactly an mixture of PEG and water and slightly different ratio of these two components, the dielectric constant should be very similar with this value. With estimation of the radii of the ions from simple bond length calculation, the  $pK_a$  shift of different indicators in hydrogel can be estimated, in the range of 0.3 - 0.5 pH units, which is slightly smaller than the shifts we observed.

As for physically entrapped indicators, their  $pK_a$  shifts in hydrogel is smaller compared to covalently bound indicators.  $\Delta pK_a$  of physically entrapped FS and HPTS are about 0.2

and 0.7, respectively.  $\Delta pK_a$  of covalently bound indicators HPDS, HNDS and CR are 1.4, 0.4 and 1.1, respectively. The smaller  $pK_a$  shifts of physically entrapped indicators might be a result of the positively charged ammonium ions on the ion-pair reagent, CTAB, which has an effect of lowering the indicator  $pK_a$  values [123].

#### 4.3.5 Fluorescence lifetime measurements

The fluorescence lifetimes of fluorescent dyes FS, HPTS, DHPDS, DHNDS, HNDS in both solution and PEG hydrogel were measured and are listed in Table 4.4.

**Table 4.4**  
Fluorescence lifetimes of fluorescent dyes in solution and PEG hydrogels.

Name	$\lambda_{ex}$ , nm	$\lambda_{em}$ , nm	Lifetime, ns	$\chi^2$	condition
FS	490	520	$4.2 \pm 0.1$	1.054	pH 6.65
FS-CTAB in hydrogel	500	530	$3.9 \pm 0.1$	1.056	pH 9.08
HPTS	415	510	$5.4 \pm 0.1$	1.026	pH 4.13
HPTS	470	510	$5.5 \pm 0.1$	0.9928	pH 7.01
HPTS-CTAB in hydrogel	470	510	$5.5 \pm 0.1$	1.000	pH 10.4
HPDS-PEG	400	504	$4.7 \pm 0.1$	0.975	0.1 M HCl
HPDS-PEG	470	504	$4.6 \pm 0.1$	1.006	0.1 M NaOH
DHNDS	366	460	$16.6 \pm 0.2$	0.9843	pH 9.40
HNDS	366	457	$16.9 \pm 0.2$	1.018	pH 9.40
HNDS-PEG	366	460	$11.7 \pm 0.1$	1.040	pH 8.9

Fluorescent indicator ion-pairs, FS-CTAB and HPTS-CTAB were physically entrapped in hydrogel matrix, their fluorescence lifetimes in hydrogel remained unchanged compared to in buffer solution. As for FS, the lifetimes for excited state deprotonated form was around 4.0 ns. For excited state deprotonated HPTS, the lifetime was around 5.4 ns in both hydrogel and buffer solution. The fluorescence decay curves and fitting for FS and HPTS in solution and hydrogel are shown in Figure 4.41, (top) and (bottom), respectively.

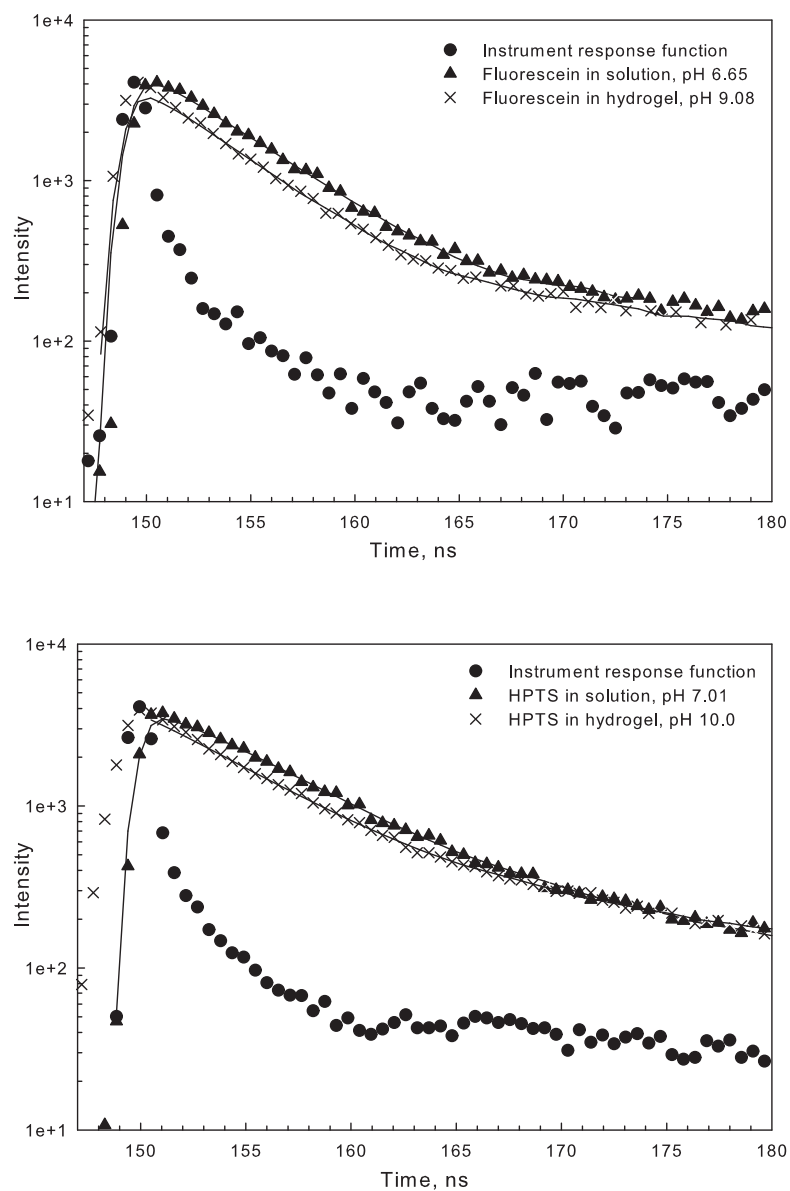


**Figure 4.41.** Fluorescence decay curves for fluorescent indicators physically entrapped in hydrogel. The solid lines represent the best fits to the data. (top): FS, with  $\lambda_{ex} = 467$  nm for solution and hydrogel and  $\lambda_{em} = 515$  nm for solution, and  $\lambda_{em} = 530$  nm for hydrogel; (bottom): HPTS, with  $\lambda_{ex} = 470$  nm and  $\lambda_{em} = 510$  nm for solution and hydrogel.

For fluorescent indicator methacryloyl analogs, MA-HPDS and MA-HNDS, which were covalently bound in hydrogel, their fluorescence lifetimes in hydrogel decreased com-

pared to the same indicators in solution as shown in Figure 4.42, (top) and (bottom), respectively. For HPTS and HPDS-PEG hydrogel, the fluorescence lifetimes of excited state deprotonated form were 5.4 ns and 4.6 ns, respectively. For DHNDS and HNDS-PEG hydrogel, the fluorescence lifetimes of excited state deprotonated form were 16.9 ns and 11.7 ns, respectively.

#### **4.3.6 Sensor performance**

##### *4.3.6.1 Potential use of CR-PEG hydrogel as reusable "pH paper"*

CR-PEG hydrogel changed color from yellow to purple when the pH of the buffer solution changed from 8.5 to 10.5 as shown in Figure 4.43. In addition, because of the covalent binding of cresol red in hydrogel matrix, no cresol red leaching to the solution was found. The color change is reproducible. For this reason, the CR-PEG hydrogel can be used as reusable pH "paper" with a detection range of pH 8.5 - 10.5.

##### *4.3.6.2 Equilibrium time*

The hydrogel samples is super-porous hydrogel with interconnected open cell structure ( $>1\ \mu\text{m}$ ). The driving force for ionic exchange is the concentration difference inside and outside of the hydrogel. The equilibrium time of the dye in hydrogel against the solution pH change is highly depended on the size of the hydrogel samples. Smaller size results in shorter equilibrium time. The dimensions of the CR-PEG hydrogel we tested were around  $1\text{ cm} \times 2\text{ cm} \times 1\text{ mm}$ . The equilibrium time for indicators immobilized in hydrogels was

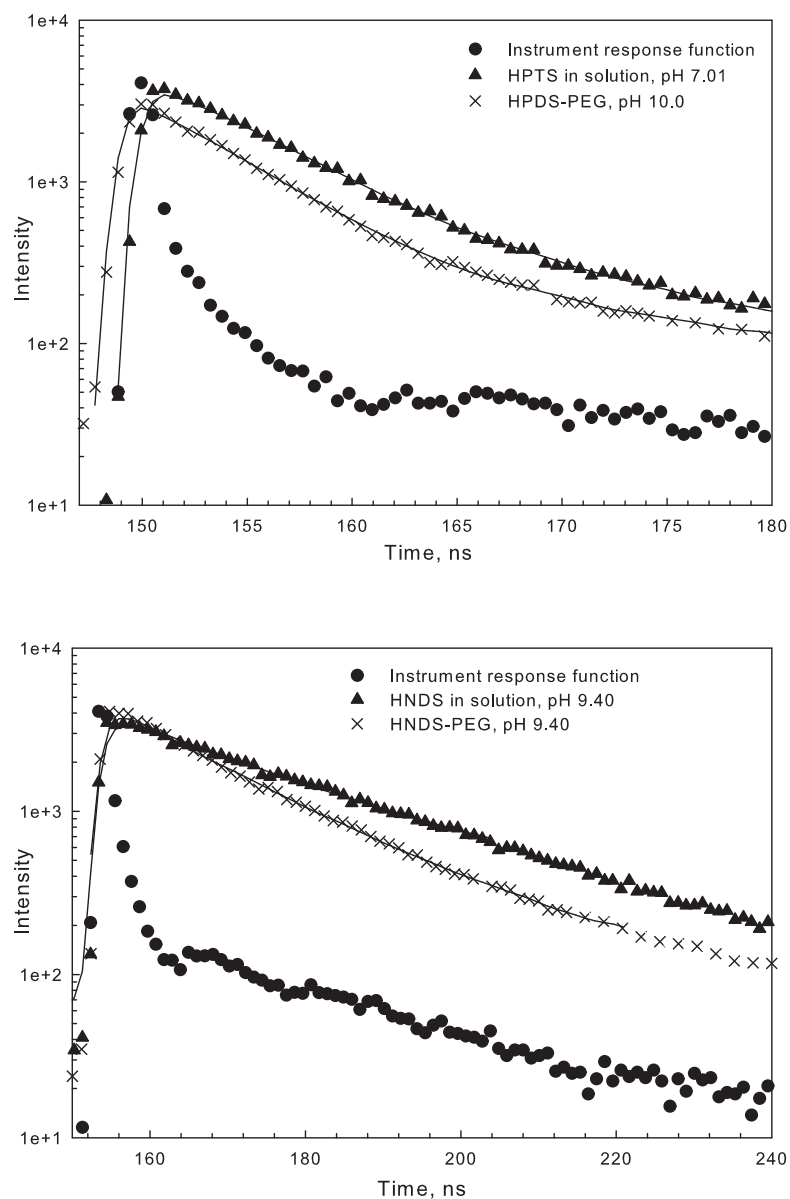


**Figure 4.42.** Fluorescence decay curves for fluorescent indicators bound in hydrogel. The solid lines represent the best fits to the data. (top): HPTS and HPDS-PEG, with  $\lambda_{ex} = 470$  nm and  $\lambda_{em} = 510$  nm for solution and HPDS-PEG hydrogel; (bottom): DHNDS and HNDS-PEG, with  $\lambda_{ex} = 366$  nm and  $\lambda_{em} = 460$  nm for solution and HNDS-PEG hydrogel.

evaluated. Figure 4.44 shows that the equilibrium time for CR-PEG hydrogel upon solution pH changes is about 2 minutes with slightly stirring. Without stirring, the equilibrium time



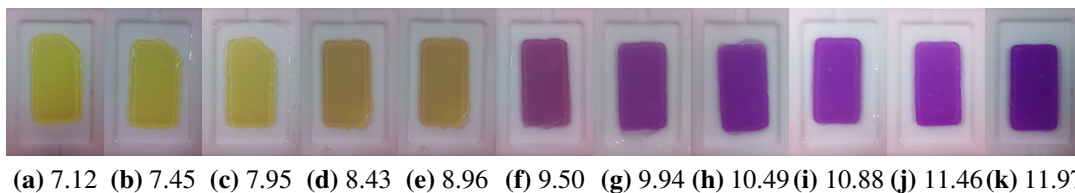


**Figure 4.43.** The Color change of CR-PEG in different pH buffer solution. The bottom line are the pH of the buffer solution.

would be much longer. We did not observe a difference in equilibrium time of increasing media pH or decreasing media pH. The similar result for HPDS-PEG hydrogel was obtained with equilibrium time of about 4 minutes as shown in Figure A.11; the difference is a result of bigger sample size.

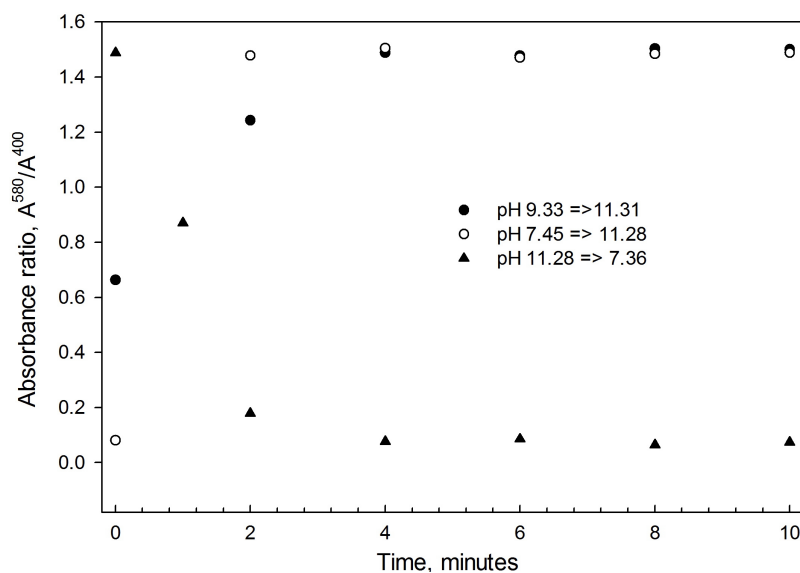


**Figure 4.44.** The equilibrium time of CR-PEG upon media pH change.

#### 4.3.6.3 Long term stability

All immobilized indicators in hydrogel remained pH sensitivity for at least 6 months, except HNDS-PEG. Due to the indicator instability, HNDS-PEG hydrogel is not very stable. After 6 months, HNDS-PEG hydrogels become nonfluorescent.

## 4.4 Conclusion

PEGDA was used as precursor/crosslinker in hydrogel synthesis. Both free radical initiator and redox initiation system were used for PEG hydrogel synthesis. The structural properties of PEG hydrogel were studied. The swelling ratio of the hydrogel was reciprocally proportional to the percentage of precursor percentages as the other parameters were unchanged. For hydrogel formed with 9.8% precursor percentage, which is used for indicator immobilization, the swelling ratio is 11.8 (as 92% water content). The average molecular weight between adjacent crosslinks ( $\bar{M}_c$ ) and the network mesh size ( $\xi$ ) for PEG hydrogel decrease with increasing of precursor percentages. As for 9.8% PEG hydrogel,  $\bar{M}_c$  and  $\xi$  are 293 g/mol and 2.6 nm, respectively.

Indicators were immobilized in hydrogel both physically and chemically. FS and HPTS were ion-paired with a common ion-pair reagent, CTAB, and then physically entrapped into hydrogel matrix. DHPDS, DHNDS and CR were reacted with methacrylic anhydride and methacryloyl groups were successfully covalently attached to the indicator compounds. The indicators were then covalently bound into the hydrogel matrix through copolymerization reaction. These indicator retained their pH sensitivity in hydrogel.

A  $pK_a$  shift to higher pH range in hydrogel compared to in solution was observed. As listed in Table 4.4. The  $pK_a$  values for FS in solution and hydrogel were 5.68 and 5.90a, respectively. For HPTS, the  $pK_a$  values in solution and hydrogel were 7.35 and 8.06, respectively. The  $pK_a$  value of HPDS-PEG was compared with HPTS in solution, because for HPDS-PEG, only one hydroxy group was available for photon dissociation, which is more similar to HPTS than DHPDS. For HPDS-PEG, the  $pK_a$  in hydrogel was 8.8, much larger than HPTS in solution, 7.35. For HNDS-PEG, also, only one hydroxy group available for dissociation, the  $pK_a$  value in hydrogel is 9.5, which is larger than HNDS in solution, 9.16. The calculated  $pK_a$  of CR in solution and CR-PEG were 8.23 and 9.36, respectively. This  $pK_a$  shift to higher pH range probably is a result of the slightly hydrophobic environment of the hydrogel.

The fluorescence lifetime of fluorescent indicators were recorded. For physically entrapped indicators, FS and HPTS, their lifetimes remained almost the same with those in solution. For covalently bound indicators, DHPDS and DHNDS, their lifetimes decreased compared to those in solution.

The CR-PEG hydrogel changed color in different buffer solution, which can be used as a reusable "pH sensor".

## 4.5 Future work

The pH sensitivity of indicators immobilized in a hydrogel was very promising. Further study needs to be conducted before it can be eventually applied to pH measurement in the real word.

The ionic strength and temperature effects on  $pK_a$  of indicators immobilized in hydrogel will be studied. An equation will be developed for solution pH measurement based on the fluorescence or absorbance ratios of the indicators.

Hydrogel can be deposited to quartz slides through covalent binding. Compound such as allyltriethoxysilane will be used to form a monolayer on the quartz slide with surface silanol groups. The alkenyl group on the monolayer can participate in the polymerization reaction with PEGDA. In this way, hydrogel can be covalently bound to the quartz slide which is used as a solid support.

For pH measurement in a more broad range, several indicators can be immobilized in the same hydrogel but in separated regions to avoid interfering with each other. As a inspiration of the commercially available pH paper, these pH indicators can be covalently bound into hydrogel matrix. The pH probe will show similar color change in a much broad pH range, ideally, 0-14. Because of the covalently binding, the indicators can not leach out from the hydrogel matrix, the pH probe can be reused many times as a so called reusable "pH paper".

## 5. CONCLUSIONS

The activity of hydrogen ions (pH) is one of the most important parameters for chemical and biological applications such as environmental monitoring, biomedical research. The pH of an aqueous solution is usually measured by a glass electrode with the advantages such as simplicity and low cost. However, the electrodes need to be calibrated frequently and they are difficult to miniaturize. In addition, due to the liquid junction potential between the standard solution and the sample solution, up to 1 pH unit error could be introduced if the ionic strength of the sample solution is very low (such as fresh water samples). Optical pH sensors based on immobilization of pH sensitive indicators to a solid support were studied and developed to overcome the defects of the potentiometric methods. Optical pH sensors have many advantages including high sensitivity, no need for a reference signal, easy miniaturization and immunity to electrical interference. In this research project, three different optical pH sensors based on three different porous supporting materials were evaluated. The supporting materials were characterized and the spectral behavior and pH sensitivity of various immobilized indicators were studied. Their performance including sensitivity, equilibrium time, reproducibility, and long term stability were evaluated as potential optical pH sensors.

The first optical pH probe was developed by covalently binding of the fluorescent pH

indicator fluorescein-5-isothiocyanate (FITC) onto the inner surface of mesoporous silica (Figure 2.6) . The immobilized FITC retained its pH sensitivity with fluorescence spectral behavior very similar to fluorescein in solution. Fluorescence intensity of FITC bound in mesoporous silica was greatly increased relative to that on a planar quartz slide, resulting from the high surface area of the mesoporous silica (Figure 2.18). The excited state  $pK_a$  value of FITC in mesoporous silica was 5.58 (Figure 2.21), which is slightly smaller than that of fluorescein in solution, 5.68 (Figure 2.16). The small shift of  $pK_a^*$  is due to the free silanol group on the inner surface of mesoporous silica, which acted as an additional buffer. The pH of the bulk solution can be calculated using the modified equation 2.9; which matched with the pH values from electrode measurement. The pH sensitive range for this optical sensor is 4.5 - 6.5, with error less than 0.11 pH units. Great reproducibility was observed by shifting different buffer solution as shown in Figure 2.28. After washing thoroughly, no leaching was detected and the sensor was stable for over 4 months. However, this probe experienced a long equilibrium time up to 100 minutes due to the small pores and relative thick porous silica membrane (0.5 mm).

Sol-gel films have been used to entrap pH indicators to work as pH sensors because of their optical transparency, mechanical stability, chemical inertness and flexibility in terms of shaping sensor configurations. Two different precursors, ethyltriethoxysilane (ETEOS) and 3-Glycidoxypropyltrimethoxysilane (GPTMS) were used for sol-gel process. The pH sensitive fluorescent indicators fluorescein-5-(and-6)-sulfonate (FS) and 8-hydroxypyrene-1,3,6-trisulfonate (HPTS) were ion-paired with a common surfactant cetyltrimethylammonium bromide (CTAB) before physically entrapment in sol-gel films. After immobilization in sol-gel films, the excitation and emission peaks of FS were red shifted by 15 - 20 nm compared to in solution phase. For HPTS, the excitation spectra of both protonated and deprotonated forms remained the same as in solution phase. However, in the sol-gel, emis-

sion was visible from both protonated (435 nm) and deprotonated (510 nm) HPTS, unlike in solution where emission was only observed from the deprotonated form (510 nm) as shown in Figure 3.15 and Figure 3.4, respectively. This reveals either the decrease in photoacidity of HPTS after immobilization or a fraction of -OH groups in HPTS were blocked from deprotonation. The calculated  $pK_a$  values of both FS and HPTS in sol-gel film were lower than those in solution, 4.22 and 5.68, and 5.58 and 7.35, respectively. This  $pK_a$  shift was attributed to the silanol groups on silica oxide surface. In addition, the indicators were surrounded by positive charged ammonium groups from the surfactant. For the sol-gel films with a thickness of around 472 nm, the equilibrium was less than 5 minutes (Figure 3.22). No leaching was observed after thorough washing, and the sensor was stable for at least a few months.

Hydrogel was also used for pH indicator immobilization for pH sensing because of its capability of imbibing a significant amount of aqueous solution. Various pH indicators were immobilized in hydrogels through both physically entrapment and covalently binding. pH sensitive ion-pairs, FS-CTAB and HPTS-CTAB synthesized in chapter 3 were immobilized in hydrogels during the polymerization process initiated by the free radical initiators in DMF. Three indicators, 6,8-hydroxypyrene-1,3-disulfonate (DHPDS) and 2,7-dihydroxynaphthalene-3,6-disulfonate (DHNDS) and cresol red (CR) were first reacted with methacrylic anhydride to form methacryloyl-analogs and then copolymerized in hydrogel films with redox initiation system. A  $pK_a$  shift to higher pH value was observed for all these indicators in hydrogel than in solution. This shift can be explained with the medium effect on acid dissociation constant, which can be estimated using equation 4.10. With superporous structure, the equilibrium time of indicators in hydrogel was short (within 4 minutes) even with a large dimensions  $1\text{ cm} \times 2\text{ cm} \times 0.5\text{ mm}$  (Figure 4.44). The equilibrium time can be reduced by decreasing the size of the hydrogel samples. These sensors

showed a great long term stability (for at least 6 months) except HNDS-PEG, which became nonfluorescent after 6 months as a result of instability of this indicator. CR-PEG hydrogel changes color from yellow to purple with pH changing from 8.5 to 10.5. In addition, covalent binding prevented indicators from leaching, making a possibility of CR-PEG to work as a reusable pH "paper " with working range 8.5 - 10.5.

The properties of these three different matrix used for indicator immobilization were summarized and compared in Table 5.1

**Table 5.1**  
Comparison of properties of mesoporous silica, sol-gel films and hydrogels

Properties	Mesoporous silica	Sol-gel films	Hydrogels
Transparent	✓	✓	✓
No leaching	✓	✓	✓
Hydrophilic	✓	×	✓
Fast equilibrium	×	✓	✓
Robust	×	✓	×
pK <sub>a</sub> shift	✓	✓	✓

All matrices were transparent and no leaching of indicators were observed after through washing. As for mesoporous silica, it required long equilibrium time (up to 100 minutes) and it was not robust because the high stress during the oxidation of mesoporous silicon broke the matrix easily. Compared to mesoporous silica, sol-gel films were robust and had short equilibrium time because the film thickness were controlled in range of 60 nm - 1300 nm with spin-coating. However, because of the induction of the organic functional groups, sol-gel films were less hydrophilic. Hydrogels are hydrophilic due to its ability of absorbing a significant amount of water, and its equilibrium time was short because of the superporous structure. Hydrogels was less robust compare to sol-gel films which can be deposited on a quartz slides. However, this disadvantages could be overcome by introducing a monolayer of allyltriethoxysilane which can covalently bound to silica surface and copolymerized with



polyethylene diacrylate. In this way, hydrogel could be deposited on quartz slide also, increasing its robustness. As for the  $pK_a$  shift of indicators in these matrices relative to in solution phase, the shifts existed in all these matrices. However, this property can not be defined as an disadvantage, because the inner surface properties of the matrices can be studied and  $pK_a$  values can be tuned to the desired pH range.

Both fluorescein and pyrene based indicators showed high fluorescence quantum yield and great photostability in the experiments. However, the naphthalene based indicators were not stable in basic conditions, which makes them not quite suitable for optical pH sensor development.

## REFERENCES

- (1) C. Westcott, pH measurements, Academic press, The University of Michigan, 1978.
- (2) O. Korostynska, K. Arshak, E. Gill, A. Arshak, Review on state-of-the-art in polymer based pH sensors, *Sensors* 7 (2007) 3027–3042.
- (3) J. Janata, Do optical sensors really measure pH, *Analytical Chemistry* 59 (1987) 1351–1356.
- (4) M. J. Gardner, R. Gill, J. E. Ravenscroft, Control samples for pH determination in low ionic-strength waters, *Analyst* 115 (1990) 371–374.
- (5) S. G. Yuan, M. D. Degrandpre, Evaluation of indicator-based pH measurements for freshwater over a wide range of buffer intensities, *Environmental Science & Technology* 42 (2008) 6092–6099.
- (6) Y. Nakano, H. Kimoto, S. Watanabe, K. Harada, Y. W. Watanabe, Simultaneous vertical measurements of in situ pH and CO<sub>2</sub> in the sea using spectrophotometric profilers, *Journal of Oceanography* 62 (2006) 71–81.
- (7) C. R. French, J. J. Carr, E. M. Dougherty, L. A. K. Eidson, J. C. Reynolds, M. D. Degrandpre, Spectrophotometric pH measurements of freshwater, *Analytica Chimica Acta* 453 (2002) 13–20.

- (8) T. R. Martz, J. J. Carr, C. R. French, M. D. DeGrandpre, A submersible autonomous sensor for spectrophotometric pH measurements of natural waters, *Analytical Chemistry* 75 (2003) 1844–1850.
- (9) W. S. Yao, R. H. Byrne, Spectrophotometric determination of freshwater pH using bromocresol purple and phenol red, *Environmental Science & Technology* 35 (2001) 1197–1201.
- (10) M. P. Seidel, M. D. DeGrandpre, A. G. Dickson, A sensor for in situ indicator-based measurements of seawater pH, *Marine Chemistry* 109 (2008) 18–28.
- (11) J. Lakowicz, *Principles of Fluorescence Spectroscopy*, Springer, New York, 1999.
- (12) H. S. Rye, J. M. Dabora, M. A. Quesada, R. A. Mathies, A. N. Glazer, Fluorometric assay using dimeric dyes for double-stranded and single-stranded-DNA and RNA with picogram sensitivity, *Analytical Biochemistry* 208 (1993) 144–150.
- (13) D. Wencel, B. D. MacCraith, C. McDonagh, High performance optical ratiometric sol-gel-based pH sensor, *Sensors and Actuators B-Chemical* 139 (2009) 208–213.
- (14) M. Y. Berezin, K. Guo, W. Akers, R. E. Northdurft, J. P. Culver, B. Teng, O. Vasalatiy, K. Barbacow, A. Gandjbakhche, G. L. Griffiths, S. Achilefu, Near-infrared fluorescence lifetime pH-sensitive probes, *Biophysical Journal* 100 (2011) 2063–2072.
- (15) D. M. Jordan, D. R. Walt, F. P. Milanovich, Physiological pH fiberoptic chemical sensor based on energy-transfer, *Analytical Chemistry* 59 (1987) 437–439.
- (16) N. Yapici, S. Jockusch, S. Moscatelli, A. Mandalapu, Y. Itagaki, D. Bates, S. Wiseman, K. Gibson, N. Turro, L. Bi, New rhodamine nitroxide based fluorescent probes

for intracellular hydroxyl radical identification in living cells, *Organic letters* 14 (2012) 50–53.

- (17) J. I. Peterson, S. R. Goldstein, R. V. Fitzgerald, D. K. Buckhold, Fiber optic pH probe for physiological use, *Analytical Chemistry* 52 (1980) 864–869.
- (18) L. A. Saari, W. R. Seitz, pH sensor based on immobilized fluoresceinamine, *Analytical Chemistry* 54 (1982) 821–823.
- (19) J. Lin, Recent development and applications of optical and fiber-optic pH sensors, *Trac-Trends in Analytical Chemistry* 19 (2000) 541–552.
- (20) M. C. Moreno, A. Martinez, P. Millan, C. Camara, Study of a pH sensitive optical fiber sensor based on the use of cresol red, *Journal of Molecular Structure* 143 (1986) 553–556.
- (21) V. Misra, H. Mishra, H. C. Joshi, T. C. Pant, An optical pH sensor based on excitation energy transfer in Nafion (R) film, *Sensors and Actuators B-Chemical* 82 (2002) 133–141.
- (22) S. H. Lee, J. Kumar, S. K. Tripathy, Thin film optical sensors employing polyelectrolyte assembly, *Langmuir* 16 (2000) 10482–10489.
- (23) M. Ammam, B. Keita, L. Nadjo, J. Fransaer, pH sensor based on the crown heteropolyanion  $K_{28}Li_5H_7P_8W_{48}O_{184}$  immobilized using a layer by layer assembly process, *Sensors and Actuators B-Chemical* 142 (2009) 347–354.
- (24) J. Goicoechea, C. R. Zamarreno, I. R. Matias, F. J. Arregui, Minimizing the photobleaching of self-assembled multilayers for sensor applications, *Sensors and Actuators B-Chemical* 126 (2007) 41–47.

- (25) J. Goicoechea, C. R. Zamarreno, I. R. Matias, F. J. Arregui, Optical fiber pH sensors based on layer-by-layer electrostatic self-assembled neutral red, *Sensors and Actuators B-Chemical* 132 (2008) 305–311.
- (26) Y. N. Shi, C. J. Seliskar, Optically transparent polyelectrolyte-silica composite materials: Preparation, characterization, and application in optical chemical sensing, *Chemistry of Materials* 9 (1997) 821–829.
- (27) S. Hulth, R. C. Aller, P. Engstrom, E. Selander, A pH plate fluorosensor (optode) for early diagenetic studies of marine sediments, *Limnology and Oceanography* 47 (2002) 212–220.
- (28) A. Hakonen, S. Hulth, A high-performance fluorosensor for pH measurements between 6 and 9, *Talanta* 80 (2010) 1964–1969.
- (29) D. A. Nivens, M. V. Schiza, S. M. Angel, Multilayer sol-gel membranes for optical sensing applications: single layer pH and dual layer CO<sub>2</sub> and NH<sub>3</sub> sensors, *Talanta* 58 (2002) 543–550.
- (30) M. F. Choi, Spectroscopic behaviour of 8-hydroxy-1,3,6-pyrenetrisulphonate immobilized in ethyl cellulose, *Journal of Photochemistry and Photobiology a-Chemistry* 104 (1997) 207–212.
- (31) M. M. F. Choi, Spectroscopic behaviour and protolytic equilibrium of fluorescein immobilized in ethyl cellulose, *Journal of Photochemistry and Photobiology a-Chemistry* 114 (1998) 235–239.
- (32) A. Hakonen, S. Hulth, A high-precision ratiometric fluorosensor for pH: Implementing time-dependent non-linear calibration protocols for drift compensation, *Analytica Chimica Acta* 606 (2008) 63–71.

- (33) D. A. Nivens, Y. K. Zhang, S. M. Angel, A fiber-optic pH sensor prepared using a base-catalyzed organo-silica sol-gel, *Analytica Chimica Acta* 376 (1998) 235–245.
- (34) I. Sanchez-Barragan, J. M. Costa-Fernandez, A. Sanz-Medel, M. Valledor, F. J. Ferrero, J. C. Campo, A ratiometric approach for pH optosensing with a single fluorophore indicator, *Analytica Chimica Acta* 562 (2006) 197–203.
- (35) F. R. Zaggout, A. E. F. A. Qarraman, S. M. Zourab, Behavior of immobilized Alizarin Red S into sol-gel matrix as pH sensor, *Materials Letters* 61 (2007) 4192–4195.
- (36) S. Bidmanova, A. Hlavacek, J. Damborsky, Z. Prokop, Conjugation of 5(6)-carboxyfluorescein and 5(6)-carboxynaphthofluorescein with bovine serum albumin and their immobilization for optical pH sensing, *Sensors and Actuators B-Chemical* 161 (2012) 93–99.
- (37) C. S. Chu, Y. L. Lo, Fiber-optic carbon dioxide sensor based on fluorinated xerogels doped with HPTS, *Sensors and Actuators B-Chemical* 129 (2008) 120–125.
- (38) D. Wencel, M. Barczak, P. Borowski, C. McDonagh, The development and characterisation of novel hybrid sol-gel-derived films for optical pH sensing, *Journal of Materials Chemistry* 22 (2012) 11720–11729.
- (39) M. D. Gulcev, G. L. G. Goring, M. Rakic, J. D. Brennan, Reagentless pH-based biosensing using a fluorescently-labelled dextran co-entrapped with a hydrolytic enzyme in sol-gel derived nanocomposite films, *Analytica Chimica Acta* 457 (2002) 47–59.
- (40) I. Kasik, J. Mrazek, T. Martan, M. Pospisilova, O. Podrazky, V. Matejec,

- K. Hoyerova, M. Kaminek, Fiber-optic pH detection in small volumes of biosamples, *Analytical and Bioanalytical Chemistry* 398 (2010) 1883–1889.
- (41) F. J. Arregui, M. Otano, C. Fernandez-Valdivielso, I. R. Matias, An experimental study about the utilization of liquicoat (R) solutions for the fabrication of pH optical fiber sensors, *Sensors and Actuators B-Chemical* 87 (2002) 289–295.
- (42) H. R. Kermis, Y. Kostov, P. Harms, G. Rao, Dual excitation ratiometric fluorescent pH sensor for noninvasive bioprocess monitoring: Development and application, *Biotechnology Progress* 18 (2002) 1047–1053.
- (43) C. R. Schroder, B. M. Weidgans, I. Klimant, pH fluorosensors for use in marine systems, *Analyst* 130 (2005) 907–916.
- (44) L. N. Xue, B. Y. Li, Q. Fei, G. D. Feng, Y. F. Huan, Z. Shi, Carboxylate-modified squaraine dye doped silica fluorescent pH nanosensors, *Nanotechnology* 21 (2010) 215502–215506.
- (45) Y. Kostov, S. Tzonkov, L. Yotova, M. Krysteva, Membranes for optical pH sensors, *Analytica Chimica Acta* 280 (1993) 15–19.
- (46) A. A. Ensafi, A. Kazemzadeh, Optical pH sensor based on chemical modification of polymer film, *Microchemical Journal* 63 (1999) 381–388.
- (47) S. G. Schulman, S. X. Chen, F. L. Bai, M. J. P. Leiner, L. Weis, O. S. Wolfbeis, Dependence of the fluorescence of immobilized 1-hydroxypyrene-3,6,8-trisulfonate on solution pH - extension of the range of applicability of a pH fluorosensor, *Analytica Chimica Acta* 304 (1995) 165–170.
- (48) N. Stromberg, E. Mattsson, A. Hakonen, An imaging pH optode for cell studies

based on covalent attachment of 8-hydroxypyrene-1,3,6-trisulfonate to amino cellulose acetate films, *Analytica Chimica Acta* 636 (2009) 89–94.

- (49) Z. H. Liu, F. L. Luo, T. L. Chen, Phenolphthalein immobilized membrane for an optical pH sensor, *Analytica Chimica Acta* 510 (2004) 189–194.
- (50) H. Offenbacher, O. S. Wolfbeis, E. Furlinger, Fluorescence optical sensors for continuous determination of near-neutral pH values, *Sensors and Actuators* 9 (1986) 73–84.
- (51) A. Lobnik, I. Oehme, I. Murkovic, O. S. Wolfbeis, pH optical sensors based on sol-gels: Chemical doping versus covalent immobilization, *Analytica Chimica Acta* 367 (1998) 159–165.
- (52) Y. Ando, S. Iino, K. Yamada, K. Umezawa, N. Iwasawa, D. Citterio, K. Suzuki, A ratiometric fluorescent pH glass optode based on a boron-dipyrromethene derivative, *Sensors and Actuators B-Chemical* 121 (2007) 74–82.
- (53) A. Schulz, J. Wotschadlo, T. Heinze, G. J. Mohr, Fluorescent nanoparticles for ratiometric pH-monitoring in the neutral range, *Journal of Materials Chemistry* 20 (2010) 1475–1482.
- (54) B. Vilozy, A. Schiller, R. A. Wessling, B. Singaram, Multiwell plates loaded with fluorescent hydrogel sensors for measuring pH and glucose concentration, *Journal of Materials Chemistry* 21 (2011) 7589–7595.
- (55) H. R. Kermis, Y. Kostov, G. Rao, Rapid method for the preparation of a robust optical pH sensor, *Analyst* 128 (2003) 1181–1186.



- (56) R. Badugu, Y. Kostov, G. Rao, L. Tolosa, Development and application of an excitation ratiometric optical pH sensor for bioprocess monitoring, *Biotechnology Progress* 24 (2008) 1393–1401.
- (57) J. Y. Choi, D. I. Lee, C. J. Kim, C. H. Lee, I. S. Ahn, Synthesis of peg hydrogel with dityrosine for multi-functionality and pH-dependent fluorescence, *Journal of Industrial and Engineering Chemistry* 18 (2012) 611–616.
- (58) L. P. Zhao, T. Nakayama, H. Tomimoto, Y. Shingaya, Q. Huang, Functionalization of carbon nanotubes with a pH-responsive molecule to produce a pH sensor, *Nanotechnology* 20 (2009).
- (59) S. Motellier, M. H. Michels, B. Dureault, P. Toulhoat, Fiberoptic pH sensor for insitu applications, *Sensors and Actuators B-Chemical* 11 (1993) 467–473.
- (60) S. Y. Dong, M. Luo, G. D. Peng, W. H. Cheng, Broad range pH sensor based on sol-gel entrapped indicators on fibre optic, *Sensors and Actuators B-Chemical* 129 (2008) 94–98.
- (61) O. S. Wolfbeis, H. Offenbacher, Fluorescence sensor for monitoring ionic-strength and physiological pH values, *Sensors and Actuators* 9 (1986) 85–91.
- (62) A. Hakonen, S. Hulth, S. Dufour, Analytical performance during ratiometric long-term imaging of pH in bioturbated sediments, *Talanta* 81 (2010) 1393–1401.
- (63) Y. Avnir, Y. Barenholz, pH determination by pyranine: Medium-related artifacts and their correction, *Analytical Biochemistry* 347 (2005) 34–41.
- (64) A. J. Amali, N. H. Awwad, R. K. Rana, D. Patra, Nanoparticle assembled microcapsules for application as pH and ammonia sensor, *Analytica Chimica Acta* 708 (2011) 75–83.

- (65) A. J. Amali, S. Singh, N. Rangaraj, D. Patra, R. K. Rana, Poly(l-lysine)-pyranine-3 coacervate mediated nanoparticle-assembly: fabrication of dynamic pH-responsive containers, *Chemical Communications* 48 (2012) 856–858.
- (66) R. Sjoback, J. Nygren, M. Kubista, Absorption and fluorescence properties of fluorescein, *Spectrochimica Acta Part a-Molecular and Biomolecular Spectroscopy* 51 (1995) L7–L21.
- (67) J. Y. Han, A. Loudet, R. Barhoumi, R. C. Burghardt, K. Burgess, A ratiometric pH reporter for imaging protein-dye conjugates in living cells, *Journal of the American Chemical Society* 131 (2009) 1642–1643.
- (68) W. Y. Shi, S. He, M. Wei, D. G. Evans, X. Duan, Optical pH sensor with rapid response based on a fluorescein-intercalated layered double hydroxide, *Advanced Functional Materials* 20 (2010) 3856–3863.
- (69) S. Schreml, R. J. Meier, O. S. Wolfbeis, M. Landthaler, R. M. Szeimies, P. Babilas, 2D luminescence imaging of pH in vivo, *Proceedings of the National Academy of Sciences of the United States of America* 108 (2011) 2432–2437.
- (70) S. Schreml, R. J. Meier, K. T. Weiss, J. Cattani, D. Flittner, S. Gehmert, O. S. Wolfbeis, M. Landthaler, P. Babilas, A sprayable luminescent pH sensor and its use for wound imaging in vivo, *Experimental Dermatology* 21 (2012) 951–953.
- (71) X. D. Wang, R. J. Meier, O. S. Wolfbeis, A fluorophore-doped polymer nanomaterial for referenced imaging of pH and temperature with sub-micrometer resolution, *Advanced Functional Materials* 22 (2012) 4202–4207.
- (72) X. Wang, O. S. Wolfbeis, Fiber-optic chemical sensors and biosensors (2008-2012), *Analytical Chemistry* 85 (2012) 487–508.

- (73) W. D. Bare, N. H. Mack, W. Y. Xu, J. N. Demas, B. A. DeGraff, Multicomponent lifetime-based pH sensors utilizing constant-lifetime probes, *Analytical Chemistry* 74 (2002) 2198–2209.
- (74) H. M. R. Goncalves, C. D. Maule, P. A. S. Jorge, J. C. G. E. da Silva, Fiber optic lifetime pH sensing based on ruthenium(II) complexes with dicarboxybipyridine, *Analytica Chimica Acta* 626 (2008) 62–70.
- (75) S. M. Borisov, K. Gatterer, I. Klimant, Red light-excitable dual lifetime referenced optical pH sensors with intrinsic temperature compensation, *Analyst* 135 (2010) 1711–1717.
- (76) A. Richter, G. Paschew, S. Klatt, J. Lienig, K. F. Arndt, H. J. P. Adler, Review on hydrogel-based pH sensors and microsensors, *Sensors* 8 (2008) 561–581.
- (77) A. Richter, A. Bund, M. Keller, K. F. Arndt, Characterization of a microgravimetric sensor based on pH sensitive hydrogels, *Sensors and Actuators B-Chemical* 99 (2004) 579–585.
- (78) G. Gerlach, M. Guenther, G. Suchaneck, J. Sorber, K. F. Arndt, A. Richter, Application of sensitive hydrogels in chemical and pH sensors, *Macromolecular Symposia* 210 (2004) 403–410.
- (79) G. Gerlach, M. Guenther, J. Sorber, G. Suchaneck, K. F. Arndt, A. Richter, Chemical and pH sensors based on the swelling behavior of hydrogels, *Sensors and Actuators B-Chemical* 111 (2005) 555–561.
- (80) C. W. Zhao, X. L. Zhuang, P. He, C. S. Xiao, C. L. He, J. R. Sun, X. S. Chen, X. B. Jing, Synthesis of biodegradable thermo- and pH-responsive hydrogels for controlled drug release, *Polymer* 50 (2009) 4308–4316.

- (81) L. N. Sun, H. S. Peng, M. I. J. Stich, D. Achatz, O. S. Wolfbeis, pH sensor based on upconverting luminescent lanthanide nanorods, *Chemical Communications* (2009) 5000–5002.
- (82) Q. Z. Zhu, R. C. Aller, Y. Z. Fan, High-performance planar pH fluorosensor for two-dimensional pH measurements in marine sediment and water, *Environmental Science & Technology* 39 (2005) 8906–8911.
- (83) R. J. Meier, S. Schreml, X. D. Wang, M. Landthaler, P. Babilas, O. S. Wolfbeis, Simultaneous photographing of oxygen and pH in vivo using sensor films, *Ange-wandte Chemie-International Edition* 50 (2011) 10893–10896.
- (84) P. A. S. Jorge, P. Caldas, J. C. G. E. Da Silva, C. C. Rosa, A. G. Oliva, J. L. Santos, F. Farahi, Luminescence-based optical fiber chemical sensors, *Fiber and Integrated Optics* 24 (2005) 201–225.
- (85) O. S. Wolfbeis, B. Kovacs, K. Goswami, S. M. Klainer, Fiber-optic fluorescence carbon dioxide sensor for environmental monitoring, *Mikrochimica Acta* 129 (1998) 181–188.
- (86) C. S. Chu, Y. L. Lo, Highly sensitive and linear optical fiber carbon dioxide sensor based on sol-gel matrix doped with silica particles and HPTS, *Sensors and Actuators B-Chemical* 143 (2009) 205–210.
- (87) N. Szita, P. Boccazzi, Z. Y. Zhang, P. Boyle, A. J. Sinskey, K. F. Jensen, Development of a multiplexed microbioreactor system for high-throughput bioprocessing, *Lab on a Chip* 5 (2005) 819–826.
- (88) A. Funfak, J. L. Cao, O. Wolfbeis, K. Martin, J. Kohler, Monitoring cell cultivation

in microfluidic segments by optical pH sensing with a micro flow-through fluorometer using dye-doped polymer particles, *Microchimica Acta* 164 (2009) 279–286.

- (89) J. Y. Han, K. Burgess, Fluorescent indicators for intracellular pH, *Chemical Reviews* 110 (2010) 2709–2728.
- (90) A. S. Kocincova, S. Nagl, S. Arain, C. Krause, S. M. Borisov, M. Arnold, O. S. Wolfbeis, Multiplex bacterial growth monitoring in 24-well microplates using a dual optical sensor for dissolved oxygen and pH, *Biotechnology and Bioengineering* 100 (2008) 430–438.
- (91) S. Arain, G. T. John, C. Krause, J. Gerlach, O. S. Wolfbeis, I. Klimant, Characterization of microtiterplates with integrated optical sensors for oxygen and pH, and their applications to enzyme activity screening, respirometry, and toxicological assays, *Sensors and Actuators B-Chemical* 113 (2006) 639–648.
- (92) J. L. Gehrich, D. W. Lubbers, N. Opitz, D. R. Hansmann, W. W. Miller, J. K. Tusa, M. Yafuso, Optical fluorescence and its application to an intravascular blood-gas monitoring-system, *Ieee Transactions on Biomedical Engineering* 33 (1986) 117–132.
- (93) M. J. P. Leiner, Optical sensors for in-vitro blood-gas analysis, *Sensors and Actuators B-Chemical* 29 (1995) 169–173.
- (94) A. Bromberg, J. Zilberstein, S. Riesemberg, E. Benori, E. Silberstein, J. Zimnavoda, G. Frishman, A. Kritzman, Optical-fibre sensors for blood gases and pH, based on porous glass tips, *Sensors and Actuators B-Chemical* 31 (1996) 181–191.
- (95) W. Z. Jin, J. J. Jiang, X. Wang, X. D. Zhu, G. F. Wang, Y. L. Song, C. X. Bai,

Continuous intra-arterial blood pH monitoring in rabbits with acid-base disorders, *Respiratory Physiology & Neurobiology* 177 (2011) 183–188.

- (96) M. I. J. Stich, M. Schaeferling, O. S. Wolfbeis, Multicolor fluorescent and permeation-selective microbeads enable simultaneous sensing of pH, oxygen, and temperature, *Advanced Materials* 21 (2009) 2216–2220.
- (97) M. I. J. Stich, L. H. Fischer, O. S. Wolfbeis, Multiple fluorescent chemical sensing and imaging, *Chemical Society Reviews* 39 (2010) 3102–3114.
- (98) A. Holobar, R. Benes, B. H. Weigl, P. O'Leary, P. Raspor, O. S. Wolfbeis, Fiber optic and non-fiber optic double-beam pH sensors for use in a flow-through cell, *Analytical Methods and Instrumentation* 2 (1995) 92–100.
- (99) X. D. Ge, M. Hanson, H. Shen, Y. Kostov, K. A. Brorson, D. D. Frey, A. R. Moreira, G. Rao, Validation of an optical sensor-based high-throughput bioreactor system for mammalian cell culture, *Journal of biotechnology* 122 (2006) 293–306.
- (100) C. von Bultzingslowen, A. K. McEvoy, C. McDonagh, B. D. MacCraith, I. Klimant, C. Krause, O. S. Wolfbeis, Sol-gel based optical carbon dioxide sensor employing dual luminophore referencing for application in food packaging technology, *Analyst* 127 (2002) 1478–1483.
- (101) F. T. Chi, L. H. Yan, H. W. Yan, B. Jiang, H. B. Lv, X. D. Yuan, Ultralow-refractive-index optical thin films through nanoscale etching of ordered mesoporous silica films, *Optics Letters* 37 (2012) 1406–1408.
- (102) K. L. Vanga, Implementation of Porous Silicon Technology for a Fluidic Flow-Through Optical Sensor for pH Measurements, Ph.D. thesis, Michigan Technological University, Houghton, MI, 2012.

- (103) M. M. Martin, L. Lindqvist, pH-dependence of fluorescein fluorescence, *Journal of Luminescence* 10 (1975) 381–390.
- (104) S. Flink, F. C. J. M. van Veggel, D. N. Reinhoudt, Functionalization of self-assembled monolayers on glass and oxidized silicon wafers by surface reactions, *Journal of Physical Organic Chemistry* 14 (2001) 407–415.
- (105) F. Ismail, C. Malins, N. J. Goddard, Alkali treatment of dye-doped sol-gel glass films for rapid optical pH sensing, *Analyst* 127 (2002) 253–257.
- (106) V. Bolis, A. Cavenago, B. Fubini, Surface heterogeneity on hydrophilic and hydrophobic silicas: Water and alcohols as probes for H-bonding and dispersion forces, *Langmuir* 13 (1997) 895–902.
- (107) S. W. Ong, X. L. Zhao, K. B. Eisenthal, Polarization of water-molecules at a charged interface - 2nd harmonic studies of the silica water interface, *Chemical Physics Letters* 191 (1992) 327–335.
- (108) A. Goswami, A. K. Singh, B. Venkataramani, 8-hydroxyquinoline anchored to silica gel via new moderate size linker: synthesis and applications as a metal ion collector for their flame atomic absorption spectrometric determination, *Talanta* 60 (2003) 1141–1154.
- (109) D. F. Liu, G. Ma, H. C. Allen, Adsorption of 4-picoline and piperidine to the hydrated SiO<sub>2</sub> surface: Probing the surface acidity with vibrational sum frequency generation spectroscopy, *Environmental Science & Technology* 39 (2005) 2025–2032.
- (110) S. Vuppu, Y. Kostov, G. Rao, Economical wireless optical ratiometric pH sensor, *Measurement Science & Technology* 20 (2009) 045202.

- (111) A. Albert, E. P. Sergeant, The determination of ionization constants, Chapman and Hall, London, 1971.
- (112) R. Markuszewski, H. Diehl, The structure and acid-base and fluorometric properties of fluorescein and calcein, Abstracts of Papers of the American Chemical Society 180 (1980) 179–ANYL.
- (113) A. G. Ryder, S. Power, T. J. Glynn, J. J. Morrison, Time-domain measurement of fluorescence lifetime variation with pH, volume 4259, 2001.
- (114) D. Magde, G. E. Rojas, P. G. Seybold, Solvent dependence of the fluorescence lifetimes of xanthene dyes, Photochemistry and Photobiology 70 (1999) 737–744.
- (115) J. P. van Dalen, J. J. Haaijman, Determination of the molar absorbance coefficient of bound tetramethyl rhodamine isothiocyanate relative to fluorescein isothiocyanate, Journal of immunological methods 5 (1974) 103–6.
- (116) C. Malins, H. G. Glever, T. E. Keyes, J. G. Vos, W. J. Dressick, B. D. MacCraith, Sol-gel immobilised ruthenium(ii) polypyridyl complexes as chemical transducers for optical pH sensing, Sensors and Actuators B-Chemical 67 (2000) 89–95.
- (117) A. Celzard, J. F. Mareche, Applications of the sol-gel process using well-tested recipes, Journal of Chemical Education 79 (2002) 854–859.
- (118) M. A. Fardad, Catalysts and the structure of SiO<sub>2</sub> sol-gel films, Journal of Materials Science 35 (2000) 1835–1841.
- (119) G. Frenzer, W. F. Maier, Amorphous porous mixed oxides: Sol-gel ways to a highly versatile class of materials and catalysts, Annual Review of Materials Research 36 (2006) 281–331.



- (120) S. H. Kim, B. Y. H. Liu, M. R. Zachariah, Ultrahigh surface area nanoporous silica particles via an aero-sol-gel process, *Langmuir* 20 (2004) 2523–2526.
- (121) T. H. Tran-Thi, T. Gustavsson, C. Prayer, S. Pommeret, J. T. Hynes, Primary ultrafast events preceding the photoinduced proton transfer from pyranine to water, *Chemical Physics Letters* 329 (2000) 421–430.
- (122) E. Pines, D. Huppert, N. Agmon, Salt effects on steady-state quantum yields of ultrafast, diffusion-influenced, reversible photoacid dissociation reactions, *Journal of Physical Chemistry* 95 (1991) 666–674.
- (123) C. Rottman, A. Turniansky, D. Avnir, Sol-gel physical and covalent entrapment of three methyl red indicators: A comparative study, *Journal of Sol-Gel Science and Technology* 13 (1998) 17–25.
- (124) B. C.J., G. Scherer, *The Physics and Chemistry of Sol-Gel Processing*, Academic Press, Inc, Boston, 1990.
- (125) A. Pierre, *Introduction to Sol-Gel Processing*, Springer, 1998.
- (126) B. M. Murari, S. Anand, N. K. Gohil, N. K. Chaudhury, Fluorescence spectroscopic study of dip coated sol-gel thin film internal environment using fluorescent probes Hoechst33258 and pyranine, *Journal of Sol-Gel Science and Technology* 41 (2007) 147–155.
- (127) C. Hille, M. Berg, D. Munzke, P. Primus, L. H.G., C. Dosche, Time-domain fluorescence lifetime imaging for intracellular pH sensing in living tissues, *Analytical and Bioanalytical Chemistry* 391 (2008) 1871–1879.
- (128) F. Ganji, S. Vasheghani-Farahani, E. Vasheghani-Farahani, Theoretical description of hydrogel swelling: A review, *Iranian Polymer Journal* 19 (2010) 375–398.

- (129) A. Mateescu, Y. Wang, J. Dostalek, U. Jonas, Thin hydrogel films for optical biosensor applications, *Membranes* 2 (2012) 40–69.
- (130) J. Ostroha, PEG-based Degradable Networks for Drug Delievry Applications, Ph.D. thesis, Drexel University, Philadelphia, PA, 2006.
- (131) N. A. Peppas, Y. Huang, M. Torres-Lugo, J. H. Ward, J. Zhang, Physicochemical, foundations and structural design of hydrogels in medicine and biology, *Annual Review of Biomedical Engineering* 2 (2000) 9–29.
- (132) G. M. Sun, C. C. Chu, Synthesis, characterization of biodegradable dextran-allyl isocyanate-ethylamine/polyethylene glycol-diacrylate hydrogels and their in vitro release of albumin, *Carbohydrate Polymers* 65 (2006) 273–287.
- (133) C. C. Lin, K. S. Anseth, PEG hydrogels for the controlled release of biomolecules in regenerative medicine, *Pharmaceutical Research* 26 (2009) 631–643.
- (134) S. Lin, N. Sangaj, T. Razafiarison, C. Zhang, S. Varghese, Influence of physical properties of biomaterials on cellular behavior, *Pharmaceutical Research* 28 (2011) 1422–1430.
- (135) S. Boral, A. N. Gupta, H. B. Bohidar, Swelling and de-swelling kinetics of gelatin hydrogels in ethanol-water marginal solvent, *International Journal of Biological Macromolecules* 39 (2006) 240–249.
- (136) T. Matsumoto, M. Okubo, T. Imai, Preparation of poly(ethyl acrylate) emulsions in absence of emulsifier and water resistance properties of its emulsion-film, *Kobunshi Ronbunshu* 32 (1975) 229–234.

- (137) C. Zhong, C. C. Chu, Biomimetic mineralization of acid polysaccharide-based hydrogels: towards porous 3-dimensional bone-like biocomposites, *Journal of Materials Chemistry* 22 (2012) 6080–6087.
- (138) J. L. He, M. Z. Zhang, P. H. Ni, Rapidly in situ forming polyphosphoester-based hydrogels for injectable drug delivery carriers, *Soft Matter* 8 (2012) 6033–6038.
- (139) G. Y. Lin, L. Cosimbescu, N. J. Karin, B. J. Tarasevich, Injectable and thermosensitive PLGA-g-PEG hydrogels containing hydroxyapatite: preparation, characterization and in vitro release behavior, *Biomedical Materials* 7 (2012) 024107.
- (140) Y. Z. Sun, Determination of fluorescence lifetime of sodium fluorescein, *Chinese Journal of Analytical Chemistry* 28 (2000) 1413–1416.
- (141) M. T. V. Rooney, W. R. Seitz, An optically sensitive membrane for pH based on swellable polymer microspheres in a hydrogel, *Analytical Communications* 36 (1999) 267–270.
- (142) Y. J. Lee, P. V. Braun, Tunable inverse opal hydrogel pH sensors, *Advanced Materials* 15 (2003) 563–566.
- (143) H. Jiang, J. Markowski, J. Sabarinathan, Near-infrared optical response of thin film pH-sensitive hydrogel coated on a gold nanocrescent array, *Optics Express* 17 (2009) 21802–21807.
- (144) A. Richter, S. Howitz, D. Kuckling, K. F. Arndt, Influence of volume phase transition phenomena on the behavior of hydrogel-based valves, *Sensors and Actuators B-Chemical* 99 (2004) 451–458.
- (145) E. Kuwana, F. Liang, E. M. Sevick-Muraca, Fluorescence lifetime spectroscopy of a

- pH-sensitive dye encapsulated in hydrogel beads, *Biotechnology Progress* 20 (2004) 1561–1566.
- (146) O. S. Wolfbeis, E. Furlinger, H. Kroneis, H. Marsoner, Fluorimetric analysis .1. a study on fluorescent indicators for measuring near neutral (physiological) pH-values, *Fresenius Zeitschrift Fur Analytische Chemie* 314 (1983) 119–124.
- (147) A. U. Kulikov, M. N. Galat, Comparison of C18 silica bonded phases selectivity in micellar liquid chromatography, *Journal of Separation Science* 32 (2009) 1340–1350.
- (148) A. A. Abdel-Shafi, Spectroscopic studies on the inclusion complex of 2-naphthol-6-sulfonate with beta-cyclodextrin, *Spectrochimica Acta Part a-Molecular and Biomolecular Spectroscopy* 66 (2007) 732–738.
- (149) A. Ravve, *Principle of Polymer Chemistry*, Springer Science + Business Media, 2012.
- (150) R. Bates, *Determination of pH: Theory and practice*, Wiley, New Work, 1973.
- (151) A. Karakoti, S. Singh, A. Kumar, M. Malinska, S. Kuchibhatla, K. Wozniak, S. W.T., S. Seal, PEGylated nanoceria as radical scavenger with tunable redox chemistry, *J. Am. Chem. Soc.* 131 (2009) 14144–14145.
- (152) J. Drobnik, E. Yeagers, On the use of quinine sulfate as a fluorescence standard, *Journal of Molecular Spectroscopy* 19 (1966) 454–455.

# **APPENDICES**

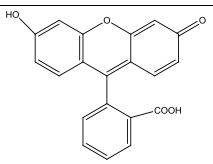
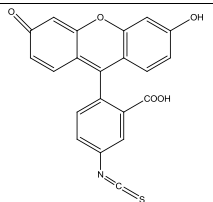
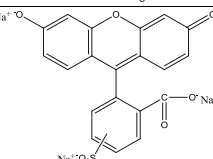
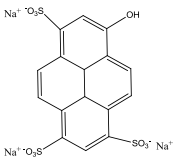
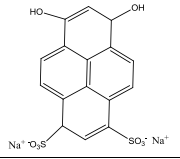
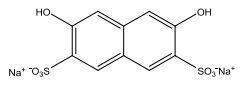
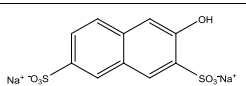
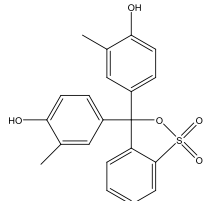
## **APPENDIX A. SUPPLEMENT INFORMATION**

### **A.1 List of indicators**

#### **A.1.1 Indicator structures**

#### **A.1.2 Indicators $\text{pK}_a$ values in solution and different matrix**

**Table A.1**  
A list of indicators used in this dissertation.

Abbreviation	Name	Structure
	fluorescein	
FITC	fluorescein-5- isothiocyanate	
FS	fluorescein-5-(and-6)- sulfonic acid, trisodium salt	
HPTS	8-hydroxypyrene-1,3,6- trisulfonic acid, trisodium salt	
DHPDS	6,8-dihydroxypyrene-1,3- disulfonic acid disodium salt	
DHNDS	2,7- dihydroxynaphthalene- 3,6-disulfonic acid, disodium salt	
HNDS	2-hydroxynaphthalene- 3,6-disulfonic acid, disodium salt	
CR	cresol red	

**Table A.2**A list of indicators  $pK_a$  values in solution and different matrix.

Indicator	Solution	Mesoporous silica	Sol-gel film	Hydrogel
Fluorescein	5.68	5.58	4.22	5.90
HPTS	7.35	\	4.78	8.06
DHPDS	7.03, 9.14	\	\	8.80
DHNDS	8.70	\	\	9.50
HNDS	8.92	\	\	\
CR	8.23	\	\	9.36

The  $pK_a$  values of indicators in buffer solution were calculated at ionic strength of 0.030 M. The  $pK_a$  value of fluorescein in mesoporous silica was calculated at ionic strength of 0.030 M. The  $pK_a$  values of FS and HPTS in sol-gel film were calculated at ionic strength of 0.050 M and 0.030 M, respectively. The  $pK_a$  values of indicators in hydrogel were calculated at ionic strength of 0.100 M.



## A.2 Supplement information for Chapter 2

### A.2.1 Extinction coefficients and quantum yield of fluorescein in buffer

The molar extinction coefficient ( $\epsilon$ ,  $\text{M}^{-1} \text{cm}^{-1}$ ) is a measurement of how strongly a chemical species absorbs light at a give wavelength. It is an intrinsic property of the species. The absorbance,  $A$ , of the species is dependent on its extinction coefficient,  $\epsilon$ , the pathlength,  $l$ , and the concentration,  $c$ . The relationship can be defined by Beer-Lambert law:

$$A = \epsilon cl \quad (\text{A.1})$$

The molar extinction coefficients of mononanion and dianion species of fluorescein in pH 4.25 and pH 8.03, respectively were determined using eq A.1 as shown in Figure A.1. The pathlength is 1 cm, the x-axis is the concentration of fluorescein in  $\mu\text{M}$ , and the y-axis is the absorbance. Thus resulting slopes are the extinction coefficients for fluorescein in at different wavelength and different pH solution.

The quantum yield of fluorescein can be calculated using a standard sample which have a fixed and known fluorescence quantum yield. Quinine sulfate was used as quantum yield standard. The absorption and fluorescence spectra of quinine sulfate in 0.05 M  $\text{H}_2\text{SO}_4$ , and fluorescein in pH 4.25 and pH 8.03 buffer solution were recorded. Plots of fluorescence intensity vs. absorbance are shown in Figure A.2. According to the following equation:

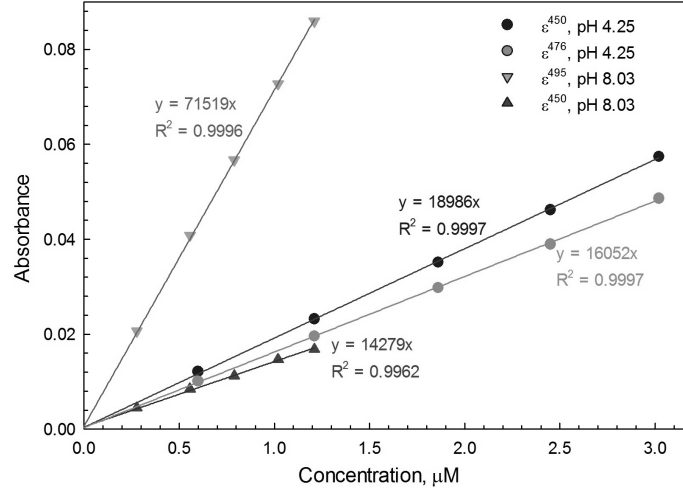


**Figure A.1.** Extinction coefficients of monoanion and dianion fluorescein in various wavelength. The pathlength of the cuvette is 1 cm.

$$\phi_u = \phi_s \frac{Grad_u \gamma_u^2}{Grad_s \gamma_s^2} \quad (A.2)$$

where  $\phi_u$  is the quantum yield for the unknown species, as in this case, fluorescein.  $\phi_s$  is the quantum yield for the standard, quinine sulfate.  $Grad_u$  and  $Grad_s$  are the gradient from the plot of integrated fluorescence intensity vs. absorbance of fluorescein and quinine sulfate, respectively.  $\gamma_u$  and  $\gamma_s$  are the refractive index of the solvent for fluorescein and quinine sulfate solutions, respectively. Because both solution were aqueous solution, I assumed the refractive index of the both solution are the same. So the quantum yield of fluorescein is proportional to the gradient. The fluorescence quantum yield of quinine sulfate in 0.05 M  $H_2SO_4$  under 390 nm excitation is 0.51.[152] So the fluorescence quantum yields of fluorescein in pH 4.25 buffer solution under 450 nm and 467 nm excitation are 0.17 and 0.26 respectively; and the fluorescence quantum yield of fluorescein in pH 8.03 buffer solution under 495 nm excitation is 0.82.

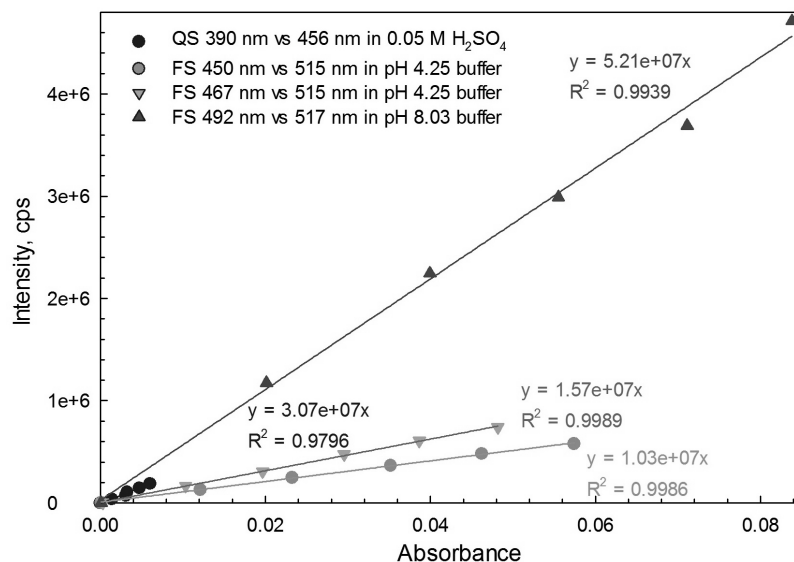


**Figure A.2.** Fluorescence intensity vs. absorbance of quinine sulfate in 0.05 M H<sub>2</sub>SO<sub>4</sub>, and fluorescein in different buffer solutions. The calculated fluorescence quantum yields of fluorescein in pH 4.25 buffer solution under 450 nm and 467 nm excitation are 0.17 and 0.26 respectively; and the fluorescence quantum yield of fluorescein in pH 8.03 buffer solution under 495 nm excitation is 0.82.

## A.2.2 Fluorescence spectra of FITC on quartz slide

## A.2.3 $pK_a^*$ of FITC on glass beads

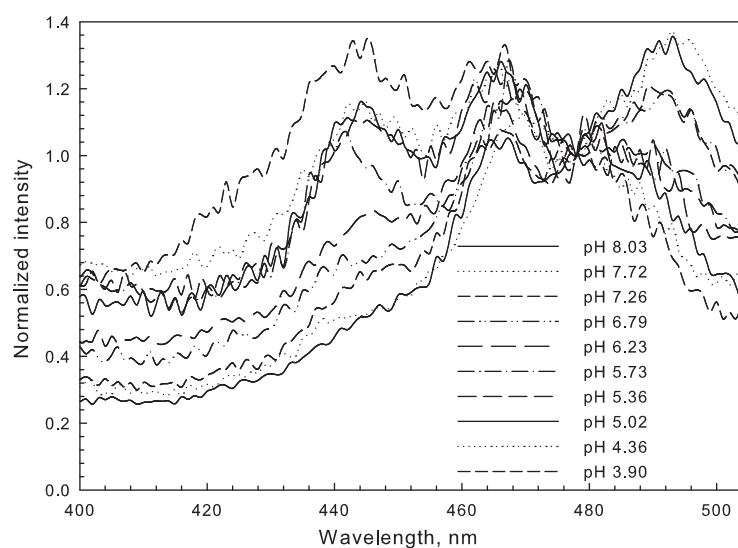


**Figure A.3.** Normalized fluorescence excitation spectra of FITC on quartz slide in solution (IS = 0.030 M) with emission wavelength at 520 nm.

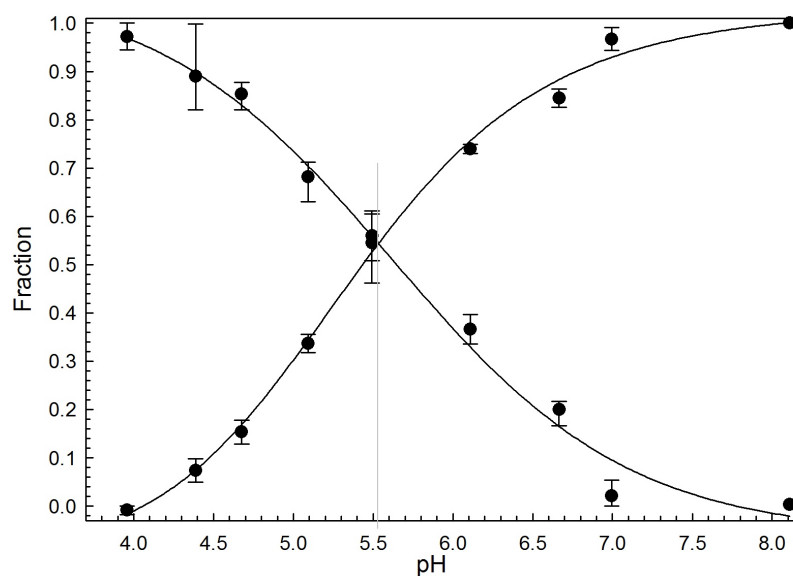


**Figure A.4.**  $pK_a^*$  of FITC on glass beads in solution (IS = 0.120 M). The standard deviation was between 0.006 - 0.037 (n=4).

## A.3 Supplement information for Chapter 3

### A.3.1 FTIR spectra of indicator ion-pairs and sol-gel films

FTIR spectra of HPTS, CTAB and indicator ion-pairs HPTS-CTAB are recorded in Figure A.5. HPTS and CTAB were ion-paired, we would expected the spectrum of HPTS-CTAB is a overlap of the spectra of HPTS and CTAB. As shown in the figure, the infrared absorption spectrum of ion-pair is a combination of the spectra of fluorescent indicator HPTS and CTAB.

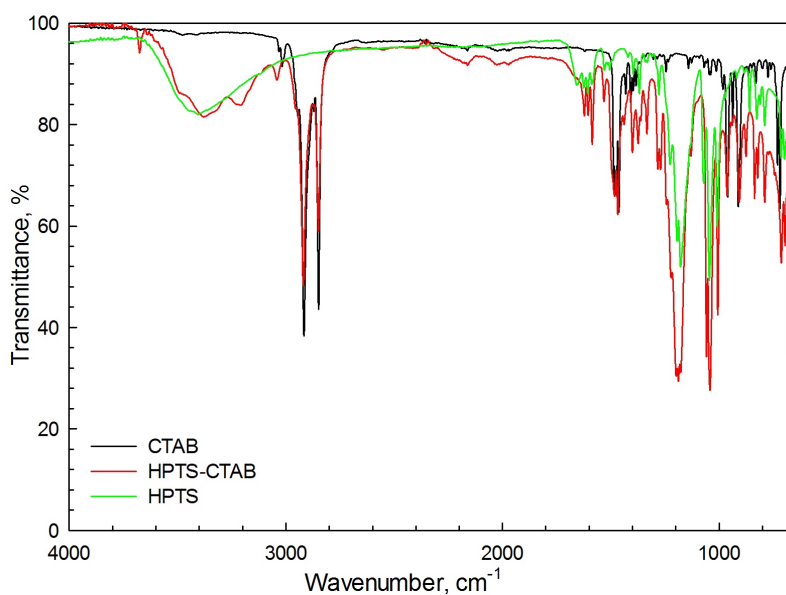


**Figure A.5.** FTIR spectra of HPTS, CTAB and indicator ion-pair HPTS-CTAB.

The FTIR spectrum of the sol-gel sample is shown in Figure A.6. Two peak bands characteristic of the Si-O-Si bonds, are centered at around 800 cm<sup>-1</sup> and 1080 cm<sup>-1</sup> and due to symmetric and asymmetric stretching of the oxygen atoms, respectively. Undesirable absorption band of the Si-OH bond at 950 cm<sup>-1</sup>, indicating there are free silanol groups on

surface of silica network. On the blue wing of this band there is a shoulder and a few bands of medium intensity. They are due to the presence of aliphatic chains, and corresponding to vibration of the carbon skeleton and bending vibrations of aliphatic groups.

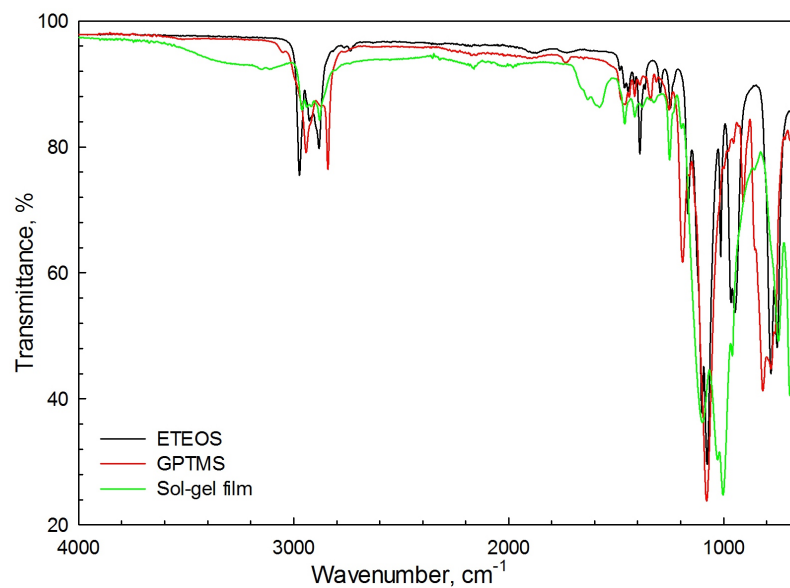


**Figure A.6.** FTIR spectra of sol-gel precursors ETEOS and GPTMS and sol-gel film.

### A.3.2 Thin film thickness of sol-gel films

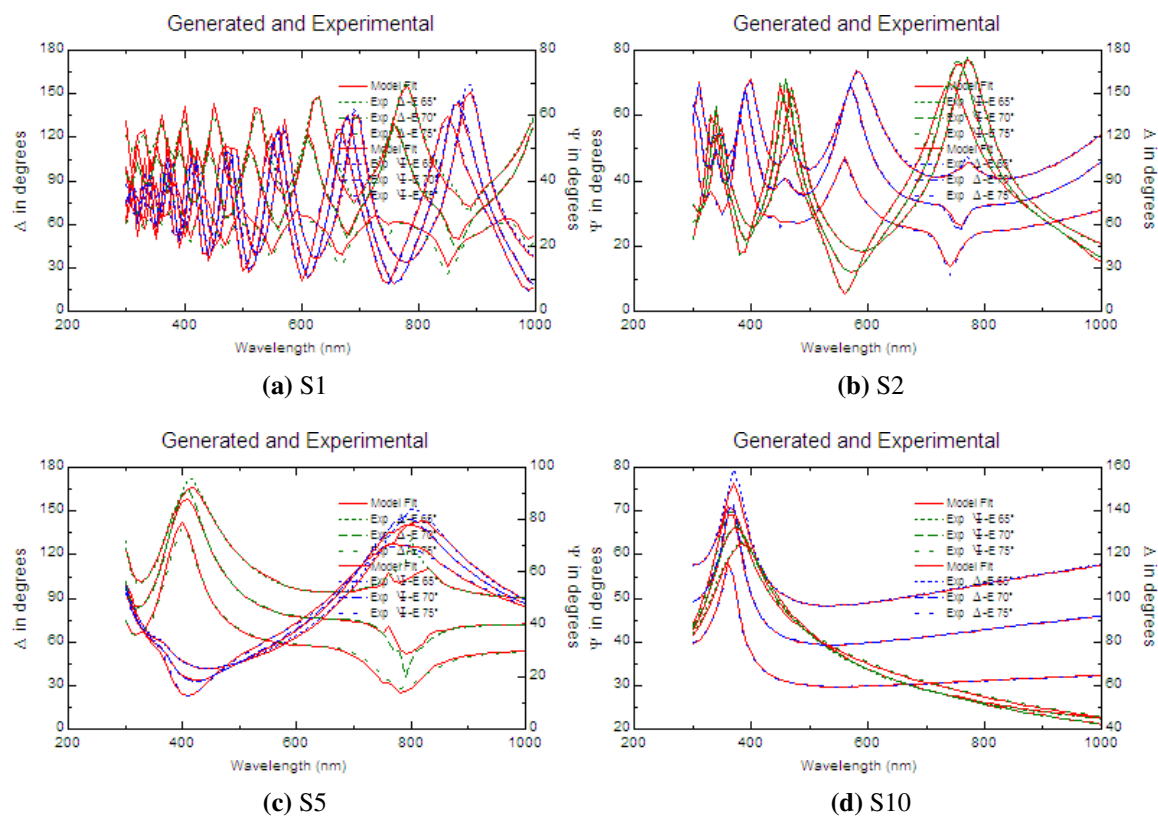


**Figure A.7.** Ellipsometry data and fitting of sol-gel thin films.

## A.4 Supplement information for Chapter 4

### A.4.1 Absorption and fluorescence excitation spectra of DHPDS in buffer

### A.4.2 Normalized absorption and fluorescence excitation spectra of DHNDS in buffer

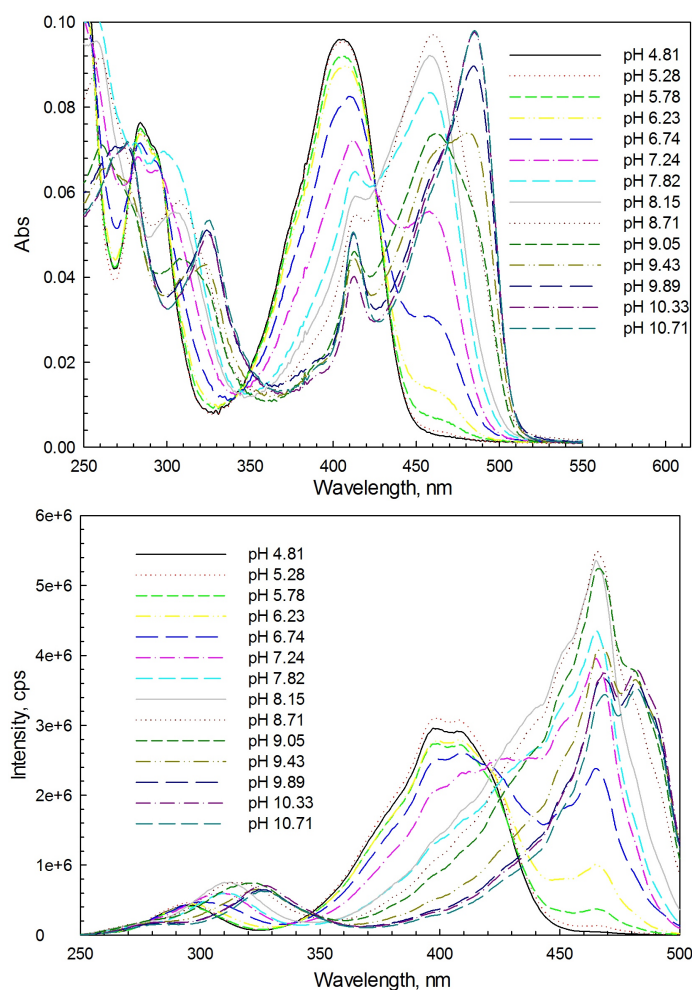


**Figure A.8.** Absorption spectra (top) and fluorescence excitation spectra (bottom) of DHPDS (1.0  $\mu$ M) in solution (IS = 0.030 M). For fluorescence excitation spectra, the emission wavelength was set at 510 nm.

#### A.4.3 Calculated swelling ratio against ionic strength of solution

#### A.4.4 Equilibrium time of HPDS-PEG hydrogel upon pH change

The equilibrium time of HPDS-PEG hydrogel upon pH change of buffer solution is short, about 4 minutes as shown in Figure A.11.



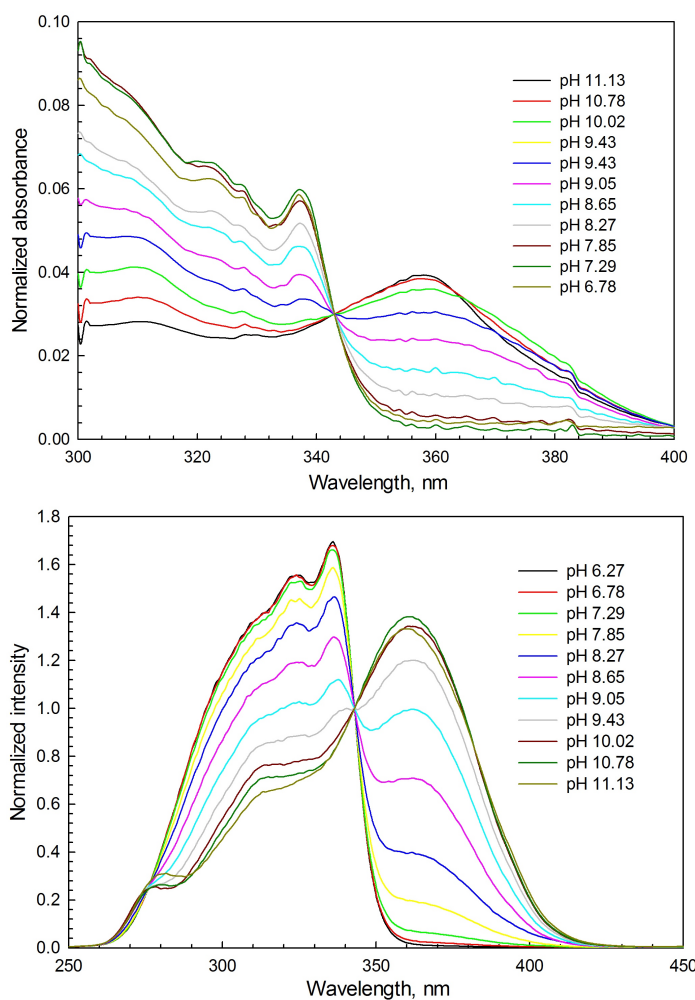


**Figure A.9.** The normalized UV-Vis absorption spectra (top) and fluorescence excitation spectra (bottom) of DHNDS (20  $\mu$ M) in solution (IS = 0.030 M).

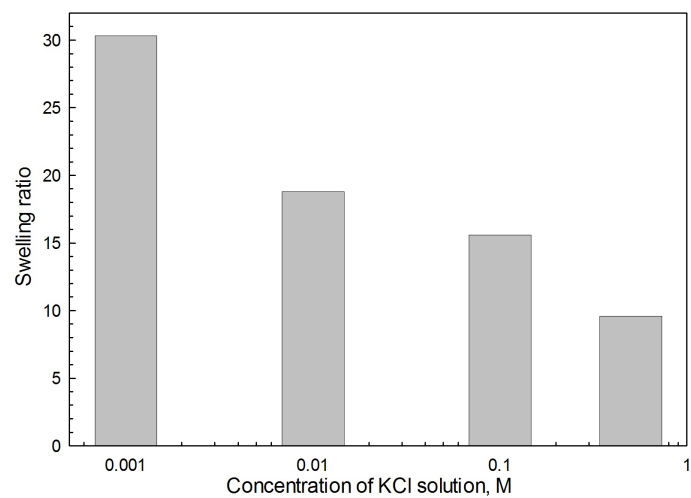


**Figure A.10.** Swelling ratio of 7.5% PEG hydrogels in KCl solution with different concentration.

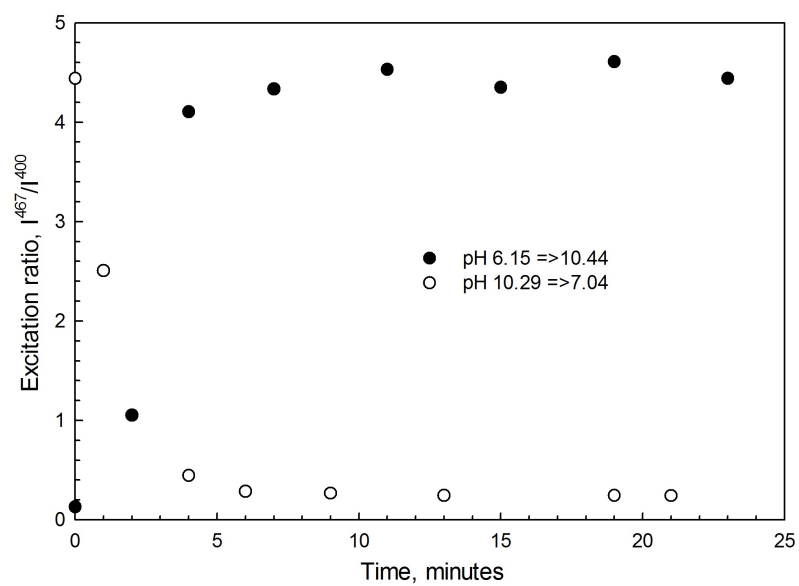


**Figure A.11.** Equilibrium time of HPDS-PEG upon pH change of solution (IS = 0.100 M).



## **APPENDIX B. COPYRIGHT AGREEMENTS**

## Figure 2.1 and 2.2.

Dear Dr. Kumar Vanga:

I am completing a doctoral dissertation at Michigan Technological University entitled "THE DEVELOPMENT AND CHARACTERIZATION OF FLUORESCENT pH SENSORS BASED ON SILICA AND HYDROGEL SUPPORT MATRICES". I would like your permission to reprint in my dissertation excerpts from the following:


[K. L. Vanga, "Implementation of Porous Silicon Technology for a Fluidic Flow-Through Optical Sensor for pH Measurements", Ph.D. dissertation, Michigan Technological University, Houghton, MI, 2012.]

The excerpts to be reproduced are: [Figure 2.5 (a) (f) and Figure 2.6]

The requested permission extends to any future revisions and editions of my dissertation, including non-exclusive world rights in all languages, and to the prospective publication of my dissertation by UMI. These rights will in no way restrict republication of the material in any other form by you or by others authorized by you. Your signing of this letter will also confirm that you own the copyright to the above-described material. If these arrangements meet with your approval, please sign this letter where indicated below and return it to me through email. Thank you very much.

Sincerely,  
Qili Hu



PERMISSION GRANTED FOR THE  
USE REQUESTED ABOVE

Sign here: 


[Dr. Kumar L. Vanga]

Date: March 23, 2013

Figure 3.1



[Home](#) [Account Info](#) [Help](#)

 **ACS Publications** High quality. High impact.

**Title:** Applications of the Sol-Gel Process Using Well-Tested Recipes  
**Author:** A. Celzard and J. F. Maréché  
**Publication:** Journal of Chemical Education  
**Publisher:** American Chemical Society  
**Date:** Jul 1, 2002  
Copyright © 2002, American Chemical Society

Logged in as:  
Qili Hu  
[LOGOUT](#)

**PERMISSION/LICENSE IS GRANTED FOR YOUR ORDER AT NO CHARGE**

This type of permission/license, instead of the standard Terms & Conditions, is sent to you because no fee is being charged for your order. Please note the following:

- Permission is granted for your request in both print and electronic formats, and translations.
- If figures and/or tables were requested, they may be adapted or used in part.
- Please print this page for your records and send a copy of it to your publisher/graduate school.
- Appropriate credit for the requested material should be given as follows: "Reprinted (adapted) with permission from (COMPLETE REFERENCE CITATION). Copyright (YEAR) American Chemical Society." Insert appropriate information in place of the capitalized words.
- One-time permission is granted only for the use specified in your request. No additional uses are granted (such as derivative works or other editions). For any other uses, please submit a new request.

If credit is given to another source for the material you requested, permission must be obtained from that source.

[BACK](#)[CLOSE WINDOW](#)

Copyright © 2013 [Copyright Clearance Center, Inc.](#) All Rights Reserved. [Privacy statement.](#)  
Comments? We would like to hear from you. E-mail us at [customer@copyright.com](mailto:customer@copyright.com)

